Tampere University

Tom Smeets

DETERMINING SMALL STRAIN SHEAR MODULUS (*G*) OF VIASVESI SAND

Resonant column - Bender Elements

Master's thesis

Faculty of Built Environment,
Civil Engineering

Tim Länsivaara
Ali Vatanshenas
Markus Haikola

May 2022

ABSTRACT

Tom Smeets: Determining small strain shear modulus *G* of Viasvesi sand
Master's thesis
Tampere University
Master in Civil Engineering
May 2022

Six samples are tested with bender element and eight samples are tested with resonant column, to respectively determine maximum shear modulus (G_{max}) and shear modulus reduction curves (G/G_{max}) for Viasvesi sand, which is a uniform sand. The stiffness is determined for increasing cell pressure from 50, to 100 and 300 kPa. Afterwards, the cell pressure is decreased again to 100 and 50 kPa to see if overconsolidation has any influence on Viasvesi sand. It is noticed overconsolidation has an important influence on both maximum shear stiffness and the stiffness reduction. Consolidation causes a deformation of the particle structure. Therefore, when the tested soil is unloaded, a stiffer response occurs. This stiffer response can be attributed to better localized restraints, but can also be attributed to more contacts which occur between the sand particles.

The values of the maximum shear modulus and shear modulus reduction curves during loading can be important in static loadings in respectively the very small and small strain area. Additionally, during dynamic loadings, for example on- and off shore wind mills, in railway construction and during service, etc. these parameters can be useful too. Therefore it is important these parameters get determined. Additionally, the effect of overconsolidation can be useful when Viasvesi sand gets preloaded. In this case, after the preload is taken away, the soil will react stiffer and deform less. Additionally, it can be useful during excavations, where the soil body will react stiffer compared to the original soil body.

The collected data with the bender elements is compared to equations of other authors during this study. During analysing the data it is noticed previously published equations are not suitable for Viasvesi sand. These equations underestimated the maximum shear stiffness. This safer estimation can be attributed to the wide range of uniformity coefficients wherefor these equations are proposed for. While the tested Viasvesi sand has a uniformity coefficient C_u of 2, the proposed equations by the other three authors are for much wider ranges of C_u, from 1.5 to 15. Therefore, a possibility exists these equations are not applicable for every type of sand.

To predict the maximum shear modulus of Viasvesi sand, two equations are proposed. The reason of proposing two equations is because of some irregularities in the measurements, some data was not comparable with each other. Therefore a decision is made to propose two equations. Eventually, it is noticed both equations have an R^2 above 0.90 which is an acceptable accuracy. Additionally, both equations are more correct on Viasvesi sand, compared to previous noticed equations.

After conducting tests, the maximum shear stiffness obtained via bender element and resonant column are plotted against each other. It is noticed the data differed not too much from each other, with R^2 above 0.98. Additionally, it is noticed bender element measurements estimate the maximum shear stiffness in most cases higher compared to resonant column tests.

Keywords: Resonant column, Bender elements, Small strain shear stiffness, Shear stiffness reduction, Overconsolidation, Viasvesi sand

PREFACE

During my Master's thesis, I have had the chance get further into contact with different geotechnical aspects. This was not always easy, because I mainly had to do my full thesis in one semester (two periods) due to my exchange. A wise man once said: 'doing research is a roller-coaster of emotions. Sometimes one simply is stuck.' Nevertheless, I tried to keep the motivation high, even when it seemed or became clear I would not be able to finish my thesis how I wanted it to be.

Due to COVID or COVID-measures, it was not always easy to reach the person(s) I needed. For example, sometimes people worked at home instead of at the university. Additionally, it also occurred that persons I needed were at home with a COVID-infection. Nevertheless, I tried to make the best of it.

I was surrounded by people motivated to help me whenever it was needed. First of all, I would like to thank Ali Vatanshenas for helping me with finding information. In addition, whenever I asked I was able to get guidance or counsel from him about writing my paper or about my laboratory work.

Next to this, I would like to thank Markus Haikola for helping me with the beginning of the practical work from my Master's thesis.

Whenever I had a problem with the resonant column or bender elements, I was able to fall back on the help of Antti Akkanen. Therefore, I would like to thank him, because without his help I would not have been able to do my testing series. Additionally, I would not have been able to start the testing series without him.

Besides, Nuutti Vuorimies deserves special thanks, because without his help the testing series would have been much more difficult to conduct. Besides, I would have been doing things in a much more complex way. Next to this, I was able to fall back on his counsel, whenever I needed it.

Finally, I would like to thank, my supervisor, professor Tim Länsivaara for the guidance he gave me during the thesis.

Tampere, 16 May 2022

Tom Smeets

CONTENTS

1.INTRODUCTION..1

2.LITERATURE REVIEW..3

2.1 Maximum shear modulus G_{max} 3

2.1.1 Affecting parameters on G_{max} and the damping............................3
2.1.2 Sample disturbance 7
2.1.3 Predicting G_{max}...8
2.1.4 Influence of grain shape and fines content on G_{max}.....................11
2.1.5 Comparing measured and predicted results...............................15
2.1.6 Effect of fines content and p' on the small strain stiffness 20
2.2 Stiffness degradation 21

2.2.1 Effect of void ratio e and effective confining pressure 21
2.2.2 Effect of plasticity index PI 23
2.2.3 Effect of cyclic shear strain amplitudes 26
2.2.4 Effect of cyclic loading...29
2.2.5 Effect of overconsolidation 31
2.3 Resonant column test 33

2.4 Bender element test 34

2.4.1 Determining G_{max} with bender elements.....................................35
2.4.2 Interpreting results of bender elements......................................36
2.5 Comparison of results from bender elements and resonant columns . 40

3.MATERIALS AND METHODOLOGY 44

3.1 Localisation of Viasvesi 44

3.2 Soil classification according to EN ISO 14 688-1...............................44

3.3 Materials and methodology 45

3.3.1 Sieving column – grain size distribution 45
3.3.2 Particle density – pycnometer 48
3.3.3 Proctor compaction and dry density 49
3.3.4 Void ratio 52
3.3.5 Moist – and dry tamping and undercompaction method 53
3.3.6 Air pluviation method 56
3.3.7 Wet pluviation 56
3.3.8 Preparing of the sample...58
3.3.9 Preparing the triaxial cell..60
3.3.10 Skempton-B factor...61
3.3.11 Resonant column and bender element test...............................65
3.3.12 Resonant column test 66
3.3.13 Bender element test..73
3.3.14 Evaluation of G_{max}...76
4.RESULTS 77

4.1 Grain size distribution..77

4.2 Particle density...78

4.3 Proctor compaction 79

4.4 Saturation degree of test specimens 80

4.5 Void ratio, height, diameter, water content and dry densities..............81

4.6 Resonant column tests 82
  4.6.1 Calibrating parameters testing device 82
  4.6.2 Results 83
4.7 Bender element tests 122
4.8 Comparison of G_{max} from bender elements, resonant column and predictions 128
4.9 Proposing equations for determining very small strain shear stiffness of Viasvesi sand 136
5. DISCUSSION 141
5.1 Occurred difficulties 141
5.2 Resonant column tests 142
  5.2.1 Shear modulus reduction for Viasvesi sand 142
  5.2.2 Normalized shear modulus reduction with normalisation with resonant column for Viasvesi sand 143
  5.2.3 Normalized shear modulus reduction with normalisation with bender elements for Viasvesi sand 144
5.3 Bender element tests 145
5.4 Comparison of G_{max} from bender elements, resonant column and predictions 145
5.5 Proposition of equation to determine very small strain shear stiffness of Viasvesi sand 146
6. CONCLUSIONS 147
7. FUTURE (RESEARCH) POSSIBILITIES 149
REFERENCES 150
TEST 6 162
TEST 7 163
TEST 8 164
TEST 9 165
TEST 10 166
TEST 11 167
TEST 12 169
TEST 13 170

LIST OF FIGURES

Figure 1. Types of shear strain and which test is suitable for the certain strain level [1] ... 1
Figure 2. Effect of PI and effective confining pressure on shear modulus ratio [16]... 5
Figure 3. Affecting processes from excavation to triaxial test [23] ... 7
Figure 4. Accelaration of a sample measured during transport [23]... 8
Figure 5. Characterization chart of particle shapes (according to Krumbein and Sloss) [22]... 12
Figure 6. Effect of the proposed formulation (9) compared to (2), (3), (4) and (5) on blue sand [22] ... 13
Figure 7. Effect of the proposed formulation (9) compared to (2), (3), (4) and (5) on Sydney sand [22] ... 14
Figure 8. Effect of the proposed formulation (9) compared to (2), (3), (4) and (5) on bricky sand [22]... 14
Figure 9. Predicted G_{max} *with M (equation (2)), SR (equation (3)), WT (equation (4)), SAP (equation (5)) (abscissa) and measured* G_{max} *(ordinate) by a resonant column [22]... 16*
Figure 10. G_{max} *by equal void ratio e=0.55, as function of* C_u*, mean effective confining pressure and* d_{50} *[17]... 17*
Figure 11. $G_{max}(e)$ *for different* C_u *and* d_{50} *[17]... 17*
Figure 12. $G_{max}(e)$ *for different uniformity coefficients* C_u *at different pressures [17]... 18*
Figure 13. Step-wise linear (a), gap-graded (b) and smoothly shaped (c) tested materials [26] ... 19
Figure 14. G_{max} *for different void ratios e at different uniformity coefficients [26] ... 19*
Figure 15. $G_{max}(FC)$ *for different p' and different* D_r *[31]... 20*
Figure 16. $G_{max}(p')$ *for different FC and different* D_r *[31] ... 20*
Figure 17. $G_{max}(e)$ *for different FC for sandy soils [31] ... 21*
Figure 18. Effect of void ratio on the shear modulus (a) and shear modulus ratio (b) [15] ... 22
Figure 19. Effect of effective confining stress on the shear modulus (a) and shear modulus ratio (b) of sand [15]... 22
Figure 20. Dynamic shear modulus ratio (a) and damping (b) as function of the cyclic strain amplitude with different plasticity indexes [34]... 24
Figure 21. Dynamic shear modulus ratio (a) and damping (b) as function of the cyclic strain with different void ratios [34] ... 24
Figure 22. Physical meaning of parameters in stress strain relation [15]... 26
Figure 23. Shear strain degradation curve at different cyclic shear strain amplitudes [34]... 27
Figure 24. Hysteresis loop of first loading, unloading and reloading [15]... 28
Figure 25. Shear modulus ratio and damping as function of the cyclic shear strain amplitude for a number of cycles [34]... 29
Figure 26. Hysteresis curves for different loading stages [34] ... 29
Figure 27. Cyclic undrained shear strain on clay [15]... 30
Figure 28. Different cyclic shear strain cycles on clay [15] ... 31
Figure 29. Effect of loading and unloading on the small strain shear modulus of Drammen clay [39], taken from [15] ... 32
Figure 30. Effect of the overconsolidation ratio for low plastic clays [15]... 33
Figure 31. Resonant column device [17]... 34
Figure 32. Fixed-free principle [40]... 34
Figure 33. Working area for bender element tests [41]... 35
Figure 34. Effect of C_u *(a) and* C_c *(b) on mean shear wave velocity [9]... 36*

Figure 35. Difference between PTP (P_i) and FTOA (S_i) [43]...................................... 37
Figure 36. Difference in shear wave velocity between MFTOA (x) and MPTP (y) [9]...................................... 37
Figure 37. Cross-correlation method [43]...................................... 38
Figure 38. Shear wave velocity as function of the source frequency by manual interpretation [9]...................................... 38
Figure 39. The difference in shear wave velocity between different analyzing methods [9]...................................... 40
Figure 40. Effect of frequency (a) and effective confining pressure (b) at the shear wave velocity by dry Fuijian sands [43]...................................... 42
Figure 41. Effect of frequency (a) and effective confining pressure (b) at the shear wave velocity by saturated clean Fuijian sands [43]...................................... 42
Figure 42. Effect of effective confining pressure at the shear wave velocity by saturated natural Hangzhou and Nanjing sands [43]...................................... 43
Figure 43. Localisation of Viasvesi...................................... 44
Figure 44. Sieving configuration...................................... 47
Figure 45. Pycnometer test...................................... 49
Figure 46. Proctor compaction set-up...................................... 49
Figure 47. Moistening of the sample...................................... 50
Figure 48. Compacting the sample...................................... 50
Figure 49. Result after compaction and flattening...................................... 51
Figure 50. Moist - and dry tamping...................................... 53
Figure 51. Preparing the sample and triaxial cell...................................... 54
Figure 52. Wet pluviation set-up with flask...................................... 56
Figure 53. Draining and loading piece...................................... 58
Figure 54. Preparing the sample with wet pluviatioin method; (a): adding sand; (b): static loading...................................... 58
Figure 55. Result of a prepared sample...................................... 60
Figure 56. Triaxial cell: (a) open; (b) closed...................................... 61
Figure 57. Evolution of Skempton-B factor with the saturation degree [62]...................................... 63
Figure 58. Output measurement of Skempton-B...................................... 64
Figure 59. Set-up to determine the Skempton-B factor...................................... 64
Figure 60. Triaxial cell with bender elements and resonant column [5]...................................... 65
Figure 61. Symmetrical ellipse around origin (resonance) and unsymmetrical ellipse (no resonance) around u (displacement) - and Q (excitation force) - axis [63]...................................... 67
Figure 62. Sample in resonance: (a) Phase shift; (b) elliptical curve of displacement and excitation force...................................... 68
Figure 63. Sample loaded below resonance frequency...................................... 68
Figure 64. Test setup of a bender element (a) and working principle (b) [41]...................................... 74
Figure 65. Near-field effect [43]...................................... 76
Figure 66. Grain size distribution Viasvesi sand...................................... 78
Figure 67. Proctor curve...................................... 79
Figure 68. Shear modulus reduction curve for increasing and decreasing pressure...................................... 89
Figure 69. Effect of loading and unloading on shear modulus reduction at 50 kPa...... 92
Figure 70. Effect of loading and unloading on shear modulus reduction at 100 kPa...................................... 94
Figure 71. Shear modulus reduction curve at constant pressure and different void ratios for test 6, 7 and 8...................................... 97
Figure 72. Shear modulus reduction curve at constant pressure and different void ratios for test 9, 10, 11, 12 and 13...................................... 99
Figure 73. Normalized shear modulus reduction curve for increasing and decreasing pressure...................................... 102

Figure 74. Effect of loading and unloading on normalized shear modulus reduction at 50 kPa ... 105
Figure 75. Effect of loading and unloading on normalized shear modulus reduction at 100 kPa ... 107
Figure 76. Normalized shear modulus reduction curve at constant pressure and different void ratios for test 6, 7 and 8 ... 110
Figure 77. Normalized shear modulus reduction curve at constant pressure and different void ratios for test 9, 10, 11, 12 and 13... 112
Figure 78. Normalized shear modulus reduction curve for increasing and decreasing pressure... 115
Figure 79. Effect of loading and unloading on normalized shear modulus reduction at 50 kPa ... 118
Figure 80. Effect of loading and unloading on normalized shear modulus reduction at 100 kPa ... 120
Figure 81. Normalized shear modulus reduction curve at constant pressure and different void ratios for test 6, 9, 10, 11, 12 and 13... 122
Figure 82. Evolution of G_{max} (a) and shear wave velocity (b) measured with bender elements for test 6... 124
Figure 83. Evolution of G_{max} (a) and shear wave velocity (b) measured with bender elements for test 9... 125
Figure 84. Evolution of G_{max} (a) and shear wave velocity (b) measured with bender elements for test 11... 126
Figure 85. Evolution of G_{max} (a) and shear wave velocity (b) measured with bender elements for test 12... 127
Figure 86. Evolution of G_{max} (a) and shear wave velocity (b) measured with bender elements for test 13... 128
Figure 87. G_{max} from bender elements and resonant column compared with Menq, Wichtmann and Triantafyllidis and Senetakis et al.... 133
Figure 88. Menq (2), Wichtmann and Triantafyllidis (4) and Senetakis et al. (5) compared to bender elements and resonant column... 135
Figure 89. Comparison of maximum shear modulus between bender elements and resonant column... 135
Figure 90. Test 6, 7 and 8 compared to the proposed equation (54)... 138
Figure 91. Test 9, 10, 11, 12 and 13 compared to the proposed equation (54) ... 138
Figure 92. Loading and unloading cycle compared with equation (54) for test 6, 7 and 8... 139
Figure 93. Loading and unloading cycle compared with equation (55) for test 9, 10, 11, 12 and 13 ... 140

LIST OF SYMBOLS AND ABBREVIATIONS

A	Area of the used sieve
ADF_a	Apparatus damping factor
(A/M) FTOA	(Automated/manual) first time of arrival
(A/M) PTP	(Automated/manual) peak-to-peak
ACC	Automated cross correlation
AZC	Automated zero crossing
B	Skempton-B factor
c	Cohesion of the soil
c_a	Apparatus damping of resonant column
C_c	Coefficient of curvature
C_u	Coefficient of uniformity
C_α	Secondary consolidation coefficient
CR_i	Torque motor input by 0.707 (index 1) respectively 1.414 (index 2) times $f_{resonance}$
d	Distance between transmitter and receiver
d	Apperture size of the sieve
d	Grain size
d	Diameter calibration rod
d_i	Diameter of parts resonant column Index 2: active and platen used to calibrate the system Index 3: active end platen used to test the soil
D	Damping
D	Diameter of the tested sample
D	Maximum grain size of the sample
D_r	Relative density
d_{10}	Sieve diameter with 10 mass% fall-through
d_{30}	Sieve diameter with 30 mass% fall-hrough
d_{50}	Sieve diameter with 50 mass% fall-through
d_{60}	Sieve diameter with 60 mass% fall-through
dV_a	Change in the pore air volume
dp'	Change in effective pressure
e	Void ratio
e_{max}	Maximum possible void ratio
e_{min}	Minimum possible void ratio

e_0	Initial void ratio
FC	Fines content
f_r	Resonance frequency
f	Frequency
f_{rod}	Resonance frequency during calibration with rod
f_a	Resonance frequency without sample or calibration rod
G_{max}	Maximum small strain shear stiffness
G/G_{max}	Shear modulus ratio or normalized shear modulus
G	Shear modulus
G_s	Secant shear modulus
G_t	Tangent shear modulus
G_{rod}	Shear stiffness calibration rod
h_i	The height of the sample after tamping layer i
H	Height of the tested sample
I_D	Density index
J	Inertia of the tested soil sample
J_a	Inertia of the active end
K_0	Neutral ground pressure
k_{rod}	Spring constant with calibration rod
k_a	Resonant column apparatus spring constant without specimen or calibration rod
L	Height of the sample
L_{tt}	Tip-to-tip travel distance of the shear wave between two bender elements
L	Length calibration rod
LL	Liquid limit
M	Dry mass of the specimen
M_d	Dry mass of the specimen
M_1	Dry mass before the sieving procedure
M_2	Dry mass after the sieving procedure
M_i	Mass of parts resonant column Index 2: active and platen used to calibrate the system Index 3: active end platen used to test the soil
MMF_{calc}	Calculated modified magnification factor
MMF_{meas}	Measured modified magnification factor
n	is the total amount of layers

N	Total amount of cycles
OCR	Overconsolidation ratio
P	Mass of fines content left in the pan after the sieving procedure
p'_0	Initial effective stress
p_{a0}	Initial air pressure
$P = P' = \sigma'_m$	Effective confining pressure
$P_a = \sigma'_{ref}$	Atmospheric pressure
PI	Plasticity index
PL	Plastic limit
R	Roundness
$R * T * r * d * g$	Output of the rotational transducer
r_t	Radial distance of the transducer to the center axis
S	Sphericity
S_{r0}	Saturation degree
S_θ	Sensitivity of accelerometer
S_a	Sensitivity of accelerometer
t	Travel time of the shear or pressure wave
t	Time
t_p	Time to end primary consolidation
T_a	Active-end inertia factor
t_g	Geological age
TMR	Torque motor ratio
$T_r * d * g$	Input current through the motor
U_i	Undercompaction degree
V_0	Initial volume
V	Volume of the can containing the sand
V	Volume
V_p	Pressure wave velocity
V_s	Shear wave velocity
V_{solids}	Volume of the solids
V_{voids}	Volume of the voids
W	mass% of water in tested sample
W_d	Dry mass of the tested sample
W_n	Moist mass of the tested sample
$W_s - W_w$	Dry mass of the aggregate
W_{sw}	Mass of water and aggregate in the pycnometer

W_w	Mass of water in the pycnometer
w_l	Liquid limit
w_p	Rollout limit
γ_a	Cyclic shear strain amplitude
γ_d	Dry weight per m³ of the sand
γ^E	Limit with elastic to elasto-plastic response
γ^P	Limit with elasto-plastic to plastic response
γ_r	Reference strain
γ_{ref}	the strain where $G = 0.7 * G_{max}$, determined with Mohr-Coulomb
ΔU_c	Difference in pore water pressure
$\Delta\gamma$	Change in shear strain
$\Delta\tau$	Change in shear stress
$\Delta\sigma_c$	Difference in confining pressure
θ	Rotation of the soil sample
θ_a	Rotational motion
θ_i	Rotation by 0.707 (index 1) respectively 1.414 (index 2) $* f_{resonance}$
κ	Isotropic compressibility of soil in elastic conditions
λ^*	Dimensionless frequency factor
σ'_1	Maximum effective stress
ρ	Dry density of the soil
ρ	Regularity
ρ_p	Particle density
ρ_w	Density of water
τ_{appl}	Applied torque during resonant column test
τ_{max}	Maximum shear stress
φ_p	Friction angle
φ'	Effective friction angle

1. INTRODUCTION

The target of this study is to define very small and small strain shear stiffness parameters for Viasvesi sand. This is done using bender elements to determine the maximum shear modulus G_{max} and a resonant column to determine the stiffness degradation as function of strain. When strains are smaller than approximately 10^{-5} to 10^{-6}, strains can be seen as very small strains, while strains lower then 10^{-3} can be seen as small strains. Figure 1 [1] gives a clear view about the different types of strain and how the normalized shear modulus decreases with increasing strain. As can be seen in Figure 1 [1], when shear strains occur in the very small strain area, the shear modulus can be seen as nearly constant, in a logaritmic scale. Additionally, Figure 1 [1] gives a view on which tests are suitable for certain strain levels.

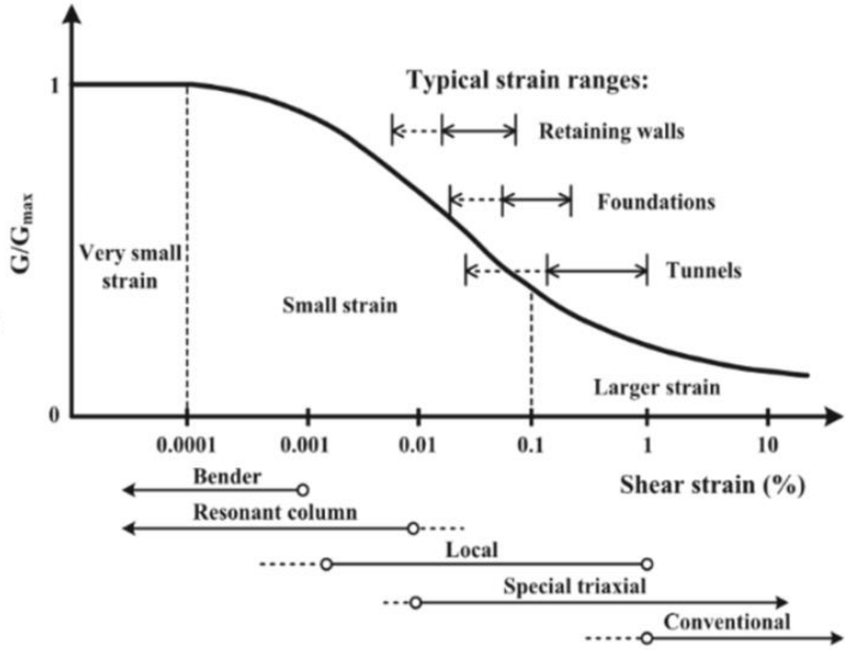

***Figure 1.** Types of shear strain and which test is suitable for the certain strain level [1]*

The very small strain shear stiffness G_{max} and the small strain shear stiffness are used in soil mechanics to determine the behavior of soils to dynamic loadings, like earthquakes, railway vibrations, off-shore oil and gas industry, off- and on-shore windmills,… but can also be used for static loadings which occur in the (very) small strain area. Therefore, the received data for G_{max}, collected with bender elements, will be compared to equations proposed by previous studies. Next, a proposal will be done at the end of the study to predict the very small strain shear stiffness G_{max} for Viasvesi sand, which is determined by bender elements. Next to proposing an equation to determine G_{max}, the small strain shear stiffness behavior will be studied. Via these data, reduction curves similar to Figure 1 [1] will be created. Following on creating the stiffness reduction curves, the data which are collected will be compared with previous studies.

During the literature review, not much information was found about earlier research where the sample was unloaded. Therefore, during this research samples will first be loaded, whereafter the necessary measurements will be done after nearly-fully consolidation in the certain pressure step. After this, the pressure will be decreased again, whereafter the necessary measurements will be done again. The effect of overconsolidation will thus be studied.

Before it is possible to start with the effective testing series, some additional data is collected. To conduct these bender element and resonant column tests, a few methods were tested to prepare the sample. These are two variants on wet pluviation, moist tamping and dry tamping. Therefore, to select the most suitable method, the reached densities, moist content and saturation degrees are studied. Before these methods to prepare samples were able to be tested, the particle density of the sand is determined. The importance of the particle density is that in previous research it is noticed that void ratio has an influence on the small strain shear stiffness and maximum shear stiffness. Via the particle density, void ratio is easily determinable. Additionally, a proctor curve is derived from testing series. This curve is for example used in the moist tamping method to define at which water content, it is possible to get the highest density with the least effort. Besides, to define the Viasvesi sand its sand type, the grain size distribution is derived. The target of determining the grain size distribution is to make it possible to compare the conducted research with previous researchers their findings.

First, the literature review is ‘briefly’ discussed. During this literature review, the findings of previous researchers will mainly be studied. Additionally, some of the results from previous conducted research is discussed in the literature review. Besides, during the literature review an introduction into the resonant column and bender elements is given. Following on the literature review, a description of materials and methodology is presented. In this section there is gone into detail in the standards and eventually used methods to define the sand its characteristics. Besides, bender element and the resonant column will be discussed furthermore. Thereafter, the results will be shown in the next section, with a brief description what can be seen in the curves. Following on the results, the meaning of these results will be discussed in the next section. Finally, a conclusion and possibilities for future research is given in the final sections.

2. LITERATURE REVIEW

2.1 Maximum shear modulus G_{max}

The very small strain shear stiffness G_{max}, or the maximum shear modulus, is the stiffness which soil has when very small shear strains are introduced. These very small strains are defined as strains of approximately 10^{-5} to 10^{-6}. As the name ‘maximum shear modulus’ makes clear, the stiffness is maximal when these very small strains are introduced. In other words, when a small change of the shear stress is introduced, the strains are minimal in comparison with greater stress changes.

In this section a description will be given of parameters which affect G_{max} and the damping. Additionally, a short explanation will be given about sample disturbance due to removal, transport and manipulation. Besides, a limited number of formulations will be given to predict the very small strain shear stiffness. Additionally, a few outcomes from other authors will be described.

2.1.1 Affecting parameters on G_{max} and the damping

In this section parameters which affect the very small strain stiffness will be discussed. Table 1 [14] gives an overview what the importance is of different parameters on G_{max}. It shows that the strain amplitude, confining stress, void ratio and diagenesis are respectively the 4 most important parameters for clean sands. In addition, the grain size characteristics and the effective material strength are seen as 2 lesser important parameters. Besides, the overconsolidation ratio, strain history, strain rate, saturation degree and the dilatancy are seen as relatively unimportant parameters, while the plasticity index is given to have no influence by clean sands. Next to the overview given by [14], the outcome from other authors on non-cohesive soils is given in Table 1.

Additionally, a brief summary will be given of the very small strain stiffness at the level of the soil particle.

Table 1**. Parameters that effect the small strain stiffness and their importance **[14]

Parameter	Clean sands [14]	Cohesive soils [14]	Other research, non-cohesive soils
Strain level	V	V	V [15]
Confining stress	V	V	V [4], [16]
Void ratio	V	V	V [17]
Plasticity index	-	V	
Overconsolidation ratio	R	L	
Diagenesis	V	V	V [18], [19]
Strain history	R	R	L [20]
Strain rate	R	R	R [21]
Effective material strength	L	L	
Size, shape, gradation	L	L	V [5], [22]
Degree of saturation	R	V	R [23]
Dilatancy	R	R	

*V is very important
*L is less important
*R is relative unimportant
*- is no influence

2.1.1.1 G_{max} on soil particle level of sand

In soil structures, different inter-particle forces occur. These inter-particle forces can be different for different soil types. Sand has a typical behavior where particles behave as single units, in contrast with cohesive soils such as clays. Besides, forces appear at the contact points to prevent penetration of other particles (born repulsion) and chemical bonding might appear between the particles (primary valence bonds). These primary valence bonds cause an increased stiffness together with other diagenesis processes.

Additionally, soil structures have a specific composition, which is for every soil or sample different. Particles have different shapes, and thus pores are composed differently. Because of this, the stiffness of the soil can be influenced.

To describe the effects of soil on particle level, it might be recommended to use numerical models. It needs to be noted that this is an elaborate task, as shown in [14].

2.1.1.2 Very affecting parameters on clean sands according to [14]

Stiffness of soils decrease with increasing strain [14]. This change of shear modulus starts at very small strains. If the load is reversed, the soil will recover its initial stiffness and the accumulated strain will be the new reference point for the strain, as shown in Figure 24 [15]**.** An explanation for the recovering of small strain shear stiffness might be that the particle structure of the soil is changed. Therefore, the soil will react stiffer during a load reversal, because more particle contacts are available or the contact points are better localized. Further notice about load reversal will be given in section 2.2.3.

Besides, for non-cohesive soils the effective confining stress has a dependency with the small strain stiffness which can be written as [14]:

$$G_{max} \propto p'^{n}$$

Where

$0.40 \leq n \leq 0.55$

In addition [4] mentions another correlation for *n* as given in section 2.1.3 with equation (4). This correlation states $1.5 \leq C_u \leq 15$, which would mean with the given correlation by equation (4), *n* can go up to 0.65 when $C_u = 15$. Hereby it can be concluded *n* has no fixed limit.

Given that the small strain stiffness is proportional with the effective confining pressure, it can be considered the shear modulus decreases at higher strain levels with increasing confining pressures [14]. A clear view about this is given by Figure 2 (a), where the shear modulus ratio *G/G_{max}* decreases later at greater effective confining stresses [16].

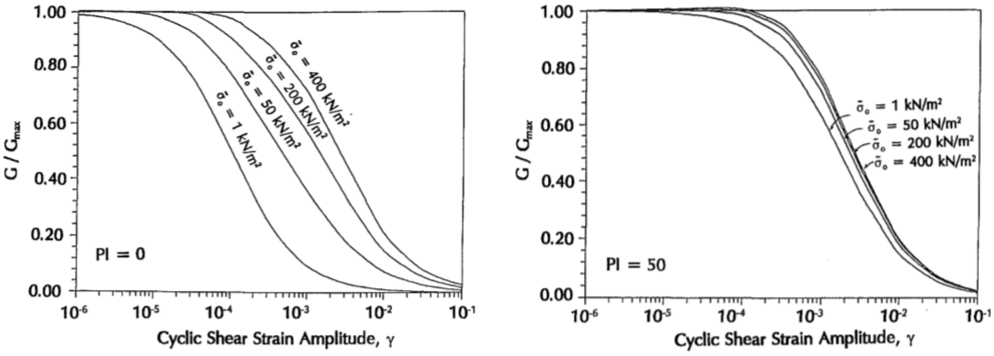

FIG. 9. G/G_{max} **versus** γ **for PI = 0 with Various** $\bar{\sigma}_0$

FIG. 10. G/G_{max} **versus** γ **for PI = 50 with Various** $\bar{\sigma}_0$

(a) (b)

Figure 2. *Effect of PI and effective confining pressure on shear modulus ratio* ***[16]***

Next to the effective confining pressure, it is well known the very small strain shear stiffness depends on the void ratio. Besides, it is stated in [14] the void ratio has few influence on the damping in non-cohesive soils. Due to this [14] gives 2 relations which are widely used to determine the very small strain shear stiffness, and are confirmed by [17]:

For round sand: $G_{max} \propto \frac{(2.17-e)^2}{1+e}$ For angular sands: $G_{max} \propto \frac{(2.97-e)^2}{1+e}$

Additionally, diagenesis, the process which influences the soil with metamorphism, can alter the stiffness of soils due to a change of the soil structure, as [14] mentions. Two processes are given to have a considerable effect: 'aging' and 'cementation'. The effect of aging mainly occurs by sands, sandstones, clays and clayey sands due to secondary compression, while cementation mainly occurs by sandy soils and is not necessarily linked to secondary compression. It should be mentioned diagenetic can be lost when stress-state changes are introduced. Due to this laboratory samples can give considerable different results than in-situ tests.

An empirical expression (1), proposed by [18], [19] is given which describes the change of the small strain stiffness over time due to diagenesis:

$$\frac{G_{max}(t)}{G_{max}(t_p)} = 1 + C_{\alpha}^{0.5} * log\left(\frac{t}{t_p}\right) \qquad (1)$$

Where

t_p is the time to end the primary consolidation

$t > t_p$ with t the past time

C_α is the secondary consolidation coefficient

2.1.1.3 Soil plasticity

According to Table 1 [14], the plasticity index *PI* has no or a negligible influence on clean sands. This can be concluded because the plastic area is extremely small or non-existent. It should be noted the plasticity will have an important influence in cohesive soils, thus if soil with an important amount of clays or silts are tested it will have an influence.

2.1.1.4 Relatively unimportant affecting parameters on clean sands according to [14]

[14] states the overconsolidation ratio of cohesive soils increases the small strain stiffness. In addition it is mentioned non-plastic soils are negligible affected by the overconsolidation ratio. Due to this it can be stated sand is not affected because the plastic area of sand is small. This is something the tests will confirm or contradict because first the confining pressure will be increased and afterwards it will be decreased.

Additionally, in cyclic loadings, the small strain, as function of the shear stress follows a hysteresis loop. During the first loading, the strain will be less than in unloading and reloading cycles, with a ratio of $\gamma_{reloading} = 2 * \gamma_{initial\ loading}$, according to [20]. Further notice about hysteresis loops will be given in section 2.2.3.

Besides, the strain rate, which is a deformation (strain) over time [21], is attributed to the plasticity of a soil. Thus it can be stated there is no or a negligible strain rate in sands. [14]

Next, [14] mentions clean sands, dry or saturated, have the same G_{max} at identical effective confining pressures. A consequence of this is that the saturation degree can be neglected while testing clean sands. It should be noted capillary effects might influence the small strain shear modulus when higher ratios of fines content are present. In this case the degree of saturation cannot be neglected. In addition [23] mentions shear modulus should be the same, both in drained and undrained tests. This is due to the given that water cannot carry shear.

2.1.1.5 Grain shape and grain size distribution

According to [14] the grain shape has a small effect on the very small strain stiffness. In contradiction with this [22] mentions it has an effect which can reduce the deviation between predicted results. Notice will be taken on the research of [22] in section 2.1.4.

In addition the grain size distribution has a considerable effect on the small strain stiffness. Further notice will be given on the effect of the grain size distribution curve on the small strain shear modulus in section 2.1.3 and 2.1.4, where formulas will be proposed to predict G_{max}. [22], [5]

2.1.2 Sample disturbance

Disturbance of the soil sample during removal from the ground, is affected by different factors. [23] explains different factors which affects the determination of the small strain stiffness on clay samples. A clear view of this is given in Figure 3 [23].

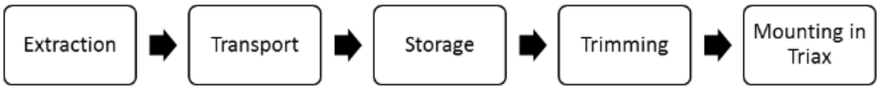

Figure 3. *Affecting processes from excavation to triaxial test* ***[23]***

First of all, the effective stress is changed, which causes the soil to react different. In addition an effect exists of the speed with which a soil sample is removed. If strains of the centerline are minimized during removal and the sample is reconsolidated afterwards to conditions in field, behavior of the field can be approximately captured.

Next to the effective stress change, a secondary disturbance often occurs, due to penetration, cutting and pressing, and extraction of the sample. These factors can cause damage to the particle structure, and thus reduce the small strain stiffness. In addition [23] mentions water redistribution, gas dissolution and chemical and biological processes during storage might affect the stiffness. Besides, Figure 4 [23] shows clearly that during transport of a sample, enormous accelerations, up to more than 20 m/s², occur. These are enormous accelerations and thus can have a big effect on the sample. Although effective stress change is the largest factor, these cumulated factors can be as big as the effects of the effective stress change. It should be noted that the previous described effects can be soil dependent, due to for example cohesion.

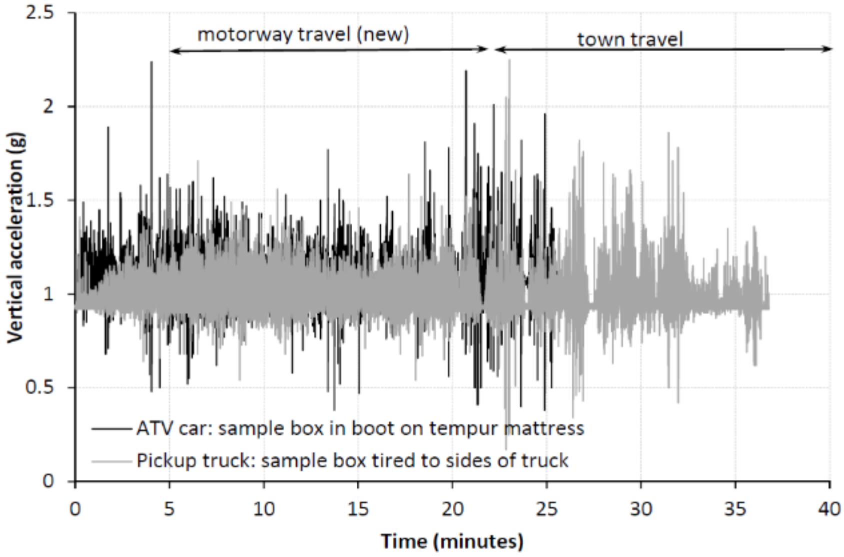

Figure 4. *Accelaration of a sample measured during transport* ***[23]***

Next to samples distracted from the field, it is also possible to build samples in the laboratory. In this case, disturbance from extraction, transport, storage and trimming will be excluded. Though, the behavior of the sample will be different, because no field circumstances will be simulated and the samples composition will be different. During this thesis, samples of sand will be built in the laboratory.

2.1.3 Predicting G_{max}

According to [22], [5], the very small strain shear modulus G_{max} is primarily dependent on the void ratio e and the mean effective confining pressure p'. In addition the small strain shear modulus is linked to the coefficient of uniformity. [22] gives expression (2) to (5) to determine G_{max}. In addition [22] gives a new expression, which is discussed in section 2.1.4 with a comparison to formula (2) to (5) with Sydney sand, blue sand and bricky sand, which have properties given in Table 2. Additionally [14], [24] mention similar formulations, with minor differences in the variables. These are not discussed because these formulations would deviate too far from the target of this study.

Table 2. *Tested sands by* ***[22]***

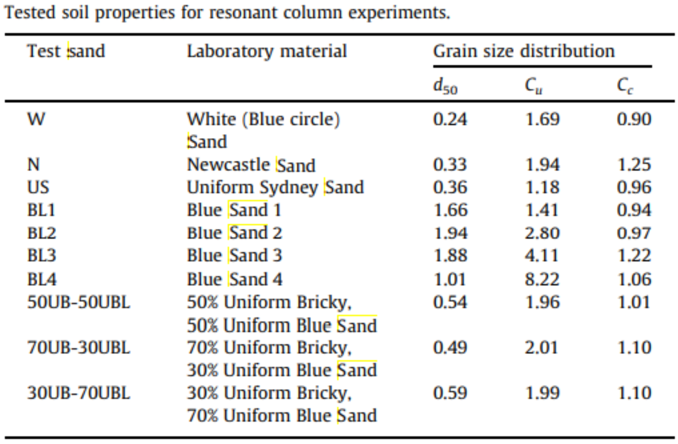

Tested soil properties for resonant column experiments.

Test sand	Laboratory material	Grain size distribution		
		d_{50}	C_u	C_c
W	White (Blue circle) Sand	0.24	1.69	0.90
N	Newcastle Sand	0.33	1.94	1.25
US	Uniform Sydney Sand	0.36	1.18	0.96
BL1	Blue Sand 1	1.66	1.41	0.94
BL2	Blue Sand 2	1.94	2.80	0.97
BL3	Blue Sand 3	1.88	4.11	1.22
BL4	Blue Sand 4	1.01	8.22	1.06
50UB-50UBL	50% Uniform Bricky, 50% Uniform Blue Sand	0.54	1.96	1.01
70UB-30UBL	70% Uniform Bricky, 30% Uniform Blue Sand	0.49	2.01	1.10
30UB-70UBL	30% Uniform Bricky, 70% Uniform Blue Sand	0.59	1.99	1.10

According to Menq (M) [25]:

$$\boldsymbol{G_{max} = A * e^{x} * (\frac{p'}{p_a})^{n}} \qquad \textbf{\textit{(2)}}$$

Where

$A = 67.1 * C_u^{-0.2}$

$x = -1 - \left(\frac{d_{50}}{20}\right)^{0.75}$

$n = 0.48 * C_u^{0.09}$

According to Saxena and Reddy (SR) [24]:

$$\boldsymbol{G_{max} = A * \frac{1}{0.3+0.7*e^{2}} * p_a^{1-n} * p'^{\,n}} \qquad \textbf{\textit{(3)}}$$

Where

$A = 428.2$

$n = 0.574$

Equation (3) is proposed for Monterey No. 0 sand with a reference strain < 10^{-5} according to [24]. This sand has a coefficient of curvature of 0.90, coefficient of uniformity of 1.50 and a mean grain size d_{50} of 0.36 mm.

According to Wichtmann and Triantafyllidis (WT) [17]:

$$\boldsymbol{G_{max} = A * \frac{(x-e)^{2}}{1+e} * p_a^{1-n} * p'^{\,n}} \qquad \textbf{\textit{(4)}}$$

Where

$A = 1563 + 3.13 * C_u^{2.98}$

$x = 1.94 * \exp(-0.066 * C_u)$

$n = 0.4 * C_u^{0.18}$

Formula (4) is used in [17], [26] and [4] on quartz sand with a subangular grain shape with a mean grain size *d₅₀* between 0.082 and 6 mm, a coefficient of uniformity between 1.5 and 8.

It is mentioned in [17] formula (4) can have recommended values for 2 different types of sand. For round sand $A = 6.9$, $a = 2.17$ and $n = 0.5$. On the other hand, for angular sands $A = 3.2$, $a = 2.97$ and $n = 0.5$. In addition [4] mentions formula (4) needs to be used within the limits $1.5 \leq C_u \leq 15$, because the curve tends to follow an asymptote when higher uniformity coefficients are reached. Additionally [4] states that formula (4) is more appropriate for $0.1\, mm \leq d_{50} \leq 6\, mm$.

According to Senetakis et al. (SAP) [27]:

$$\boldsymbol{G_{max} = A * e^x * (\frac{p'}{p_a})^n} \qquad \textit{(5)}$$

Where

$A = 57.01 - 5.88 * C_u$

$x = -0.28 * C_u - 0.98$

$n = 0.47$

P_a in (2) to (5) is the atmospheric pressure, which has a value of 100 kPa [22]. Furthermore [14] proposes relations for different types of sand, using the propositions similar to ‘Menq (2)’ and ‘Wichtman and Triantafyllidis (4)’, with a coefficient of uniformity between 1.10 and 4.40.

According to [17], the very small strain shear modulus degradation is larger for higher values of C_u. In addition the very small strain shear modulus degradation is rather independent of d_{50}.

An estimating formula (6) for the very small strain shear stiffness of sand is derived by [28] and taken from [17]:

$$\boldsymbol{G_{max} = 218.8 * K_{2,max} * p^{0.5}} \qquad \textit{(6)}$$

Where

p is the mean effective confining pressure in kPa

$K_{2,max}$ is 30 for loose sand and 75 for dense sand

$K_{2,max} = A_k * \frac{(a_k - e)^2}{1+e}$

Where

$A_k = 69.9 + 0.81 * C_u^{2.84}$

$a_k = 1.94 * \exp(-0.066 * C_u)$

Formula (6) underestimates *G_{max}* for low pressures and overestimates *G_{max}* for high pressures when *C_u* is small [17]. A possible explanation for this might be that *C_u* values are small, which would mean $n < 0.5$ in formula (4). In addition formula (6) overestimates *G_{max}* for low pressures and underestimates *G_{max}* for high pressures when *C_u* is high [17]. An explanation for this might be that *C_u* values are big, which would mean $n > 0.5$ in formula (4).

[17] also mentions 2 formulas (7) and (8), derived from [28], which determine the small strain shear stiffness by means of the relative density *D_r*. Caution should be taken with these 2 formulations, because they are less accurate than the formulas which are based on the uniformity coefficient:

$$\boldsymbol{G_{max} = 177000 * \frac{1+\frac{D_r}{100}}{\left(17.3-\frac{D_r}{100}\right)^2} * p_a{}^{0.52} * p^{0.48}} \tag{7}$$

$$\boldsymbol{K_{2,max} = 6900 * \frac{1+\frac{D_r}{100}}{\left(16.1-\frac{D_r}{100}\right)^2}} \tag{8}$$

2.1.4 Influence of grain shape and fines content on G_{max}

[22] has tested formula (2) to (5) on different sands, given in Table 2. In addition it is mentioned that particle shapes do not have a negligible effect on the determination of the very small strain shear stiffness. Therefore, a new expression, (9), was derived, which takes the shape of particles in account. Besides, it is concluded that the roughness does not have a considerable effect on *G_{max}*. An explanation for this might be that very small strain is a elastic deformation, and deformations are recoverable due to this elastic response. Additionally, *d₅₀* has few influence on the very small strain stiffness.

To determine formula (9), Tests are executed on blue sand, Sydney sand and bricky sand, on a specimen of diameter 50 mm and height 100 mm, with dry samples and at different void ratios and mean effective confining pressures.

The newly proposed formulation (9) for G_{max} by [22] is:

$$\boldsymbol{G_{max} = A_1(C_u) * A_2(shape) * e^{x(C_u)} * (\frac{p'}{p_a})^{n_1(C_u)*n_2(shape)}} \qquad \textit{\textbf{(9)}}$$

Where

$x(C_u) = -1.29$

$A_1(C_u) = 43.45 * C_u^{-0.14}$

$n_1(C_u) = 0.5 * C_u^{0.12}$

$A_2(shape) = 1.93 * \rho^{0.68}$

$n_2(shape) = -0.46 * \rho + 1.18$

Where ρ the regularity

$\rho = \frac{R+S}{2}$ [30]

Where

R is the roundness

S is the sphericity

M. Payan et al. / Computers and Geotechnics 72 (2016) 28–41

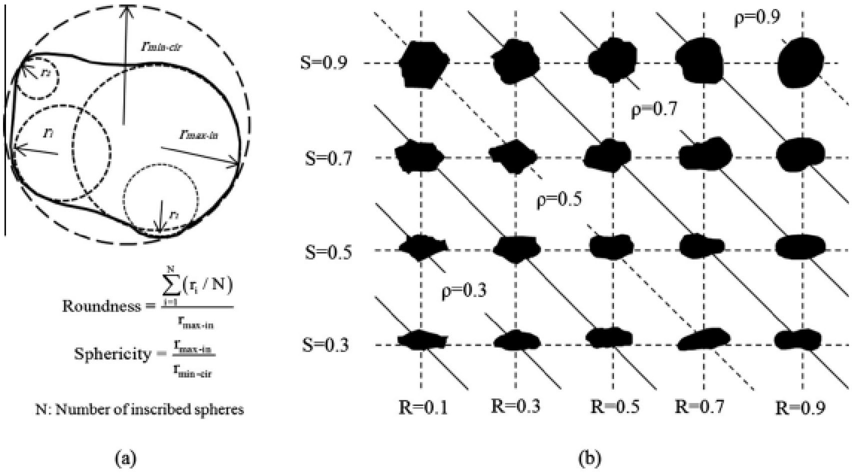

Fig. 9. Particle shape characterization chart (modified from Krumbein and Sloss [37]).

Figure 5. *Characterization chart of particle shapes (according to Krumbein and Sloss)* ***[22]***

A numerical value is given to the particle shape of grains in Figure 5 [22]. By use of this figure the roundness R (average radius to the largest inscribed sphere), the sphericity S (ratio between radius of the largest inscribed sphere to the smallest circumscribed sphere) and the regularity ρ can be determined.

Two ways exist to determine the sphericity and roundness according to [30]. It is possible to do this manually, by means of a characterization chart like given in Figure 5 [22], or with the use of an automated scanning electron micrograph. This last method is more precise.

As can be seen, the small strain shear modulus G_{max} is described by the coefficient of uniformity, the regularity, the void ratio and the mean effective confining pressure. Figure 6 shows the effect of the proposed formulation (9) and the proposed formulations (2) to (5) on blue sand. As can be seen, this new formulation is much more accurate. A reason for this might be that in this study the effect of sand particle shape is taken into account, which was not done in previous studies. A similar effect can be seen by Sydney sand and bricky sand, respectively Figure 7 and Figure 8. Because of this, the earlier mentioned expressions (2), (3), (4) and (5) are only valid for a specific range of particle shapes of sands, while the new formulated expression (9) is more general.

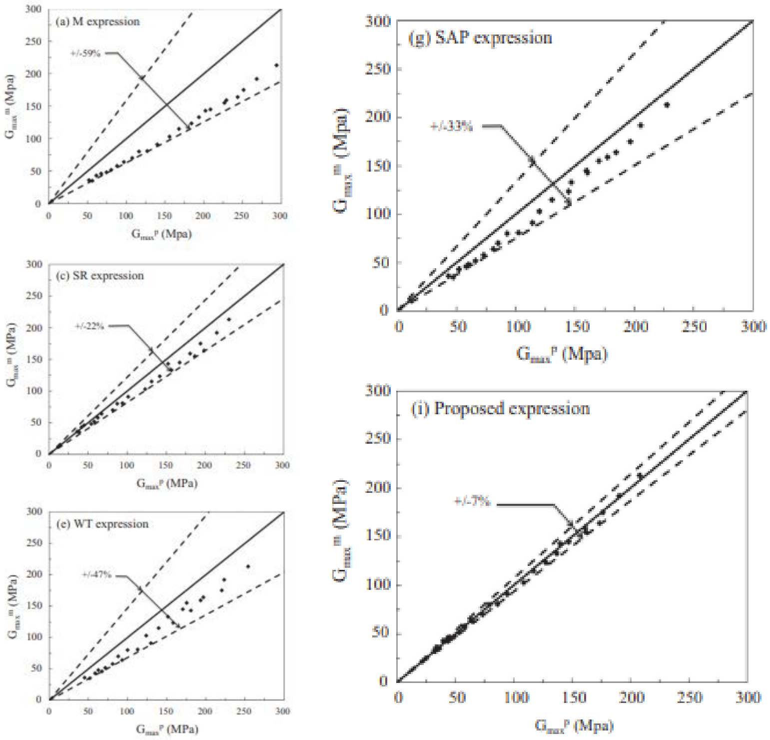

Figure 6. *Effect of the proposed formulation (9) compared to (2), (3), (4) and (5) on blue sand* ***[22]***

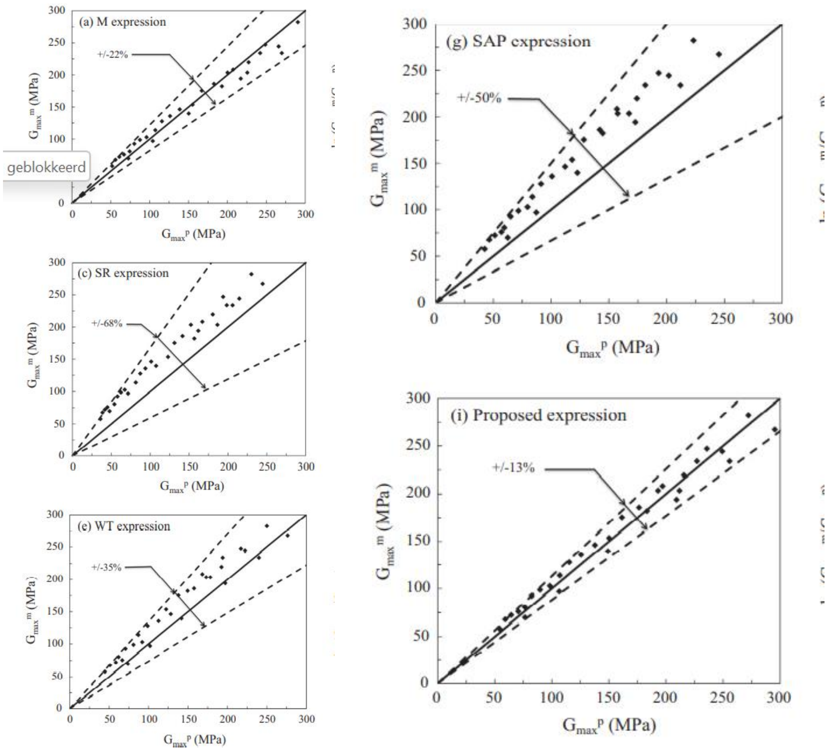

Figure 7. *Effect of the proposed formulation (9) compared to (2), (3), (4) and (5) on Sydney sand* ***[22]***

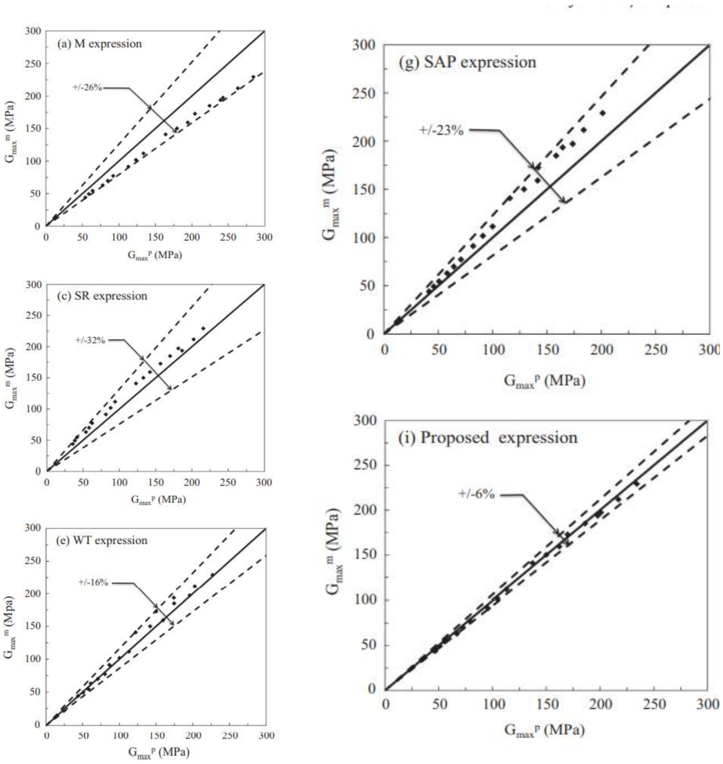

Figure 8. *Effect of the proposed formulation (9) compared to (2), (3), (4) and (5) on bricky sand* ***[22]***

Additionally, [4] has extended the use of formula (4) by quartz sands. Next to the uniformity coefficient, a proposal is done to integrate the fines content into this formula. The formulation is given by:

$$A = (1563 + 3.13 * C_u^{2.98}) * \frac{1}{2} * (\exp(-0.3FC^{1.1}) + \exp(-0.28 * FC^{0.85}))$$
$$x = 1.94 * \exp(-0.066 * C_u) * \exp\,(0.065 * FC)$$
$$n = 0.4 * C_u^{0.18} * (1 + 0.116 * \ln(1 + FC))$$

[4] mentions this extension of formula (4) should be used by lower uniformity coefficients ($1.5 \leq C_u \leq 16$), because the effect of the increase of the *FC* is less pronounced at higher uniformity coefficients.

For well-graded sands ($C_u > 15\ and\ 1 \leq C_c \leq 3$), a proposal is made for another formula by [4], which gives a more reliable result, according to them:

$$f_r(FC) = \begin{cases} 1 - 0.043 * FC & when\ FC \leq 10\% \\ 0.57 & when\ FC > 10\% \end{cases}$$
$$G_{max}(FC) = G_{max}(FC = 0) * f_r(FC)$$

As mentioned earlier, the research in [4] was done with *FC(d < 0.063 mm)* and literature often refers to *FC(d < 0.075 mm).* According to [4] this is not a problem and the results are still reliable.

2.1.5 Comparing measured and predicted results

Figure 9 gives predicted values of G_{max} for Ham River sand, compared to measured values. This is done for formula (2) to formula (5). As can be seen, the predicted and the measured values match very well. It can be concluded that formula (5) underestimates the measured small strain shear modulus, while (2) to (4) over- and underestimate the small strain shear modulus at different times. It can be concluded that these formulas give a more correct result, while formula (5) gives a safer result. [22]

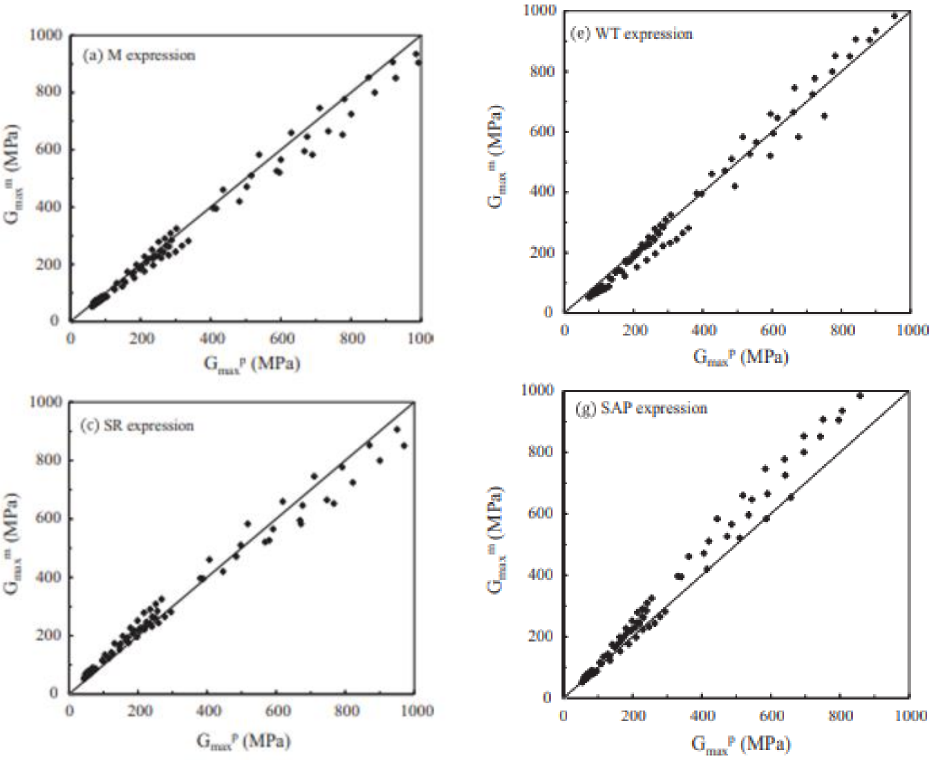

Figure 9. *Predicted G_{max} with M (equation (2)), SR (equation (3)), WT (equation (4)), SAP (equation (5)) (abscissa) and measured G_{max} (ordinate) by a resonant column* ***[22]***

Additionally, Figure 10, Figure 11 and Figure 12 [17] shows measurements of G_{max} at different pressures, executed for different mean grain sizes d_{50} and uniformity coefficients C_u on quartz sands. It can be stated that d_{50} has a small influence on the very small strain shear modulus, while C_u has a much greater influence. In addition the curves obtained by formula (4) are plotted which matches good with the results.

As Figure 10 shows, the small strain shear stiffness decreases with increasing C_u at a constant void ratio *e*. This might be explained by the relative density, which is much higher at constant void ratios when C_u is lower. A consequence for this is that smaller grains have much more possibility to move between the greater grains at a bigger ratio of C_u. Because of the possibility to move between the great grains easier, the shear strains would be greater, and thus cause reduced very small strain shear modulus's. [26] concludes the same as Figure 10.

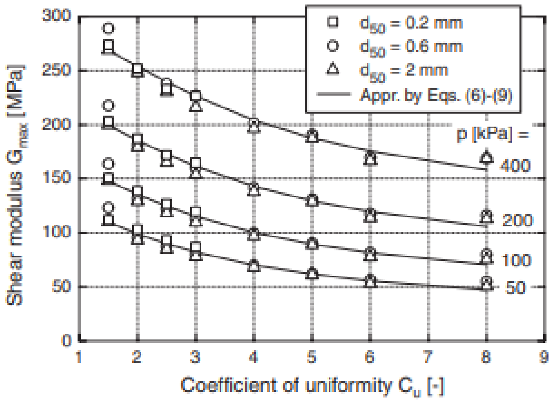

Fig. 8. Shear modulus G_{max} at e=0.55 as a function of C_u for different pressures p

Figure 10. *G_{max} by equal void ratio e=0.55, as function of C_u, mean effective confining pressure and d_{50}* ***[17]***

In addition it can be seen G_{max} increases with increasing mean effective confining pressure and decreases with an increasing void ratio *e* as shown in Figure 11 and Figure 12. An explanation might be that the granulates get more support and a more compact packing when the void ratio decreases and the mean effective confining pressure increases. This will cause the specimen to deform lesser, and thus to have a higher G_{max}. This conclusion can also be linked to the relative density, which increases with decreasing void ratio and thus has a higher small strain stiffness.

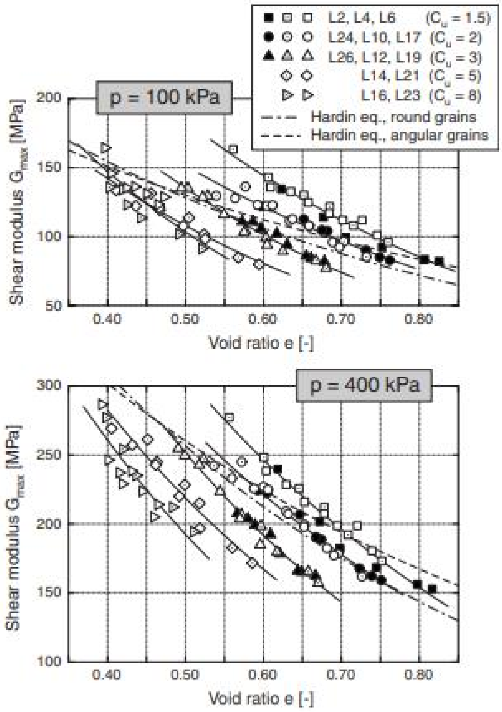

Figure 11. *G_{max}(e) for different C_u and d_{50}* ***[17]***

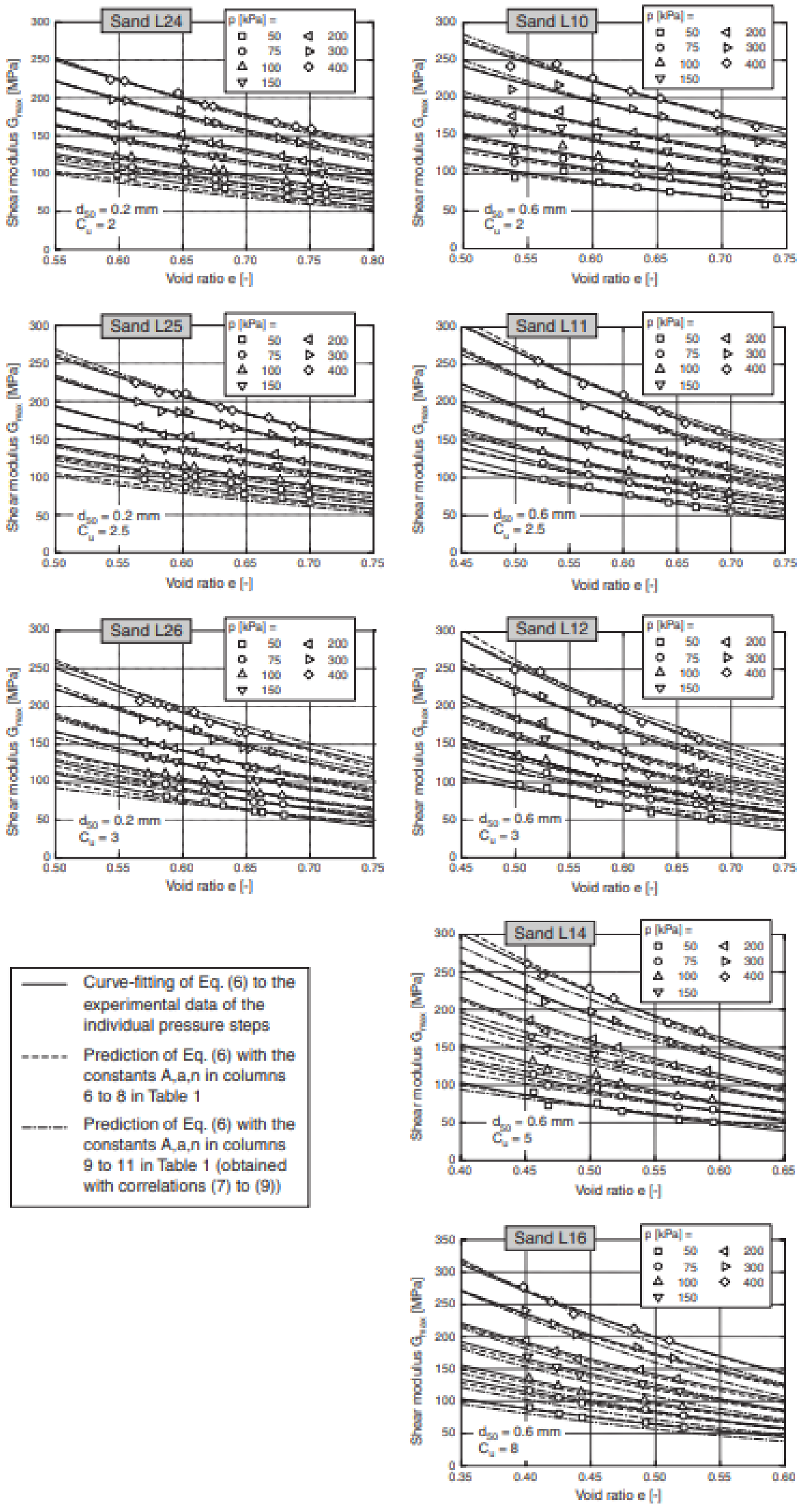

Figure 12. *G_{max}(e) for different uniformity coefficients C_u at different pressures* ***[17]***

[26] mentions higher uniformity coefficients mean very small strain shear stiffness is lower and a more pronounced degradation of G_{max} for clean quartz sands. Both of these 2 statements can be seen in Figure 14 by effective confining pressures of 100 kPa and

400kPa. It must be stated that this can only be seen by comparing the same void ratio's. The continuous line is obtained by equation (4). As shown, equation (4) approaches most of the small strain shear modulus', except for PL7, GG6 and S5, which are well graded granular materials with a greater uniformity coefficient and they contain gravel or are composed by 2 materials with significantly different grain sizes as can be seen in Figure 13. Besides, [26] states that G_{max} is rather independent of d_{50}.

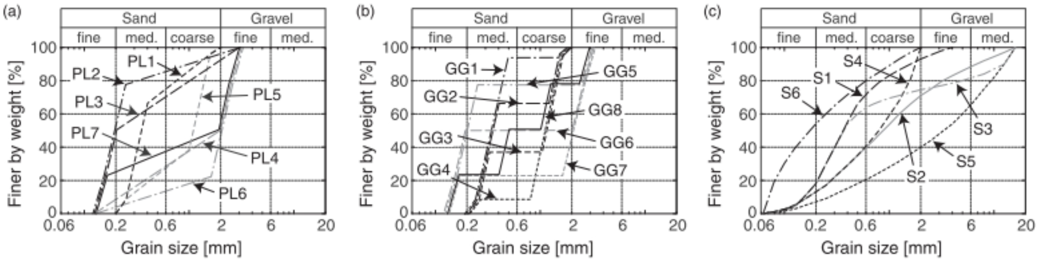

Figure 13.** Step-wise linear (a), gap-graded (b) and smoothly shaped (c) tested materials **[26]

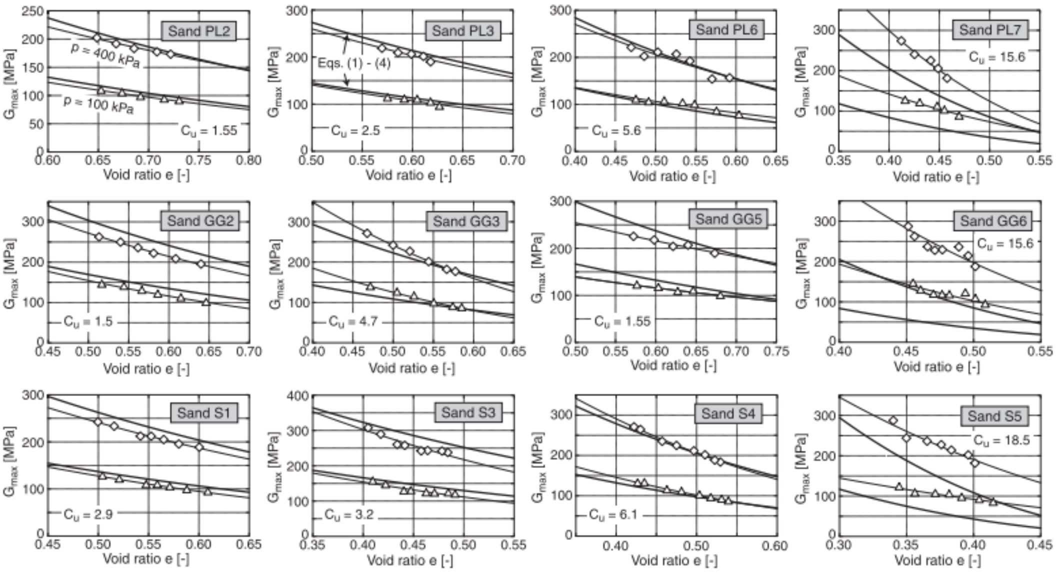

Figure 14.** G_{max} for different void ratios e at different uniformity coefficients **[26]

Besides, it is mentioned in [26] uniformity coefficients should be limited between $1.5 \leq C_u \leq 16$. This means S5 in Figure 14 needs to be neglected, although PL7 and GG6 should be looked at with great caution.

As mentioned earlier, according to [4], formula (4) needs to be used within the limits $1.5 \leq C_u \leq 15$, which would mean in Figure 14 sand PL7, GG5 and S5 should be neglected.

2.1.6 Effect of fines content and *p'* on the small strain stiffness

Figure 15 and Figure 16 show the correlation between respectively $G_{max}(FC)$ and $G_{max}(p')$, at different relative densities and *FC*. Figure 15 (a) shows clearly that the small strain stiffness for every mean effective confining pressure decreases until a *FC* of approximately 30%. At this *FC*-rate the very small strain stiffness starts to increase again, although this increase is less pronounced than the earlier mentioned decrease. In Figure 15 (b) it is clearly shown that G_{max} decreases, but the *FC* where G_{max} starts to increase again is less pronounced. Figure 15 (c) shows clearly that at a higher relative densities, G_{max} only decreases by increasing *FC*. In Figure 16 an increase of G_{max} with an increasing effective confining pressure is observed, independent of the relative density. [31]

A relation for G_{max} is shown in Figure 17 for different void ratios, *FC* and effective confining pressures. As can been seen, G_{max} increases with increasing effective confining pressure, increases with decreasing void ratio and decreases with an increase of *FC*. [31]

The values of G_{max} given in [31] should be taken with caution, because it is stated that *x* is 2.17 for angular sands and 2.97 for rounded sands, where [17] and [32] states that *x* is 2.17 for round sands and 2.97 for angular sands. This might be a fault from the author, which is overseen.

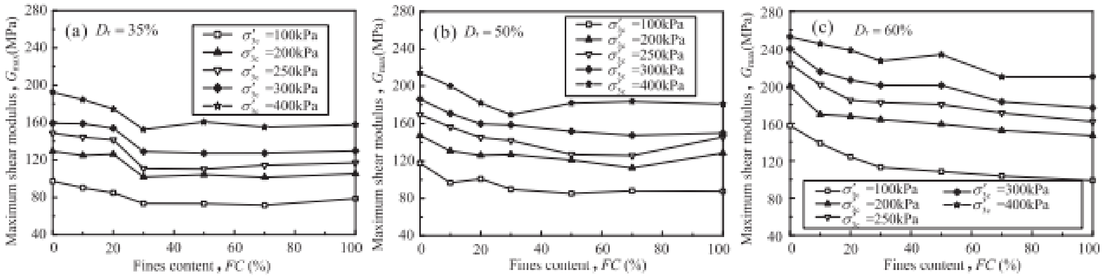

Figure 15. *$G_{max}(FC)$ for different p' and different D_r* ***[31]***

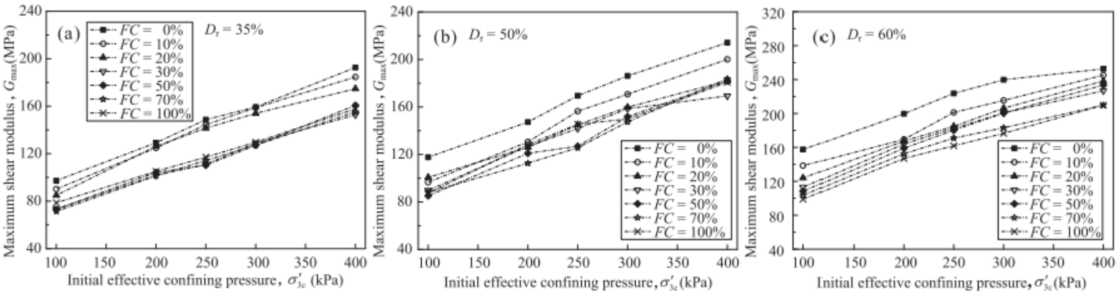

Figure 16. *$G_{max}(p')$ for different FC and different D_r* ***[31]***

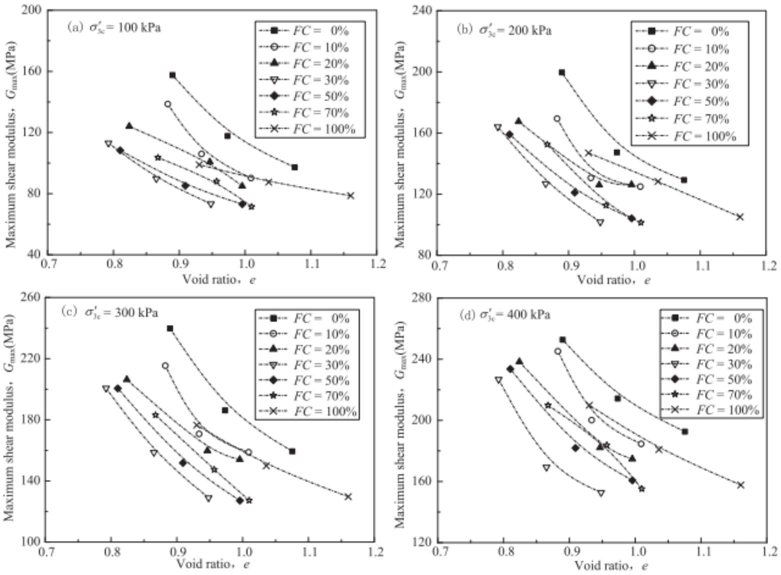

Figure 17. *G_{max}(e) for different FC for sandy soils* ***[31]***

2.2 Stiffness degradation

2.2.1 Effect of void ratio *e* and effective confining pressure

[15] explains the different effects of a few parameters on *G* and *G/G_{max}* without experimental data. First of all the void ratio is discussed. An increase of the void ratio leads to a decrease of *G_{max}*. In addition, the shear modulus ratio *G/G_{max}* increases by increasing void ratio. A possible explanation for this is that *G_{max}* and G, change differently. This is caused by the assumption that the strength is constant. This constant strength causes when higher void ratios are analyzed, *G* starts to change later to reach the same failure point, which might give a stiffer view in the shear modulus ratio. This could lead to a wrong conclusion, and therefore caution needs to be taken which curve is used. The effect is shown in Figure 18, where soil 1 has the lowest void ratio up to soil 5 with the highest void ratio.

Shortly summarized the effect of Figure 18 can be attributed to the effect that higher void ratios act relatively stiffer until higher strains, according to the shear modulus ratio, but not according to the shear modulus to reach the same failure point. As Figure 18 (a) shows, the effect of changing secant shear modulus is less pronounced at higher void ratios, which causes the shear modulus ratio (Figure 18 (b)) to be higher. This is caused by the assumption that the strength is assumed to be constant in Figure 18. If the stiffness is higher, it needs to start decreasing sooner to reach the same failure point.

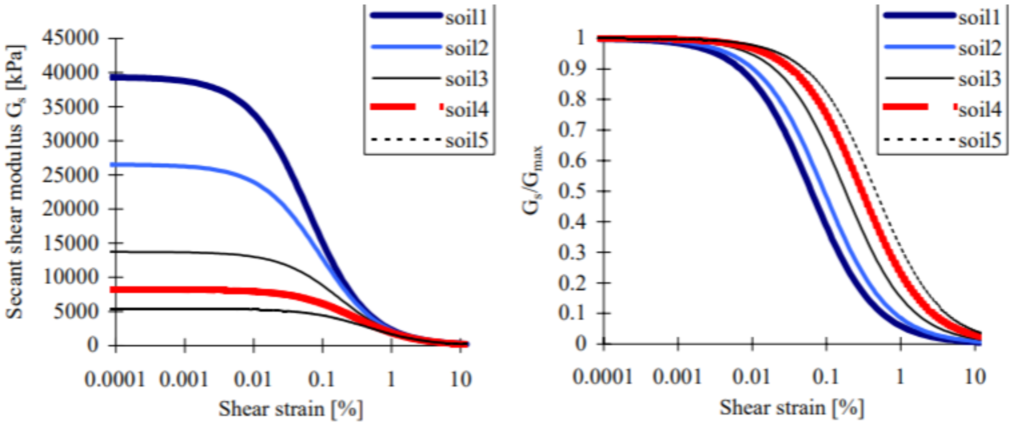

(a) (b)

Figure 18. *Effect of void ratio on the shear modulus (a) and shear modulus ratio (b)* ***[15]***

In addition, [15] shows the relation between different consolidation states. When the effective confining pressure increases G_{max} and G/G_{max} increases. Figure 19 shows the relation for sand, where soil 1 has the lowest effective confining pressure, which increases to soil 5 with the highest effective confining pressure.

Shortly explained, when the effective confining pressure increases an increase of both G and G_{max} is noticed at the same strain level. This is caused because the strength of the soil increases due to this pressure increase. The sample has a higher support which causes a stiffer response, and thus to have a higher G/G_{max} ratio. To reach the failure point, which is not fixed, both curves have to start decreasing at higher strains.

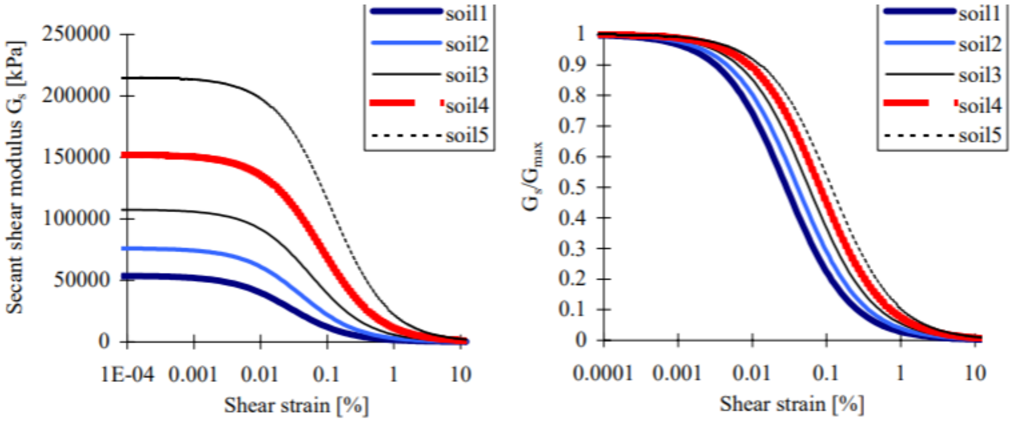

(a) (b)

Figure 19. *Effect of effective confining stress on the shear modulus (a) and shear modulus ratio (b) of sand* ***[15]***

2.2.2 Effect of plasticity index *PI*

Figure 2 [16] shows the connection between the shear modulus ratio G/G_{max} for different pressures and the cyclic shear strain amplitude. It is shown for two different plasticity indexes. According to [16] the effect of the plasticity index is great on the shear modulus ratio by small plasticity indexes, while the effect decreases for higher plasticity indexes. Therefore it is possible that by lower plastic soils, the shear modulus ratio increases more with the effective confining pressure. [33] concludes the effect of the effective confining pressure on the shape of the normalized shear modulus reduction curve is negligible by plasticity indexes exceeding 25.

As shown in Figure 2 [16], the dynamic shear modulus ratio starts to change at lower amplitudes for the cyclic shear strain, when the effective confining pressure is lower. In addition the damping will start to change earlier too. Another parameter which determines when the degradation of the stiffness begins to occur is the number of cycles which have occurred. [34]

[34] mentions that the plasticity index is one of the primary affecting parameters during dynamic loadings. When this index increases, the G/G_{max}-ratio starts to decrease at higher strains. In addition, when the plasticity increases, the damping ratio D which is obtained starts to change at higher strains. Both mechanisms are shown in Figure 20 [34]. During earlier investigations it is well recognized that loss of strength and stiffness, which is permanent, might be caused by cyclic loadings because of certain amplitudes. This is shown in Figure 21 [34], where the dynamic shear modulus ratio decreases with increasing cyclic strain amplitude. Additionally, the damping increases with increasing cyclic strain amplitude. A possible explanation for the damping increase and the loss of stiffness is that pore water pressure is accumulated, which can cause liquefication. In addition a particle structure breakdown might find place.

The very small strain stiffness modulus, G_{max} is a parameter which is primarily dependent on the void ratio e and especially for soils with low plasticity the effective confining pressure as shown in Figure 2. It is stated in comparison with G_{max}, the void ratio has fewer influence than the plasticity index on the damping and the dynamic shear modulus ratio, as shown in Figure 20 and Figure 21. [34]

When strains are applied under the elastic threshold, no energy dissipation will take place theoretically. Some studies mention that a small amount of energy will always get lost when small strains are applied as shown in Figure 21 (b), although a lower limit will exist where the cyclic degradation will be negligible. This lower limit depends on different parameters, like the value of the plasticity index and the change of pore water pressure. In addition when the linear strain threshold is exceeded, the damping will increase. [34]

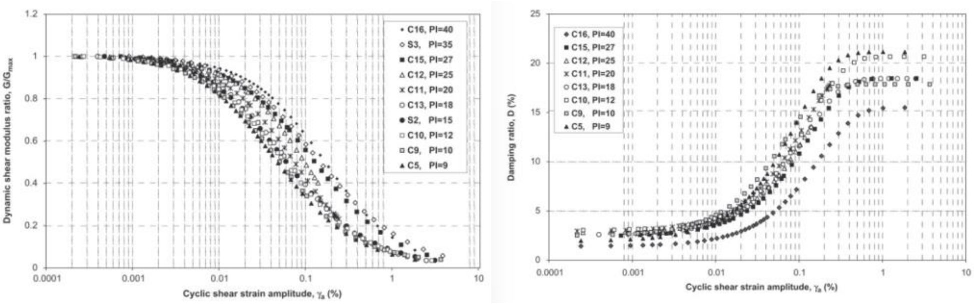

(a) (b)

Figure 20. *Dynamic shear modulus ratio (a) and damping (b) as function of the cyclic strain amplitude with different plasticity indexes* ***[34]***

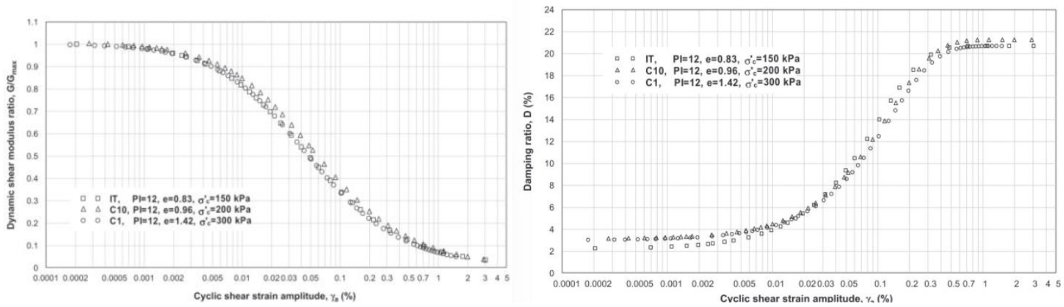

(a) (b)

Figure 21. *Dynamic shear modulus ratio (a) and damping (b) as function of the cyclic strain with different void ratios* ***[34]***

An empirical relation between the cyclic strain and the dynamic shear modulus ratio is mentioned in [34], [35], based on Kondner [36] for fine grained soils. This relation is given by:

$$\frac{\boldsymbol{G}}{\boldsymbol{G_{max}}} = \frac{\mathbf{1}}{\mathbf{1}+\frac{\boldsymbol{\gamma_a}}{\boldsymbol{\gamma_r}}} \qquad \textbf{\textit{(10)}}$$

Where

γ_a is the cyclic shear strain amplitude

$\gamma_r = \frac{1}{21*(1-\exp(-106*PI^{-1.585}))}$ is the reference strain, as function of the plasticity index, which is determined in [34] with a regression for fine grained soils

It can be seen by formula (10), with an increasing plasticity index, γ_r will become greater and *G/G$_{max}$* will thus become greater. Following on this relation, [34] proposes formula (11) to determine the damping:

$$\boldsymbol{D} = -\mathbf{18.114} * \left(\frac{\boldsymbol{G}}{\boldsymbol{G_{max}}}\right) + \mathbf{20.033} \qquad \textbf{\textit{(11)}}$$

In addition [26] gives another correlation, (12), proposed for clean quartz sands, to determine *G/G$_{max}$*:

$$\frac{G}{G_{max}} = \frac{1}{1+\frac{\gamma}{\gamma_r}*(1+a*exp\left(-\frac{\gamma}{\gamma_r}\right))} \qquad (12)$$

Where

$a = 1.070 * ln(C_u)$

$\gamma_r = \frac{\tau_{max}}{G_{max}}\ with\ \tau_{max} = p * \sin(\varphi_p)$

Where the friction angle $\varphi_p = 34° * \exp\,(0.27 * D_r^{1.8})$

When the coefficient of uniformity becomes greater *G/G_{max}* will become smaller. In addition when the effective confining pressure *p*' is increased *G/G_{max}* will become greater.

Next to [14], [35] mentions a similar equation to formula (12) proposed by [37], which is a modification of Kondner [36]. This is given by (13):

$$\frac{G}{G_{max}} = \frac{1}{1+a*(\frac{\gamma}{\gamma_{ref}})} \qquad (13)$$

Where

$a = 0.385$

γ_{ref} is the strain where $G = 0.7 * G_{max}$, determined with Mohr-Coulomb:

$\gamma_{ref} = \frac{0.385}{4*G_{max}} * (2 * c * (1 + cos(2 * \varphi')) + \sigma'_1 * (1 + K_0) * sin(2 * \varphi'))$

Where

c is the cohesion of the soil

K_0 is the neutral ground pressure

As previous equations in this section ((10) to (13)) have no clear or a complex physical meaning, another equation is proposed by [38] to define the hyperbolical relation. The shear stress can be given by (14):

$$\tau = \frac{\gamma}{a+b*\gamma} \qquad (14)$$

Next, the maximum shear stress increase can be found by taking the limit of the shear stress to infinite strain. This results in (15):

$$\tau_{max} = \frac{1}{b} \qquad (15)$$

It is well known the secant shear modulus G_s can be found by the shear stress and strain:

$$\boldsymbol{G_s = \frac{\Delta\tau}{\Delta\gamma} = \frac{1}{a+b*\gamma}} \tag{16}$$

Where

$\Delta\tau$ is the change in shear stress

$\Delta\gamma$ is the change in shear strain

Additionally, the tangent shear modulus G_t can be given by differentiating G_s:

$$\boldsymbol{G_t = \frac{d\tau}{d\gamma} = \frac{a}{(a+b*\gamma)^2}} \tag{17}$$

When the shear strain γ is zero, it can be noted that $G_t = G_s = G_{max} = \frac{1}{a}$. In other words:

$$\boldsymbol{\frac{1}{G} = \frac{\gamma}{\tau} = a + b * \gamma} \tag{18}$$

The parameters *a* and *b* thus have a clear physical meaning, as shown in Figure 22.

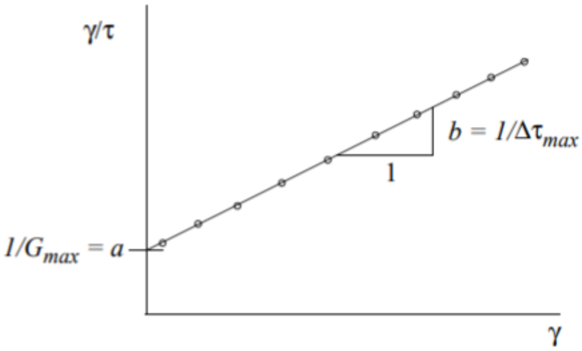

Figure 22. *Physical meaning of parameters in stress strain relation* ***[15]***

2.2.3 Effect of cyclic shear strain amplitudes

A threshold exists where the nonlinear elastic curve starts to follow an elasto-plastic curve in a logarithmic scale, as shown in Figure 23 [34]. The limit of this transition is approximately $G/G_{max} = 0.9$ according to [34], although no exact transition point exists and it is hard to define the threshold. When the stress is reduced, before it exceeds point B, the shear modulus will go back to its initial value. In this zone, no deformation of the particle structure finds place. If the stress exceeds point B, a part of the stiffness will be lost because the particle structure will start to deform. In this case the curve will tend back to point C. When the curve exceeds point F and the load is reduced again, a great loss of stiffness will occur because the yield surface is exceeded at this point. The curve will tend to point H.

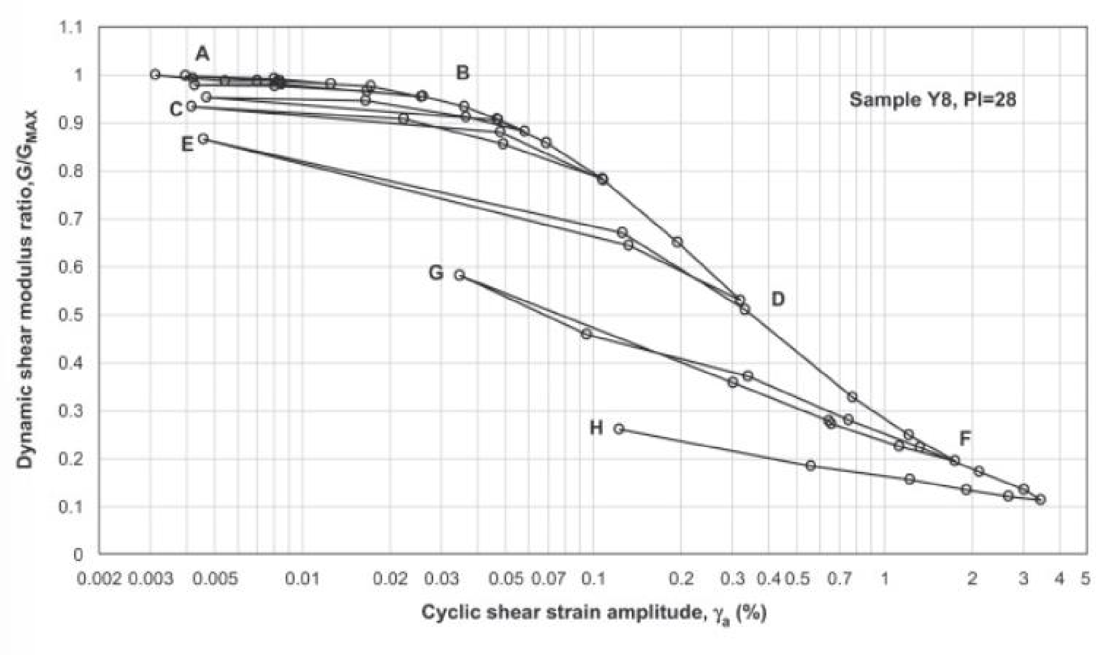

Figure 23. *Shear strain degradation curve at different cyclic shear strain amplitudes* ***[34]***

Next, hysteresis loops will be looked at, and which path they will follow to declare different stress-strain relations. A short description of the different parameters which form this loop will be discussed now, with Figure 24 [15], according to Masing's rules [20]. First of all, when the soil is loaded for the first time the curve will follow the loop from the origin to point 'a' and the shear modulus will vary from G_{max} in the origin to G in point 'a'. When the loading is now reversed and a decrease of the shear stress occurs the curve will tend to follow a hysteresis loop from 'a' to 'd', starting with a shear stress G_{max} in 'a', which varies to G in 'd'. The proposed hysteresis loop during the unloading has the same form as the original loop, although it is multiplied by a factor 2. When the load is reversed again, the loop which will be followed will follow the same principle as the unloading curve. If a maximum shear strain from an earlier loop is exceeded, the unloading or re-loading curve will start to follow the initial loading curve. [15]

Additionally, the area inside the hysteresis loop is a proportion for the damping factor. This damping in the small strain range is less during unloading and reloading compared to primary loading, according to [14].

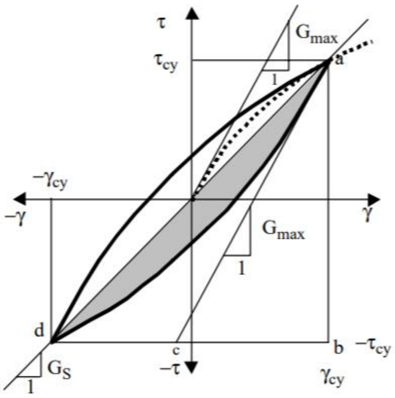

Figure 24.** Hysteresis loop of first loading, unloading and reloading **[15]

Measuring of a cyclic maximum shear modulus often happens after a load reversal. Due to this, G_{max} is often found to be independent of initial shear stresses. [15]

In Figure 25 [34] the cyclic stress is increased every five cycles. It can be seen the shear modulus ratio starts to decrease and the damping starts to increase after a number of cycles. Figure 26 shows the hysteresis loops which match with Figure 25 [34]. Figure 26 (a) shows that the hysteresis loops have the same areas and loops. It can be concluded a nonlinear elastic response is indicated by this curve. The elastic response starts to change after a certain amount of cycles, as shown in Figure 26 (b). A transition of an elastic response to an elasto-plastic response occurs, although no clear transition point can be indicated. In Figure 26 (c) the area of the loops start to increase more. It can be stated at this shear strain amplitude plastic alteration starts in the sample. Lastly, it can be seen in Figure 26 (d) a great exceeding of the deformation finds place. It can be concluded that the flow threshold is exceeded here, and the sample starts to behave visco-plastically.

To determine the transition value of the strain from an elastic to an elasto-plastic response, [34] has determined 2 empirical equations. Both formulations have a dependency on the plasticity index and as stated earlier G/G_{max}-ratio decreases at higher strains for higher PI.

Given by (19), is the limit from elastic to elasto-plastic response:

$$\gamma^{E} = \frac{0.035}{1+11.92*exp\,(-0.1*PI)} \tag{19}$$

(20) gives the limit from an elasto-plastic to plastic response:

$$\gamma^{P} = \frac{1}{1.39-0.33*PI^{0.28}} \tag{20}$$

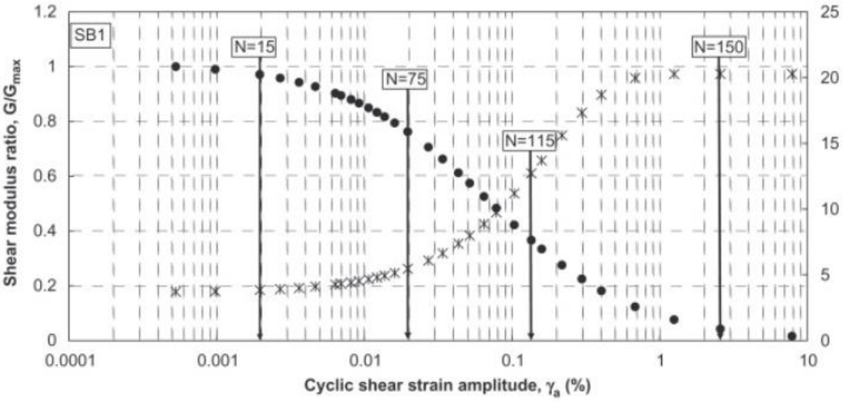

Figure 25. *Shear modulus ratio and damping as function of the cyclic shear strain amplitude for a number of cycles* ***[34]***

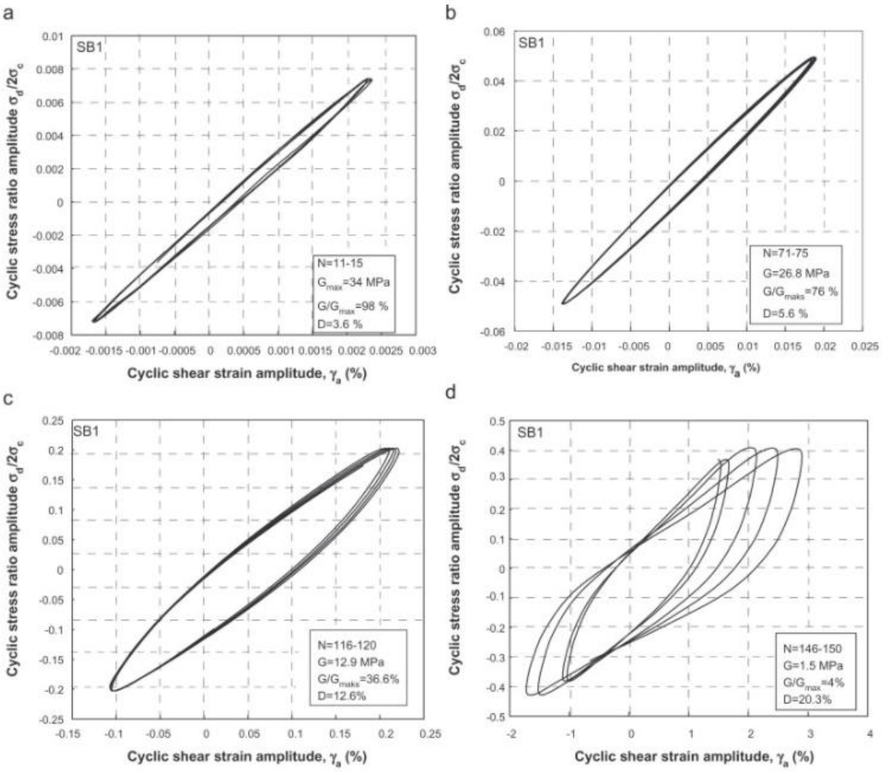

Figure 26. *Hysteresis curves for different loading stages* ***[34]***

2.2.4 Effect of cyclic loading

Stiffness of soils often change during cyclic loading. Stiffness of sands can increase, both in undrained and drained conditions. In addition for clays, the stiffness often decreases when influenced by cyclic loadings. Figure 27 [15] shows the effect of a cyclic shear strain on clay in undrained condition. A cyclic and an average pore pressure is accumulated, due to respectively a cyclic shear strain γ_{cy} which is introduced to keep a constant cyclic shear stress amplitude and an average accumulated shear strain γ_a. [15]

In general cyclic shear strains will dominate the failure mechanism and the behavior when the cycle goes both in the extension as in the compression phase close to failure. No or little average strains are accumulated in this situation, as shown in Figure 28 (a), although the stiffness decreases. In addition if the cycle goes only on one side close to failure, as shown in Figure 28 (b) and Figure 28 (c), average shear strains will have a greater influence than cyclic shear strains on the failure mechanism and behavior of the soil, due to cumulating pore water pressures. Besides, the stiffness also decreases in this situation. [15]

It is mentioned in [15] a possibility exists that shear modulus decreases in undrained cyclic loading, due to excess pore pressures which are initiated. These are generated in resonant columns, but it can be stated these are negligible in some cases due to limited strains. Additionally, this mechanism is highly dependent on the stress state in which the sample is loaded and the amplitude of this load.

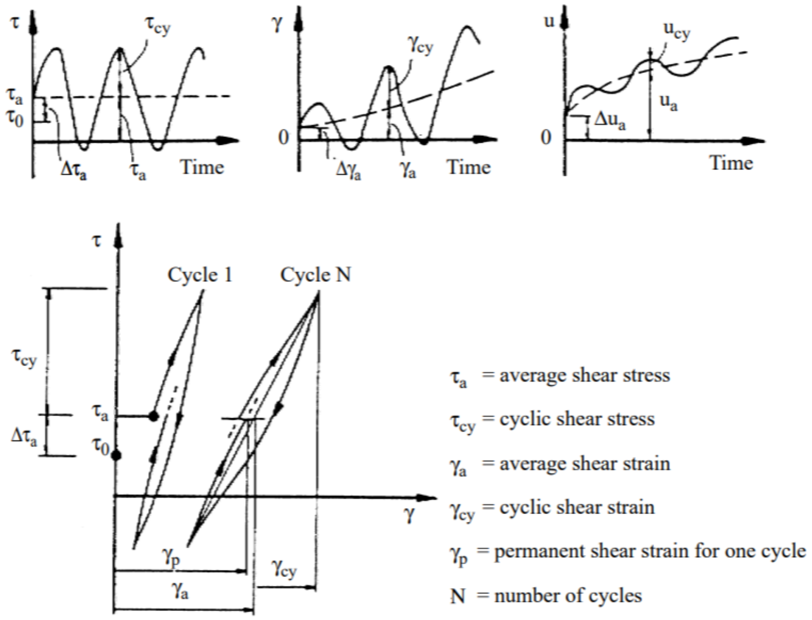

Figure 27. *Cyclic undrained shear strain on clay* ***[15]***

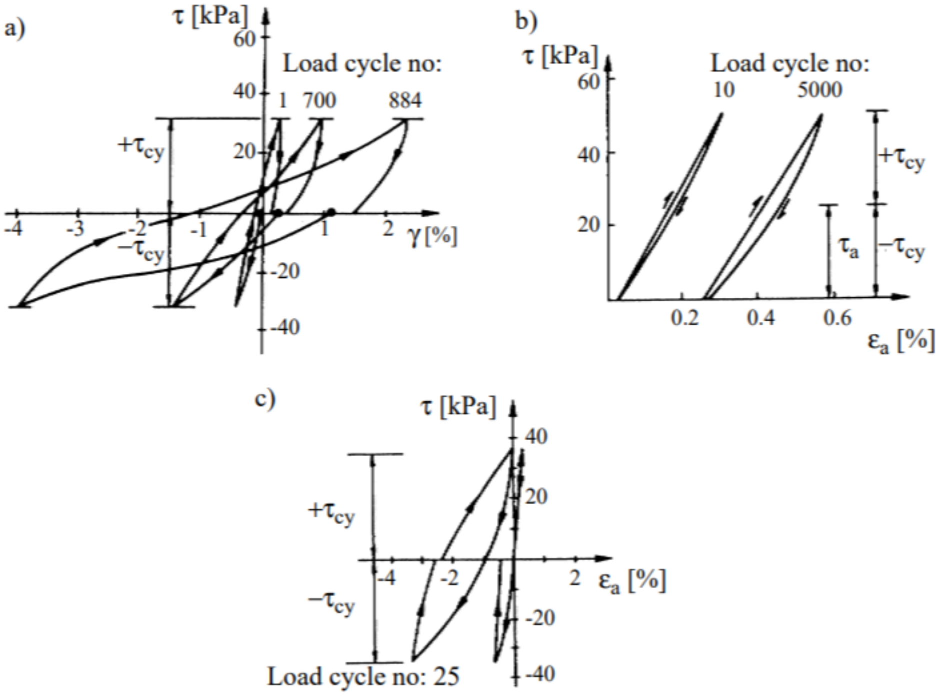

Figure 28. *Different cyclic shear strain cycles on clay* ***[15]***

2.2.5 Effect of overconsolidation

Figure 29 ([39], taken from [15]) shows the effect of a loading and unloading cycle on the small strain shear modulus. The values are received by testing Drammen clay with different testing methods, like resonant column tests and oedometer tests with bender elements. Figure 29 shows during an increase of the effective confining pressure, G_{max} increases. In addition, when the sample is kept at a constant effective confining stress, G_{max} still increases due to aging. After consolidation, the cell pressure is decreased. The decrease of the cell pressure causes a decrease of the small strain shear modulus, although the value is higher than the original G_{max}.

A possible explanation for the increased small strain shear modulus after unloading might be a deformation of the granular structure due to the increased pressure. This might have caused a decrease of void ratio and a denser structure, which increased the number of particle contacts and the number of restraints, and thus causes a higher resistance. ([39], taken from [15])

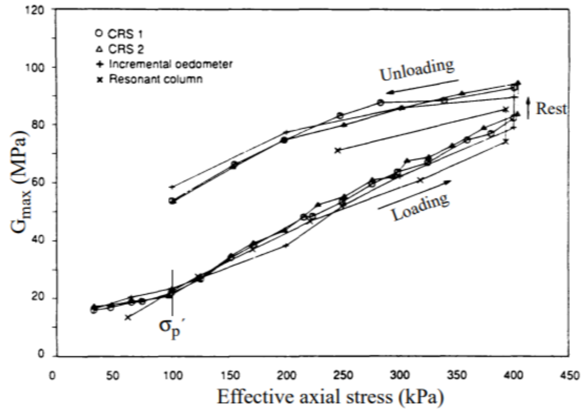

Figure 29. *Effect of loading and unloading on the small strain shear modulus of Drammen clay* ***[39]****, taken from* ***[15]***

The overconsolidation ratio might have an influence, because the *OCR* (aging) affects the small strain shear modulus as explained by Figure 29. The effect of *OCR* is more pronounced by sand compared to clay. [15]

Additionally [15] explains the effect of the overconsolidation ratio (*OCR*) at G_{max} and G/G_{max}. A consolidation pressure is proposed of $p' = 100kPa$ and σ_m' is the effective confining pressure, while $OCR = \frac{p'}{\sigma_m'}$. At low plastic clays the effect is that soils with a high overconsolidation ratio will have a higher G/G_{max} until higher strains, although G_{max} will be lower because *p'* is constant, while the effective confining pressure decreases. Figure 30 shows the relation for low plastic clays conducted on analyzing calculation methods, where soil 1 has the highest *OCR* to soil 5 with the lowest *OCR*. Additionally, the strength and maximum stiffness of the soils is edited to the effective confining pressure and *OCR*.

An explanation for the effect on low plastic clays might be, due to consolidation, the soil gets compacted and thus will react stiffer because of a higher strength compared to an underconsolidated soil. When soil 1 which is overconsolidated, gets loaded, the stiffness thus reduces at a higher strain level compared to a virgin loading. Therefore, the normalized shear modulus will be higher at higher strains. In addition soil 5 has a low *OCR* which would mean the small strain shear stiffness will be less influenced by overconsolidation, because the strength is closer to this of a soil which is loaded for the first time. Therefore, the stiffness degradation starts earlier, which causes higher deformations and thus the normalized stiffness will decrease at lower strain levels compared to overconsolidated soils.

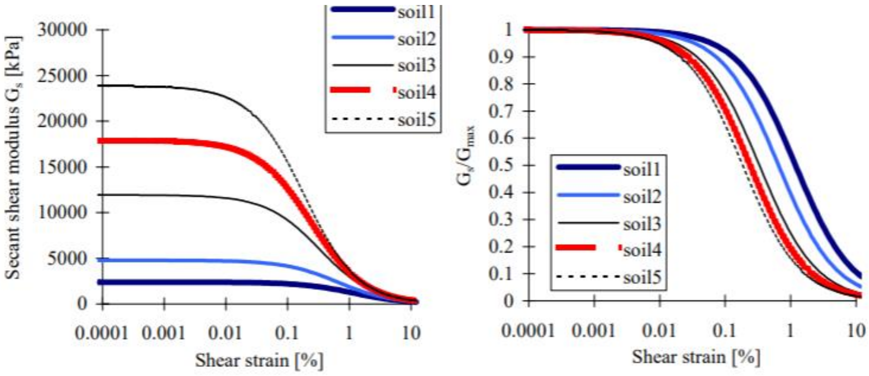

Figure 2.34 The effect of overconsolidation ratio for a low plastic clay with $k = 0$.

Figure 30. *Effect of the overconsolidation ratio for low plastic clays* ***[15]***

2.3 Resonant column test

Figure 31 shows a setup of a resonant column device. At the top, a mass is placed with 2 electrodynamic exciters. These exciters accelerate a mass and the acceleration is measured with 2 transducers. With these data, a torsional moment and a twisting angle can be calculated around the vertical axis. [17], [4]

[40] mentions the frequency of the resonant column is varied and with an accelerometer, the displacements are measured. By means of resonance frequencies, it is possible to determine the dynamic properties like G_{max} and the shear stiffness degradation. The resonance frequency is reached when the initiated torsional moment and the twisting angle have a phase shift of 90°, as discussed in [17], [4], [23].

In addition a cell pressure is initiated in [17], [4]. This cell pressure is considered isotropic mostly, although a small anisotropy is initiated by means of the top-mass, which is neglected. In the used resonant column set-up, a possibility exists to initiate anisotropic stress state. Besides, it is possible, and part of the principle to vary the cell pressure. At each pressure the small strain shear modulus is determined after a resting period of approximately 5 minutes for sand, but for less permeable soils, like clays, this consolidation period can increase. [23] mentions the consideration of an isotropic loading might give a wrong result of the small strain stiffness. This is due to the given that small strain behavior in field seldom is isotropic.

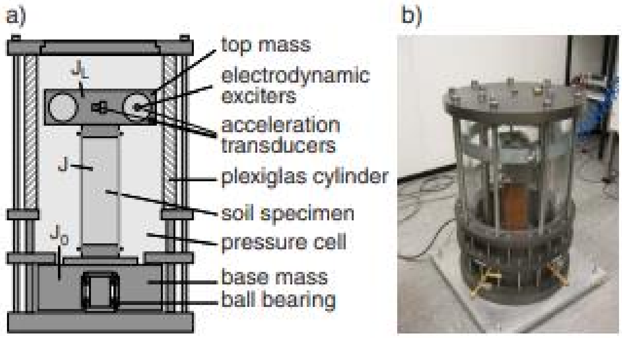

Figure 31. *Resonant column device* ***[17]***

[4] discusses a free-free resonant column device, which means that the top, as well as the base, have the possibility to freely rotate. In addition [40], [23] mentions that a fixed-free resonant column is used. In this set-up, the top-plate has the possibility to rotate, while the pedestal is fixed. Figure 32 shows the working principle of a fixed-free resonant column. More information about the resonant column will be given in section 3.3.12.

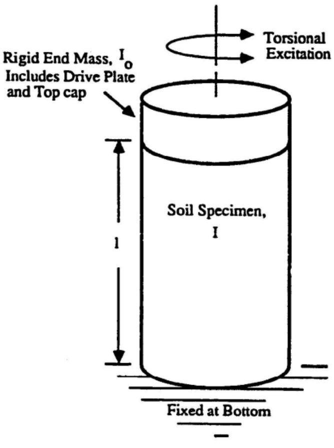

Figure 32. *Fixed-free principle* ***[40]***

2.4 Bender element test

The bender element test is a non-destructive way to determine the shear wave velocity, which can be used to determine the very small strain shear modulus G_{max}. The test is made for testing the response of a soil to determine the behavior to vehicles, vibrations, etc. but can also be used for static loadings, which occur in the very small strain area. Figure 33 shows the working area for bender elements, according to [41]. As shown in Figure 33, this test is used to determine very small shear strain (0.0001%) stiffness, where the shear stiffness is maximal. It is possible to perform this test multiple times on the same sample, because the bender element test works as a non-destructive test.

[14] confirms the shear strain range which is mentioned in [41], while [9], [23] states that bender elements are useable in another shear strain range. It is mentioned bender elements work for stiffness determination in a shear strain range of 0.001% in [9], [23]. It can be concluded that the strain range for bender elements are minimal both by [14], [9], [23] and [41].

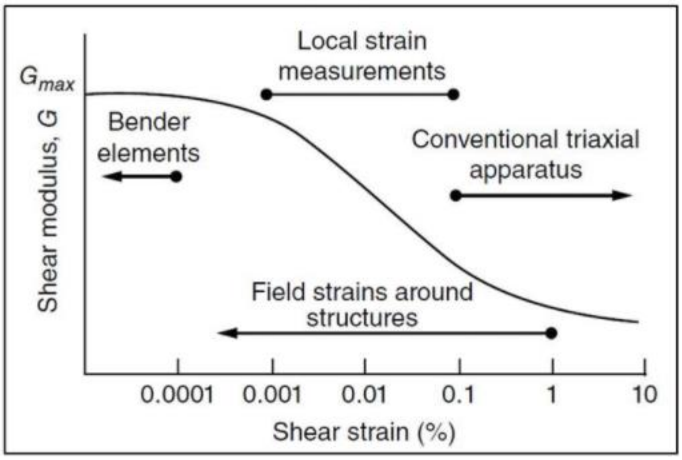

Figure 33. *Working area for bender element tests* ***[41]***

2.4.1 Determining G_{max} with bender elements

The theory behind bender elements is simple. When the transmitter introduces a shear wave, the travel time to the receiver is measured. By means of this it is possible to calculate the velocity, because the travel distance is known. The velocity of the S-wave is calculated like mentioned in [41], [9], [31], [42]:

$$v_s = \frac{L_{tt}}{t} \tag{21}$$

Where
L_{tt} is the tip-to-tip distance between the 2 bender elements (m)
t is the travel time (s)

Following on equation (21) it is possible to determine G_{max}. This is done by means of the dry density ρ [41], [9], [31], [14], [23], [42], via the elastic theory as given by equation (22):

$$G_{max} = \rho * v_s^2 \tag{22}$$

It can be seen in formula (22) that shear wave velocity has a direct influence on G_{max}. This becomes clear in Figure 34 [9], where the uniformity coefficient is shown to have an influence on the shear wave velocity, while the curvature coefficient has no pronounced influence.

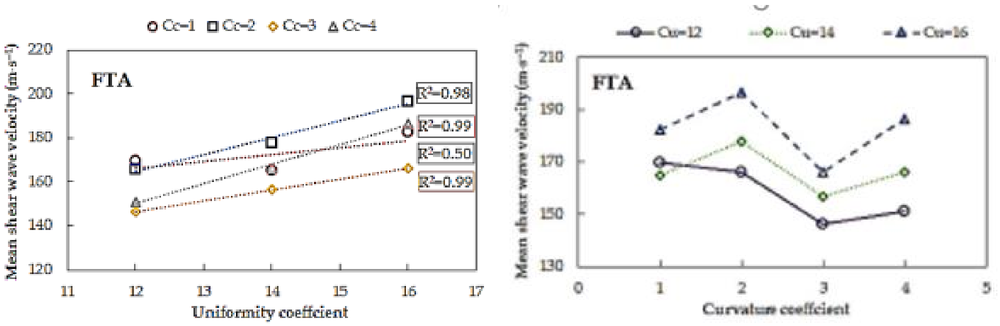

(a) (b)

Figure 34.** Effect of C_u (a) and C_c (b) on mean shear wave velocity **[9]

According to literature G_{max} depends on different factors. It depends on the void ratio and on the mean effective confining pressure $(p' = \sigma'_{3c})$. In addition G_{max} also depends on the relative density and the over-consolidation ratio. Besides, the fines content (*FC*), which is the mass percentage of particles smaller than 0.075 mm have an influence. [31]

2.4.2 Interpreting results of bender elements

A lack of agreement remains when it comes on interpreting the shear wave travel time by bender element tests. No standards are available about the research methods. [9] and [23] discuss a few different approaches when it comes on interpreting the results. All the discussed approaches depend on different factors such as soil- and signal type, test set-up and bender element system, which result in a possible different damping.

Manually interpreting of results is conducted in [9] by the first-time-of-arrival method (MFTOA) (MFTOA is the same as the start-to-start method) and the peak-to-peak method (MPTP). It should be stated that these two methods require a user intervention, which might make the result unreliable. [9] states that sine waves are used, because this gives a more reliable result in time-measuring methods. An example of the PTP- and FTOA-method is shown in Figure 35 [43].

By the PTP method, the time is measured between the peak of the transmitted and the first received peak. Caution should be taken because the signal can deform, which can cause more than one peak to arrive. It is possible to see in Figure 35 [43] that different interpretations are possible, not only for the PTP-, but also for the FTOA-method.

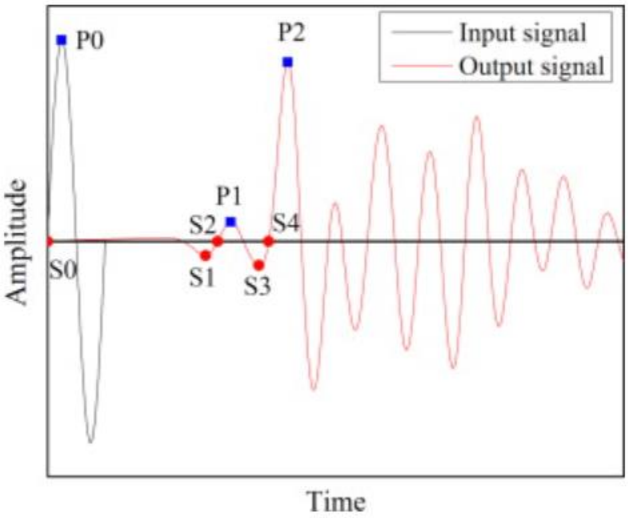

Figure 35. *Difference between PTP (P_i) and FTOA (S_i)* ***[43]***

Figure 36 shows the differences measured in shear wave velocity between the MFTOA and the MPTP method. As can be seen, the MPTP method gives higher shear wave velocities than the MFTOA method when the shear wave velocity is higher. By lower shear wave velocities the difference between the two methods is more limited. [9]

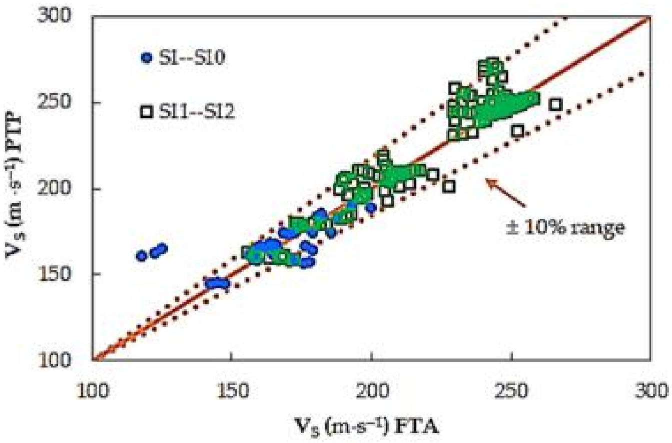

Figure 36. *Difference in shear wave velocity between MFTOA (x) and MPTP (y)* ***[9]***

In addition, a few automated tools of analysis are discussed in [9]. These are the peak-to-peak method (APTP), the zero-crossing method (AZC), the cross-correlation method (ACC) and the cross-spectrum method. This last method works in the frequency-domain, while ACC can both work in time- and frequency domain according to [23]. The 2 other methods work in the time-domain. An example for the interpretation of the cross-correlation method is shown in Figure 37 [43]. A benefit of these automated tools is that the subjectivity of the picked point is taken away.

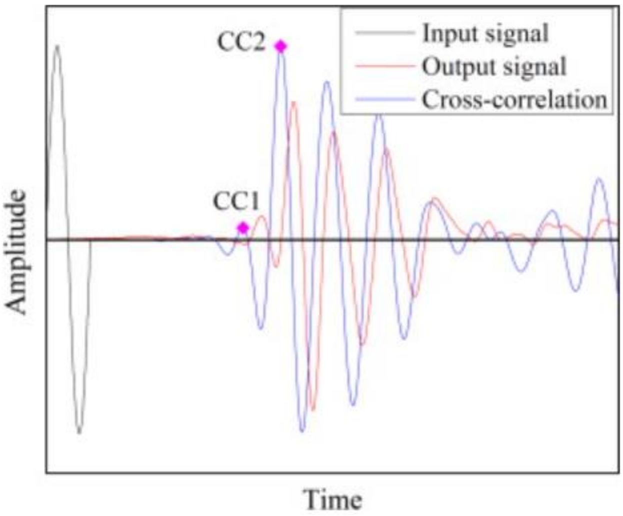

Figure 37. *Cross-correlation method* ***[43]***

As can be seen in Figure 38, the shear wave velocity decreases by an increase of the frequency at low frequencies. This curve flattens when a frequency of around 10 kHz is reached. A possible reason for the decrease of the shear wave velocity might be when lower frequencies are applied, the near-field effect might be more pronounced. [9]

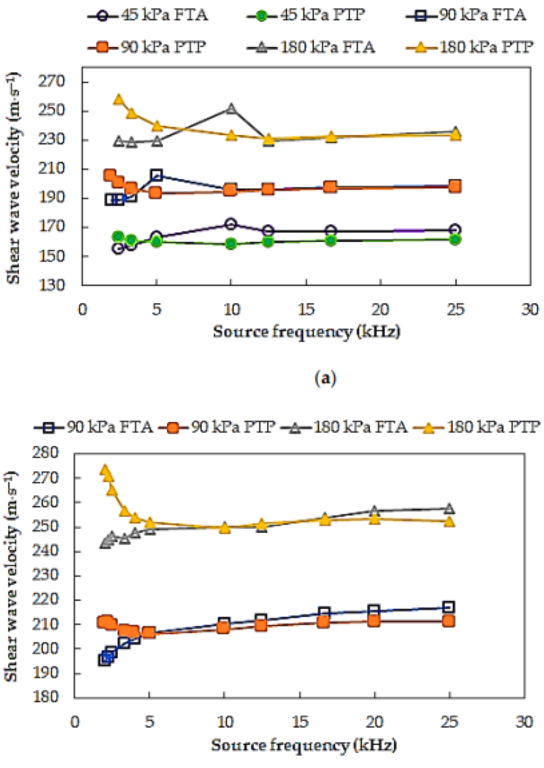

Figure 38. *Shear wave velocity as function of the source frequency by manual interpretation* ***[9]***

Figure 39 shows the shear wave velocity at different frequencies, pressures and consolidation states. Table 3 gives the different tested materials. It can be concluded that the cross-spectrum analyzing method gives higher shear wave velocities at higher frequencies. In addition the AZC-method gives higher shear wave velocities in some cases. It can be concluded that those two methods give unreliable data while the MPTP, MFTOA, ACC and the APTP are the most reliable methods. [9]

According to [23] it is preferable to take the first arrived shear wave when using the FTOA-method. A possibility exists to take the second arrived wave, but caution needs to be taken that due to damping, the signal can be strongly reduced and thus unclear. In addition according to [23] the PTP method is more reliable, although due to dispersion and distortion it is recommended to compare results from both FTOA and PTP. Next, [23] states more complex analyzing methods do not give better results than simple methods in the time domain, like FTOA and PTP, given that a sine wave is used with a frequency which is high enough.

To receive a less subjective result [23] also uses ACC method, although it is necessary to post-process the result because the ACC uses the greatest received peak. This would mean if no post-processing is done, the shear wave velocity would be too small. Next, [23] repeats measurements with FTOA and PTP method when the results differ significantly. Additionally, to improve the obtained results from the ACC [23] has used a spectral analysis.

Table 3. *Tested wave periods and tested mean effective stresses* ***[9]***

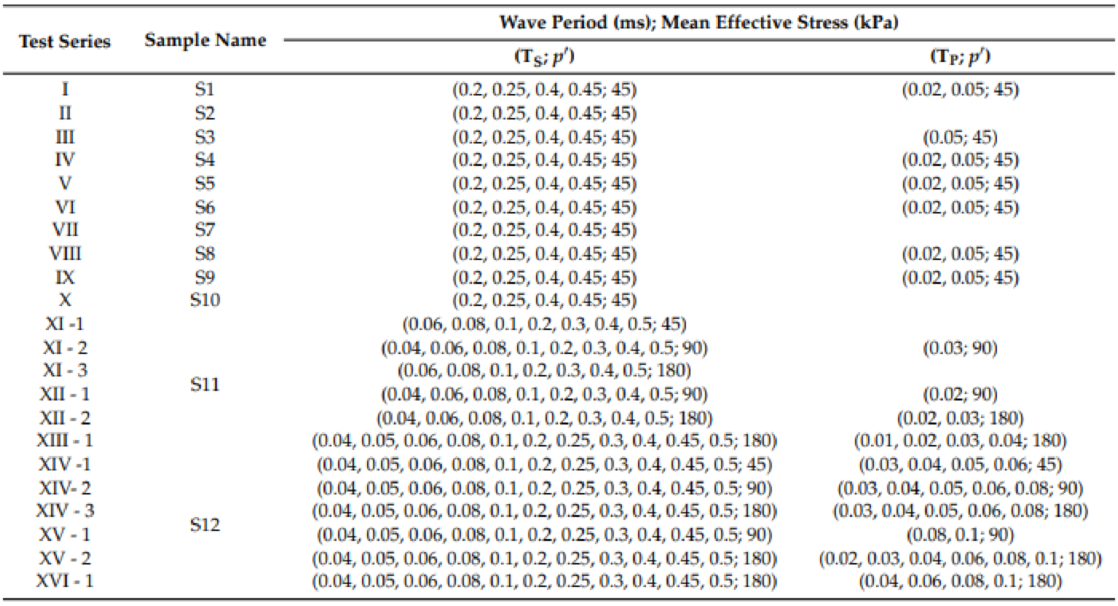

Test Series	Sample Name	Wave Period (ms); Mean Effective Stress (kPa)	
		(T_S; p')	(T_P; p')
I	S1	(0.2, 0.25, 0.4, 0.45; 45)	(0.02, 0.05; 45)
II	S2	(0.2, 0.25, 0.4, 0.45; 45)	
III	S3	(0.2, 0.25, 0.4, 0.45; 45)	(0.05; 45)
IV	S4	(0.2, 0.25, 0.4, 0.45; 45)	(0.02, 0.05; 45)
V	S5	(0.2, 0.25, 0.4, 0.45; 45)	(0.02, 0.05; 45)
VI	S6	(0.2, 0.25, 0.4, 0.45; 45)	(0.02, 0.05; 45)
VII	S7	(0.2, 0.25, 0.4, 0.45; 45)	
VIII	S8	(0.2, 0.25, 0.4, 0.45; 45)	(0.02, 0.05; 45)
IX	S9	(0.2, 0.25, 0.4, 0.45; 45)	(0.02, 0.05; 45)
X	S10	(0.2, 0.25, 0.4, 0.45; 45)	
XI -1	S11	(0.06, 0.08, 0.1, 0.2, 0.3, 0.4, 0.5; 45)	
XI - 2		(0.04, 0.06, 0.08, 0.1, 0.2, 0.3, 0.4, 0.5; 90)	(0.03; 90)
XI - 3		(0.06, 0.08, 0.1, 0.2, 0.3, 0.4, 0.5; 180)	
XII - 1		(0.04, 0.06, 0.08, 0.1, 0.2, 0.3, 0.4, 0.5; 90)	(0.02; 90)
XII - 2		(0.04, 0.06, 0.08, 0.1, 0.2, 0.3, 0.4, 0.5; 180)	(0.02, 0.03; 180)
XIII - 1	S12	(0.04, 0.05, 0.06, 0.08, 0.1, 0.2, 0.25, 0.3, 0.4, 0.45, 0.5; 180)	(0.01, 0.02, 0.03, 0.04; 180)
XIV -1		(0.04, 0.05, 0.06, 0.08, 0.1, 0.2, 0.25, 0.3, 0.4, 0.45, 0.5; 45)	(0.03, 0.04, 0.05, 0.06; 45)
XIV- 2		(0.04, 0.05, 0.06, 0.08, 0.1, 0.2, 0.25, 0.3, 0.4, 0.45, 0.5; 90)	(0.03, 0.04, 0.05, 0.06, 0.08; 90)
XIV - 3		(0.04, 0.05, 0.06, 0.08, 0.1, 0.2, 0.25, 0.3, 0.4, 0.45, 0.5; 180)	(0.03, 0.04, 0.05, 0.06, 0.08; 180)
XV - 1		(0.04, 0.05, 0.06, 0.08, 0.1, 0.2, 0.25, 0.3, 0.4, 0.45, 0.5; 90)	(0.08, 0.1; 90)
XV - 2		(0.04, 0.05, 0.06, 0.08, 0.1, 0.2, 0.25, 0.3, 0.4, 0.45, 0.5; 180)	(0.02, 0.03, 0.04, 0.06, 0.08, 0.1; 180)
XVI - 1		(0.04, 0.05, 0.06, 0.08, 0.1, 0.2, 0.25, 0.3, 0.4, 0.45, 0.5; 180)	(0.04, 0.06, 0.08, 0.1; 180)

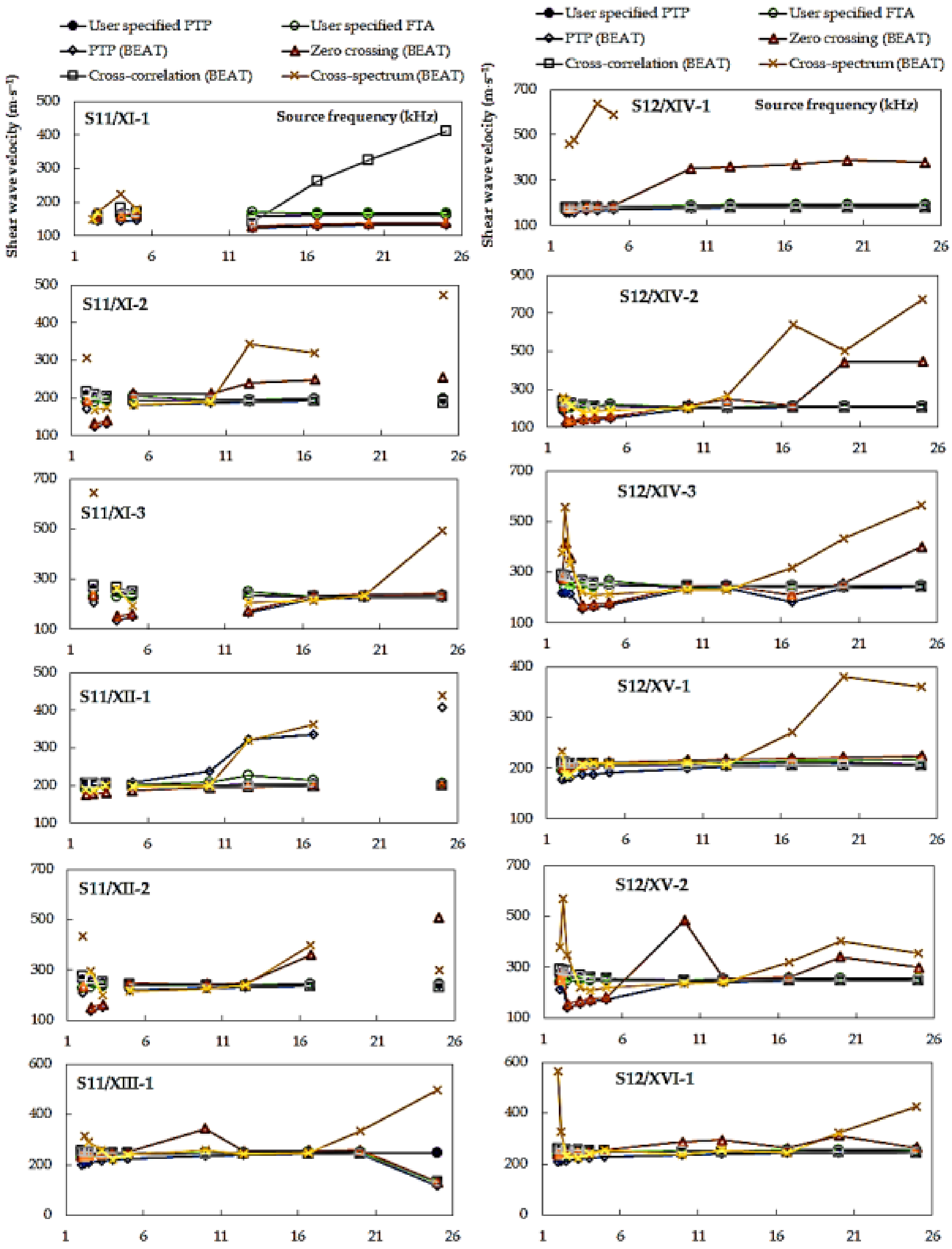

Figure 39. *The difference in shear wave velocity between different analyzing methods* ***[9]***

2.5 Comparison of results from bender elements and resonant columns

According to [5] test results from resonant columns and bender elements compared, give a consistent result on sands from 0-2 and 0-4 mm up to 200 kPa effective confining pressure. Above 200 kPa bender elements begin to give higher values, although the difference is limited. At sands with grain size 0-8 mm this tendency is not seen, while at greater maximum grain sizes considerable higher results are found by bender elements in comparison with resonant columns. Thus according to [5] when grain sizes are above 8 mm resonant columns are more reliable.

A more extensive explanation of this is given in [43], which is briefly summarized in this section by means of the shear wave velocity as function of the effective confining pressure. In addition the shear velocity is described as function of the excitation frequency.

First, the effect of the frequency and effective confining pressure will be discussed in dry sands (Figure 40 (a)) and saturated clean sand (Figure 41 (a)). Figure 40 (a) and Figure 41 (a) shows the difference received on results between different excitation frequencies and analyzing methods explained in Figure 35 and Figure 37 by bender elements. An increase of the excitation frequency causes an increase of the shear wave velocity. In addition results under 5 kHz are scattered between the different analyzing methods. The spreading of the results between the different analyzing methods stays approximately the same at frequencies higher than 20 kHz, which concludes that the near-field effect stays because of a rebound from S-waves. Besides, the effect of the resonant column is shown in Figure 40 (a), which proves to be a more reliable method. [43]

Additionally, Figure 40 (b) and Figure 41 (b) shows the effect of the effective confining pressure on the shear wave velocity, by different analyzing methods, on dry sands respectively saturated clean sand. It can be seen that bender elements and resonant columns are both a reliable source to determine the small strain shear modulus, although the results from bender elements are approximately 5 – 10 % higher than those received from resonant column tests by saturated clean sands. A possible reason might be that dispersion of S-waves has an influence on the shear wave velocity, because clean sands contain fewer *FC* than natural sands. [43]

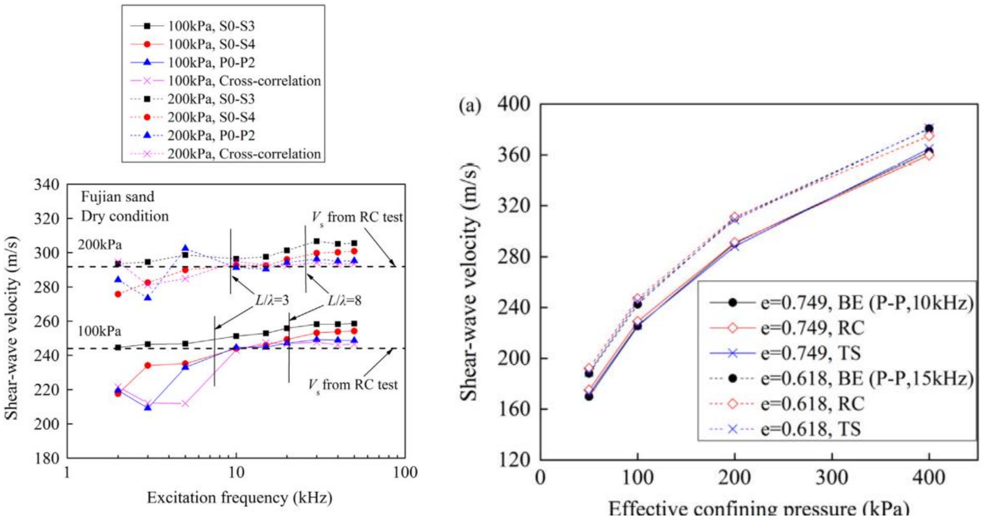

(a) (b)

Figure 40.** Effect of frequency (a) and effective confining pressure (b) at the shear wave velocity by dry Fuijian sands **[43]

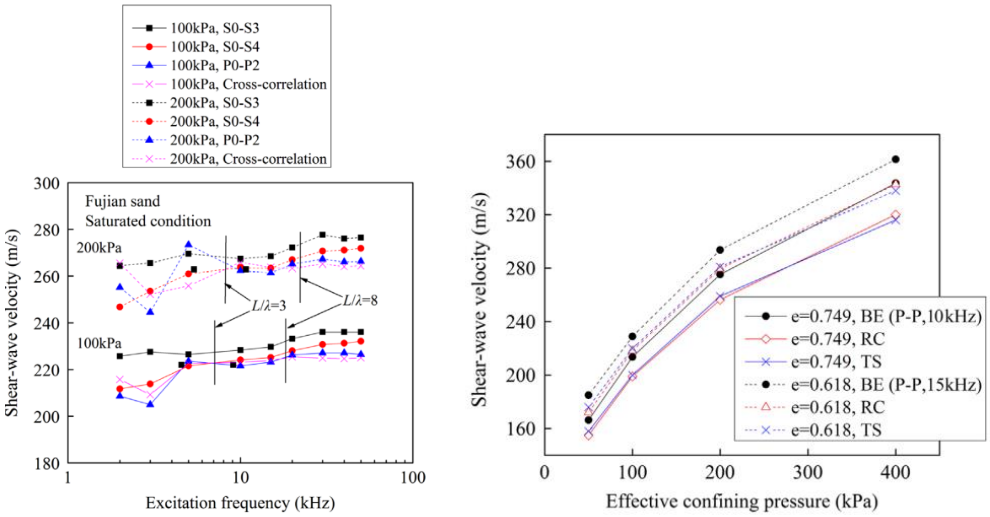

(a) (b)

Figure 41.** Effect of frequency (a) and effective confining pressure (b) at the shear wave velocity by saturated clean Fuijian sands **[43]

Figure 42 (a) shows that the shear wave velocity by saturated natural sands in bender element tests is 5 – 10 % higher than the results contained with resonant columns, independent of the effective confining pressure. In addition Figure 42 (b) shows that the shear wave velocity by saturated natural sands is approximately the same between bender element – and resonant column tests. The results in Figure 42 (b) are explainable by the fines content, which this sand contains more compared to Figure 42 (a), which might change the soil properties. [43]

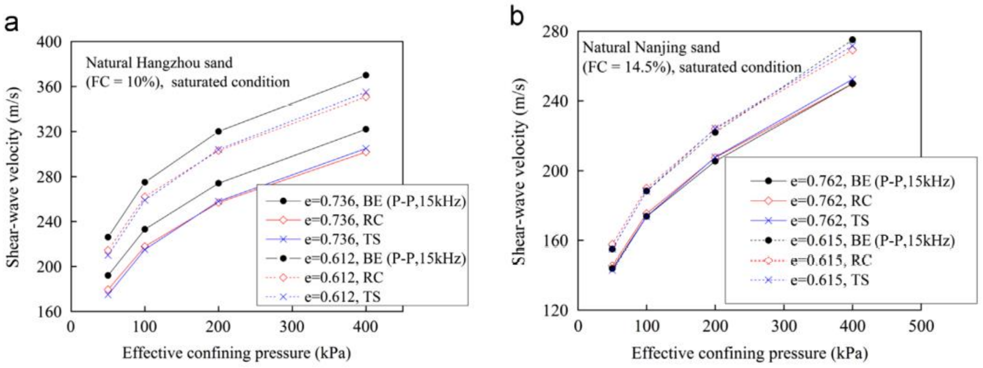

(a) (b)

Figure 42.** Effect of effective confining pressure at the shear wave velocity by saturated natural Hangzhou and Nanjing sands **[43]

Finally, the effect of moisture content in unsaturated sands will be discussed. According to [44], the shear modulus’ obtained by poorly graded soils in moist condition is lower than these of a moist well graded sample. In dry conditions the effect is the opposite and poorly graded soils have a higher shear modulus compared to well graded samples. A possible explanation is that capillary effects have more influence in moist well graded samples compared to moist poorly graded samples. Additionally, in dry conditions the effect can be explained by the given that the smaller grains have more chance to move between the greater grains, and thus causes a lower stiffness in well graded samples.

3. MATERIALS AND METHODOLOGY

3.1 Localisation of Viasvesi

During the testing series, Viasvesi sand will be used to perform resonant column and bender element tests on. Viasvesi is located at the western/south-western coast of Finland, near Pori. Figure 43 shows where Viasvesi is located.

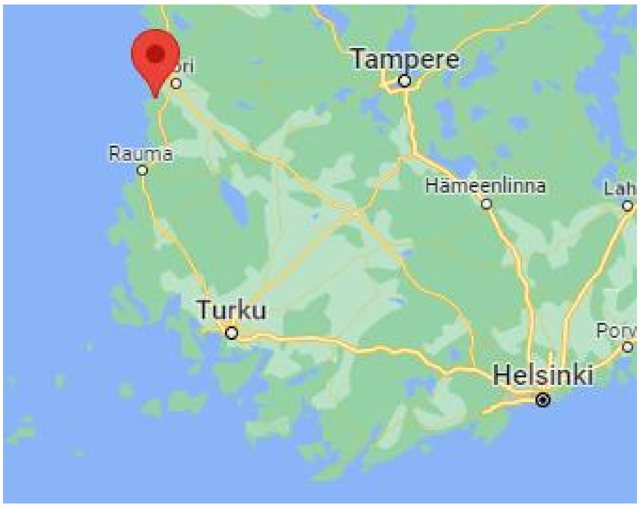

Figure 43. *Localisation of Viasvesi*

3.2 Soil classification according to EN ISO 14 688-1

Table 4 give the classifications, used in EN ISO 14688-1 [2], [3] to define different grain sizes. According to [4] the fines content *FC* of soils is defined as soils with a particle size smaller than 0.063 mm, by means of DIN 18196, which matches with silt. Although, most literature mentions *FC* contains all soils, which have a fall-through on a sieve of 0.075 mm. In [5] grain size distribution curves stop at 0.074 mm. Due to this it can be stated fines content is seen as particles smaller than 0.074 mm, although silt is seen as particles smaller than 0.06 mm. Additionally, an alternative soil classification is given by [6], which matches with the old classification in Europe.

Table 4. *Particle size fractions* ***[2]***

Soil group	Particle size fractions	Range of particle sizes (mm) [2], [3]	Range of particle sizes (mm) [6]
Very coarse soil	Large boulder (lBo)	> 630	-
Very coarse soil	Boulder (Bo)	$> 200\ to\ \leq 630$	> 200
Very coarse soil	Cobble (Co	$> 63\ to\ \leq 200$	$> 60\ to\ \leq 200$
Coarse soil	Coarse gravel (cGr)	$> 20\ to\ \leq 63$	$> 20\ to\ \leq 60$
Coarse soil	Medium gravel (mGr)	$> 6.3\ to\ \leq 20$	$> 6\ to\ \leq 20$
Coarse soil	Fine gravel (fGr)	$> 2\ to\ \leq 6.3$	$> 2\ to\ \leq 6$
Coarse soil	Coarse sand (cSa)	$> 0.63\ to\ \leq 2$	$> 0.6\ to\ \leq 2$
Coarse soil	Medium sand (mSa)	$> 0.2\ to\ \leq 0.63$	$> 0.2\ to\ \leq 0.6$
Coarse soil	Fine sand (fSa)	$> 0.063\ to\ \leq 0.2$	$> 0.06\ to\ \leq 0.2$
Fine soil	Coarse silt (cSi)	$> 0.02\ to\ \leq 0.063$	$> 0.02\ to\ \leq 0.06$
Fine soil	Medium silt (mSi)	$> 0.0063\ to\ \leq 0.02$	$> 0.006\ to\ \leq 0.02$
Fine soil	Fine silt (fSi)	$> 0.002\ to\ \leq 0.0063$	$> 0.002\ to\ \leq 0.006$
Fine soil	Clay (Cl)	≤ 0.002	≤ 0.002

3.3 Materials and methodology

A short description will be given about the used equipment to determine the sand its specific characteristics, while next to this the followed procedure will be mentioned. These characteristics are the grain size distribution, particle density and the proctor curve. Next, a brief description is given about moist tamping, dry tamping, wet pluviation and air pluviation. Besides, Skempton's-B value is briefly discussed, together with a link to the saturation degree. Additionally, a description will be given about the methods and materials used to prepare the sand samples for testing, the triaxial cell and on how to use the resonant column and bender elements.

3.3.1 Sieving column – grain size distribution

Table 5 gives classifications, used in EN ISO 14688-2 [7], [8] to define different grain size distribution curves, by means of uniformity coefficient C_u and coefficient of curvature C_c. In addition it is stated in [9] that medium graded soils have $6 \leq C_u \leq 15$ and well graded soils have a $C_u > 15$.

Table 5. *Grading curves for different shapes* ***[7], [8]***

Term	C_u	C_c
Uniformly graded	< 3	< 1
Poorly graded	$3\ to\ 6$	< 1
Medium graded	$6\ to\ 15$	< 1
Well graded	> 15	$1\ to\ 3$
Gap graded	> 15	< 0.5

In addition, ASTM D 2487-06 [10] mentions clean sands have a uniformity coefficient greater than 6 and a curvature coefficient between 1 and 3. In contrast with EN ISO 14688-2 [7], [8], ASTM D 2487-06 [10] mentions a well-graded sand is identified by a coefficient of curvature greater than 6.

[9] mentions which soils will compact well. This depends on the coefficient of curvature C_c, which is given by:

$$\boldsymbol{C_c = \frac{{d_{30}}^2}{d_{10} * d_{60}}} \tag{23}$$

Where

d_i is the grain size with a fall-through on the sieve of i %

If C_c is between 1 and 3, a soil will compact well, while at other C_c-values, the soil will not compact well.

Besides, the earlier mentioned coefficient of uniformity C_u is given by:

$$\boldsymbol{C_u = \frac{d_{60}}{d_{10}}} \tag{24}$$

Determining the grain size distribution and fines content FC of the Viasvesi sand is done according to (NBN) EN 933-1 [11], [12], with a small modification.

According to (NBN) EN 933-1 [11], [12], it is necessary to sieve at least 200 g of soil, because it is expected the maximum grain size is smaller than 4 mm, as mentioned in Table 6. The eventually followed procedure is: approximately 800 grams of dry Viasvesi sand is weighed. The weight of this sample is noted (M_1). To remove as much as fines content as possible, the sample is washed until clear water flows out of a 0.063 mm sieve, as shown in Figure 44 (a). This is done by filling a bucket with the sand and repeatedly filling this bucket with water and removing the water out of the bucket by flowing it over the sieve. Afterwards, the sand is placed in a scale, and dried in an oven. When the sand is dry the mass is noted again (M_2).

Thereafter, the sand is placed in a sieving column (Figure 44 (b)) and shaken for approximately 15 minutes. Table 7 shows the sieving configuration, according to NBN EN 933-2 [13], which is used in the sieving column. In addition a pan is placed at the bottom to have no loss of fines content.

To prevent overloading, the mass of soil on each sieve should be limited. The maximum mass on each sieve is given by [11], [12]:

$$\boldsymbol{m = \frac{A * \sqrt{d}}{200}} \tag{25}$$

Where

A is the area of the sieve (mm²)

d is the aperture size of the sieve (mm)

After the sieving procedure, the retaining mass on each sieve is measured (R_i with $i = 1$ for the coarsest sieve and n for the smallest sieve). In addition the retaining mass on the pan can be measured (P). After this, the fines content can be determined. This is done by equation (26):

$$\boldsymbol{FC}(\%) = \frac{\boldsymbol{M_1 - M_2 + P}}{\boldsymbol{M_1}} * \boldsymbol{100} \tag{26}$$

Table 6. *Mass of aggregates which needs to be sieved* ***[11]****,* ***[12]***

Aggregate size *D* (mm)	**Mass of aggregates (kg)**
90	80
32	10
16	2.6
8	0.6
<4	0.2

*Note: aggregates of other sizes, below 90 mm, the minimum test mass may be interpolated by $M = (D/10)^2$

(a) *(b)*

Figure 44. *Sieving configuration*

Table 7. *Used sieve sizes*

Sieve size (mm)
2.0
1.0
0.50
0.25
0.125
0.063
Pan

3.3.2 Particle density – pycnometer

It is possible to use 2 methods, based on the same principle, to determine the particle density [50]. Two pycnometers are filled via a funnel with approximately 1 kg of dry sand. Afterwards, these pycnometers are filled with water and the air is removed by slightly shaking it and turning it around. The sand is soaked in the water for at least 1 day to remove all enclosed air. A second type of funnel is placed on the pycnometer and filled with water until a marked level. The mass of the pycnometer, together with the soil, water and funnel is measured (W_{sw}). Afterwards the pycnometer is emptied and cleaned. In addition, the sand is placed in a drying oven for 24 hours. The pycnometer and the funnel are filled with water again until the marked level and the mass is measured (W_w). When the soil is dry, the mass of the dry aggregate is measured (W_s-W_a).

After these measurements the particle density can be determined via equation (27) by [50]:

$$\boldsymbol{\rho_p = \frac{\rho_w * (W_s - W_a)}{(W_s - W_a) - (W_{sw} - W_w)}} \qquad \textbf{(27)}$$

Where

ρ_w is the density of water

According to both NBN and SFS EN 1097-6 [51], [52] the test portion needs to be sieved on a 0.063 mm sieve to remove finer particles, before determining the particle density. The fines content is removed with the same procedure as mentioned in section 3.3.1. In addition, the mass which is tested should be at least 300 g. More information about determining the particle density can be found in NBN and SFS EN 1097-6 [51], [52]. The pycnometers and funnel to add sand in the pycnometer are shown in Figure 45.

Figure 45. *Pycnometer test*

3.3.3 Proctor compaction and dry density

Figure 46 (a) shows the materials which are used to prepare the sample for the proctor test. A mold (diameter 100 mm and height 120 mm [45]) with a protection against bumps (the left cylinder in Figure 46 (a)) is placed on a pedestal (right in Figure 46 (a)). After the mold is filled, the protection is taken away and a ruler is used to flatten the surface. A brush is used to clean the materials in different stages. To compact the sample, a proctor hammer is used, as shown in Figure 46 (b).

(a) *(b)*

Figure 46. *Proctor compaction set-up*

To start the proctor test, 3 samples of approximately 2 kg are weighed. In addition, the mass of the mold and scales is weighed. Next, a specific amount of water is added to every sample. The buckets (Figure 47) are closed and shaken to get a uniform, moist sample. One hour is waited, to let the sand soak in the water. Afterwards, the proctor mold is filled in 5 layers for each sample and after each layer the moist sample is compacted 25 times with a proctor hammer, as shown in Figure 48. When the sample is prepared, the protection at the top of the mold is removed and the top of the sample is flattened (Figure 49). The mold is placed on a cylinder (in the middle of Figure 46 (a)) and pushed out by slightly letting the proctor hammer fall on it. The sand is caught in a scale, all materials are cleaned above the scale (make sure no loss of sand occurs) and everything is weighed. Afterwards, all samples are placed in a drying oven to determine the dry weight.

Figure 47. *Moistening of the sample*

(a) *(b)*

Figure 48. *Compacting the sample*

Figure 49. *Result after compaction and flattening*

To determine the dry density of the samples ρ_d, an excel file made available for the proctor curve is used. Because the wet weight W_n, the water content W and the volume V of the mold is known, it is possible to calculate the dry density. This is done as follows:

$$V = \frac{\pi * D^2 * H}{4} \tag{28}$$

$$\rho_d = \frac{W_n}{\left(1+\frac{W}{100}\right) * V}$$

Additionally, a similar method can be used to determine the dry density during the resonant column and bender element tests.

Both NBN and SFS EN 1097-3 [53], [54] give a slightly different method to determine the dry density. Despite that, this method is based on the same principle and thus can be used. Additionally, NBN and SFS EN 1097-3 [53], [54] gives the volumes which are necessary to determine the bulk density, in this case used to determine the dry density, as function of the upper grain size of the aggregate.

Table 8. *Necessary volume to determine the bulk density according to NBN and SFS EN 1097-3* ***[53]****,* ***[54]***

Upper size of aggregate *D* (mm)	**Capacity (L)**
Up to 4	1
Up to 16	5
Up to 31.5	10
Up to 63	20

3.3.4 Void ratio

The void ratio *e* is the ratio between the volume of voids V_{voids} in a sample plotted against the volume of solids V_{solids} in a sample [55], [56]:

$$e = \frac{V_{voids}}{V_{solids}}$$

Due to this definition the void ratio *e* is directly proportional with the change of volume of the voids. The consequence of this is that a sample, tested in a drained condition, the void ratio will be able to change. In addition when saturated samples are tested in undrained condition, the void ratio will be constant because water is neglectable or not deformable and will not have the chance to flow out of the sample. Due to short consolidation times during bender element and resonant column tests, when a saturated sample is tested in drained condition, the change of void ratio will be minimal and it can be stated that the void ratio is constant. [56]

It is not always easy to determine the volume of voids. To solve this problem, a slightly different formulation for the void ratio is used. It is well known that $V_{voids} = V - V_{solids}$ with *V* the actual volume of the sample and as mentioned in section 3.3.2 and 3.3.3 the particle density respectively the dry density can be determined. The consequence is that the void ratio can be written as (29):

$$\boldsymbol{e = \frac{V - V_{solids}}{V_{solids}} = \frac{\frac{M_d}{\rho} - \frac{M_d}{\rho_p}}{\frac{M_d}{\rho_p}}} \qquad \textbf{(29)}$$

When the void ratio is known, a possibility exists to determine the relative density D_r. This density can be calculated as mentioned in [4], [29] by:

$$\boldsymbol{D_r = \frac{e_{max} - e}{e_{max} - e_{min}}} \qquad \textbf{(30)}$$

Where

e_{max} is the void ratio which is maximum reachable

e_{min} is the minimum void ratio which is reachable

It should be noted e_{max} and e_{min} needs to be determined with specific procedures, which are shortly noticed in [6]. To determine the maximum density, and thus the minimum void ratio, a one liter mold is filled with water and sand is brought in it. This soil is then compacted with a tamper, connected to a vibrating hammer. Afterwards, the sample is dried in an oven. Additionally, the minimum density, and thus the maximum void ratio, can be determined by bringing 1 kg of dry soil into a cylinder. This cylinder is closed with a cork and the sample is shaken. Afterwards, the volume is determined.

3.3.5 Moist – and dry tamping and undercompaction method

Figure 50 shows the used set-up during tamping. A stative is used to accurately place all equipment. First of all, a disk is used to prevent the mold from moving (Figure 50: long dashed line). In addition, a ring is placed in this disk to prevent too much loss of soil after removing the disk. Besides, a second disk (Figure 50: short dashed line) is used to support the tamper (Figure 50: long-short dashed line), and thus tamp the layers, accurately. In addition, a funnel is used to fill the mold without loss of soil.

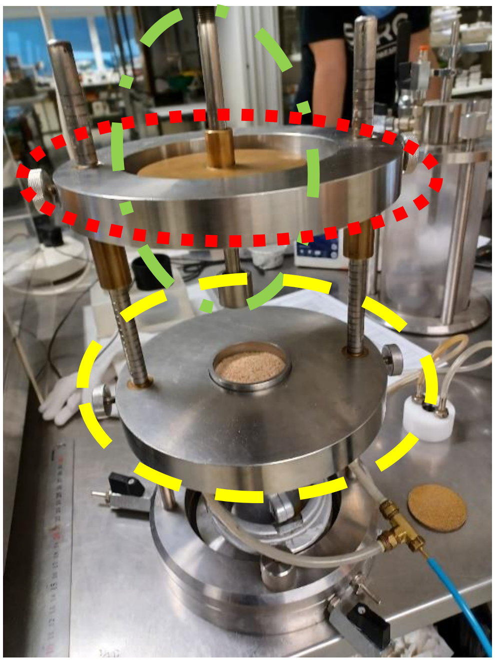

Figure 50. *Moist - and dry tamping*

(a) (b)

Figure 51. *Preparing the sample and triaxial cell*

In the moist tamping method, a mold with a membrane in it is filled in different layers with a moist soil which has uniform water content. This is done in a homogenous, isotropic structure. After placing a layer, the soil is tamped. [57]

The benefit of this method is that it is possible to provide a wide range of void ratios [58]. The soil is used in a moist condition to lubricate the grains, which makes the tamping easier. A possible way to moisten it is to use a syringe, to moisten it in small amounts accurately with the correct amount of water. [59] suggests 10 mass% is ideal to moisten the soil, but the exact amount needs to be determined with the proctor test.

Some data is necessary to know the amount of soil which needs to be prepared. [59] mentions the necessary amount of soil for each layer can be calculated by:

$$\boldsymbol{W_d = \frac{\pi * D^2 * H}{4} * \frac{\gamma_d}{n}} \qquad \textbf{\textit{(31)}}$$

$$\boldsymbol{W_n = W_d * \left(1 + \frac{W}{100}\right)} \qquad \textbf{\textit{(32)}}$$

Where

W_d is the dry mass of the sand

W_n is the wet mass of the sand

W is the necessary mass% of water

D is the diameter of the tested sample

H the height of the tested sample

γ_d is the dry weight per m^3 of the sand

n is the total amount of layers

In addition it is suggested the height of a layer should not be greater than 12 mm as [21] mentions, although in this study a layer is taken of approximately 20 mm for each layer.

The dry tamping method follows the same principle as the moist tamping method, although the soil is oven-dry.

Additionally, it is possible to use under compaction, a more complex technique to prepare samples. A mold is filled in different layers of moist soil of approximately 5 – 10 mass% water (depends on the results from the proctor test). The water is added to provide an extra stiffness, when the mold is taken away, due to capillary forces. After inserting a layer, the soil is compacted with a tamper. During the tamping, layers under the new one are also tamped. Because of this, it is important to anticipate how hard lower layers are tamped, to provide a uniform structure at the end. [60]

In literature, a few formulas are given to determine the thickness of each layer. [59] mentions that the under-compaction degree can be calculated by equation (33):

$$\boldsymbol{U_i = U_1 * \frac{U_1 - U_n}{n-1} * (i-1)} \tag{33}$$

Following on equation (33), the thickness of the sample after tamping a certain amount of i layers can be calculated by:

$$\boldsymbol{h_i = \frac{H}{n} * \left((n-1) + \left(1 + \frac{U_i}{100}\right)\right)} \tag{34}$$

Where

U is the under-compaction degree

H is the height of the sample

h_i is the height of the sample after tamping layer *i*

n is the total amount of layers

It needs to be mentioned that U_1 needs to be calculated by empirical equations or estimated. Due to this, under compaction can be complex.

3.3.6 Air pluviation method

By the air pluviation method, soil falls from a height. The benefit of this method is that it is possible to get homogenous samples. Caution needs to be taken that the elevating air does not influence the soil too hard. An ideal height to drop the soil from is around 20 to 30 cm, although small differences can exist on this height due to grain size distribution. [59]

The flow rate at the air pluviation method depends on different factors. Therefore, it is important to choose the correct sieve/perforations pattern, density and size. [59]

3.3.7 Wet pluviation

Different authors mention slightly different methods of preparing sand samples with wet pluviation. To start, 2 authors their method will be discussed, whereafter the eventually used method will be discussed.

According to [46], a membrane is filled with water. Additionally, a flask is filled with a prepared water-sand mixture and closed with a cork. This flask with the mixture is placed mounted on a clamp, with the opening slightly under water. Next, the cork is removed and the flask is vibrated until all sand is deposited in the mold. During this process, water present in the mold, dislocates to the flask and replaces the volume of sand in the flask. Figure 52 shows the set-up used to perform the wet pluviation method with a flask.

Figure 52. *Wet pluviation set-up with flask*

In addition, another method is proposed by [47], where water is also brought into a membrane. First, the measurements of the mold are measured whereafter it is possible to determine the necessary mass with the preferred density.

$$\boldsymbol{M = \rho * V} \tag{35}$$

Where

V is the volume of the mold

ρ is the preferred density

Next, the mass of sand can be weighed and water is added, according to [47]. Additionally, a funnel is mounted on a clamp, as shown in Figure 54 (a), and placed just below the water surface. Wet sand is gradually added in the funnel with a spoon, to be able to control the amount of added sand. Besides, when adding sand to the funnel, water is gradually drained from the mold. The water level needs to stay approximately the same when draining water and adding sand at the same time.

During this research, samples were eventually prepared using the method noticed in [47], with some minor modification. To receive different densities, the sample is prepared in 5 layers. After preparing each layer, a constant static loading, as shown in Figure 54 (b), is introduced. This is done by a designed helping piece, which is placed on the sample in combination with a filter paper for approximately 10 to 15 minutes, consolidates the sample in combination with the static loading and makes it possible that water can flow away. The filter paper prevents sand to come in the pipes of the designed helping piece. The 3D-printed helping piece is shown in Figure 53.

Once the last layer is deposited, the static load is kept constant on the sample overnight. When the sample is ready, a small vacuum is introduced in the sample to make the sample more steady.

It needs to be noted that the static load did not have much influence on the density. This can be explained by the membrane that was not in complete vacuum, which caused the membrane to provide a resistance to the helping piece. Therefore, a movement downwards was prevented or resisted. When higher loads were applied, the load became unstable and therefore it was not possible to use the full potential of the technique.

Figure 53. *Draining and loading piece*

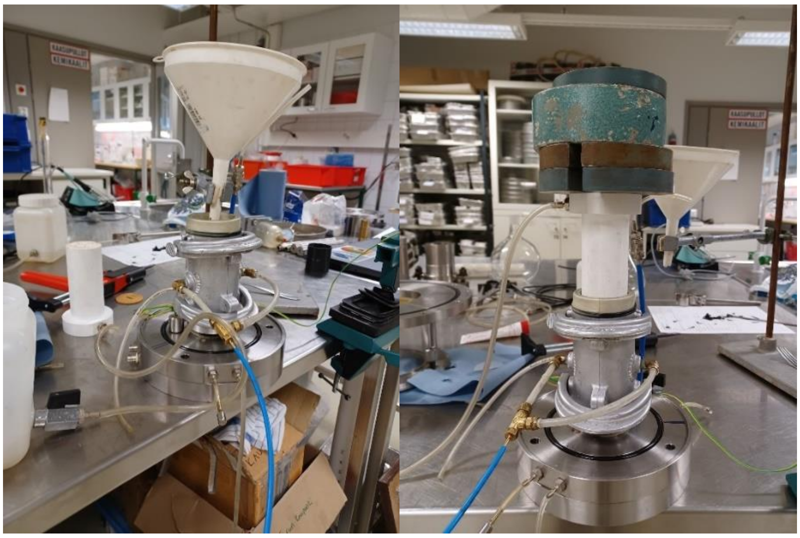

(a) (b)

Figure 54. *Preparing the sample with wet pluviatioin method; (a): adding sand; (b): static loading*

3.3.8 Preparing of the sample

3.3.8.1 Preparing method of the sample

To prepare the triaxial cell, a porous stone, with a bender element, is placed at the bottom of the testing device. Next, a mold of 2 shells, with in it a membrane in vacuum and two O-rings at the bottom and top, is placed over the pedestal. The pedestal is greased before, to prevent confining fluid penetrating the membrane at the contact point. Afterwards, the bottom part of the membrane is brought in touch with the pedestal.

Once the preparation of the mold is ready, it is possible to prepare the sample. This is eventually done by moist tamping (section 3.3.5).

It is clear different specimen diameters and heights can be used during testing. This possibly depends on the grain sizes which are tested and the equipment which is available. This becomes clear by analyzing different authors, like [22], [17], [31]. Tests will thus be executed on samples with diameter 50 mm and height 100 mm, with equipment used by [5], [44].

After preparing the sample, it is possible to remove the mold. Before removal of the mold a saturated porous stone and a greased pressure cap with bender element is placed at the top. Besides, the membrane is brought in contact with the top cap and two O-rings are placed around the contact point. Next, before effectively removing the mold, a vacuum of approximately 5 to 10 kPa is applied on the sample for approximately 5 minutes. This vacuum serves as an extra support of the sample and to keep the sample intact. [5], [44]

While preparing the sample, it is from utmost importance the tips from the bender element make good contact with the soil. If this is not the case, the signals might not transmit while performing the test. By inserting the specimen on the pedestal, it is important that the specimen is not rotated. This might cause loss of good contact. Additionally, when inserting the top (receiver) on the specimen, it is important to push good, to let the bender element penetrate the sample well. [41]

The result of a prepared sample can be seen in Figure 55. In this case 2 membranes are used because the first membrane was broken.

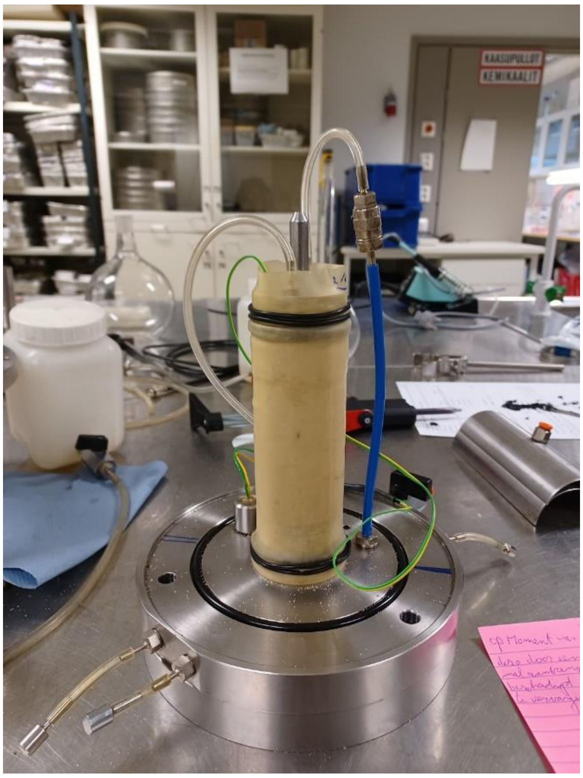

Figure 55. *Result of a prepared sample*

3.3.8.2 Method to repair bender elements

While preparing the sample it is important the bender element does not come in contact with water. This might shorten the electrical circuit. A solution to prevent shortening the circuit, is to put the element in a waterproof case. [42]

Next, the bender element is placed in a slot and surrounded by an epoxy in the slot. Thereafter a porous stone is placed and glued around the elements. While doing this, the bender element is not allowed to touch the porous stone, because this might prevent movement of the bender element. The gap between the porous stone and the bender elementis filled with a rubber. [42]

3.3.9 Preparing the triaxial cell

After preparing the sample, it is possible to place the pressure cell around the sample, as shown in Figure 56. Oil is brought in the cell, with an open vent valve. When the oil is at height in the cell, the vent valve is closed and the enclosed air is brought under pressure. This enclosed air is used as pressure source, which makes a triaxial test under constant confining pressure possible.

When the cell is enclosed and the oil is at level, it is possible to saturate the sample, if the saturation degree is not high enough because of the preparing method, which was the case with moist tamping. Therefore a can with water is placed above the soil sample and connected with a valve at the bottom of the cell. In addition an (nearly) empty can is placed under the soil sample and connected with a valve which is connected with the top of the sample. (Nearly-)Full saturation is reached when the value of the Skempton-B factor is high enough, as section 3.3.10 explains.

It is possible to vent the soil before saturating it. This can be done in triaxial devices by venting the specimen with CO_2. Afterwards deaired-water is flowed through the specimen. It is important the confining pressure is higher than the pressure of the CO_2 and water which flows through the sample. Alternatively it is possible to vent the soil by putting it into a vacuum, although this method loads the soil if the cell is not brought under a lower pressure. In this case it might cause the soil to consolidate. [60]

Figure 60 [5] shows an intersection of the used triaxial device. As can be seen, 2 porous stones are used. In addition at the top porous stone a pressure cap is placed. Additionally, taps are provided to saturate the specimen, to vent the cell and to change the cell pressure. Besides, the pressure cell placed around the sample can be seen.

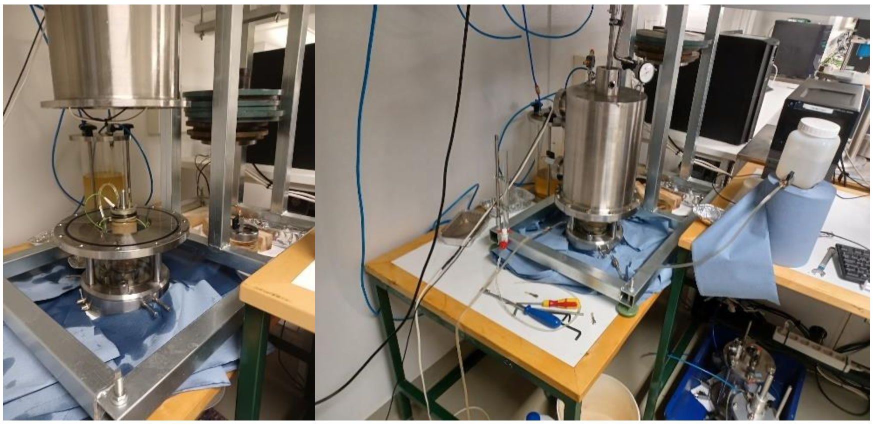

(a) (b)

Figure 56. *Triaxial cell: (a) open; (b) closed*

3.3.10 Skempton-B factor

According to [61], when a confining pressure is applied in triaxial devices, a porewater pressure is developed. It is possible to calculate when a soil is saturated:

$$B = \frac{\Delta U_c}{\Delta \sigma_c} \qquad (36)$$

Where

ΔU_c is the difference in pore water pressure

$\Delta \sigma_c$ is the difference in confining pressure

Skempton's pore pressure parameter *B* characterizes when a soil is saturated. When the porewater pressure does not increase enough with an increasing confining pressure, the sample is not saturated and $B < 1$. In addition when the soil is fully saturated $B = 1$, although a fully saturated soil is hard to accomplish. [61]

[59], [9] and [43] mention it can be concluded that a B-value of 0.95 to 0.98 can be seen as a fully saturated soil, although this is hard to accomplish. [59] shows the relation between the degree of saturation and the pore pressure coefficient of Skempton-B. By example, it can be seen in Table 9 that a B-value of 0.85 corresponds with a saturation degree of approximately 99.5% by loose sands.

Table 9. *Degree of saturation (S) for loose, medium-dense and dense sands and different B-values* ***[59]***

Saturation degree (%)	Loose sand	Medium dense sand	Dense sand
98.0	B=0.53	B=0.45	B=0.38
98.5	B=0.60	B=0.53	B=0.47
99.0	B=0.69	B=0.62	B=0.56
99.5	B=0.85	B=0.80	B=0.75
100.0	B=1.00	B=1.00	B=1.00

Additionally, [62] gives a relation between the B-value and the degree of saturation (Figure 57). It can be seen the change of the B-value with the saturation degree is not linear. This author discusses 2 methods, one without suction taken into account (curve from equation 19 in Figure 57) and one with suction taken into account (curves with s_e). Suction will not be taken into account during this research, because it is a complex calculation, for little more accuracy, as Figure 57 shows.

To receive the saturation degree, the isotropic compressibility is determined by (37):

$$-\frac{dV_a}{V_0} = \frac{\kappa}{p'_0 * (1+e_0)} * dp' \qquad \textbf{(37)}$$

Where

dV_a is the change in the pore air volume

V_0 is the initial volume

κ is the isotropic compressibility of soil in elastic conditions

p'_0 is the initial effective stress

e_0 is the initial void ratio

dp' is the change in pressure

Next, it is possible to determine the saturation degree out of the B-value. This is done as follows with equation (38):

$$\boldsymbol{B} = \frac{\mathbf{1}}{\mathbf{1} + \boldsymbol{p}_{\mathbf{0}}' * \boldsymbol{e}_{\mathbf{0}} * (\mathbf{1} - \boldsymbol{S}_{\boldsymbol{r}\mathbf{0}}) / (\boldsymbol{\kappa} * \boldsymbol{p}_{\boldsymbol{a}\mathbf{0}})} \qquad \textit{(38)}$$

Where

S_{r0} is the saturation degree

p_{a0} is the initial air pressure

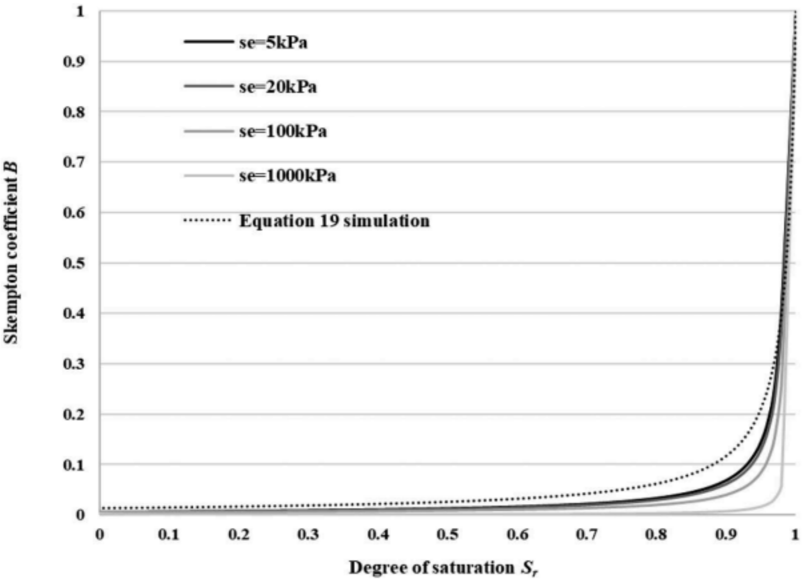

Figure 57. *Evolution of Skempton-B factor with the saturation degree* ***[62]***

To determine the Skempton-B factor, two pressure meters are used. One pressure meter is connected to the air pressure channel, while the other one is connected to one of the valves to saturate the sample. When both pressure meters are connected, the cans with water are disconnected from the cell and draining is blocked. A computer program shows what the increase of air – and water pressure is. When the measurements are started, the software sets all values to zero. Afterwards, it is allowed to increase the pressure. An increase of approximately 10 kPa air pressure is sufficient. When the water pressure approaches the air pressure enough, it can be concluded that the saturation degree is high enough. After measuring the B-factor, the air pressure is set back to the initial value. Figure 59 shows the set-up to determine the Skempton-B factor, while Figure 58 shows the output of a measurement of the Skempton-B value. In Figure 58, the red line is the increase in cell pressure, while the blue line is the increase in pore water pressure.

1,416

13,55

nimetön

Figure 58. *Output measurement of Skempton-B*

Figure 59 shows the setup to saturate the sample and to determine the Skempton-B factor. First of all a connection can be seen where the pressure meter is connected with the air pressure (short-dashed line). Additionaly, a water pressure meter is connected to the cell (short-long dashed line). Both pressure meters are connected with a computer, with a program to give the output of the measurements. The two cans used to saturate the sample are also shown (long-dashed line)

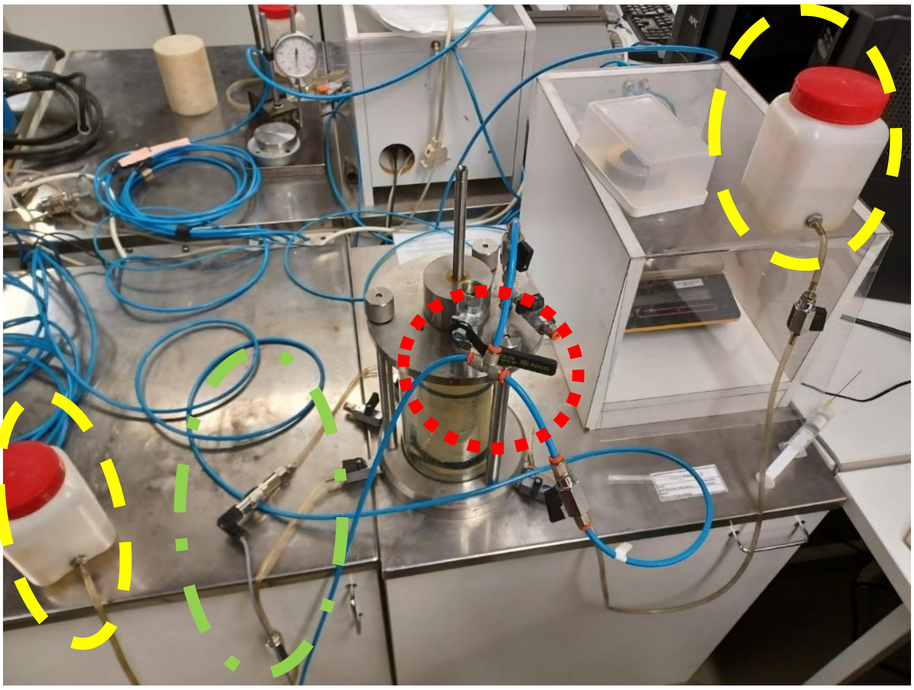

Figure 59. *Set-up to determine the Skempton-B factor*

3.3.11 Resonant column and bender element test

Resonant column and bender element tests are conducted simultaneously at every pressure step. The main equipment which is present in both tests will be described here. The main principle of the testing series will additionally be explained briefly in this section.

3.3.11.1 Test equipment

A triaxial cell is the main part in both tests, as shown in Figure 60 [5], with oil as confining fluid. To execute resonant column tests, different set-ups exist. In this case a fixed-free set-up is used with a Hardin-type oscillator. This Hardin oscillator is a device to provide a torque on the sample [48], and is placed on the upper part with a reaction mass. In addition both top cap and pedestal are equipped with piezoelectric crystals to perform bender element tests. Besides, a counterbalance is provided, to balance the reaction mass and the top cap. [5]

Additionally, a burette is used to measure the change in volume of the sample. Besides, a displacement gauge is used to analyze the change in height from the sample. This displacement gauge is connected with the loading piston, while the other part is supporting on the cell.

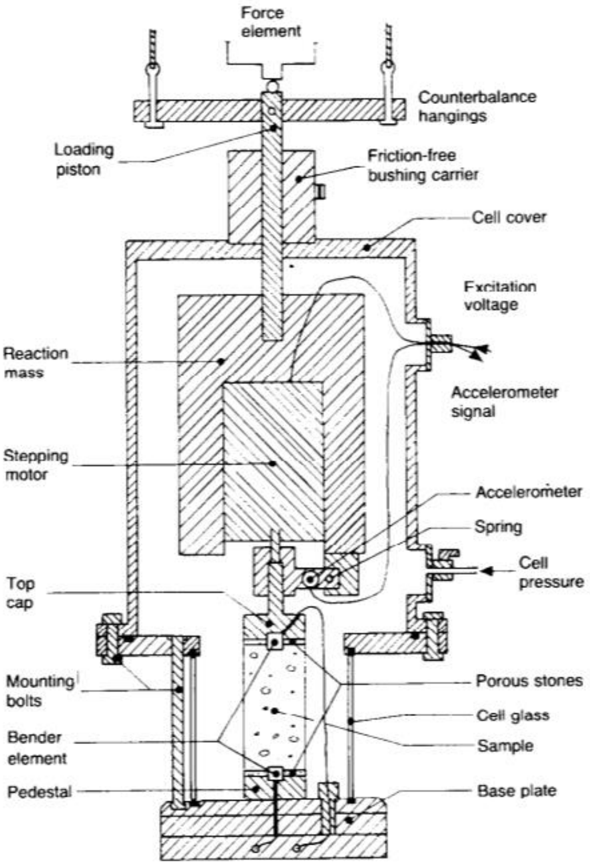

Figure 60.** Triaxial cell with bender elements and resonant column **[5]

3.3.11.2 Main principle of the testing series

13 tests are conducted. The first 5 tests failed and are therefore not further discussed. During the last 8 tests (test 6 to 13), data is eventually collected. During the tests, measurements are done on five pressure steps. First, the pressure is increased from 50, to 100, to 300 kPa. Thereafter, the pressure is decreased again to 100 and 50 kPa. Between every pressure step, a consolidation time of at least 10 minutes is respected, as mentioned in [43]. Additionally, test 12 and 13 are conducted with a consolidation time of 50 minutes, to see if any difference in results can be noticed. The mentioned consolidation time should be taken with caution, due to the given that this time is soil dependant and can be longer for less permeable soils.

After consolidation, the change in height and volume is measured. This is done to correct the density and travel distance. The reason why this is measured, is due to the given that if the change is big enough, this might have a not neglectible effect on the shear modulus and shear modulus reduction.

3.3.12 Resonant column test

In resonant columns, cyclic torsional loadings are produced on a soil sample. The frequency is changed until resonance is established and the (very) small strain stiffness can be determined out of this resonance frequency. In this section a brief description will be given about resonant column tests.

3.3.12.1 Resonant column

The used resonant column device in this test series is a fixed-free, device type 1 (DT1) according to [49], resonant column. At the top, a mass is placed on the resonant column. Here, an accelerometer is connected to, to measure the acceleration of the top mass. This data is used to determine the torsional moment and the twisting angle.

The working principle of a resonant column is that the frequency, is changed, until resonance is reached. With this frequency, it is possible to determine dynamic properties of the soil. Resonance is reached when a phase shift of 90° is reached between the torsional moment and twisting angle. As mentioned in [63], when the elliptical curve is symmetric around the displacement (u) - and excitation force (Q) – axis, resonance is reached. In other cases, the system is not in resonance. Figure 61 [63] shows when the system is or is not in resonance. When the frequency is below the resonance frequency, the stiffness of the system will be dominant, while at a higher frequency the mass of the system will be dominant. Additionally, when the system is in resonance, a 90° phase shift can be noticed between displacement (u) - and excitation force (Q) – axis. Additionaly, a cell pressure is initiated in the resonant column. This cell pressure is considered isotropic, although in the used testing device a possibility exists to initiate an anisotropic stress-state. After consolidation is considered ended, and the necessary measurements (height change, volume change and bender element measurement) are conducted, the resonance frequency is determined.

With a function generator, a sinusoidal signal is generated. This signal is varied in frequency and amplitude until the earlier mentioned resonance frequency has been found. The received signal is measured with a computerscope, which is connected with a device where a volt - and frequency meter are introduced into one device.

During the tests, it is necessary to change the frequency to determine the acceleration. By try and error, it was noticed the frequency needs to be decreased together with an increase of the amplitude to get a decreasing stiffness reduction according to ASTM D4015-15 [49]. Figure 62 gives an image of a sample loaded with the resonance frequency, while Figure 63 gives an image of 2 possible graphs of a sample loaded below resonance frequency.

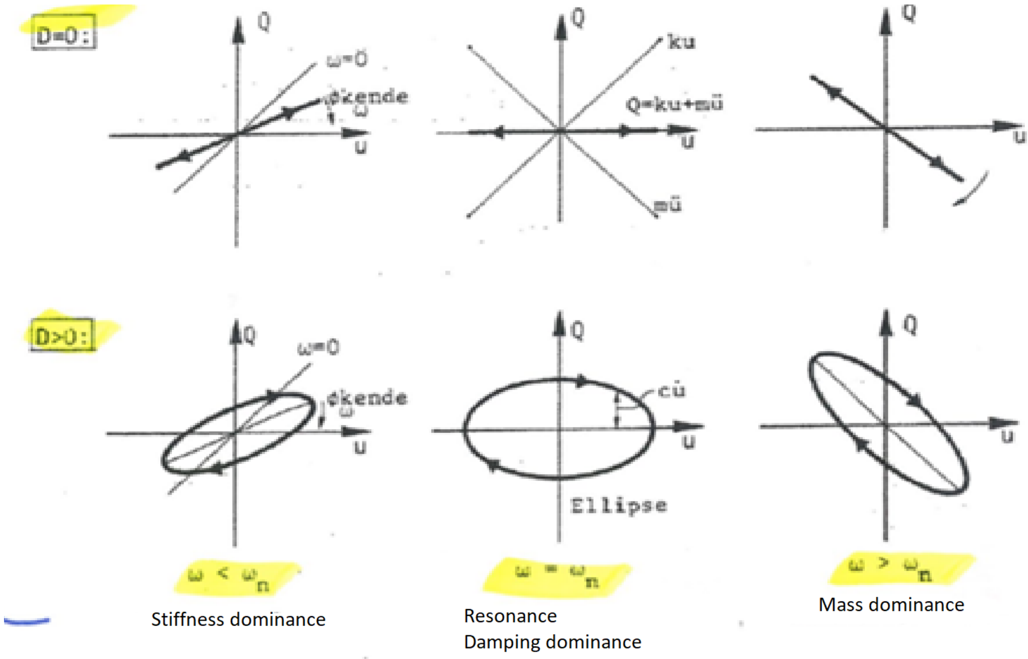

Figure 61. *Symmetrical ellipse around origin (resonance) and unsymmetrical ellipse (no resonance) around u (displacement) - and Q (excitation force) - axis* ***[63]***

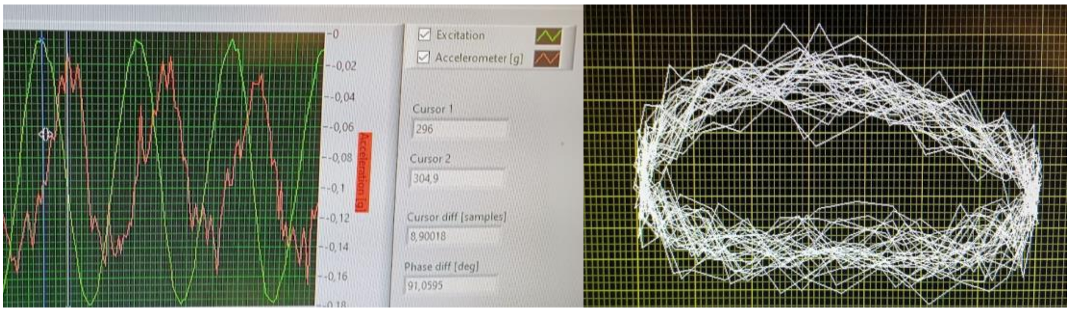

Cursor 1
296

Cursor 2
304,9

Cursor diff [samples]
8,90018

Phase diff [deg]
91,0595

(a) (b)

Figure 62. *Sample in resonance: (a) Phase shift; (b) elliptical curve of displacement and excitation force*

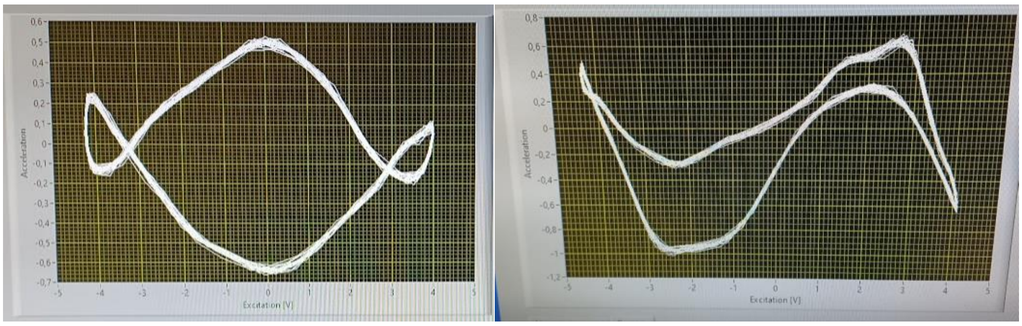

(a) (b)

Figure 63. *Sample loaded below resonance frequency*

[49] discribes the method to determine the very small strain shear stiffness by means of the resonance frequency. [40] and [23] mention an alternative method to determine the inertia I of the sample and vibration source, which might be difficult, and therefore ASTM D4015-15 [49], is used to determine the small strain stiffness reduction. The method, described in [49], will be discussed in section 3.3.12.2.

3.3.12.2 Determining G_{max} via resonant columns with ASTM D4015-15

The passive end platen is directly connected to the fixed base, which means according to [49], a resonant column device type 1 (DT1) is used during the testing series. On this type of resonant column a torque is applied to the active end, while the passive end is fixed. In addition the rotation on this type of resonant column is measured at the active end. The frequency is varied until resonance is reached. Because the geometry, mass and system parameters are known, it is possible to determine the shear modulus (reduction) - and the damping. By varying the amplitude (increase) and frequency (decrease), it is possible to vary the damping and the shear modulus, as function of the shear strain.

Requirements of the test set-up and test specimen

According to [49], a few requirements are necessary. First, it is required the active and the passive end of the resonant column are at least ten times stiffer than the tested material. In addition, the porous stones also need to be ten times stiffer. Next, the porous stones are required to have a diameter which is at least the diameter of the sample. Besides, the excitation frequency on the torque motor needs to be at least 10 Hz to 1 kHz. In addition the torque needs to be measured with an accuracy of 5 % at least. Besides, the readout instruments need to be able to measure the acceleration, velocity or deformation with an accuracy of 5 %, while the frequency needs to be measured with a resolution of 0.1 Hz.

[49] mentions it might be necessary to support the vibrating device. This might be necessary to prevent excessive axial stress. Besides, the mass of the balances need to be measured with an accuracy of 0.1 %.

To get a representative resonant column test, the diameter of the sample needs to be at least 33 mm. In addition the specimen needs to have a diameter of at least six times the maximum grain size. Besides, $2 \leq \frac{length\ of\ the\ specimen}{diameter\ of\ the\ specimen} \leq 7$. [49]

Rotational motion transducer [49]

According to [49], the sensitivity of the accelerometer can be calculated by:

$$\boldsymbol{S_\theta = S_a * r_t * \frac{(2*\pi*f)^2}{9.81}} \qquad \textit{[mV/rad]} \qquad \textbf{\textit{(39)}}$$

Where

r_t is the radial distance of the transducer to the center axis

f is the measured frequency

Following on the sentitivity it is possible to determine the rotation of the specimen:

$$\boldsymbol{\theta = \frac{R*T*r*d*g}{S_\vartheta}} \qquad \textit{[rad]} \qquad \textbf{\textit{(40)}}$$

Where

$R * T * r * d * g$ is the output of the rotation transducer

Active-end rotational inertia [49]

$$\boldsymbol{J_a = J_1 - J_2 + J_3} \qquad \textbf{\textit{(41)}}$$

Where $J_1 = \frac{k_{rod}}{(2*\pi)^2*(f_{rod}^2 - f_a^2)}$

Where

k_{rod} is the spring constant with calibration rod [Nm]

$$k_{rod} = \frac{\frac{\pi * d^4}{32} * G_{rod}}{L}$$

Where

G_{rod}: stiffness rod

L: Length rod

d: diameter rod

f_{rod} is the resonance frequency during calibration [Hz]

f_a is the resonance frequency without sample or calibration rod

$$J_i = \frac{1}{8} * M_i * d_i^2$$

Where

M_i is the mass of the solid cilindrical component [kg]

d_i is the diameter of the solid cilindrical component [m]

$Index$ 2: active end platen used to calibrate the system

$Index$ 3: active end platen used to test the soil

Apparatus damping [49]

$$\boldsymbol{c_a = \frac{\tau_{appl}}{\theta * \omega}} \tag{42}$$

Where

τ_{appl} is the torque

θ is the amplitude of the rotation of the specimen

$\omega = 2 * \pi * f$ with f the resonance frequency during calibration

τ_{appl} is determined through doing a test on the resonant column device, with all parts, except the soil sample, but by use of a calibration rod. First, the resonant frequency is determined. Thereafter both by $0.707 * f_{resonance}$ and $1.414 * f_{resonance}$ a torque is introduced, which has an amplitude of 10 times the noise of the surrounding area. Afterwards it is possible to determine τ_{appl} through:

$$\boldsymbol{\tau_{appl} = TMR * T_r * d * g} \tag{43}$$

Where

$T_r * d * g$ is the input current through the motor, determined with the input voltage during the resonant column measurements

$TMR = 0.5 * k_a * (C_1 + C_2)$ is the torque motor ratio

Where

$$k_a = (2 * \pi * f_a)^2 * J_a$$

$$C_1 = \frac{\theta_1}{2 * CR_1}$$

$$C_2 = \frac{\theta_2}{CR_2}$$

Where

θ_i is the rotation by 0.707 (index 1) respectively 1.414 (index 2) $* f_{resonance}$

CR_i is the torque motor input by 0.707 (index 1) respectively 1.414 (index 2) $* f_{resonance}$ in ampère

Procedure determining the shear modulus and damping

As earlier mentioned, the resonance frequency is reached when the torque and the rotational acceleration are 90° out of phase. According to [49], the received graph will be ellipsoidal, while the axes will be horizontal and vertical. The resonance frequency is determined through starting measurements at a low frequency and increasing this frequency until resonance is reached. Additionally it is possibly necessary to change the amplitude to get a signal without too much noise.

The calculation of the shear modulus and damping is be summarized short:

The soil mass density is determined via equation (35). Besides, it is possible to determine the specimen rotational inertia:

$$\boldsymbol{J = \frac{M * d_i^{2}}{8}} \qquad \textbf{\textit{(44)}}$$

Where

d is the diameter of the specimen

As the total inertia of the active end platen *J_a* and the rotational inertia *J* is known, it is possible to determine the active-end inertia factor T_a and the apparatus damping factor ADF_a:

$$\boldsymbol{T_a = \frac{J_a}{J} * (1 - \left(\frac{f_a}{f_r}\right)^2)} \qquad \textbf{\textit{(45)}}$$

Where

f_a is the apparatus resonance frequency without specimen

f_r is the resonance frequency of the apparatus and the specimen

$$\boldsymbol{ADF_a = \frac{c_a}{2 * \pi * f_r * J}} \qquad \textbf{\textit{(46)}}$$

Where

ADF_a is the apparatus damping factor

f_r is the resonance frequency of the apparatus and the specimen

Because the applied torque τ_{appl} and the rotational motion θ_a at the active end are known, it is possible to determine the measured modified magnification factor *MMF_{meas}*:

$$\boldsymbol{MMF_{meas} = J * \omega^2 * [Re\left(\frac{\theta_a}{\tau_{appl}}\right) + i * Im\left(\frac{\theta_a}{\tau_{appl}}\right)]} \qquad \textbf{\textit{(47)}}$$

Where

$\omega = 2 * \pi * f$ with f the resonance frequenecy

θ_a is the rotational motion at the active end

As MMF_{meas} is known it is possible to determine the dimensionless frequency factor λ^* by comparing it with MMF_{calc}:

$$\boldsymbol{MMF_{meas} = MMF_{calc} = \frac{1}{-T_a + i * ADF_a + \frac{1}{\lambda^* * tan(\lambda^*)}}} \qquad \textbf{\textit{(48)}}$$

Following on these calculations it is possible to determine the shear modulus *G* and the damping *D*:

$$\boldsymbol{G = \rho * (\omega * L)^2 * F_a} \qquad \textbf{\textit{(49)}}$$

Where

$$F_a = \frac{\lambda_{Re}^2 - \lambda_{Im}^2}{(\lambda_{Re}^2 + \lambda_{Im}^2)^2}$$

$$\boldsymbol{D = \frac{-\lambda_{Re} * \lambda_{Im}}{\lambda_{Re}^2 - \lambda_{Im}^2}} \qquad \textbf{\textit{(50)}}$$

Average strain

The average strain is determined according to [49] for device type 1 by:

$$\boldsymbol{\gamma_{avg}}(\%) = \frac{\boldsymbol{r_{avg}}}{\boldsymbol{L}} * \boldsymbol{\theta_a} * \mathbf{100} \tag{51}$$

Where

θ_a is the rotation motion at the active end

$r_{avg} = 0.4 * d$

Where

d is the diameter of the specimen

3.3.12.3 Difference in testing method compared to ASTM D4015-15

ASTM D4015-15 [49] mentions to determine shear strains at different amplitudes, the same procedure needs to be followed to determine the resonance frequency. Thus, the ellipse needs to be received as Figure 61 shows and explained in 3.3.12.1. It is noticed that at constant frequencies, no pronounced change in shear stiffness occurred. Besides, when the frequency increased, the small strain shear stiffness increased. Therefore, during measurements the frequency is decreased during an increase of the amplitude. The used method eventually gave curves similar to Figure 62 and Figure 63.

3.3.13 Bender element test

3.3.13.1 Test equipment

The testing series are done with a modernized test set-up which is described in [5].

Figure 64 (a) shows a test setup of bender elements and Figure 64 (b) shows the principle of the deformation of the bender element [41]. As can be seen it is possible to have horizontal and vertical bender elements. In this study vertical bender elements are used.

Additionally, as Figure 64 (b) shows when a voltage is applied to one of the bender elements, one of the plates becomes longer, while the other shortens. The result is a small displacement and thus a shear wave. At the other side of the specimen the same principle is used, although a displacement provides a voltage. [42]

A bender element device contains 2 transducers which can convert electrical in mechanical energy and vice versa. The transmitter introduces a deformation, which produces S(hear)- and P(ressure)-waves, which are specified by the applied (DC) voltage. In addition, a (smaller) (DC) voltage is introduced when the receiver deforms through a received wave. Bender elements examine the propagation of the ground waves and measure their velocity. This velocity depends on the elastic properties of the soil. [41], [23]

[40] mentions it is recommended the length of both bender elements is equal. In addition [40] notices it is recommended that $3\,mm \leq length\,of\,the\,bender\,element \leq 9\,mm$. To prevent shortening of the electrical circuit, both bender elements are surrounded by an epoxy coating.

Two extra devices are necessary to perform a bender element test [41], [5]. First of all, a function generator is needed to create the preferred sinusoidal wave. To select an amplitude, it needs to be checked if the received signal is clear enough to determine the travel time. In most cases a voltage between 1 and 12 V and a frequency of 1 to 50 kHz is enough. The used function generator in this study was only able to send 1 frequency. Additionally, the send voltage provided by the function generator was 20 V. In addition, an oscilloscope or computerscope is necessary to measure the captured signals and synchronize the received signal with the transmitted signal. Due to the reduction of voltage, it might be necessary to amplify the received signal, which can also be done with an oscilloscope [23].

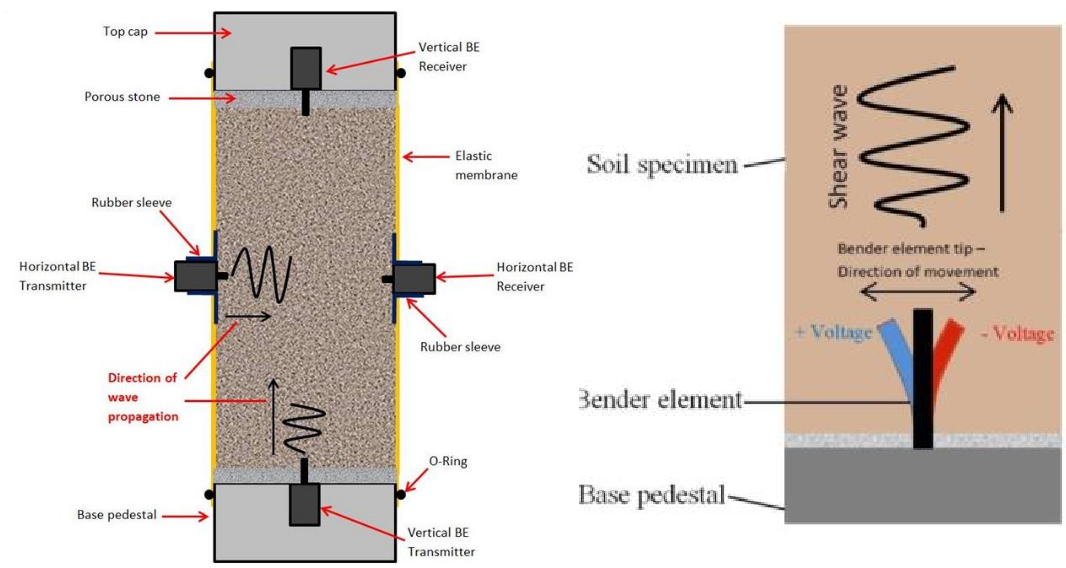

(a) (b)

Figure 64. *Test setup of a bender element (a) and working principle (b)* ***[41]***

3.3.13.2 Test procedure

As noticed in section 2.4.2, different methods exist to interpret bender element measurements. It was mentioned that the cross-spectrum analyzing method gives higher shear wave velocities at higher frequencies. In addition the AZC-method gives higher shear wave velocities in some cases. It can be concluded that those two methods give unreliable data while the MPTP, MFTOA, ACC and the APTP are the most reliable methods.

Therefore, during the test series, MFTOA will mainly be used. Due to noise on the received signal, MPTP is not used, because it was too hard to determine an exact point on the received signal to do the measurement.

The pedestal-bender element provides a sinusoidal wave in the specimen. When the top-bender element does not receive a clear signal, it might be recommended to increase the voltage. The transmitter and receiver should work in the same frequency-area. When working on the resonance frequency, the amplitude received at the top-bender element is maximal. [41]

It is possible impurities are present. By example: because of the near-field effect, which is discussed in section 3.3.13.3, or noise which is present due to poor insulation of the bender elements, damage on the test device, etc. [41]

When the consolidation-time is ended and the volume- and height-change are measured, the travel time is measured under the only possible frequency. By means of this, it is possible to calculate the velocity, because the travel distance is known. Next, the very small strain stiffness G_{max} is calculated as mentioned in section 2.4.1.

3.3.13.3 Near-field effect

When a bender element test is performed, a possibility exists that P-waves and S-waves interfere [14]. This problem is caused by the different travelling speeds of both wave-types where:

$$\boldsymbol{v_s \approx \frac{1}{2} * v_p} \tag{52}$$

Where

v_s is the shear wave velocity

v_p is the pressure wave velocity

At short distances from the source, P-waves and S-waves are still coupled, which causes the wave to have an irregular form. Though, in the far field P-waves arrive much earlier than S-waves. This causes the waves to not interfere with each other. The field is supposed to be a near-field when:

$$\boldsymbol{\frac{d}{\lambda} \leq 2} \tag{53}$$

Where

d is the distance between the transmitter and the receiver

λ is the wave length

It is mentioned in [64] that the ratio between the distance of the transmitter and the receiver and the wavelength is around 2 or greater. In this case, the near-field effect will be excluded or neglectable. In addition [9], [23] mention that due to the near-field effect, $\frac{L_{tt}}{wavelength}$ should be bigger than 2. Besides, the ratio should not exceed a value of 9 [9] or 10 [23].

Figure 65 shows the near-field effect by different frequencies. When the frequency reaches 15 kHz, the near-field effect stabilizes. When higher frequencies are used, there is no remarkable decrease of the near-field effect, which might be caused by the rebound of S-waves. [43]

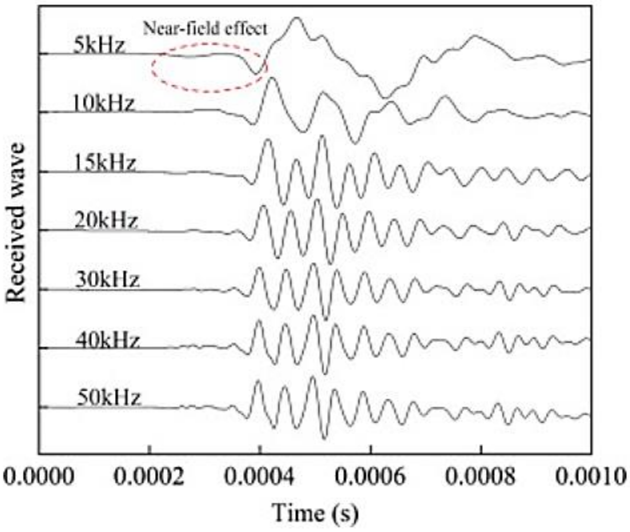

Figure 65. *Near-field effect* ***[43]***

3.3.14 Evaluation of G_{max}

Evaluation of G_{max} will be done according to section 2.1.3. The received data will be compared with formulations (2), (3), (4) and (5) in these sections, while equation (6), (7) and (8) will not be studied because they are less accurate. Additionally, equation (9) and the alternative version for equation (4) with *FC* discussed in section 2.1.4 will not be studied because lesser influence was noticed for Viasvesi sand. Afterwards, a relation for Viasvesi sand will be proposed.

4. RESULTS

4.1 Grain size distribution

Table 10 shows the results of the sieving procedure. In addition, Figure 66 shows the grain size distribution curve received from the sieving procedure. As it is possible to see in Figure 66, a uniform sand is used to perform resonant column and bender element tests. Table 11 confirms the uniformity of the sand, which can be determined by the coefficient of uniformity and coefficient of curvature, which are both 2. Because of these values, according to Table 5, a uniform sand is used in the testing series in case the coefficient of curvature is neglected. In addition, Table 11 shows grain size distribution characteristics like the different grain sizes with a fall-through of a specific percentage of mass d_{10}, d_{30}, d_{50} and d_{60}.

Additionally, the calculation of the uniformity coefficient, given by equation (24), coefficient of curvature, given by equation (23) and fines content, given by equation (26) is given:

$$FC = \frac{733.4-727.0+0.1}{733.4} * 100 = 0.82\ \%$$

$$C_u = \frac{0.5}{0.25} = 2$$

$$C_c = \frac{0.5^2}{0.25*0.5} = 2$$

Table 10. *Grain size distribution Viasvesi sand*

Weight before sieving (g)	**733,4**	**date:**	21,1,2022
sieve (mm)	**left on sieve (g)**	**left on sieve (%)**	**Fall-through (%)**
2	0,0	0	100
1	0,5	0	100
0,5	218,6	30	70
0,25	371,4	51	19
0,125	132,3	18	1
0,063	4,2	0,6	0,0
Base	0,1	0,0	
Total	727,1		

Table 11. *Grain size distribution characteristics Viasvesi sand*

FC **(%)**	**0,82**
d_{10} **(mm)**	0,25
d_{30} **(mm)**	0,5
d_{50} **(mm)**	0,5
d_{60} **(mm)**	0,5
C_c	2
C_u	2

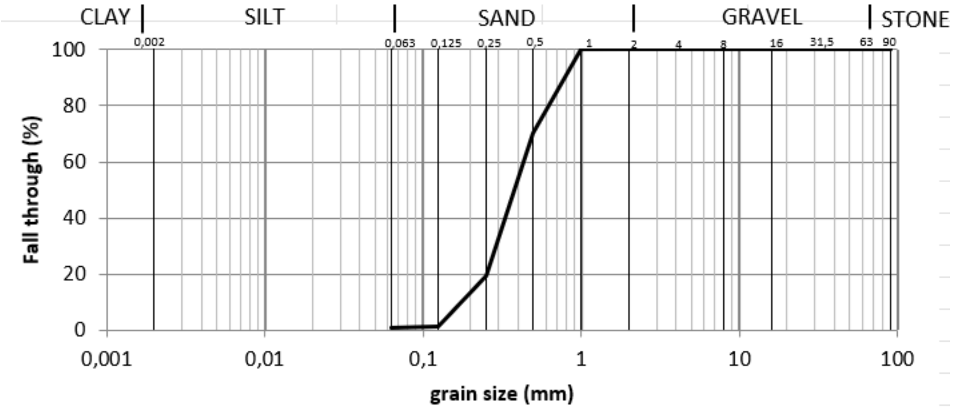

Figure 66. *Grain size distribution Viasvesi sand*

4.2 Particle density

Table 15 shows the particle densities received with the pycnometer. The average value of the particle density is 2628 kg/m³. Two tests are performed to determine the average particle density, with the data given in Table 12, Table 13 and Table 14. The calculation of the particle density for pycnometer 5, with equation (27), is given by:

$$\rho_p = 997.8 * \frac{934.98}{934.98-(2587.54-2008.11)} = 2624\ kg/m^3$$

Table 12. *Water density during pycnometer tests*

ρ_w (kg/m³)	997.8

Table 13. *Mass of water and soil during test with pycnometer 5*

	M **(g)**
W_{sw}	2587.54
W_w	2008.11
$W_s - W_a$	934.98

Table 14. *Mass of water and soil during test with pycnometer 9*

	M **(g)**
W_{sw}	2568.25
W_w	2006.93
$W_s - W_a$	904.06

Table 15. *Particle density Viasvesi sand*

Pycnometer	ρ_{particle} **(kg/m³)**
5	2624
9	2632
Average	2628

4.3 Proctor compaction

Figure 67 shows the curve received from the proctor tests on Viasvesi sand. The calculation of the dry densities is similar to the calculation given in section 4.5. Three tests are conducted to determine the optimal water content for the sample. No pronounced differences between the density and the water content are found, as shown in Figure 67. Due to this, it might be concluded that water content does not play a significant role to receive higher densities by Viasvesi sand. Therefore a water content of approximately 6 % is used during the testing series to prepare the sand samples, as

Table 17 shows.

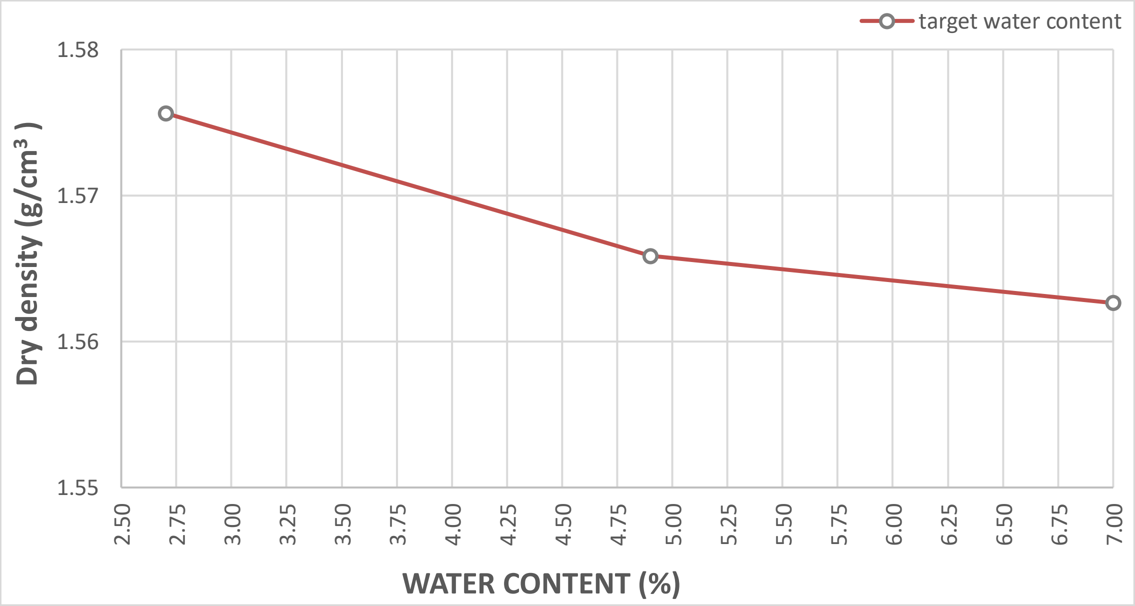

Figure 67. *Proctor curve*

4.4 Saturation degree of test specimens

Table 16 shows the values used for the calculation of the saturation degree and the eventual saturation degree. The used values are the Skempton-B, the initial cell pressure *p*, the void ratio *e*, the initial effective stress σ' and the change in effective stress $\Delta\sigma'$. The saturation degrees are calculated by an estimated change of air volume of 10^{-3}. The chosen change of air volume is not measured because of the complexity, but is estimated by back calculating values of κ given in [62].

The Skempton-B value is determined for each measurement with equation (36). This gives for the first measurement during test 6 (values given in appendix A):

$$B = \frac{1.06}{12.65} = 0.08$$

From all these calculations, an average is taken which gives the effective Skempton-B, as given in Table 16. When the Skempton-B value is determined, it is possible to determine the saturation degree with equation (37) and (38). This gives:

$$10^{-3} = \frac{\kappa}{100*(1+0.69)} * 13 \rightarrow \ \kappa = 0.013$$

$$0.09 = \frac{1}{1+100*0.69*(1-S_{r0})/(-0.013*100)} \rightarrow S_{r0} = 81.48\ \%$$

As can be noticed in Table 16, the saturation degree varies between 79.63 % and 96.43 %. Therefore, it can be concluded all samples were nearly saturated with caution taken into account because the change in air volume is back calculated with a certain value of κ, which causes the saturation degree to be not fully correct.

Table 16. *Saturation degree of the tested samples*

	B-value (-)	p (kPa)	e (-)	σ' (kPa)	$\Delta\sigma'$ (kPa)	S_{r0} (%)
TEST 6	0.09	100	0.69	100	13.00	81.48
TEST 7	0.14	100	0.57	100	11.60	85.81
TEST 8	0.20	100	0.53	100	10.57	88.90
TEST 9	0.38	110	0.64	110	12.81	96.43
TEST 10	0.11	110	0.66	110	13.89	84.13
TEST 11	0.12	110	0.60	110	13.45	84.02
TEST 12	0.09	116	0.70	116	13.30	79.63
TEST 13	0.12	118	0.67	118	12.83	82.46

4.5 Void ratio, height, diameter, water content and dry densities

Table 17 gives an overview of the void ratios *e* and dry densities, which are used while testing the samples. As can be seen, a wide range of void ratios is tested (from 0.53 to 0.70). The densities and heights are corrected during the testing series using values of the change in volume, respectively the height, given in appendix C. Additionally, an overview is given of the height, diameter and water content *W* during preparing the samples. The dry density is determined by equation (28), as follows for test 13:

$$\boldsymbol{V = 0.10674 * \frac{\pi * 0.0516^2}{4} = 0.22 * 10^{-3}\ m}^3$$

$$\rho_d = \frac{\frac{373.58 * 10^{-3}}{\left(1+\frac{6.13}{100}\right)}}{\mathbf{0.22 * 10^{-3}}} = 1577\ kg/m^3$$

The void ratio is determined by equation (29). This is done as follows for test 13:

$$e = \frac{1577^{-1} - 2628^{-1}}{2628^{-1}} = 0.67$$

.

The values in appendix C are the changes recorded during consolidation of the certain pressure step. Therefore, a sum needs to be taken with the change in volume and height in previous pressure steps to correct the density, respectively the height of the sample.

Table 17. *Void ratio e, height H, diameter D, water content W and dry densities of the tested samples*

	e **(-)**	ρ_{dry} **(kg/m³)**	***H*** **(mm)**	***D*** **(mm)**	***W*** **(%)**
TEST 6	0.69	1560	114.36	50.00	6.17
TEST 7	0.57	1671	110.04	50.25	6.30
TEST 8	0.53	1713	108.27	51.00	6.15
TEST 9	0.64	1606	117.00	50.75	5.90
TEST 10	0.66	1581	113.73	50.50	6.29
TEST 11	0.60	1647	111.48	51.00	6.09
TEST 12	0.70	1548	114.61	50.90	6.09
TEST 13	0.67	1577	106.74	51.60	6.13

4.6 Resonant column tests

4.6.1 Calibrating parameters testing device

Table 18 gives an overview of the inertias used to calculate the shear modulus reduction curves, using the resonant column. The inertia of the resonant column device is calculated by equation (41), as follows:

$$J_1 = \frac{858.64}{(2*\pi)^2*(143.3^2-84.3^2)} = 1.620 * 10^{-3} kg * m^2$$

Where

$$k_{rod} = \frac{\frac{\pi*(14\ mm)^4}{32}*25000\ N/mm^2}{109.81\ mm} = 858.6\ N*m$$

$$J_2 = \frac{0.33203\ kg*(0.05008\ m)^2}{8} = 0.104 * 10^{-3}\ kg * m^2$$

$$J_3 = \frac{0.34063\ kg*(0.04999\ m)^2}{8} = 0.106 * 10^{-3}\ kg * m^2$$

After determining the separate inertias, it is possible to determine the inertia of the active end. This gives:

$$J_a = (1.620 - 0.104 + 0.106) * 10^{-3} = 1.622 * 10^{-3}\ kg * m^2$$

Table 18. *Inertia resonant column*

Mass of the solid cilindrical component	M_{1a1}	-0.332	kg
diameter of the solid cilindrical component	d_{1a1}	0.050	m
Mass of the solid cilindrical component	M_{2a1}	0.34063	kg
diameter of the solid cilindrical component	d_{2a1}	0.04999	m
Inertia	J_{1a2}	0.001620	kg*m²
Total inertia of the active end	J_a	0.001622	kg*m²

Table 19 gives an overview of the resonance frequency of the calibration rod and the apparatus resonance frequency, without any device, used to calculate the shear modulus reduction curves.

***Table 19.** Calibration frequencies resonant column*

Resonance frequency of the apparatus only	f_a	84.3	Hz
Resonance frequency of the apparatus with calibration rod	f_r	143.3	Hz

Table 20 gives an overview of the input and output in the electrical circuit, and the output from the accelerometer during these measurements, used to calibrate the resonant column. These measurements are conducted at $0.707 * f_r$, f_r and $1.414 * f_r$.

***Table 20.** Input and output in the electrical circuit during calibration*

Electrical resistance motor	R	0.60	Ohm
Torque motor input by resonance frequency (calibration rod)	U_{fr}	0.49	V
Torque motor input by 101.3 Hz (calibration rod)	$U_{0.707fr}$	0.68	V
Torque motor input by 202.6 Hz (calibration rod)	$U_{1.414fr}$	0.43	V
Output of the rotation transducer at 101.3 Hz (calibration rod)	*Acceleration (Z)*	0.168	g
Output of the rotation transducer at 101.3 Hz (calibration rod)	*R*T*r*d*g*	30.35	mV
Torque motor input by 101.3 Hz (calibration rod)	CR_1	1.13	Ampère
Output of the rotation transducer at 202.6 Hz (calibration rod)	*Acceleration (Z)*	0.231	g
Output of the rotation transducer at 202.6 Hz (calibration rod)	*R*T*r*d*g*	40.48	mV
Torque motor input by 202.6 Hz (calibration rod)	CR_2	0.72	Ampère

4.6.2 Results

To start, a calculation according to ASTM-D 4015 – 15 [49] will be written out, followed by the results of all measurements in the next sections. These results will be the shear modulus reduction curves and the normalized shear modulus reduction curves, both with G_{max} from the resonant column and G_{max} from the bender elements.

4.6.2.1 Calculation of a measurement

Under this section, a calculation of test 13 during the loading 100 kPa cycle will be written out. This will be done for the resonance frequency. First of all, the rotational motion of the accelerometer will be determined by equation (39). This happens as follows:

$$S_\theta = 178.61 * 0.029 * \frac{(2*\pi*139.4)^2}{9.81} = 405069.5\, mV/rad$$

Where

$S_a = 178.61\, mV/g$, determined via linear interpolation of the calibration data of the accelerometer

$r_t = 0.029\, m$

$f = 139.4\, Hz$

Following on the rotational sensitivity, it is posible to determine the rotation:

$$\theta = \frac{34.0\,mV}{405069.5\frac{mV}{rad}} = 8.38 * 10^{-5}\,rad$$

Where

$$R * T * r * d * g = 34.0\,mV$$

Besides, it is possible to determine the apparatus damping. This is done by equation (43) to determine the applied torque, whereafter the apparatus damping is determined by equation (42):

$$C_1 = \frac{140.2*10^{-6}\,rad}{2*1.133\,amp\grave{e}re} = 6.19 * 10^{-5}\,rad/amp\grave{e}re$$

Where

$\theta_1 = 140.2 * 10^{-6}\,rad$ is determined similar to θ, with $0.707 * f_{rod} = 101.3\,Hz$

$CR_1 = 1.133\,amp\grave{e}re$ is determined by measuring the input of the motor during applying $0.707 * f_{rod} = 101.3\,Hz$

$$C_2 = \frac{48.2*10^{-6}\,rad}{0.717\,amp\grave{e}re} = 6.73 * 10^{-5}\,rad/amp\grave{e}re$$

Where

$\theta_2 = 48.2 * 10^{-6}\,rad$ is determined similar to θ, with $1.414 * f_{rod} = 202.6\,Hz$

$CR_1 = 0.717\,amp\grave{e}re$ is determined by measuring the input of the motor during applying $1.414 * f_{rod} = 202.6\,Hz$

$$k_a = (2 * \pi * 84.3\,Hz)^2 * 0.001622\,kg * m^2 = 455.1\,N * m$$

With these data, the torque motor ratio becomes:

$$TMR = 0.5 * 455.1 * (6.19 + 6.73) * 10^{-5} = 0.0294\,(N * m)/amp\grave{e}re$$

With the torque motor ratio and the input current through the motor during the measurement with the resonant column known, it is possible to determine the applied torque on the sample. The applied torque becomes with equation (43):

$$\tau_{appl} = 0.0294\,\frac{N*m}{amp\grave{e}re} * 1.867\,amp\grave{e}re = 0.0548\,N * m$$

Next, it is possible to determine the apparatus damping. This is done by equation (42), which gives:

$$c_a = \frac{0.0548\,N*m}{8.38*10^{-5}\,rad*(2*\pi*143.3\,Hz)} = 0.7271\,(N * m * s)/rad$$

Following on previous calculations, it is possible to determine the shear modulus of the sample. This is done as follows: first, the rotational inertia of the sand sample is determined by equation (44):

$$J = \frac{0.345\ kg*(0.0516\ m)^2}{8} = 114.82*10^{-6}\ kg*m^2$$

Besides, it is possible to determine the density of the soil. This is done by equation (35), together with the change of volume ΔV as follows:

$$V = \left(0.10674*\frac{\pi*0.05160^2}{4}\right)\ m^3 = 0.22321*10^{-3}\ m^3$$

$$\Delta V = 1.6\ ml = 1.6*10^{-6}\ m^3$$

$$\rho = \frac{0.345\ kg}{V-\Delta V} = 1557\ kg/m^3$$

The total inertia of the active end platen J_a and the rotational inertia J of the sample are known. Therefore it is possible to determine the active-end inertia factor T_a with equation (45) and the apparatus damping factor ADF_a with equation (46). This gives:

$$\boldsymbol{T_a = \frac{1.622*10^{-3}\ kg*m^2}{114.82*10^{-6}\ kg*m^2}*\left(1-\left(\frac{84.3}{139.4}\right)^2\right) = 8.960}$$

$$\boldsymbol{ADF_a = \frac{0.7271\ (N*m*s)/rad}{2*\pi*143.3\ Hz*114.82*10^{-6}\ kg*m^2} = 7.230}$$

Because the applied torque τ_{appl} and the rotational motion $\theta_a = \theta$ at the active end are known, it is possible to to determine the measured modified magnification factor MMF_{meas} by equation (47):

$$MMF_{meas} = 114.82*10^{-6}\ kg*m^2*(2*\pi*139.4\ Hz)^2*\left[Re\left(\frac{8.38*10^{-5}\ rad}{0.0548\ N*m}\right)+i*Im\left(\frac{8.38*10^{-5}\ rad}{0.0548\ N*m}\right)\right]$$

$$MMF_{meas} = 0.13455 + i*0.13455$$

MMF_{meas} is now known, and therefore it is possible to determine the dimensionless frequency factor λ^* by comparing it with MMF_{calc}. This dimensionless frequency factor is determined by iterating equation (48) in excel, until a value is reached where the difference between the equations is small enough:

$$\boldsymbol{0.13455 + i*0.13455 = \frac{1}{-8.960+i*7.230+\frac{1}{\lambda^**tan(\lambda^*)}}}$$

$$\boldsymbol{\lambda^* = -0.08735 + i*0.23019}$$

Finally, it is possible to determine the shear modulus, by equation (49). This gives:

$$\boldsymbol{G = 1557\ kg/m^3 * (2 * \pi * (0.10674\ m - 0.07\ m)^2 * F_a}$$

Where

$$F_a = absolute[\frac{(-0.08735)^2-(0.23019)^2}{((-0.08735)^2+(0.23019)^2)^2}]$$

An absolute value is taken because the dimensionless frequency factor can have more solutions and excel only gives one solution

$$G = 165.8\ MPa$$

Additionally, it is also possible to determine the average strain. This is done by equation (51).

$$\gamma_{avg}(\%) = \frac{0.4*0.0516\ m}{0.10674-0.07\ m} * 8.38 * 10^{-5}\ rad * 100 = 0.00163\ \%$$

4.6.2.2 Shear modulus reduction for Viasvesi sand

8 succesful tests were done on Viasvesi sand. The results on the shear modulus reduction curves are shown in Figure 68 to Figure 72. Figure 68 shows the result of every test seperately, from 50, to 100, to 300 kPa and back to 100 and 50 kPa. Figure 69 and Figure 70 shows the results of Figure 68 more in detail, respectively for both 50 kPa steps and both 100 kPa steps. Next, Figure 71 and Figure 72 compare the effect of different void ratios at the same effective confining pressure with each other. Test ’6, 7 and 8 (Figure 71)’ and ’9, 10, 11, 12 and 13 (Figure 72)’ are taken seperately because, due to the improving skill of preparing the sample, the results of these 2 testing series do not stroke with each other. Additionally, the average strain and shear modulus used to create these curves, is given in appendix B.

Figure 68 shows the curves received by different tests on different pressures. Tests are conducted on 50, 100 and 300 kPa increasing the effective confining pressure and back to 100 and 50 kPa. For every test the outcome is that an effective confining pressure of 300 kPa has the highest stiffness. In addition, all tests in the loading cycle on 50 kPa have the lowest stiffness. During test 8, 9, 12 and 13, respectively Figure 68 (C), (D), (G) and (H) the unloading cycle on 50 kPa has the second lowest stiffness, whereafter respectively the loading cycle on 100 kPa and the second cycle on 100 kPa, the unloading cycle, follows.

During test 6 (Figure 68 (A)) the loading cycle of 100 kPa follows on the loading cycle of 50 kPa, whereafter the unloading cycle of 50 kPa and then the unloading cycle of 100 kPa have respectively the third - and second highest stiffness.

Additionally, in test 7 and 10, respectively Figure 68 (B) and (E), the unloading cycle of 100 kPa has a lower stiffness than the loading 100 kPa. Though, the unloading cycle of 50 kPa has a higher stiffness than the first, loading cycle. Besides, in test 11 (Figure 68 (F)) the unloading cycle of 100 kPa has a higher stiffness than the loading 100 kPa, but the unloading cycle of 50 kPa has a higher stiffness than both 100 kPa’s.

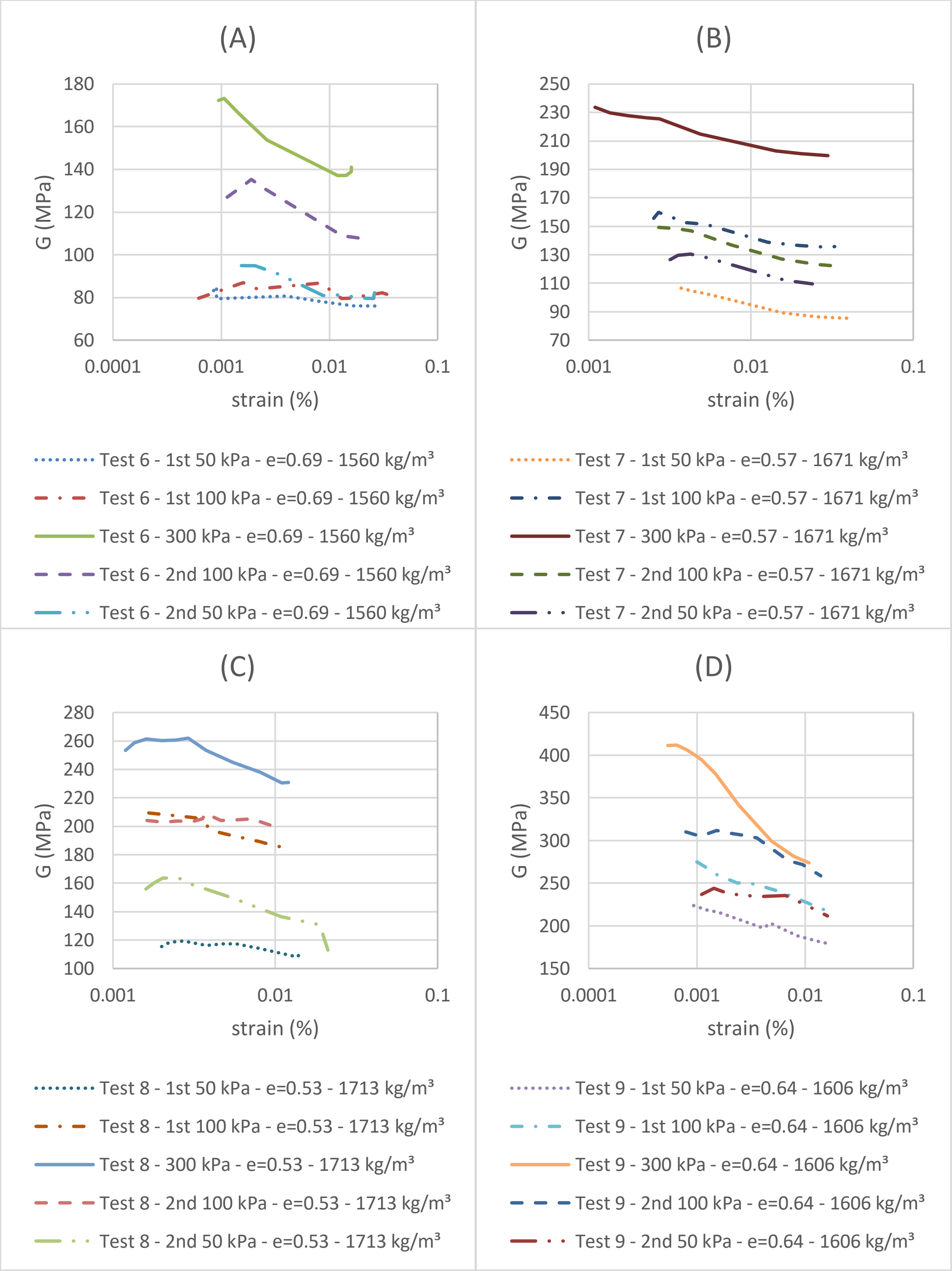

Figure 68. Shear modulus reduction curve for increasing and decreasing pressure (continue)

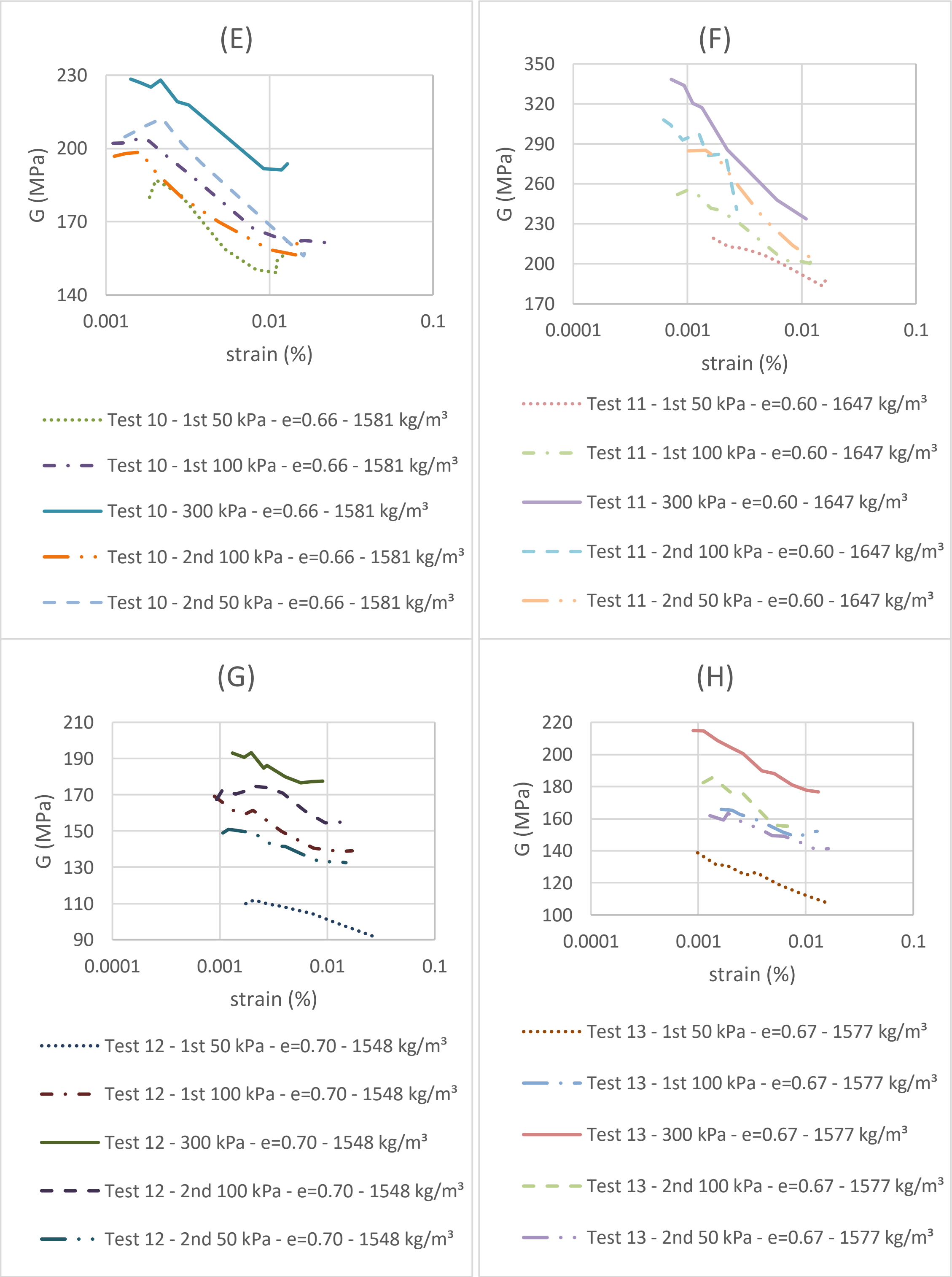

***Figure 68.** Shear modulus reduction curve for increasing and decreasing pressure*

Figure 69 shows the effect of loading and unloading during the pressure steps of 50 kPa, while Figure 70 shows the same effect between the 100 kPa pressure steps.

In Figure 69 all unloading cycles of 50 kPa react stiffer than the first cycle, although the behavior is not the same for every tested sample. During test 6 and 11, respectively Figure 69 (A) and (F), no parallel behavior and no relation between the curves is found. Additionally, in all other tests the curves of the loading and unloading cycle are parallel to each other. During test 7, 9, 10 and 13, respectively Figure 69 (B), (D), (E) and (H) the unloading cycle starts to decrease later, at a higher strain level. Next to this, during test 8 (Figure 69 (C)) and 12 (Figure 69 (G)), both cycles start to decrease approximately at the same strain level.

In Figure 70, with the relation between both 100 kPa cycles, the behavior is more complicated. During test 6, 8, 11 and 13, respectively Figure 70 (A), (C), (F) and (H), no clear relation is found between the loading and unloading curve. Additionally, during test 9 (Figure 70 (D)), 10 (Figure 70 (E)) and 12 (Figure 70 (G)) the curves have a parallel behavior, while the unloading curve decreases at a higher strain level than the loading curves. Next to this, in test 7 (Figure 70 (B)) both unloading and loading curve start to decrease at approximately the same strain level.

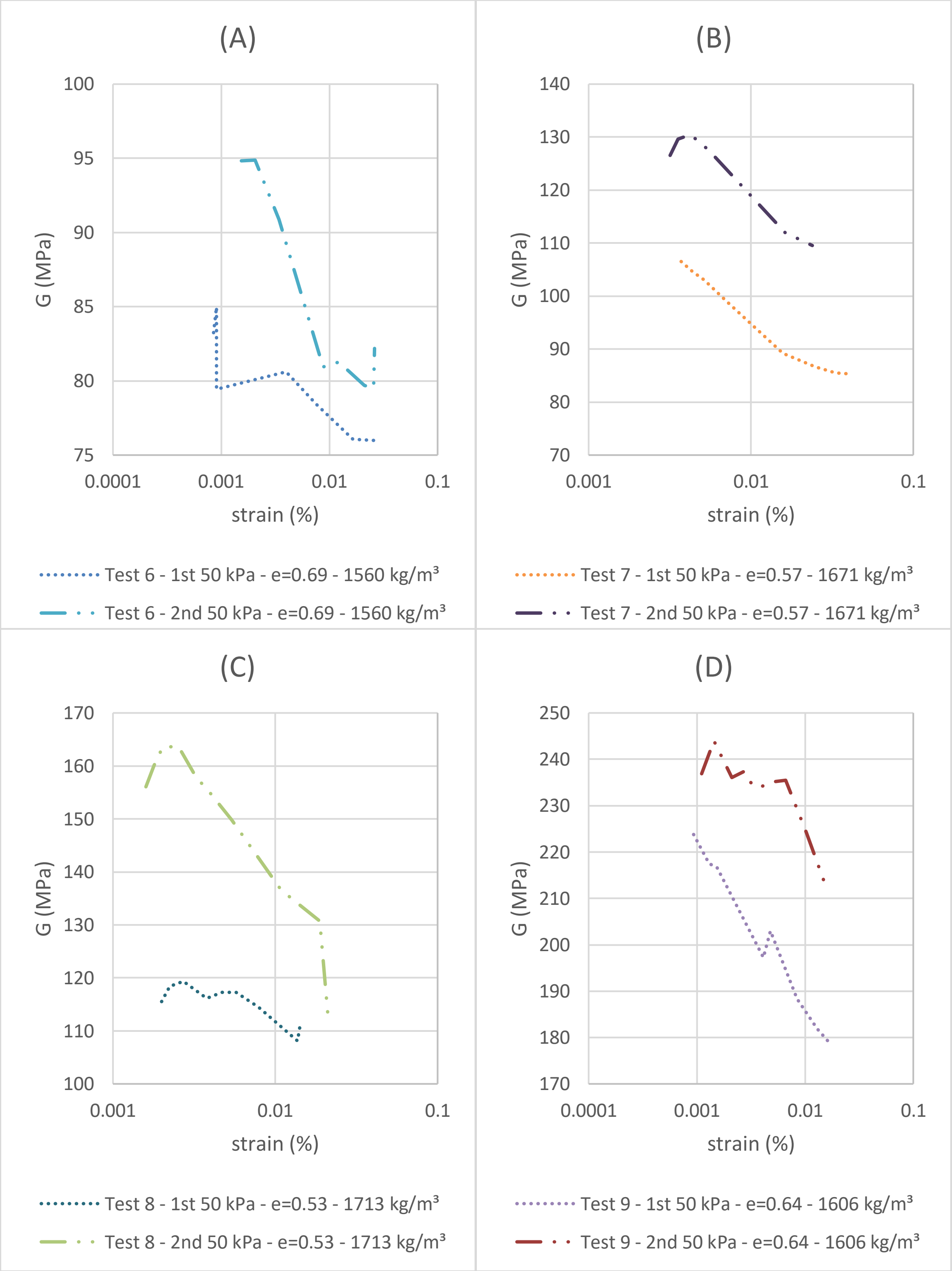

Figure 69. Effect of loading and unloading on shear modulus reduction at 50 kPa (continue)

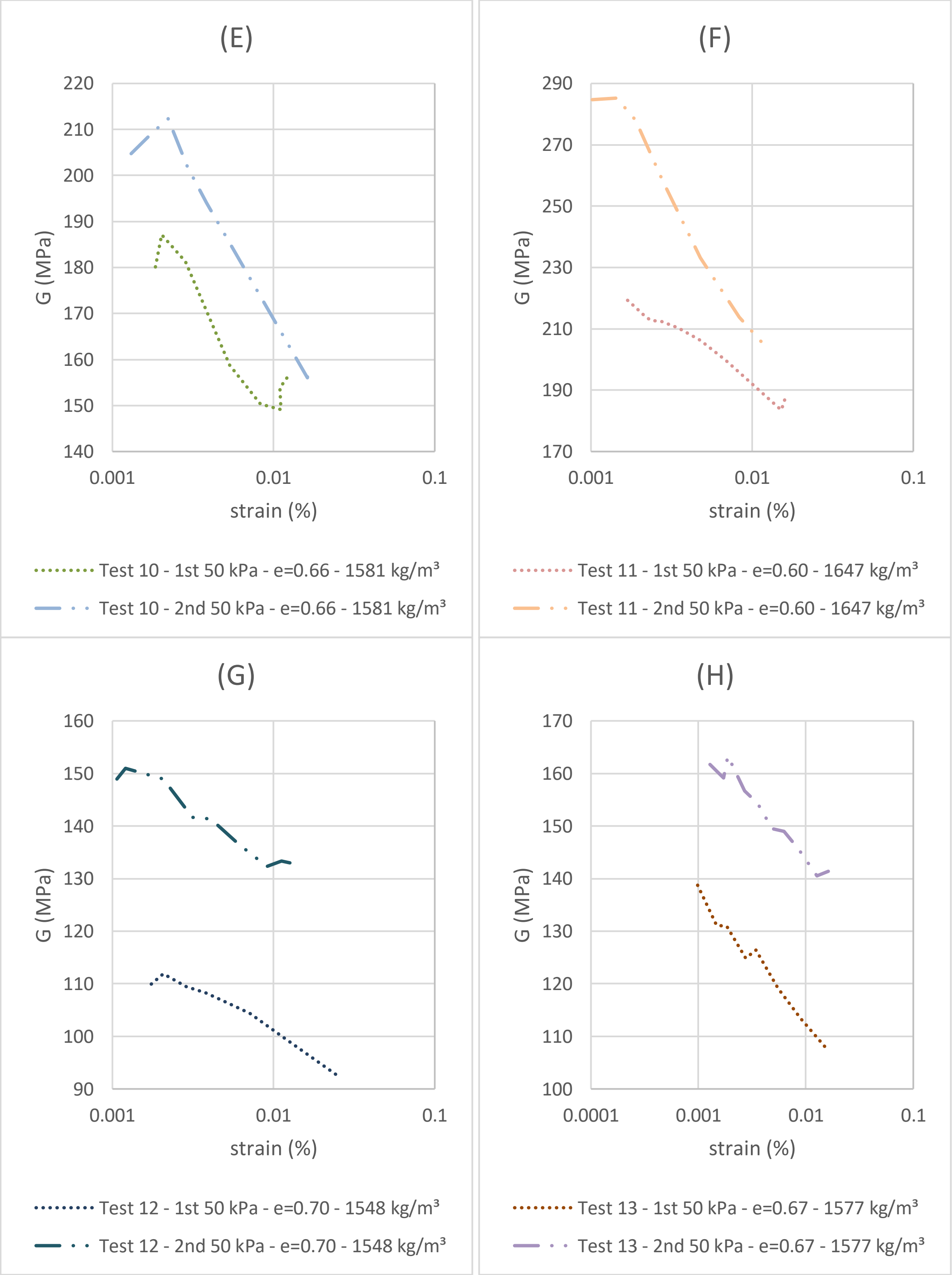

Figure 69. *Effect of loading and unloading on shear modulus reduction at 50 kPa*

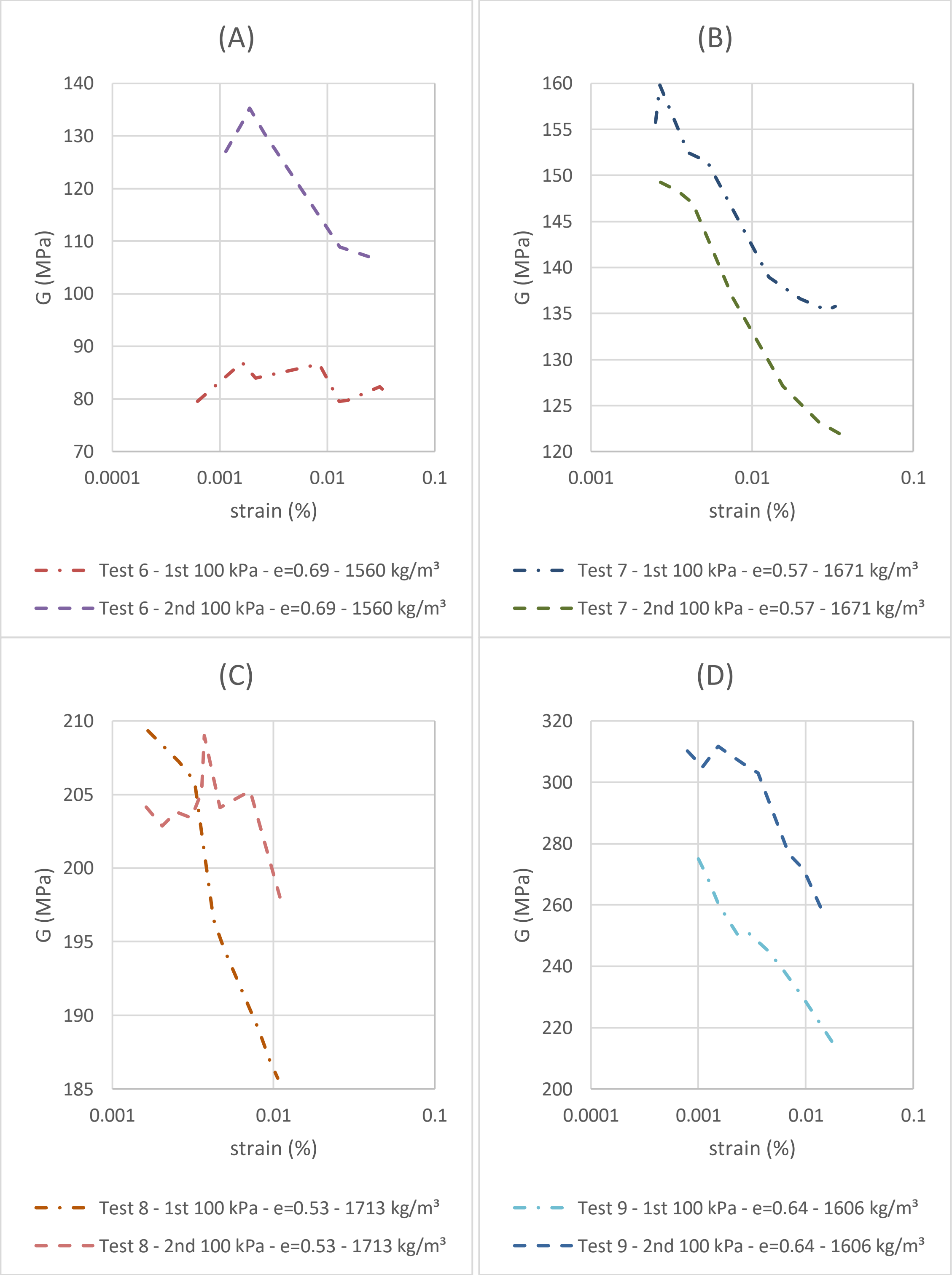

Figure 70. Effect of loading and unloading on shear modulus reduction at 100 kPa (continue)

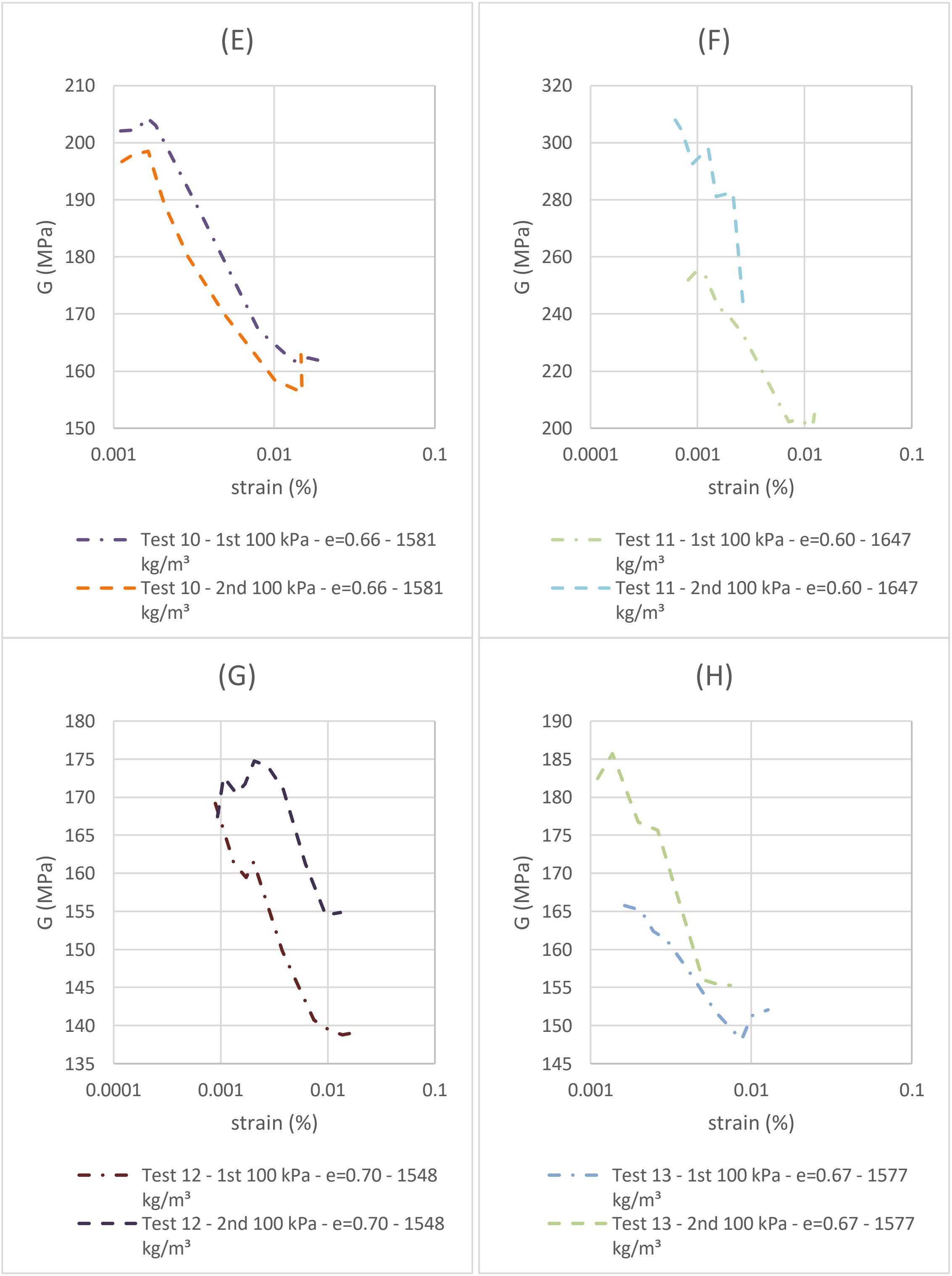

Figure 70. *Effect of loading and unloading on shear modulus reduction at 100 kPa*

Figure 71 shows the effect of the void ratio in the same pressure steps for test 6, 7 and 8. Additionally, Figure 72 shows the influence of the void ratio in test 9, 10, 11, 12 and 13 in the same pressure steps. These curves are shown separately because due to improving skills in preparing samples, these results are not comparable.

As Figure 71 shows clearly, the stiffness is higher in every pressure step with lower void ratio. Additionally, Figure 72 shows the same as Figure 71, except that in the pressure step of 0.64 void ratio (test 9) and 0.60 void ratio (test 11) a small deviation occurs. This deviation is that test 11 has a lower stiffness compared to test 9, while it is expected to be reversed.

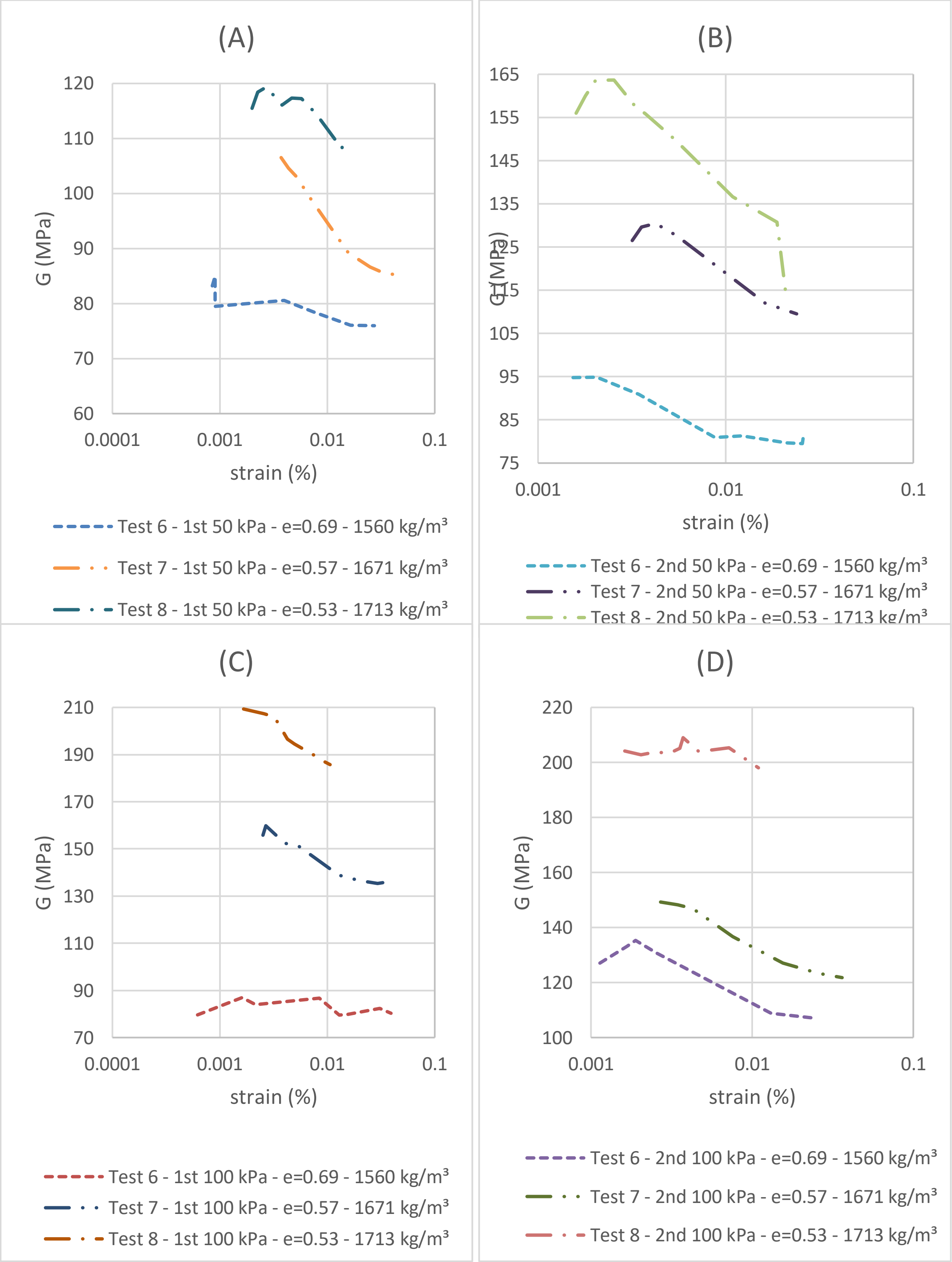

Figure 71. Shear modulus reduction curve at constant pressure and different void ratios for test 6, 7 and 8 (continue)

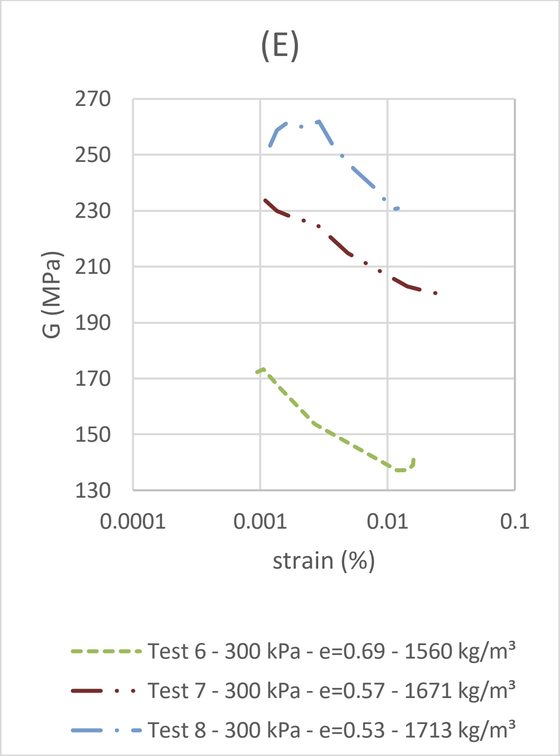

Figure 71. *Shear modulus reduction curve at constant pressure and different void ratios for test 6, 7 and 8*

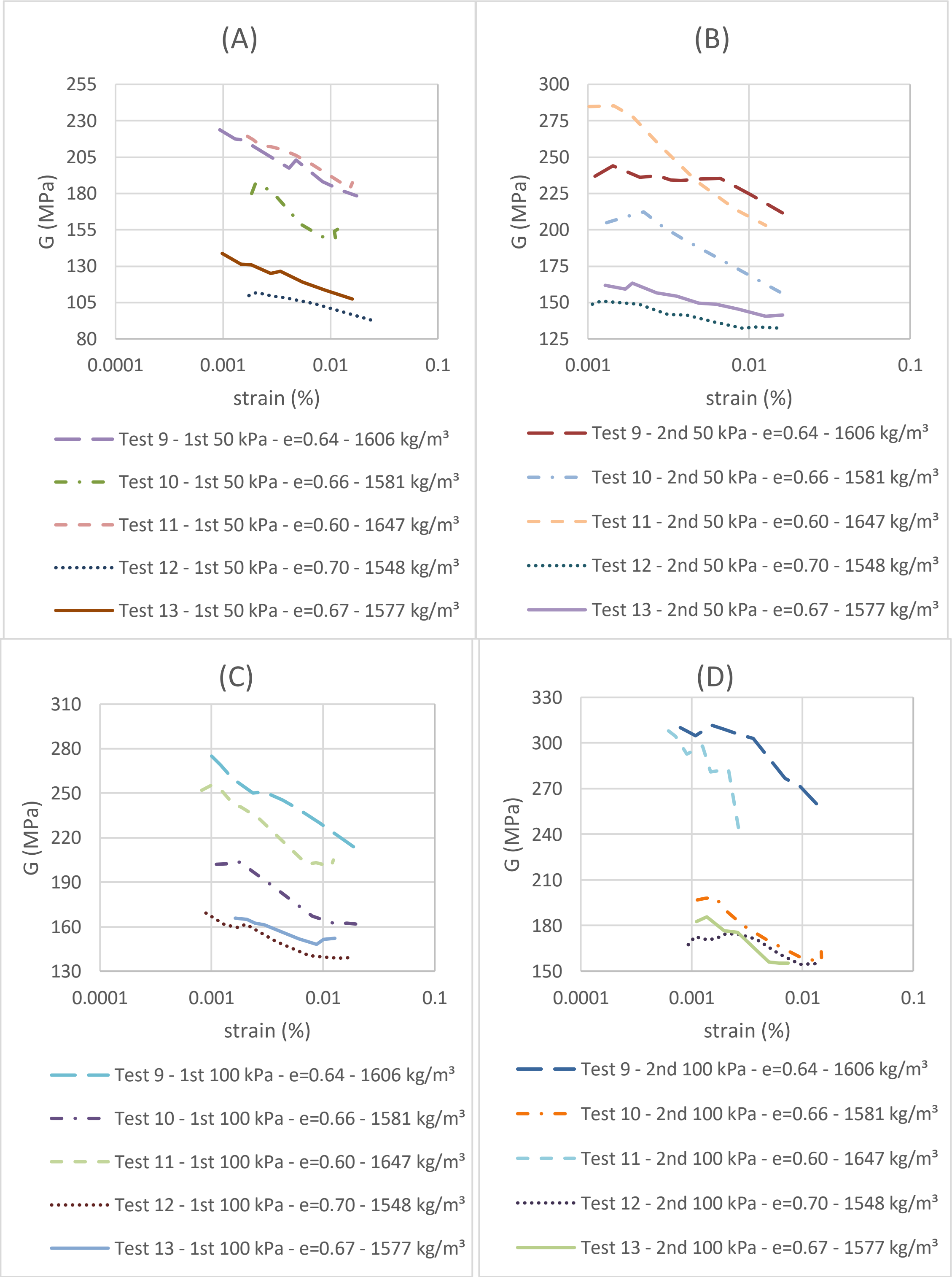

Figure 72. Shear modulus reduction curve at constant pressure and different void ratios for test 9, 10, 11, 12 and 13 (continue)

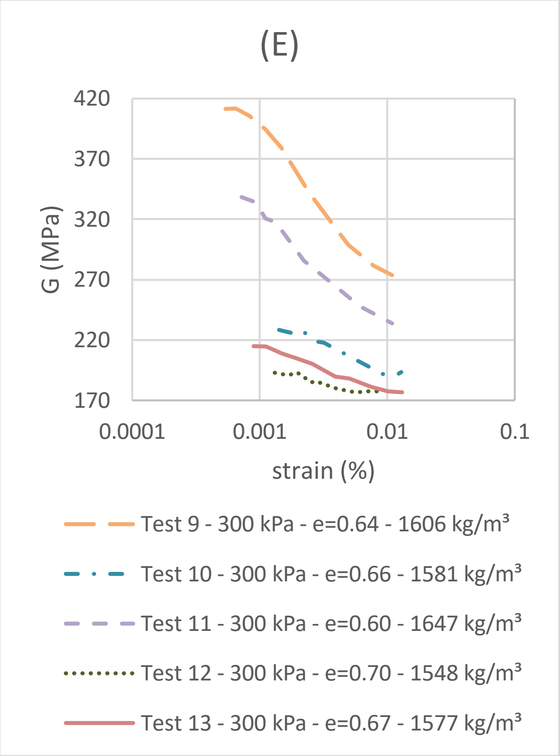

Figure 72. *Shear modulus reduction curve at constant pressure and different void ratios for test 9, 10, 11, 12 and 13*

4.6.2.3 Normalized shear modulus reduction normalized with resonant column for Viasvesi sand

8 succesful tests were done on Viasvesi sand. The results on the normalized shear modulus reduction curves are shown in Figure 73 to Figure 77. Figure 73 shows the result of every test seperately, from 50, to 100, to 300 kPa and back to 100 and 50 kPa. Figure 74 and Figure 75 shows the results of Figure 73 more in detail, respectively for both 50 kPa steps and both 100 kPa steps. Next, Figure 76 and Figure 77 compare the effect of different void ratios at the same effective confining pressure with each other. Test '6, 7 and 8 (Figure 76)' and '9, 10, 11, 12 and 13 (Figure 77)' are taken seperately because, due to the improving skill of preparing the sample, the results of these 2 test series do not stroke with each other. Additionally, the average strain and normalized shear modulus used to create these curves, is given in appendix B.

Figure 73 shows the normalized shear modulus curves, normalized with G_{max} from the resonant column. It is hard to see a relation between the curves, because they reduce randomly. Therefore, no conclusion is taken out of Figure 73, although they actually should have a relation, as shown in Figure 2 [16] and Figure 30 [15]. In Figure 2 [16], at low plasticity indexes, as for sand is the case, the normalized curves start to decrease at higher strain levels when higher confining pressures are initiated. This is something that should have been noticed during the testing series, but what is not noticed. Additionally, Figure 30 [15] mentions the normalized curves from low plastic clays should decrease at higher strain levels when overconsolidated clays are studied. This would mean during the unloading steps, the normalized shear modulus decreases at higher strain levels compared to the virgin loadings. For Figure 30 [15] must be noted that this curve is made without laboratory data and some parameters are thus stated constant, although this is something that is not the case in effective laboratory tests. Therefore this might have an influence on the results in Figure 30.

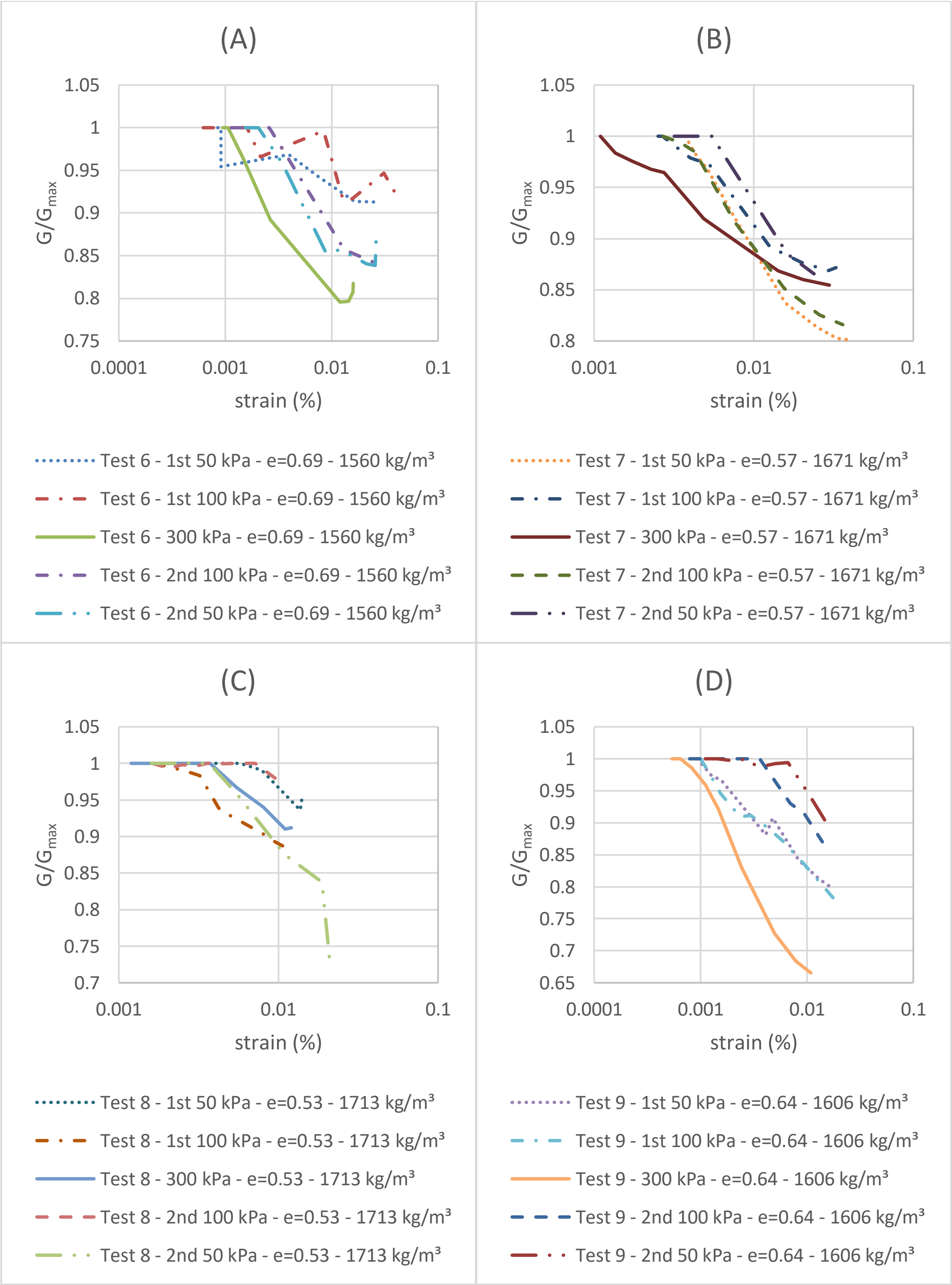

Figure 73. Normalized shear modulus reduction curve for increasing and decreasing pressure (continue)

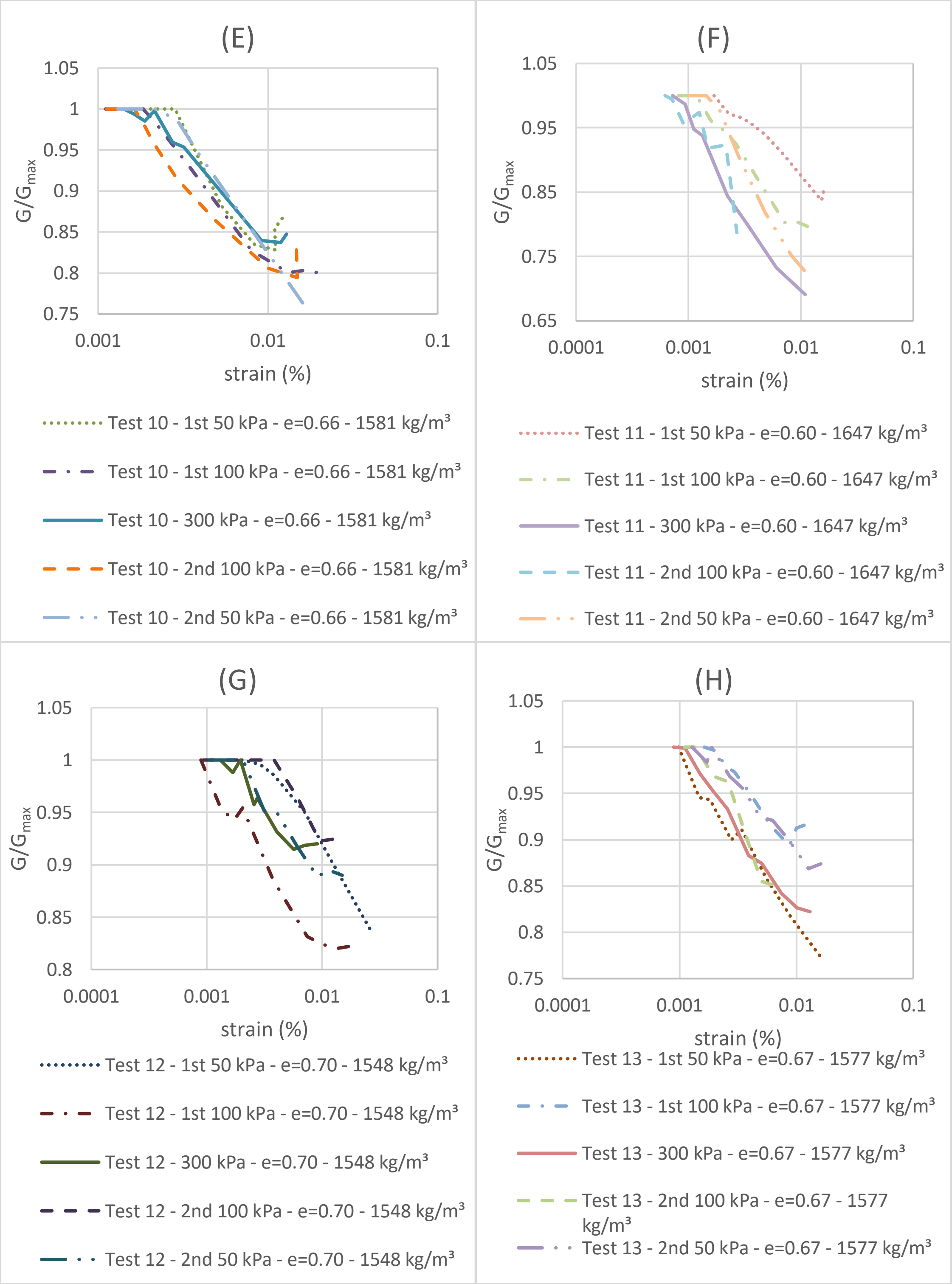

Figure 73. *Normalized shear modulus reduction curve for increasing and decreasing pressure*

Figure 74 and Figure 75 show the normalized shear modulus reduction curves for both 50, respectively 100 kPa steps. Most of the curves follow the same trend, although some deviate a little from the other curves.

First of all, both unloading cycles of 50 and 100 kPa start to decrease later in test 6 (Figure 74 (A) and Figure 75 (A)), compared to the loading cycles, but they decrease steeper wherefor they cross the first cycle at a certain strain level. Next to this, it is actually better to neglect both loading 50 and 100 kPa cycles because they are irregular.

Additionally, in test 7 and 9, respectively Figure 74 (B) and (D), the unloading cycle of 50 kPa starts to decrease at a higher strain level. Next to this, the loading cycle runs parallel to the unloading cycle. In test 7 (Figure 75 (B)), the loading cycle of 100 kPa starts to decrease later than the unloading cycle. Additionally, both loading and unloading cycles run parallel to each other. In test 9 (Figure 75 (D)), the unloading cycle of 100 kPa starts to decrease at a higher strain level than the loading cycle, while also here both loading and unloading cycles run parallel to each other.

During test 8 and 12, respectively Figure 74 (C) and (G), the loading cycle of 50 kPa decreases at a higher strain level, compared to the unloading cycle, although also here approximately parallel curves are noticed. During test 12 (Figure 75 (G)), the unloading cycle of 100 kPa starts to decrease at higher strain level compared to the loading cycle. Additionally, during this test, both cycles follow a parallel curve. For test 8 (Figure 75 (C)), a shortage of data occurs in the 100 kPa cycles, to pronounce the development of the curves compared to each other.

In test 10 (Figure 74 (E)) both 50 kPa curves start to decrease at approximately the same strain level. Additionally, the path both 50 kPa cycles follow, is approximately the same. Figure 75 (E) is neglected, because the values received via these measurements do not stroke with the measurements at other pressure steps.

Besides, in test 11, both loading 50 and 100 kPa, respectively Figure 74 (F) and Figure 75 (F), decrease less pronounced, although they start to decrease at the same strain level.

Finally, in test 13, the unloading cycle of the 50 kPa (Figure 74 (H)) curves decreases at a higher strain level. Next to this, both curves follow an approximately parallel path. In the 100 kPa curves in test 13 (Figure 75 (H)), the unloading and loading curve are reversed compared to the 50 kPa curves, and thus the unloading cycle starts to decrease at a lower strain level compared to the loading cycle.

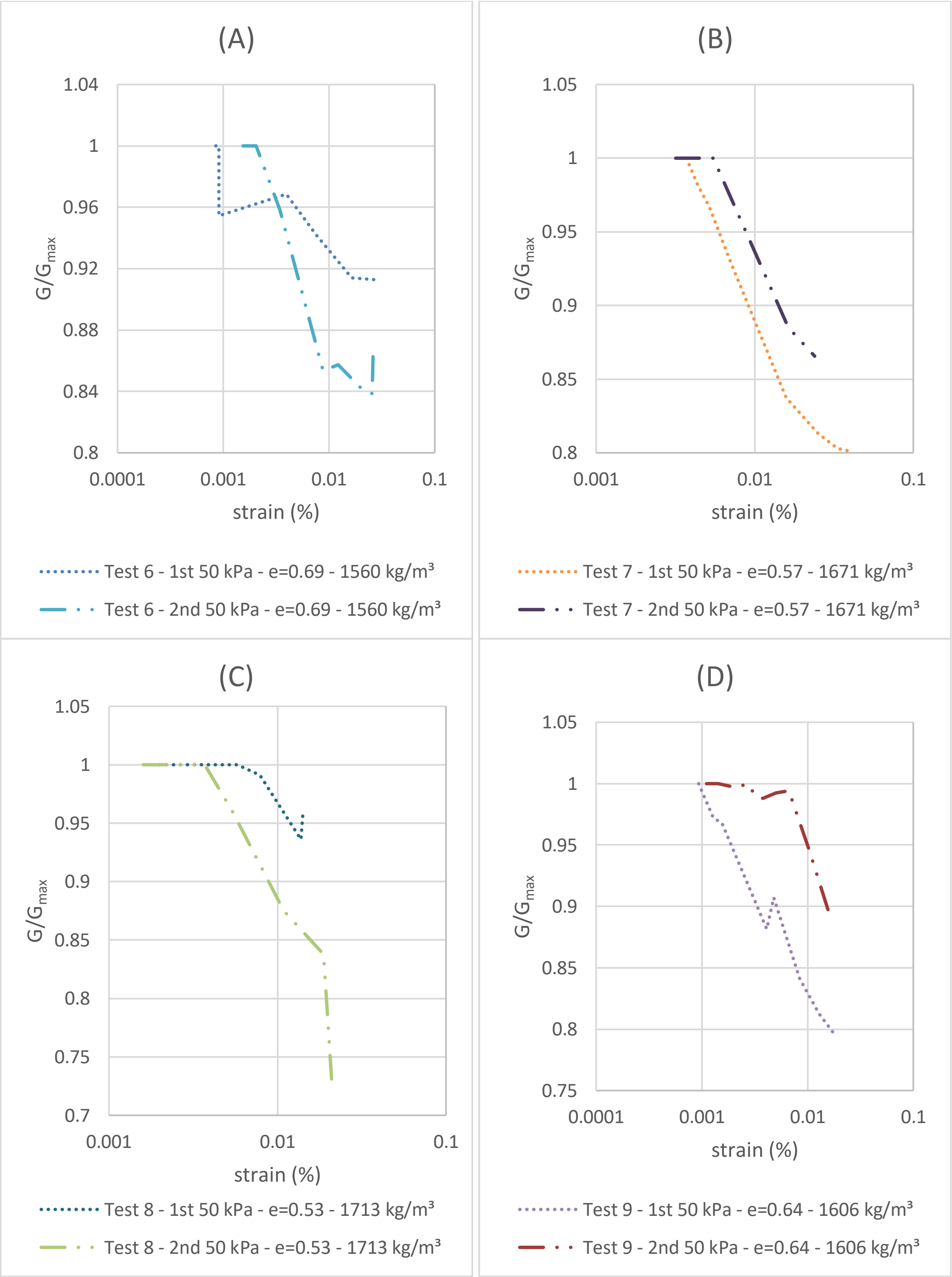

Figure 74. Effect of loading and unloading on normalized shear modulus reduction at 50 kPa (continue)

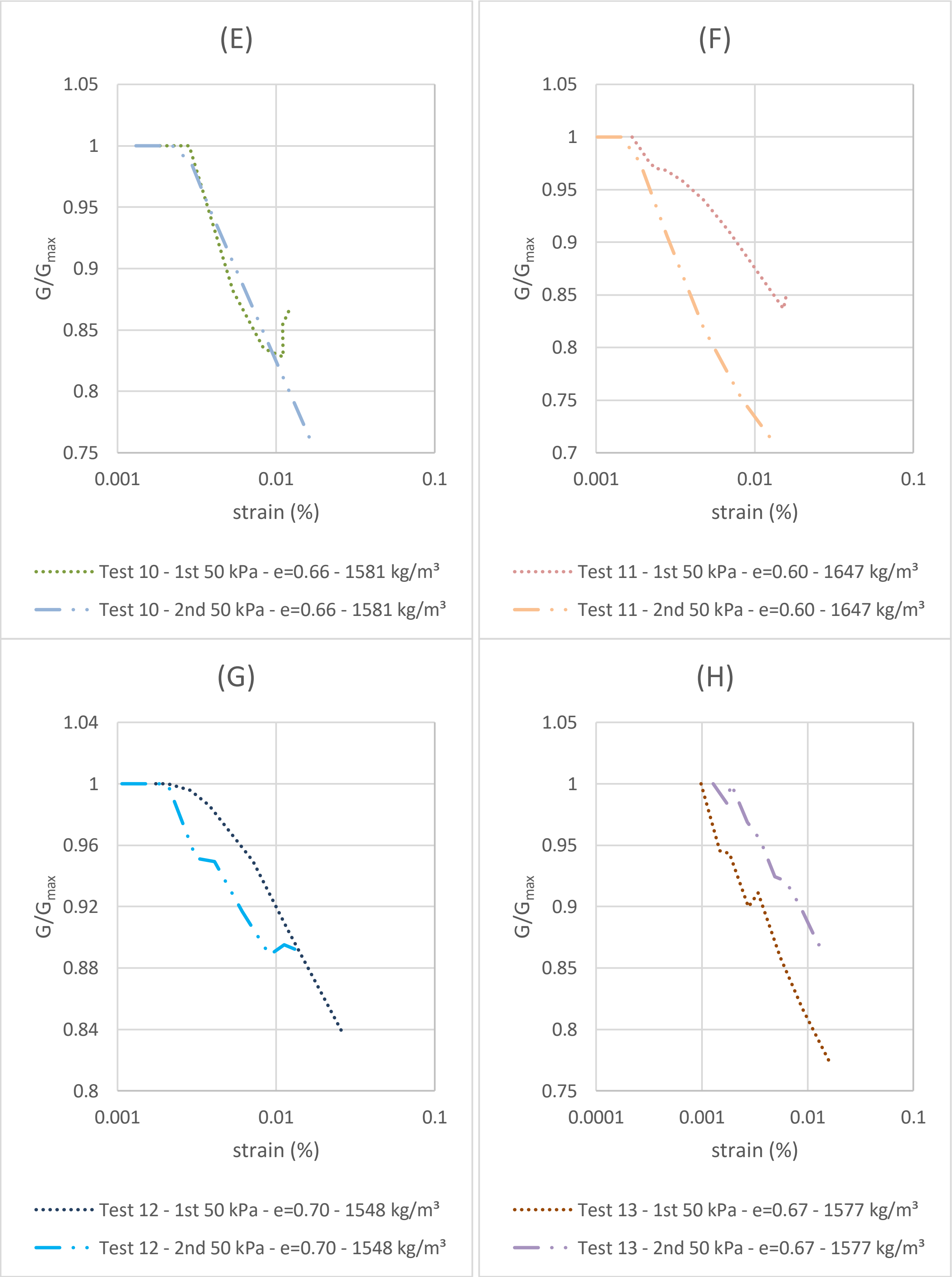

Figure 74. *Effect of loading and unloading on normalized shear modulus reduction at 50 kPa*

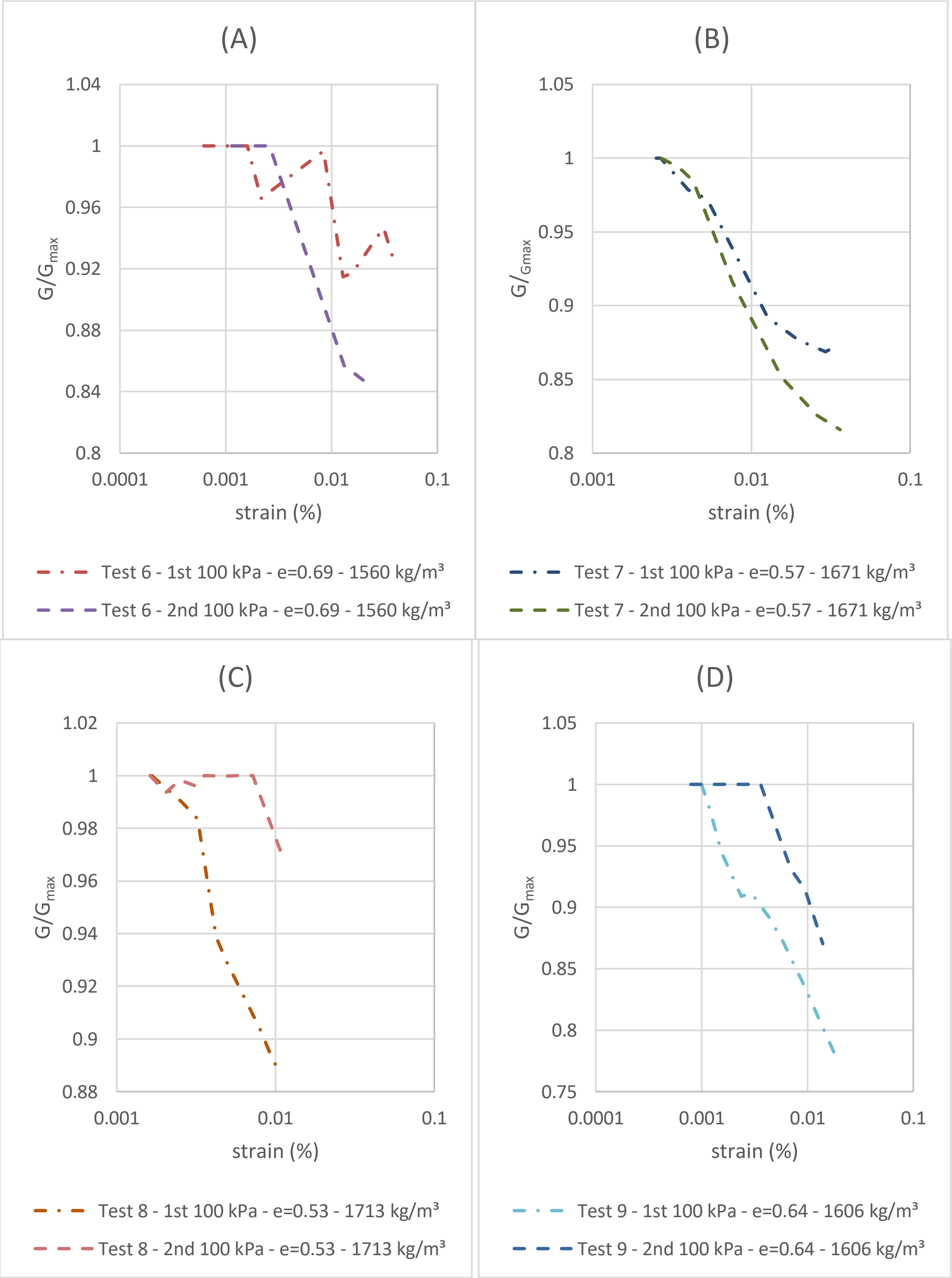

Figure 75. Effect of loading and unloading on normalized shear modulus reduction at 100 kPa (continue)

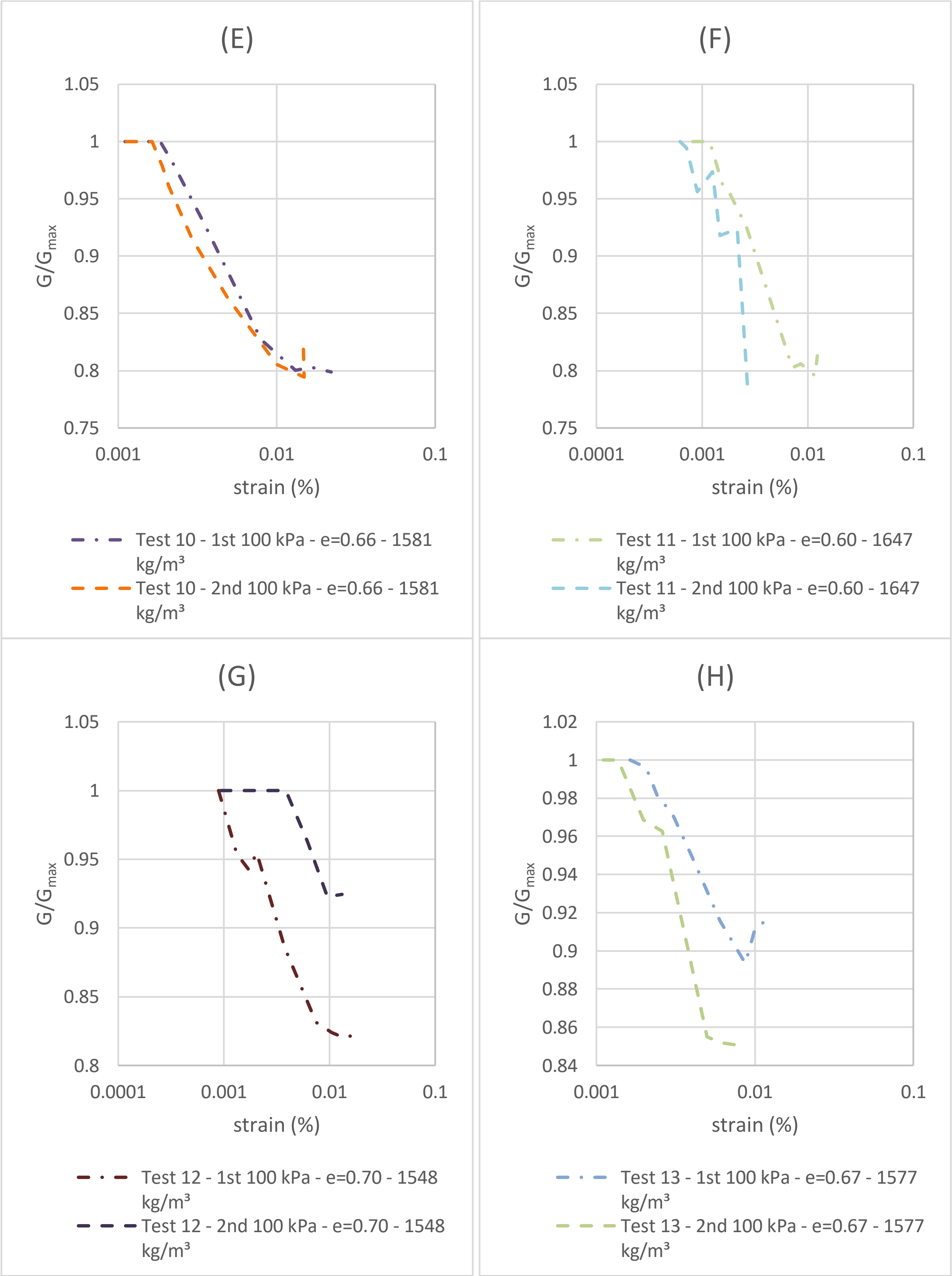

Figure 75. *Effect of loading and unloading on normalized shear modulus reduction at 100 kPa*

Figure 76 and Figure 77 shows the normalized curves at the same pressure for different void ratios. Figure 76 shows these curves for test 6, 7 and 8, while Figure 77 shows this for test 9, 10, 11, 12 and 13. The reason why these curves are split, is because the data is not comparable due to improving skills with preparing the samples during the testing series.

As can be seen in Figure 76, most curves (A, C and D) starts to decrease at higher strain levels when a lower void ratio is tested. During the loading 100 kPa and unloading 50 kPa in test 8, respectively Figure 76 (B) and (E), with the lowest void ratio, starts to decrease earlier than test 7, with the second lowest void ratio. A possible explanation might be that, due to the given that the void ratios of these 2 tests are so close to each other, a difference occurs compared to the other measurements. Therefore these 2 curves are turned. In test 6, the loading 100 kPa (Figure 76 (B)) is unpronounced.

In Figure 77, no clear correlation can be found between the data, which is possibly explainable by more parameters which affect the normalized reduction curves.

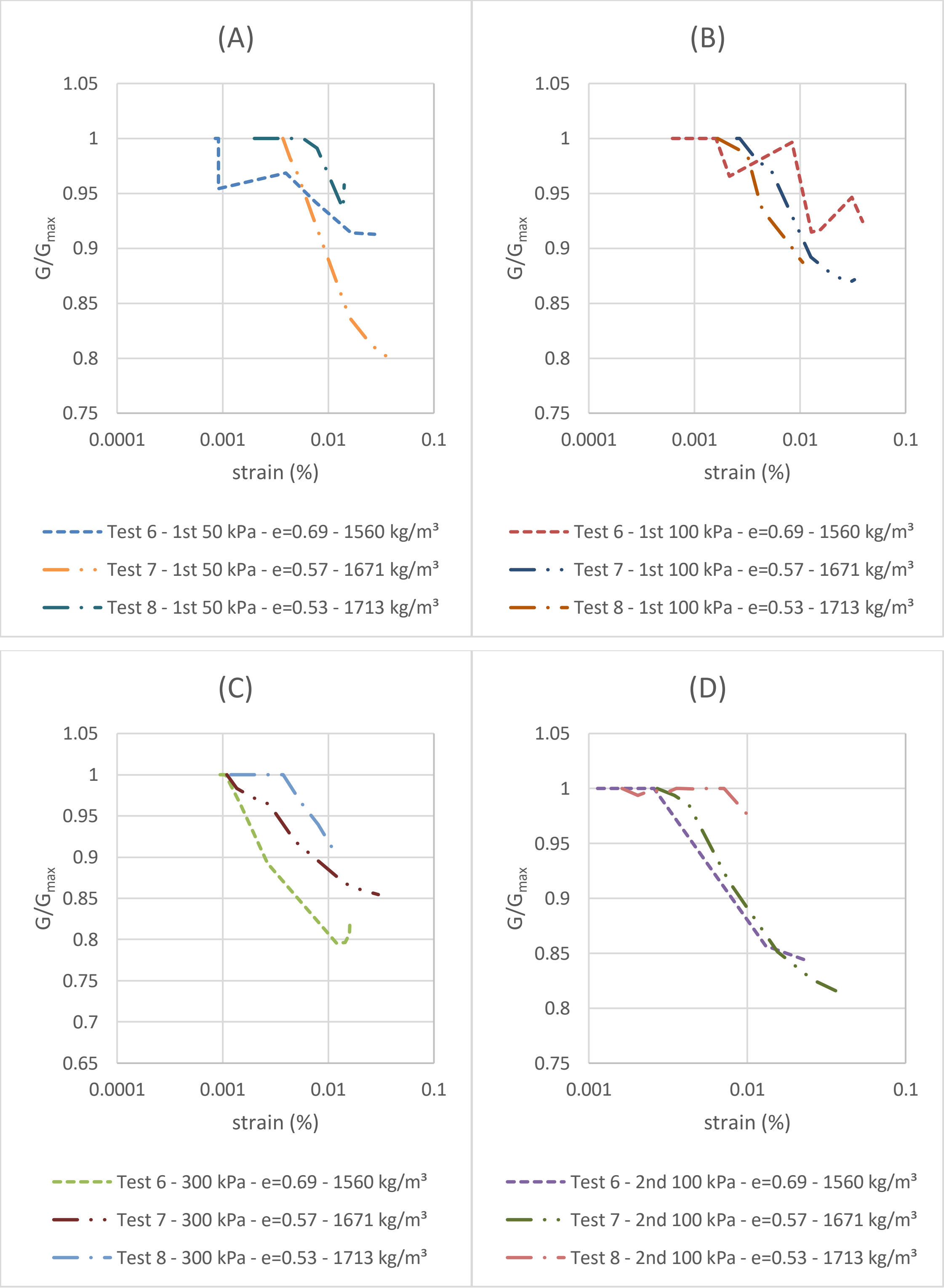

Figure 76. Normalized shear modulus reduction curve at constant pressure and different void ratios for test 6, 7 and 8 (continue)

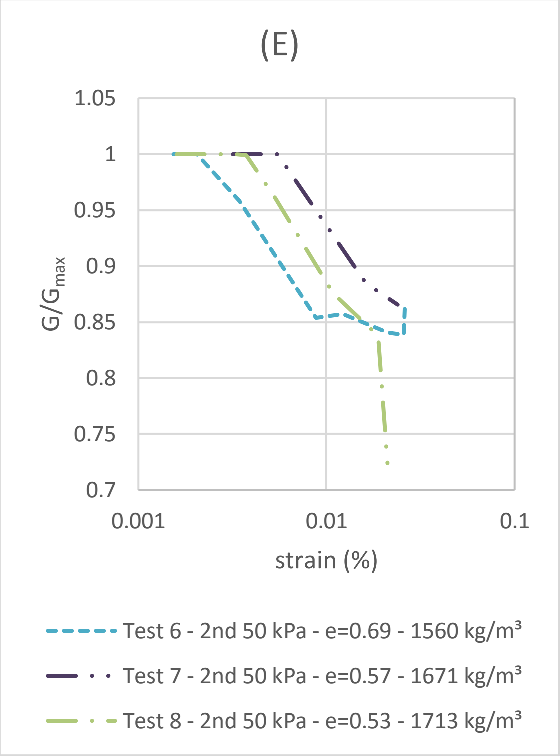

Figure 76. *Normalized shear modulus reduction curve at constant pressure and different void ratios for test 6, 7 and 8*

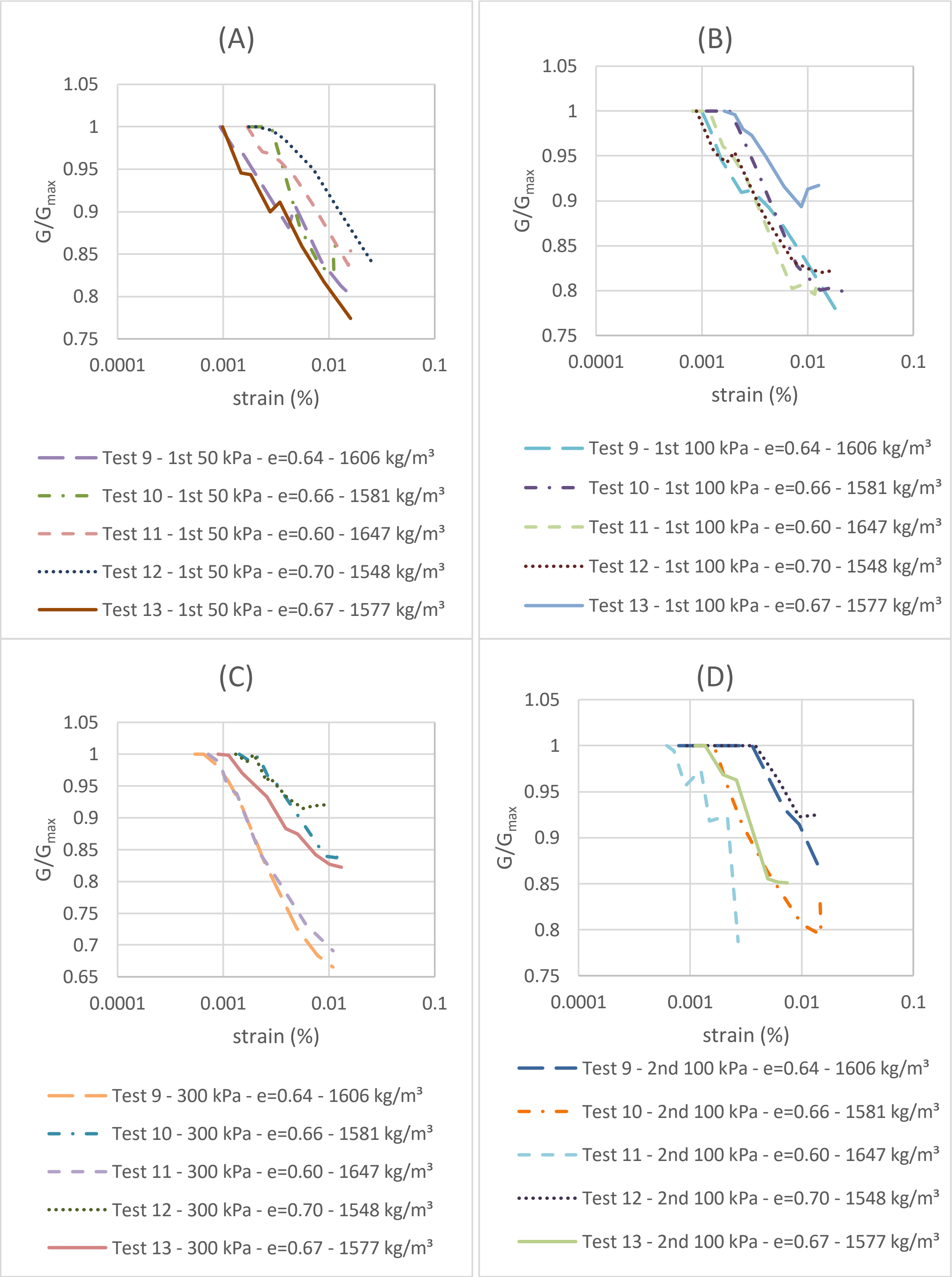

Figure 77. Normalized shear modulus reduction curve at constant pressure and different void ratios for test 9, 10, 11, 12 and 13 (continue)

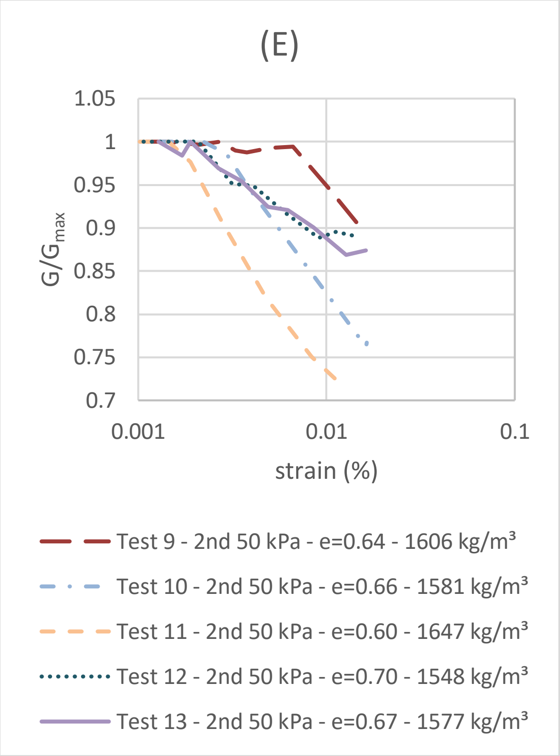

Figure 77. *Normalized shear modulus reduction curve at constant pressure and different void ratios for test 9, 10, 11, 12 and 13*

4.6.2.4 Normalized shear modulus reduction normalized with bender elements for Viasvesi sand

Figure 78, Figure 79, Figure 80 and Figure 81 show the normalized shear modulus reduction curves, normalized with G_{max} received from the bender elements. Figure 78 shows the curve per test, with increasing and decreasing cell pressure. Figure 79 shows the difference between the loading and unloading 50 kPa, while Figure 80 shows the difference between unloading and loading for the 100 kPa cycles. Figure 81 shows the difference between different tests, conducted with different void ratios.

During test 6 (Figure 78 (A)), the loading cycle of 50 and 100 kPa are neglected, because they are irregular. Between the 300 kPa cycle and the two unloading cycles, a certain correlation can be seen. The 300 kPa cycle starts to decrease at the lowest strain level, followed by the unloading 100 kPa and 50 kPa cycles. Caution needs to be taken by this relation, because the 50 kPa unloading cycle is only horizontal, which might be caused by a G_{max} value which is determined too low during the bender element test.

During test 9 (Figure 78 (B)), the last cycle of the test, the 50 kPa unloading cycle, is neglected because the value of G_{max}, determined with the bender elements, is much higher compared to the other measurements. As can be noticed, the 300 kPa cycle starts to decrease at the lowest strain level, followed by the loading 50 kPa, unloading 100 kPa and the loading 100 kPa.

In test 10 (Figure 78 (C)), the unloading 100 kPa becomes neglected, because the values of G, both by resonant column and bender elements, do not stroke with the other measurements. As can be seen in the other measurements during this test, the unloading 50 kPa starts to decrease at the lowest strain level, followed by both loading 50 and 100 kPa. The 300 kPa cycle starts to decrease at the highest strain level. Test 10 thus strokes with Figure 2 [16], where the loading cycles needs to start to decrease at higher strain levels when higher confining pressures are initiated.

During test 11 (Figure 78 (D)), the 300 kPa cycle starts to decrease at the lowest strain level, followed by the unloading 50 kPa cycle. Following on this, both 100 kPa cycles decrease at approximately the same strain level. The loading 50 kPa decreases at the highest strain level.

Additionally, test 12 (Figure 78 (E)), the loading cycle of 50 kPa gets neglected because the value differs from the other measurements. Next to this, the 300 kPa and loading 100 kPa cycle start to decrease at the lowest strain level. Following on this, the unloading cycle of 50 kPa decreases at the second lowest strain level, followed by the unloading 100 kPa cycle.

Due to an irregularity, a horizontal progression, the loading 100 kPa and unloading 50 kPa gets neglected in test 13 (Figure 78 (F)). Additionally, all other 3 curves decrease at approximately the same strain level.

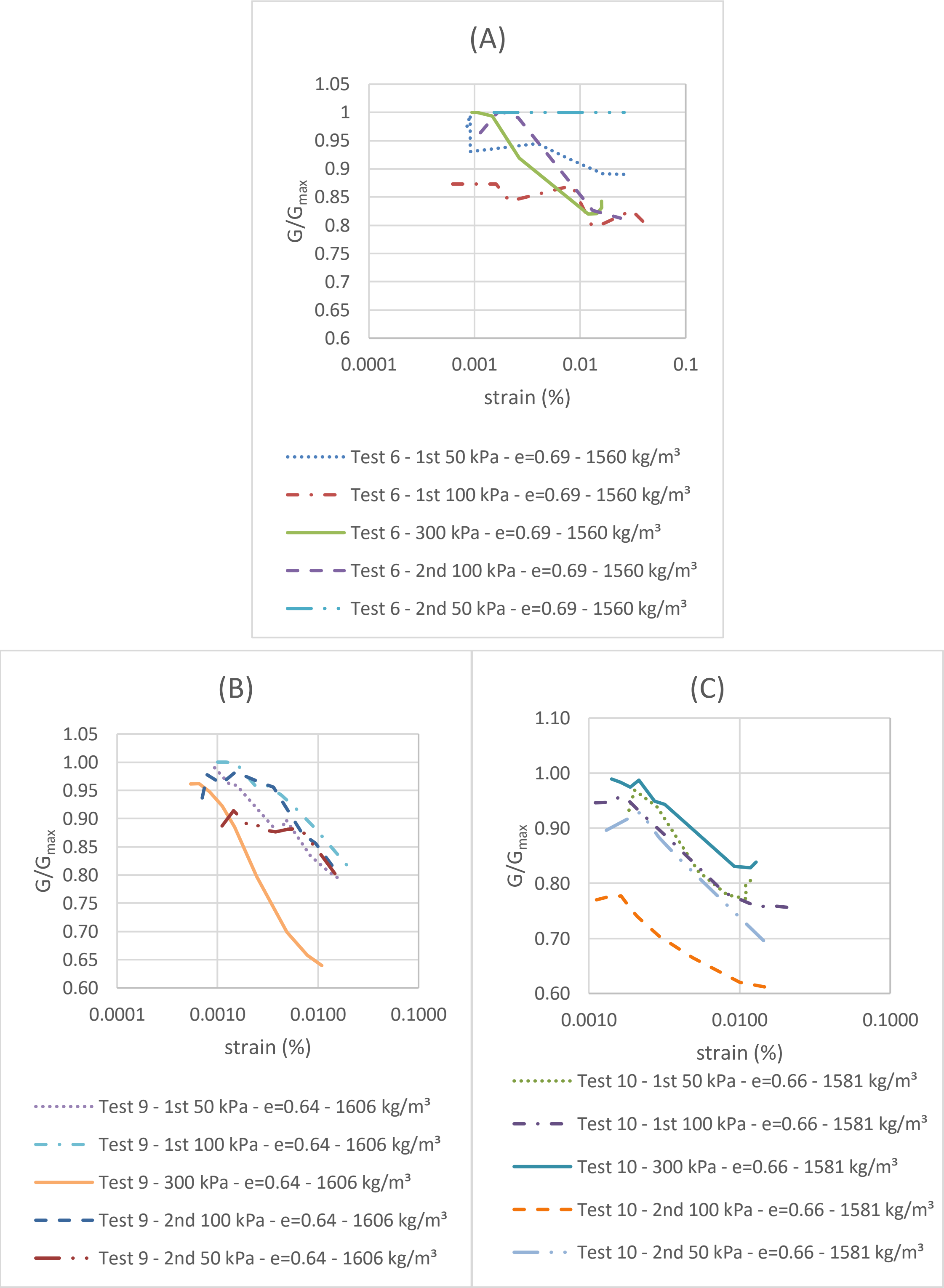

Figure 78. Normalized shear modulus reduction curve for increasing and decreasing pressure (continue)

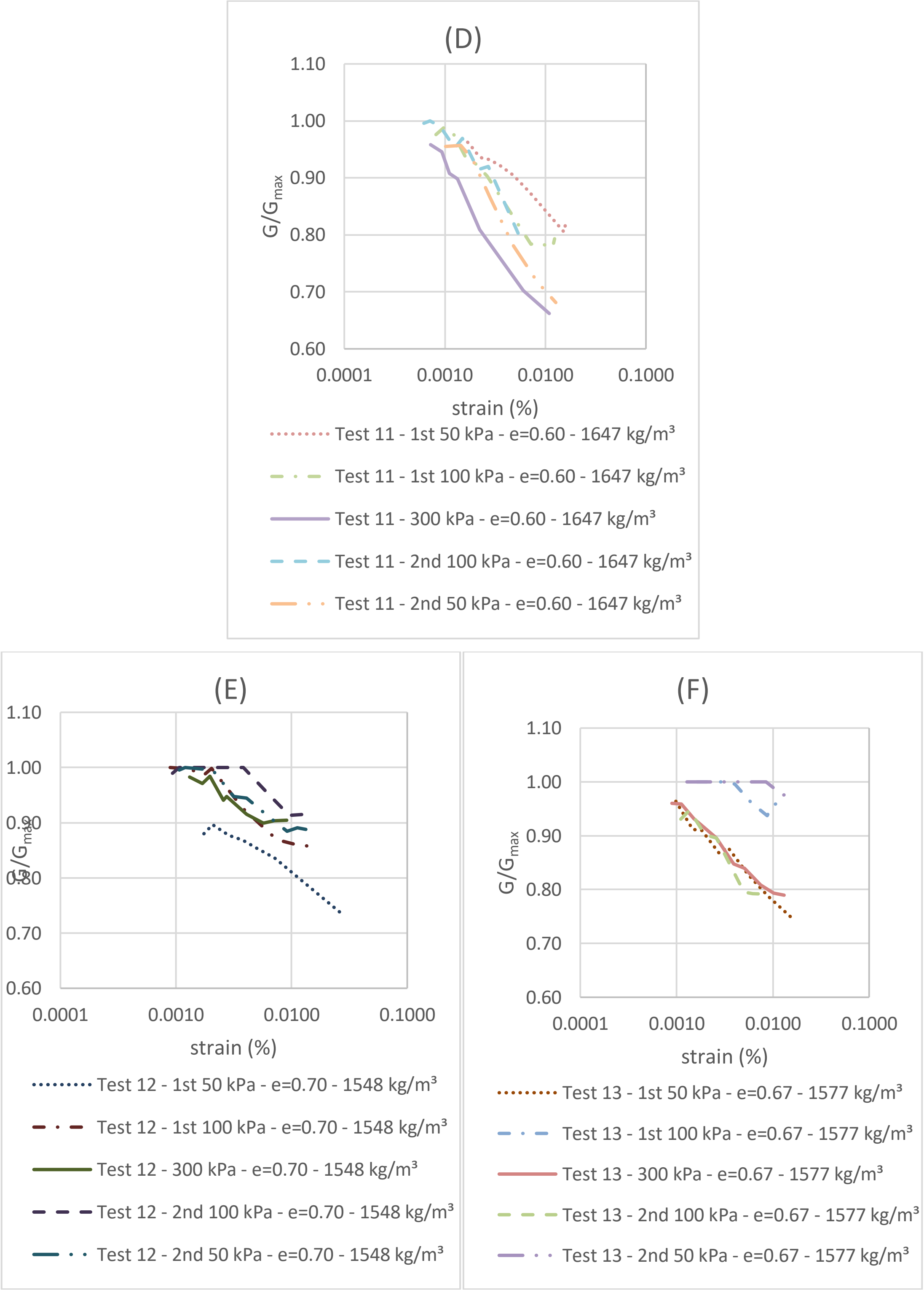

Figure 78. *Normalized shear modulus reduction curve for increasing and decreasing pressure*

Figure 79 compares the normalized shear stiffness of the loading step of 50 kPa with the unloading step of 50 kPa during different tests. Test 6 (Figure 79 (A)) is neglected, because no clear relation can be found between the 2 curves. Test 9 (Figure 79 (B)) is neglected because the shear stiffness determined via the bender elements is differing too hard from the resonant column values during the unloading step.

As can be noticed in the Figure 79 (C) (test 10), the unloading cycle of 50 kPa starts to decrease a bit later than the loading cycle. Next to this, the unloading cycle its normalisation lies a bit lower than the loading cycle, which can be explained by a value of the bender elements which is too high compared to the value received by the resonant column.

In the graph of test 11 (Figure 79 (D)), the normalized value of *G* decreases at a higher strain level for the loading curve. Caution should be taken to draw a conclusion of this graph, because the loading cycle has no horizontal part with a constant stiffness. Therefore, it might be possible the unloading curve reacts stiffer and starts to decrease at a higher strain level. Additionally, a fault in the bender element value might have occurred during both tests, because the normalized value is not 1.

During test 12 (Figure 79 (E)), both curves start to decrease at approximately the same strain level. It needs to be noticed that the measurements of the unloading cycle start at a lower strain level, while the loading cycle has a small increase in the beginning of the curve. Additionally, the unloading cycle has a horizontal part which equals to one, while the loading curve starts at a lower normalized shear stiffness. Therefore, caution should be taken with drawing conclusions out of this curve.

Finally, during test 13 (Figure 79 (F)), the unloading curve starts to decrease at a much higher strain level than the loading curve. Next to this, the loading curve only decreases with increase of the strain level. Therefore, also by this curves caution should be taken drawing conclusions.

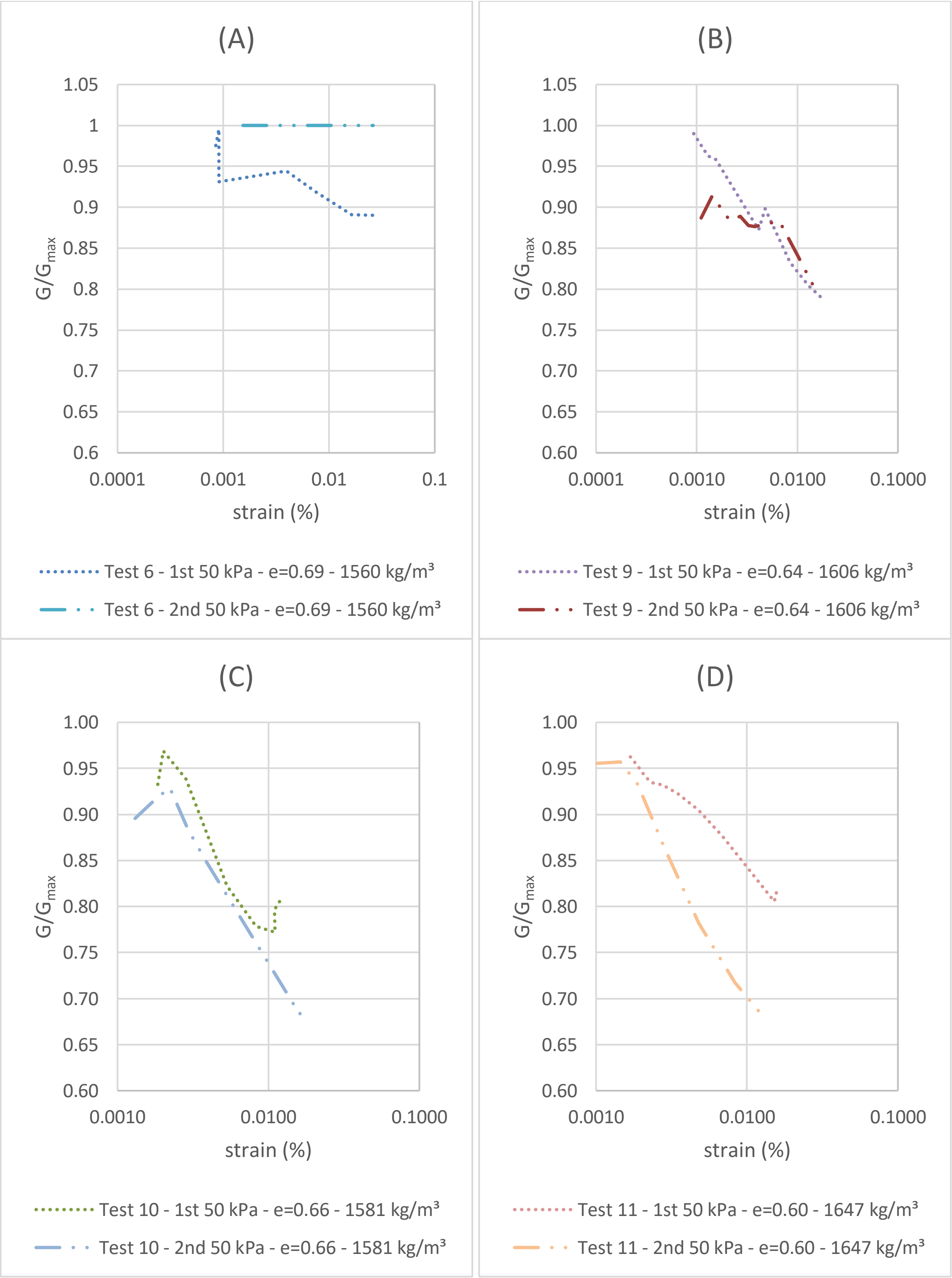

Figure 79. Effect of loading and unloading on normalized shear modulus reduction at 50 kPa (continue)

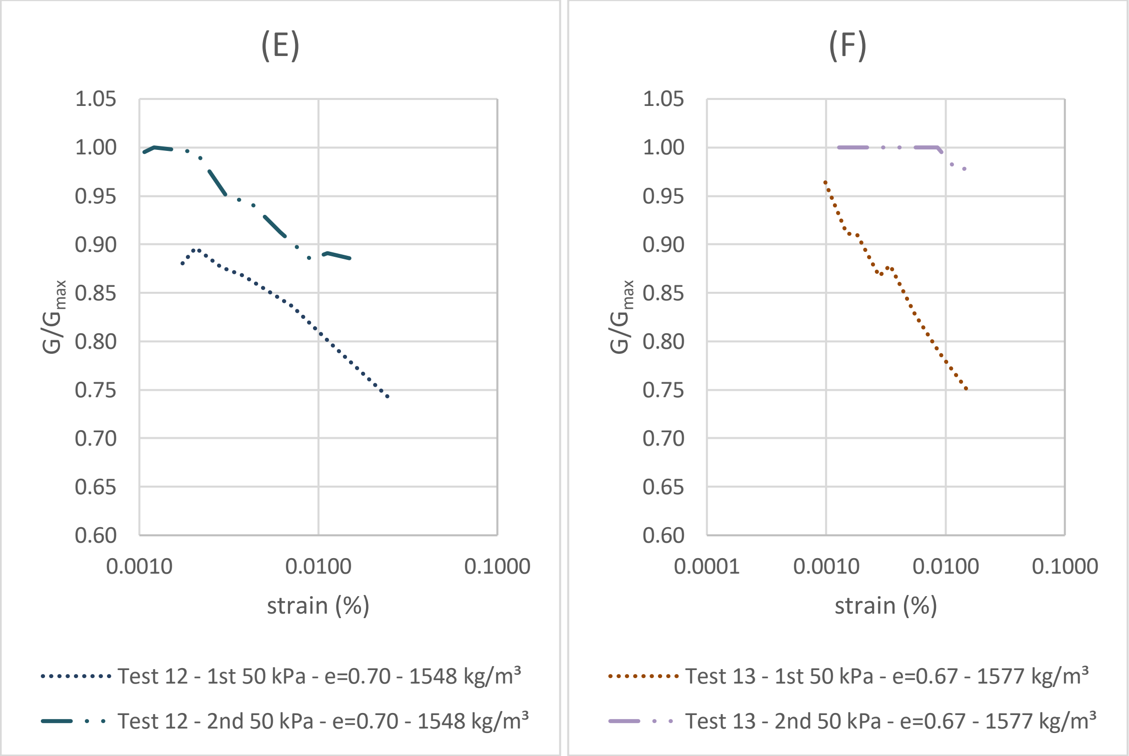

Figure 79. *Effect of loading and unloading on normalized shear modulus reduction at 50 kPa*

Figure 80 compares the normalized shear stiffness of the loading step of 100 kPa with the unloading step of 100 kPa during different tests. Test 6 (Figure 80 (A)) is neglected, because no clear correlation can be found between the 2 curves. Test 10 (Figure 80 (C)) is neglected because the results of the second cycle of 100 kPa do not stroke with the other measurements of this test.

During test 9 (Figure 80 (B)), both loading and unloading 100 kPa start to decrease at approximately the same strain level. In test 11 (Figure 80 (D)), the same occurs as in Figure 80 (B), although caution should be taken by test 11 because no horizontal part with constant stiffness occurs by both curves.

During test 12 (Figure 80 (E)), the unloading cycle decreases at a higher strain level, compared to the loading curve. Therefore it is possible to think, as by Figure 79 and Figure 30 [15], that the stiffness needs to start decrease at a higher strain level during unloading cycles.

Finally, in Figure 80 (F) (test 13), the loading cycle starts to decrease at a higher strain level compared to the unloading cycle.

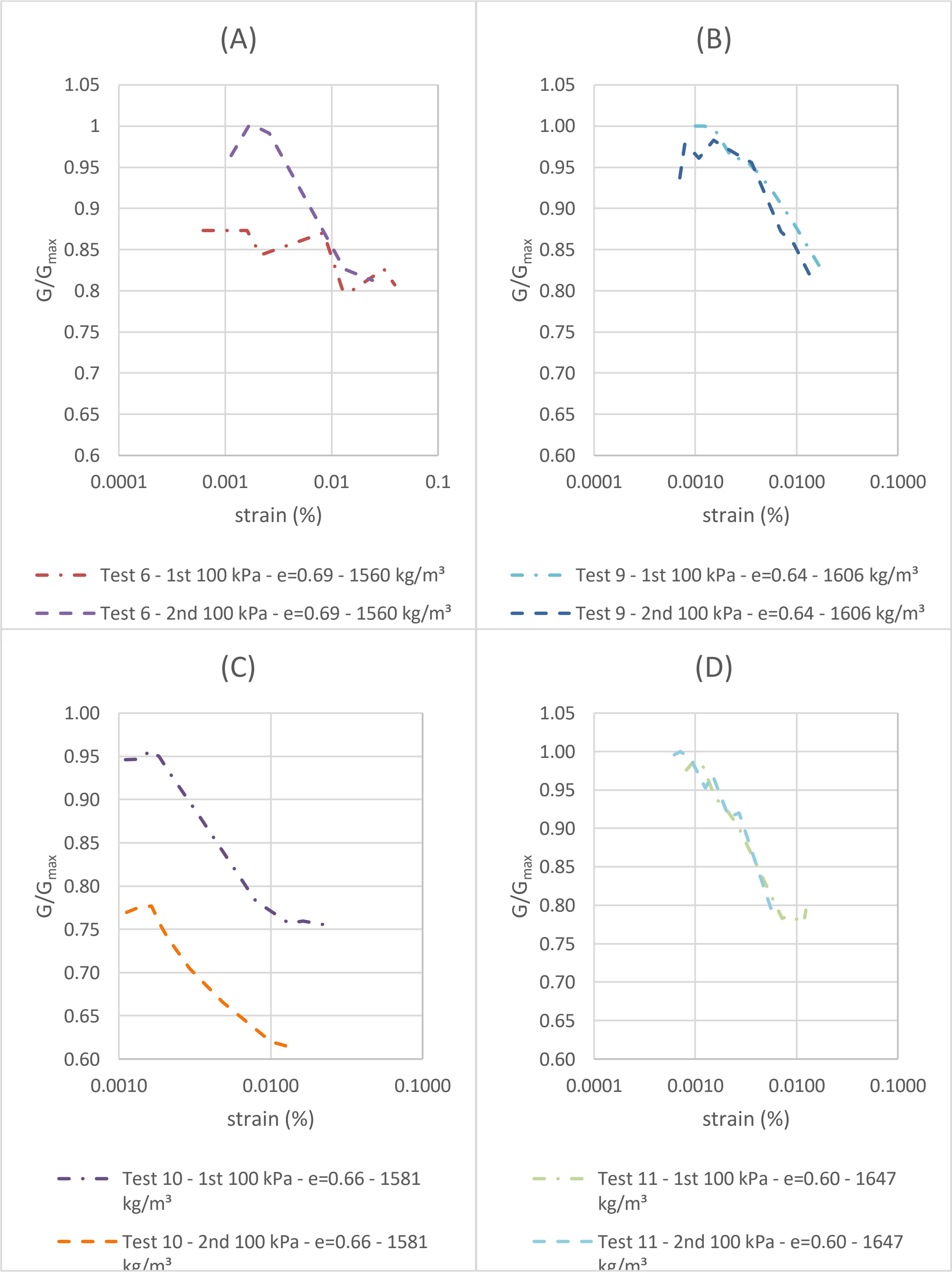

Figure 80. Effect of loading and unloading on normalized shear modulus reduction at 100 kPa (continue)

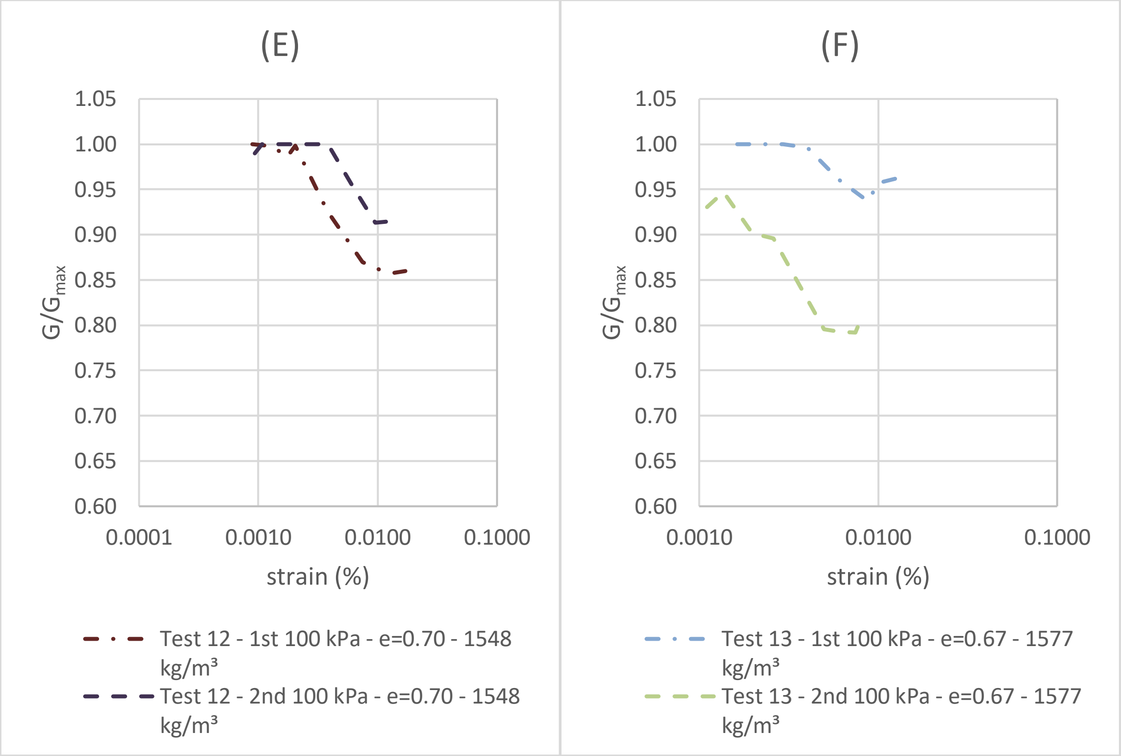

Figure 80. *Effect of loading and unloading on normalized shear modulus reduction at 100 kPa*

In Figure 81, where all the conducted tests are drawn for each pressure step for different void ratios, no clear correlation can be found between the curves. Every curve seems to start to decrease at the lowest or highest strain level once. Therefore, no conclusion is drawn out of these curves. A possible explanation why no clear correlation is found is that G_{max} values obtained by bender elements are in most cases higher compared to G_{max} obtained via resonant column. Additionally, the ratio between the G_{max} in different tests deviates from each other. Therefore a possibility exist a deviation exists, which causes the data in Figure 81, to have no correlation.

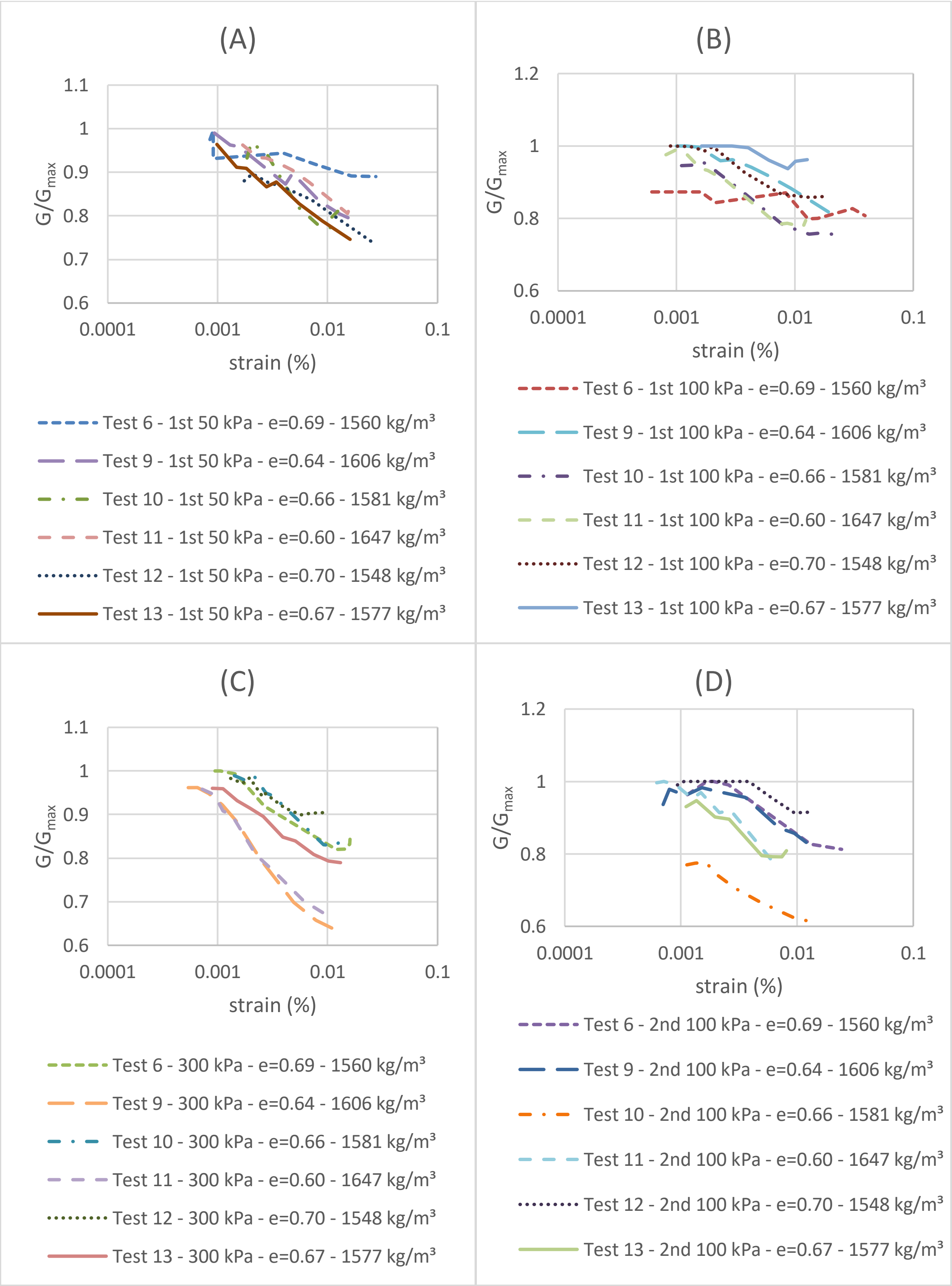

Figure 81. Normalized shear modulus reduction curve at constant pressure and different void ratios for test 6, 9, 10, 11, 12 and 13 (continue)

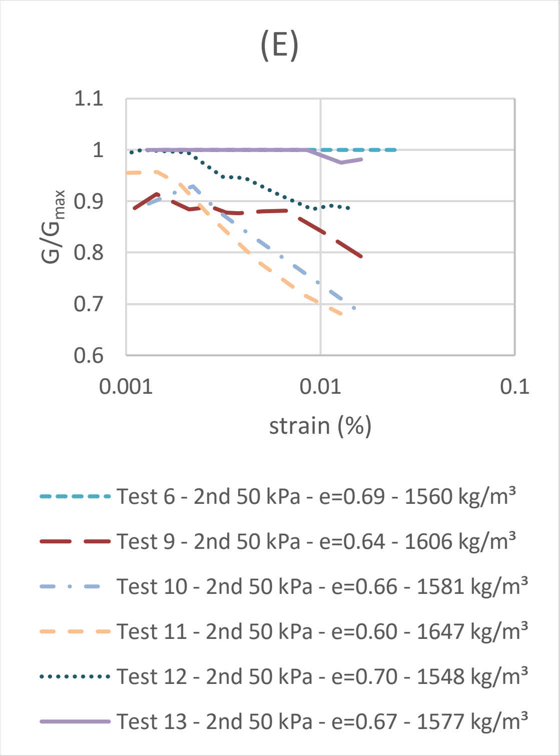

Figure 81. *Normalized shear modulus reduction curve at constant pressure and different void ratios for test 6, 9, 10, 11, 12 and 13*

4.7 Bender element tests

Figure 82 to Figure 86 give the curves for G_{max} (a) and shear wave velocity (b) determined with bender elements as function of the confining pressure for respectively test 6, 9, 11, 12 and 13. Additionally, Table 21 to Table 28 give numerical values for G_{max}, determined both by resonant column and bender elements. Next,

Table 21 to Table 28 give the numerical values of shear wave velocities measured with bender elements.

Some tests give 2 values for the same pressure step. In these bender element measurements, a measurement is done in the beginning and at the end of the pressure step.

Additionally, the calculation of the first measurement of the loading 50 kPa of test 13 will be written out. This calculation is done according to equation (21) to determine the shear wave velocity and (22) to determine the maximum shear stiffness. The shear wave velocity according to equation (21) becomes:

Tip-to-tip travel distance:

$$l_{tt} = 106.74 - 0.6 - 2 * 5.55 = 95.04\ mm$$

Where $l_{avg,BE} = 5.55\ mm$ is the average length of each bender element

$\Delta l_{height} = 0.6\ mm$ is the change in height

Shear wave velocity:

$$v_s = \frac{95.04\ mm}{0.0003112\ s} = 304.62\ m/s$$

According to equation (22), the maximum shear stiffness of the sample is determined. This gives:

$$G_{max} = 1551\frac{kg}{m^3} * \left(304.62\frac{m}{s}\right)^2 = 144\ MPa$$

Figure 82, Figure 85 and Figure 86 show the result of the measurements for respectively test 6, 12 and 13. As can be seen in Figure 82 and Figure 86, the soil reacts stiffer in the very small strain area during the unloading 100 kPa cycle, compared to the loading cycle. Between the 50 kPa cycles, the effect of a stiffer reaction is lesser pronounced. A small decrease is noticed in test 6, while in test 13 a small increase is noticed. Additionally, in Figure 85 both unloading 50 and 100 kPa cycles react stiffer than the virgin loading.

Besides, in Figure 82, Figure 85 and Figure 86 a second bender element measurement, at the end of the pressure cycle, is shown. As can be noticed, the stiffness during this measurement is lower in all 3 cases, during the 100 kPa measurements, but the effect is less pronounced for the 50 kPa measurements. During test 12 and 13, respectively Figure 85 and Figure 86, the 300 kPa measurement is lower compared to the measurements immediately after consolidation. Next to this, during the 50 kPa cycle, the effect can be explained by the given the sample is experiencing less support from the confining pressure, which can cause the effect that during the 50 kPa cycle a less pronounced effect is noticed. Besides, the *OCR* might have a higher influence which causes the stiffness to be higher.

During test 9 and 11, respectively Figure 83 and Figure 84 there is done no measurement at the end of the cycle. Though, it can be noticed soil reacts stiffer in both testing series during the unloading cycle. As shown in Table 25, test 10 does not give clear data and is therefore not analysed in this section. Additionally, in test 7 (Table 22) and test 8 (Table 23), no bender elements tests were conducted because one of the bender elements was broken.

Table 21. *G_{max} for resonant column and bender elements and the shear wave velocity at a certain pressure step for test 6*

	p' **(kPa)**	***G****max, RC* **(MPa)**	***G****max, BE* **(MPa)**	***v****s* **(m/s)**
TEST 6	50	83	85	231.06
			-	-
	100	87	100	248.23
			74	213.44
	300	172	167	319.38
			168	319.86
	100	127	132	284.00
			109	258.34
	50	95	77	217.79
			70	207.32

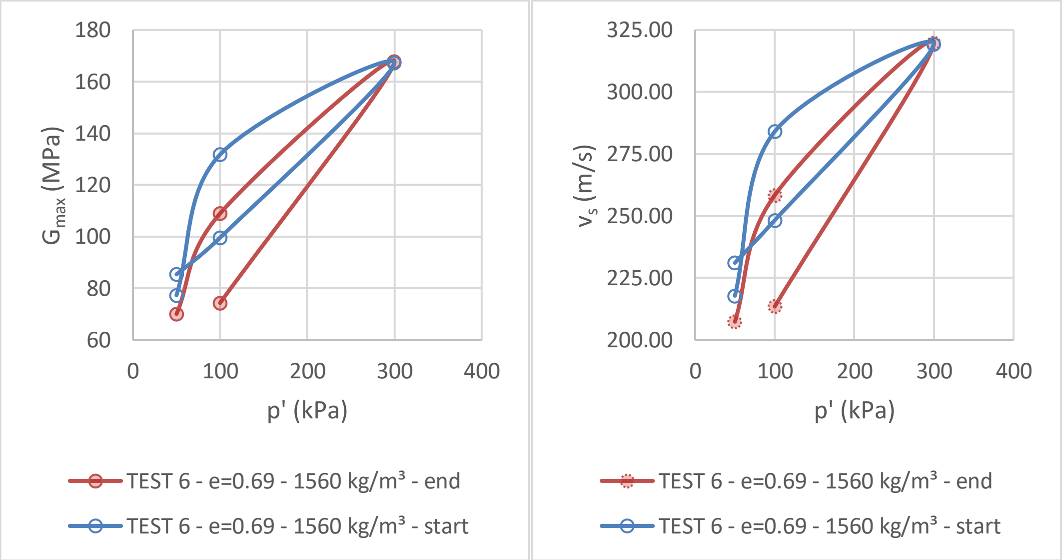

(a) (b)

Figure 82. *Evolution of G_{max} (a) and shear wave velocity (b) measured with bender elements for test 6*

Table 22. *G_{max} for resonant column and bender elements and the shear wave velocity at a certain pressure step for test 7*

	p' **(kPa)**	***G****max, RC* **(MPa)**	***G****max, BE* **(MPa)**	***v****s* **(m/s)**
TEST 7	50	107	-	-
	100	156	-	-
	300	234	-	-
	100	149	-	-
	50	127	-	-

Table 23. *G_{max} for resonant column and bender elements and the shear wave velocity at a certain pressure step for test 8*

	p′ (kPa)	**$G_{max, RC}$ (MPa)**	**$G_{max, BE}$ (MPa)**	**v_s (m/s)**
TEST 8	50	115	-	-
	100	209	-	-
	300	253	-	-
	100	204	-	-
	50	156	-	-

Table 24. *G_{max} for resonant column and bender elements and the shear wave velocity at a certain pressure step for test 9*

	p′ (kPa)	**$G_{max, RC}$ (MPa)**	**$G_{max, BE}$ (MPa)**	**v_s (m/s)**
TEST 9	50	224	226	373.14
	100	275	261	398.86
	300	411	428	509.31
	100	297	317	439.17
	50	237	neglected	neglected

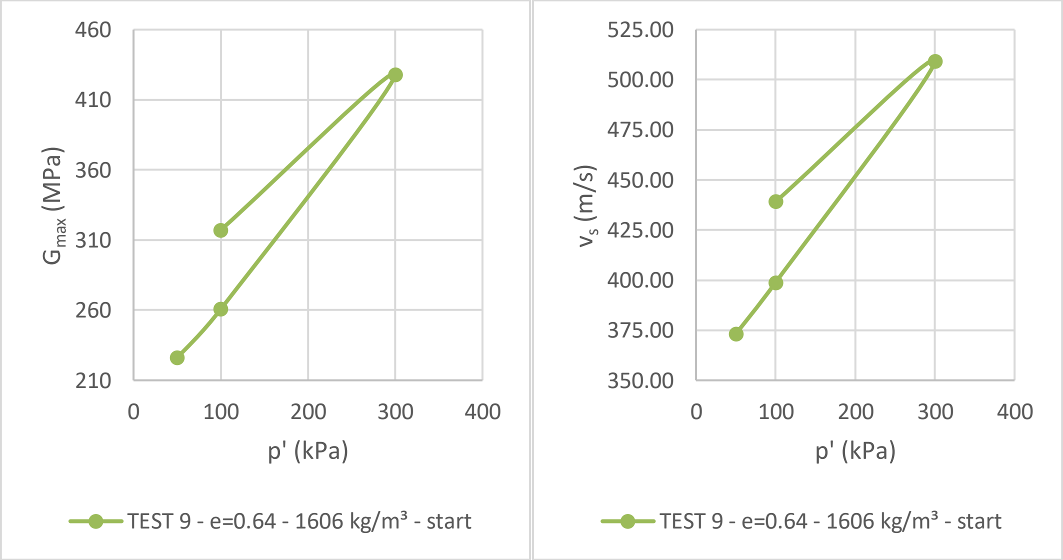

(a) (b)

Figure 83. *Evolution of G_{max} (a) and shear wave velocity (b) measured with bender elements for test 9*

Table 25. *G_{max} for resonant column and bender elements and the shear wave velocity at a certain pressure step for test 10*

	p′ (kPa)	**$G_{max, RC}$ (MPa)**	**$G_{max, BE}$ (MPa)**	**v_s (m/s)**
TEST 10	50	180	193	376.04
	100	202	214	387.14
	300	228	231	399.31
	100	neglected	neglected	neglected
	50	205	229	378.36

Table 26. *G_{max} for resonant column and bender elements and the shear wave velocity at a certain pressure step for test 11*

	p' **(kPa)**	**$G_{max,\,RC}$ (MPa)**	**$G_{max,\,BE}$ (MPa)**	**v_s (m/s)**
TEST 11	50	219	228	371.78
	100	252	258	395.20
	300	338	353	461.02
	100	306	307	430.68
	50	285	298	424.29

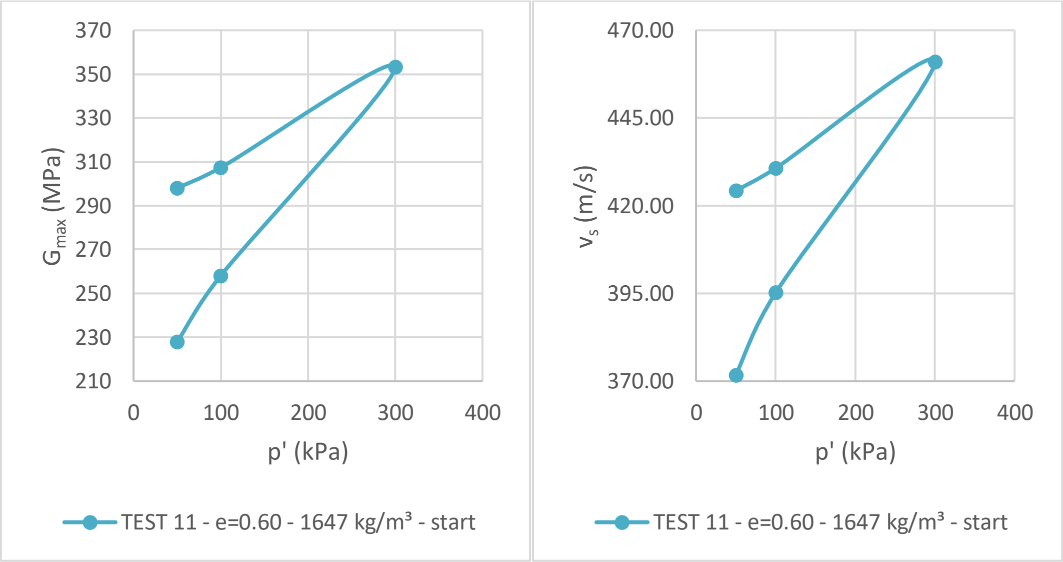

(a) (b)

Figure 84. *Evolution of G_{max} (a) and shear wave velocity (b) measured with bender elements for test 11*

Table 27. *G_{max} for resonant column and bender elements and the shear wave velocity at a certain pressure step for test 12*

	p' **(kPa)**	**$G_{max,\,RC}$ (MPa)**	**$G_{max,\,BE}$ (MPa)**	**v_s (m/s)**
TEST 12	50	110	125	283.55
			145	305.93
	100	169	162	321.41
			156	315.19
	300	193	196	353.37
			174	332.20
	100	167	169	328.27
			149	307.72
	50	149	150	308.69
			152	310.68

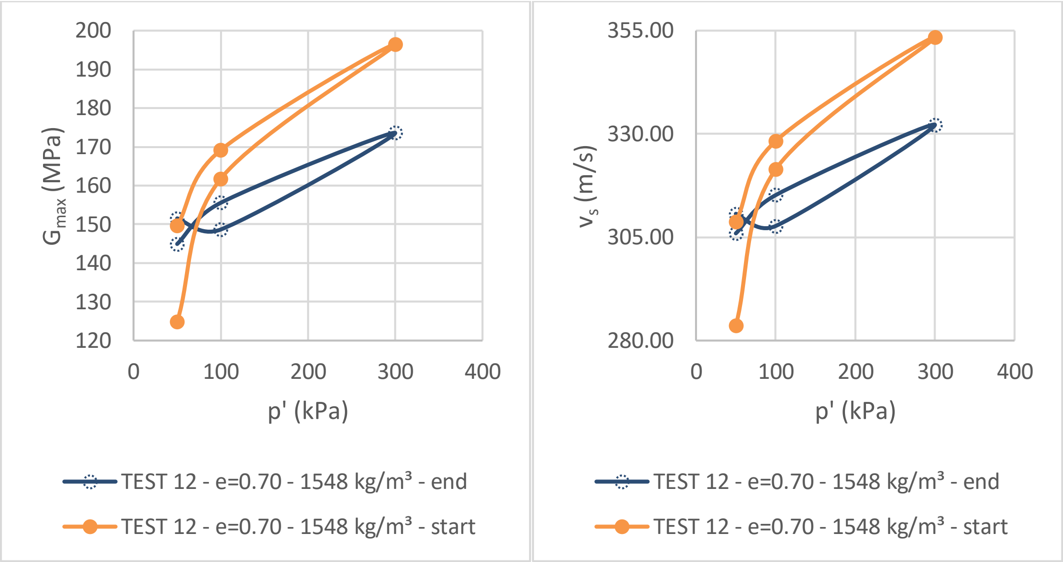

(a) (b)

Figure 85. *Evolution of G_{max} (a) and shear wave velocity (b) measured with bender elements for test 12*

Table 28. *G_{max} for resonant column and bender elements and the shear wave velocity at a certain pressure step for test 13*

	p' (kPa)	**$G_{max, RC}$ (MPa)**	**$G_{max, BE}$ (MPa)**	**v_s (m/s)**
TEST 13	50	139	144	304.62
			149	310.26
	100	166	158	318.59
			154	314.37
	300	215	224	377.76
			216	371.02
	100	182	196	354.25
			187	346.13
	50	162	144	303.97
			149	309.61

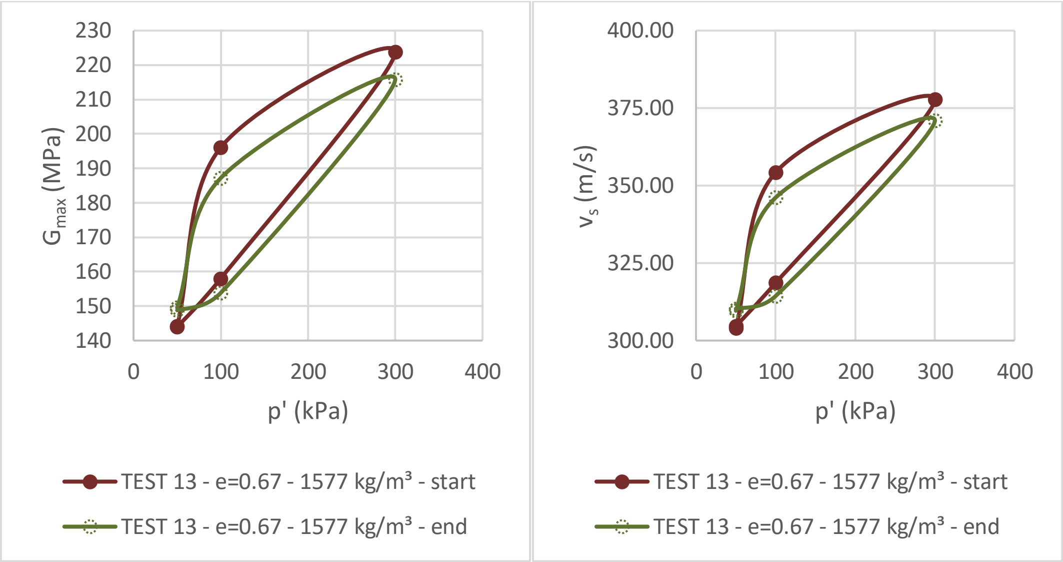

(a) (b)

Figure 86. *Evolution of G_{max} (a) and shear wave velocity (b) measured with bender elements for test 13*

4.8 Comparison of G_{max} from bender elements, resonant column and predictions

Figure 87 gives a view of G_{max} determined via data obtained with bender elements and resonant column tests. Next to this, a comparison is given with 3 equations – 'Menq (2)', 'Wichtmann and Triantafyllidis (4)' and 'Senetakis et al. (5)' - discussed in section 2.1.3. Additionally, the parameters used to gain these curves are shown in appendix D, while both equations (2), (4) and (5) will be written out once for test 13. As can be noticed in equations (2), (4) and (5), no *OCR* is included in these calculations.

First, the calculation via 'Menq', according to equation (2) will be written out. This is done for an effective confining pressure of 50 kPa.

$$\boldsymbol{G_{max} = A * 0.67^{x} * \left(\frac{50}{100}\right)^{n} = 63\ MPa}$$

Where $A = 67.1 * 2^{-0.2} = 58.41$

$$x = -1 - \left(\frac{0.5}{20}\right)^{0.75} = -1.06$$

$$n = 0.48 * 2^{0.09} = 0.51$$

Next, a calculation according to ‘Wichtmann and Triantafyllidis’ with equation (4) will be shown. This is done again for an effective confining pressure of 50 kPa.

$$\boldsymbol{G_{max} = A * \frac{(x-0.67)^2}{1+0.67} * 100^{1-n} * 50^n = 74\ MPa}$$

Where $A = 1563 + 3.13 * 2^{2.98} = 1587.70$

$x = 1.94 * \exp(-0.066 * 2) = 1.70$

$n = 0.4 * 2^{0.18} = 0.45$

Finally, ‘Senetakis et al.’s’ equation (5) will be calculated. Again, this is done for an effective confining pressure of 50 kPa.

$$\boldsymbol{G_{max} = A * 0.67^x * \left(\frac{50}{100}\right)^n = 60\ MPa}$$

Where $A = 57.01 - 5.88 * 2 = 45.25$

$x = -0.28 * 2 - 0.98 = -1.54$

$n = 0.47$

As can be seen in appendix D, ‘Saxena and Reddy (3)’ is also calculated. No figures are made from these calculations, because the values differed to hard from the rest of the calculations. For some test series no figures are made. This is because equations (2), (4) and (5) their values underestimated the maximum stiffness too hard to make them comparable with the testing data.

Next to this, the equations mentioned in section 2.1.4 for the grain shape and for the fines content are tested if they would have any influence. It is noticed the fines content did not have a big influence on the Viasvesi sand because of the small amount of *FC*. Additionally, the grain shape is hard to define accurately, and was noticed to have little influence while testing the equation with values. Therefore these equations are not compared to the values of the very small strain stiffness, received with the testing series. The grain shape is in line with what [14] mentions, that it has a negligible influence, while the grain size distribution has an influence according to [4], [14] but is not tested because only one distribution is tested, with a small percentage of fines content.

Additionally, Figure 88 shows data obtained via tests and equations (2), (4) and (5). Besides, Figure 89 shows the difference between results obtained with resonant column and bender elements. Both Figure 88 and Figure 89 give the R^2 values for these calculations.

During comparison of values obtained from bender elements, resonant column and predicting equations discussed in section 2.1.3 one general line is found. This line will now briefly be discussed.

First, the differing tests will be discussed. In the data of test 6 (Figure 87 (A)), it is noticed all 3 predictions are comparable to the loading cycle, while the unloading cycle has much higher stiffness. Next to this, the equation by 'Wichtmann and Triantafyllidis (4)' is comparable with the maximum shear stiffness obtained by the bender elements, while this value is much higher than the value obtained by the resonant column. Additionally, the equation by 'Senetakis et al. (5)' gives both by bender elements and resonant column a maximum stiffness which is lower than the obtained value. Next to this, the value obtained by 'Menq (2) ' gives a value which is lower than the bender elements and comparable to the value obtained by the resonant column.

Additionally, the data obtained during test 9 and 11, as shown in appendix D, have a much higher stiffness compared to the equation by 'Menq (2)', 'Senetakis et al. (5)' and 'Wichtmann and Triantafyllidis (4)'.

Test 10 (Figure 87 (D)), where only the loading cycle is shown from, all predictions – 'Menq (2)', 'Wichtmann and Triantafyllidis (4)' and 'Senetakis et al. (5)' – are below the obtained values of stiffness by this test

In test 7 and 8, respectively Figure 87 (B) and (C), where only resonant column data is available from, and test 12 and 13, respectively Figure 87 (E) and (F), where both resonant column and bender element data is available from, all predictions are lower compared to the obtained data during the testing series, both by loading and unloading which makes them acceptable to use. Although, 'Wichtmann and Triantafyllidis (4)' is the most correct prediction.

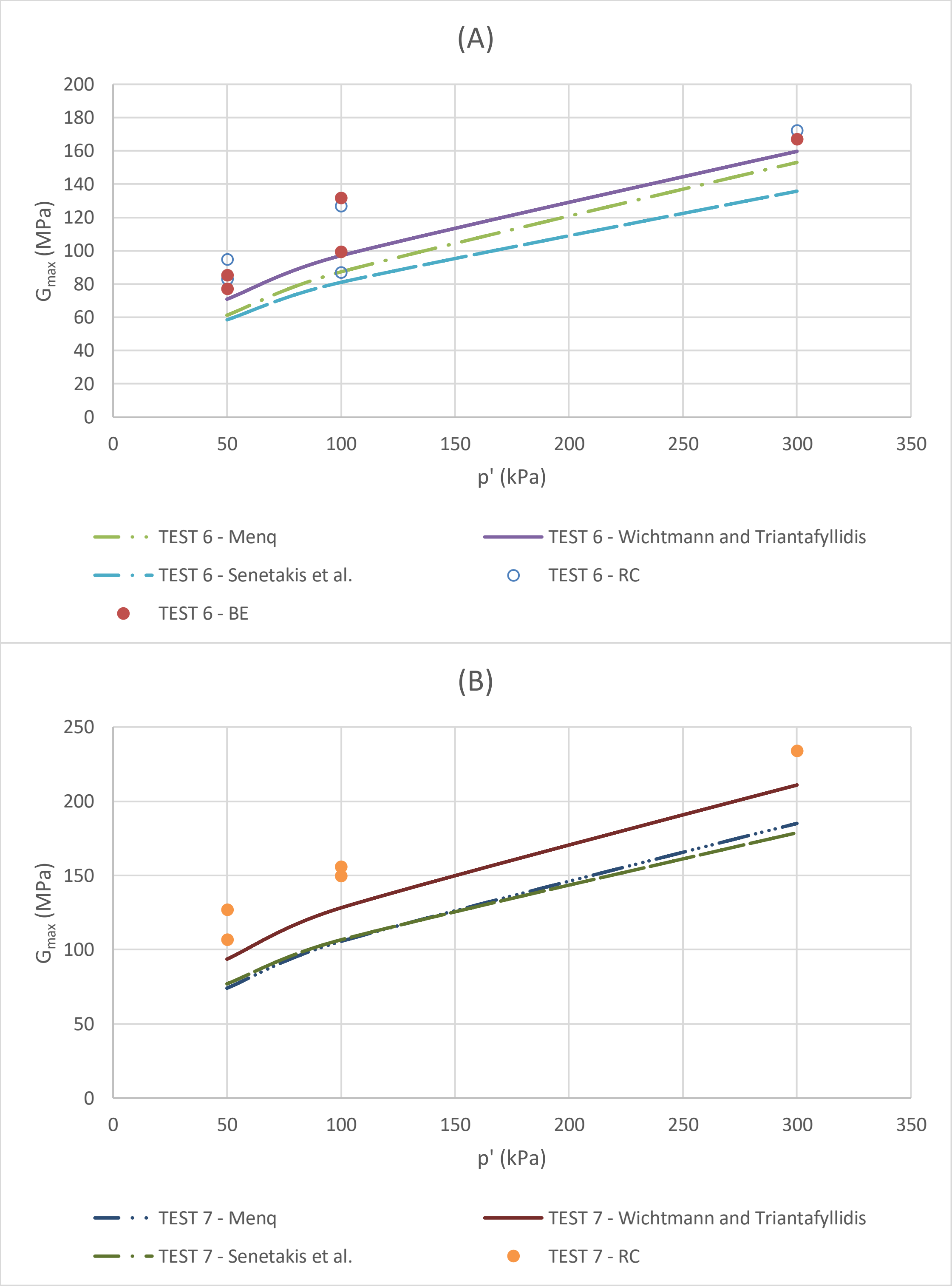

Figure 87. G_{max} from bender elements and resonant column compared with Menq, Wichtmann and Triantafyllidis and Senetakis et al. (continue)

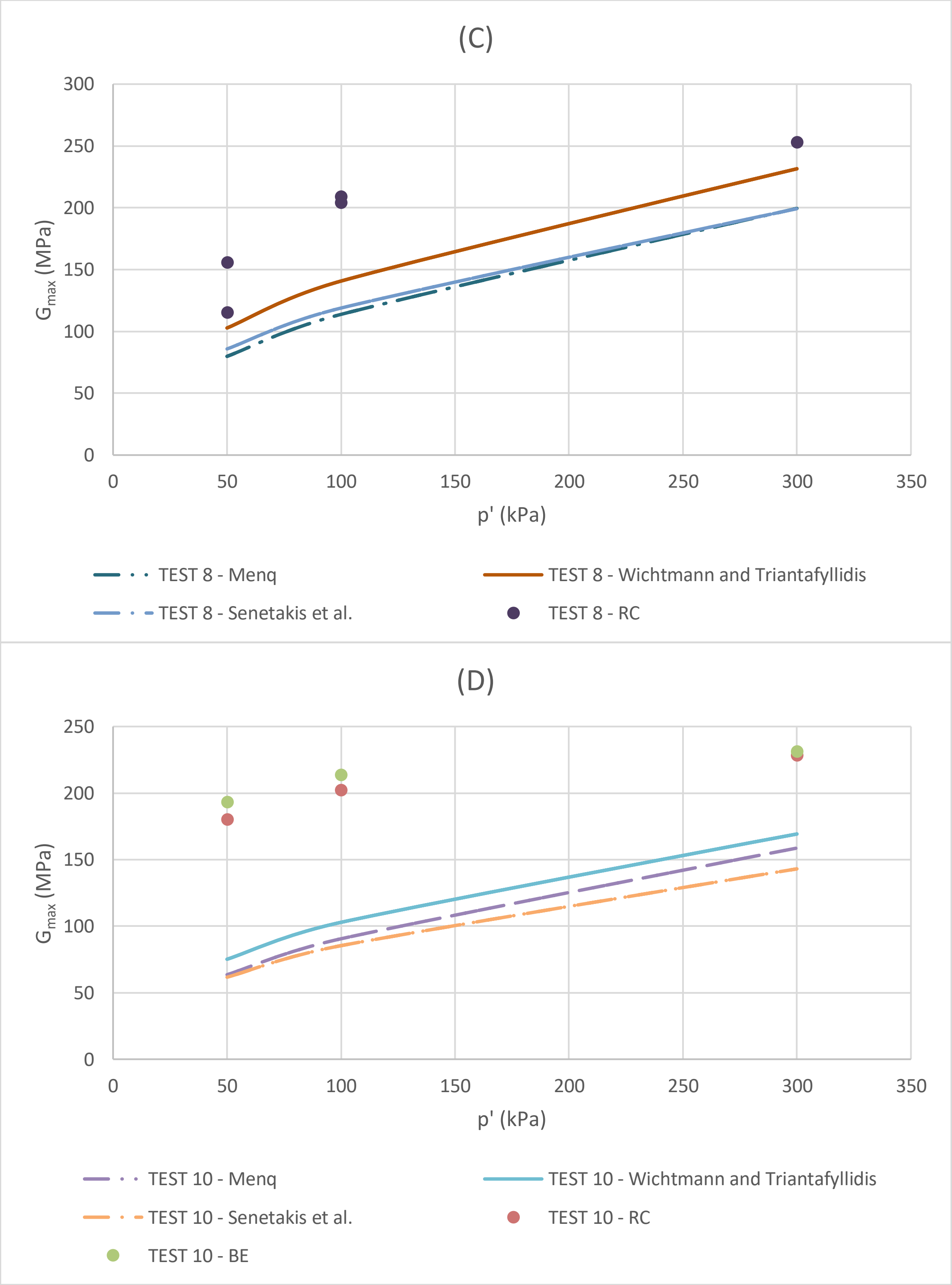

Figure 87. G_{max} from bender elements and resonant column compared with Menq, Wichtmann and Triantafyllidis and Senetakis et al. (continue)

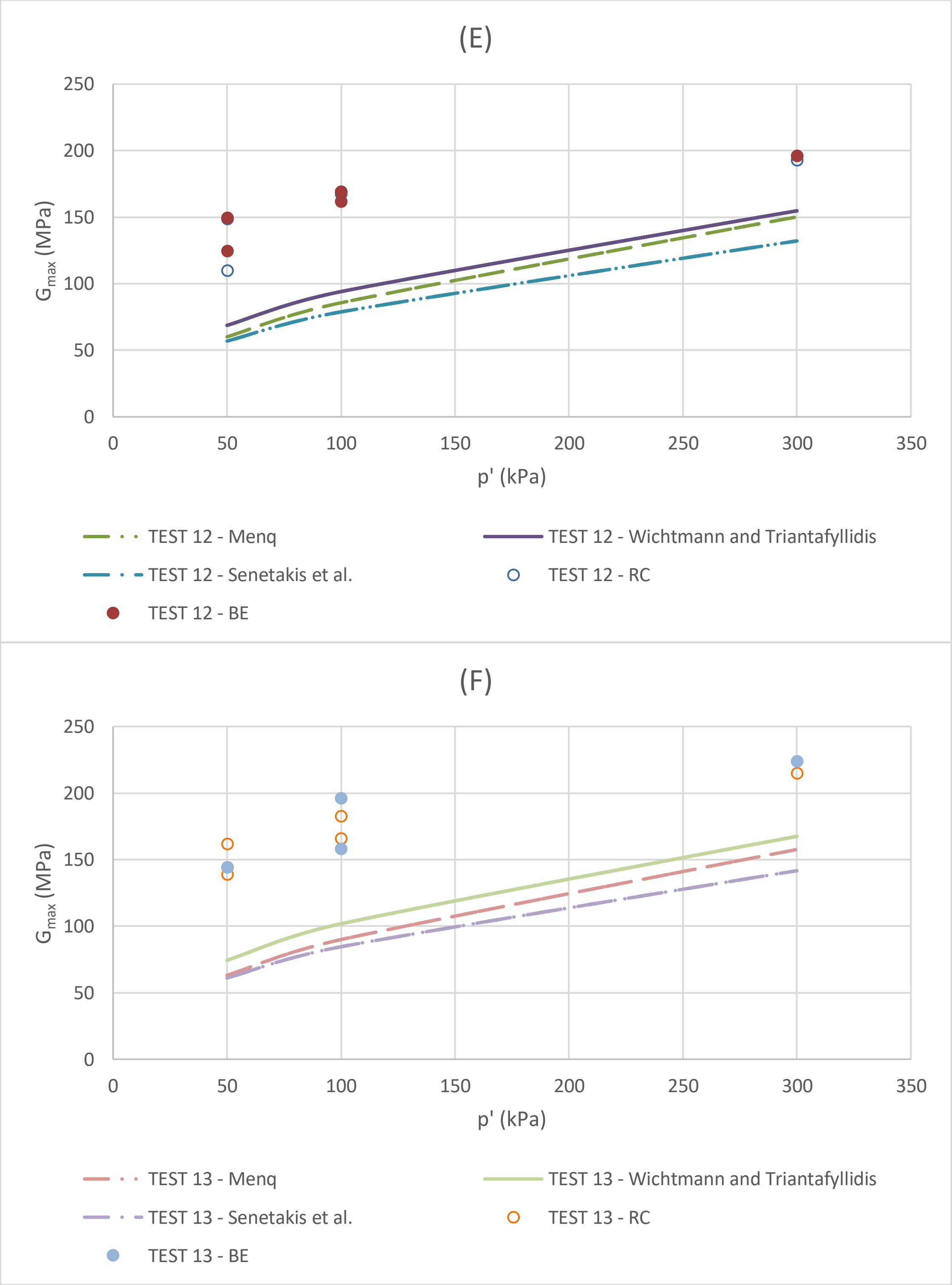

Figure 87. *G_{max} from bender elements and resonant column compared with Menq, Wichtmann and Triantafyllidis and Senetakis et al.*

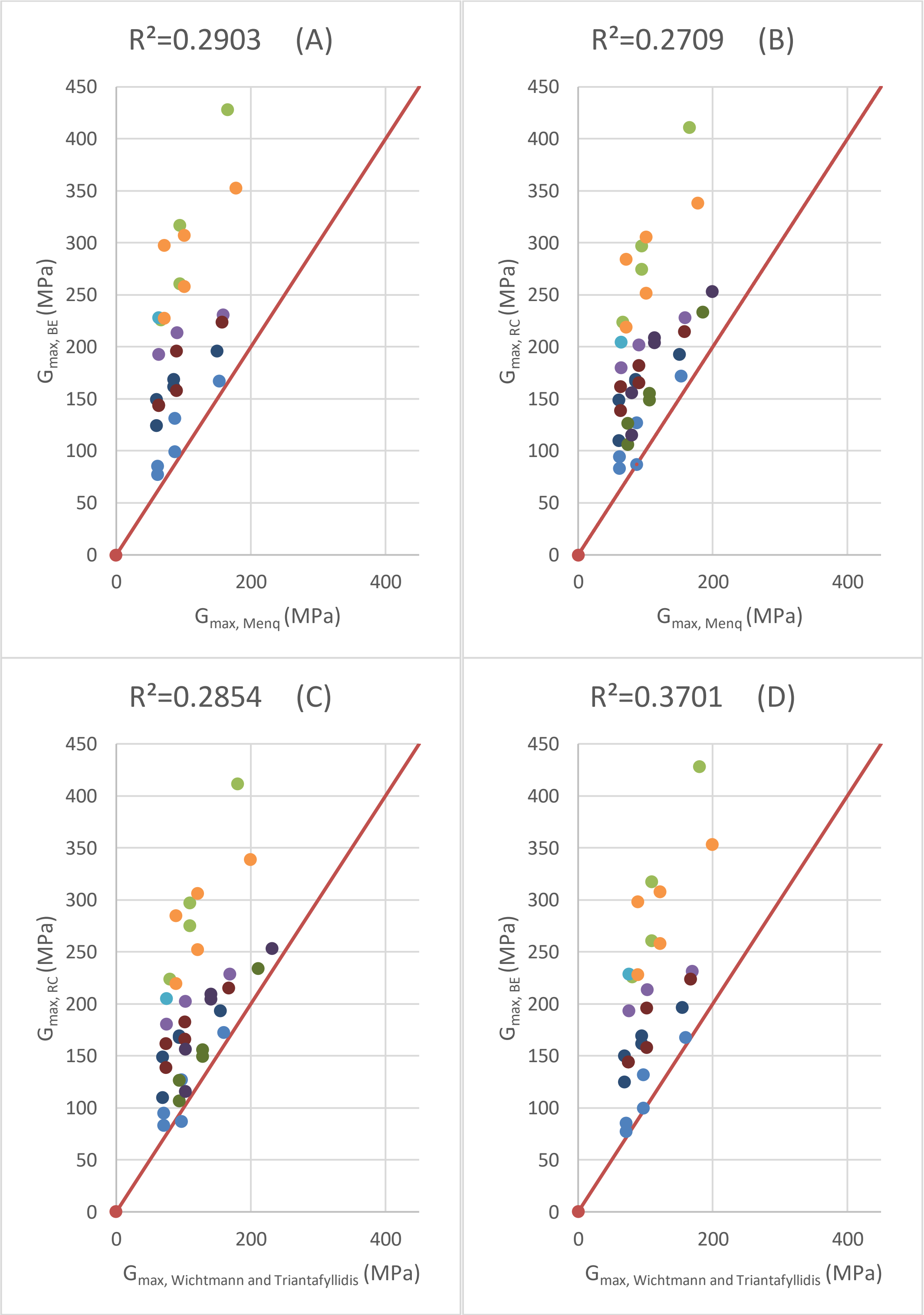

Figure 88. Menq (2), Wichtmann and Triantafyllidis (4) and Senetakis et al. (5) compared to bender elements and resonant column (continue)

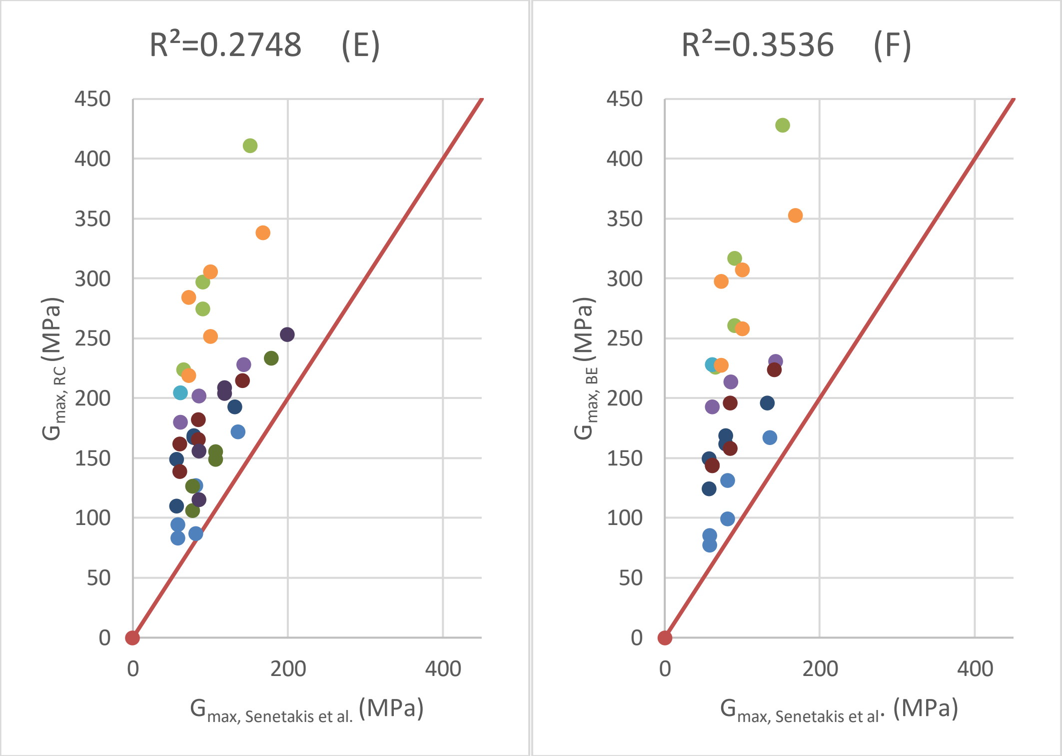

Figure 88. *Menq (2), Wichtmann and Triantafyllidis (4) and Senetakis et al. (5) compared to bender elements and resonant column*

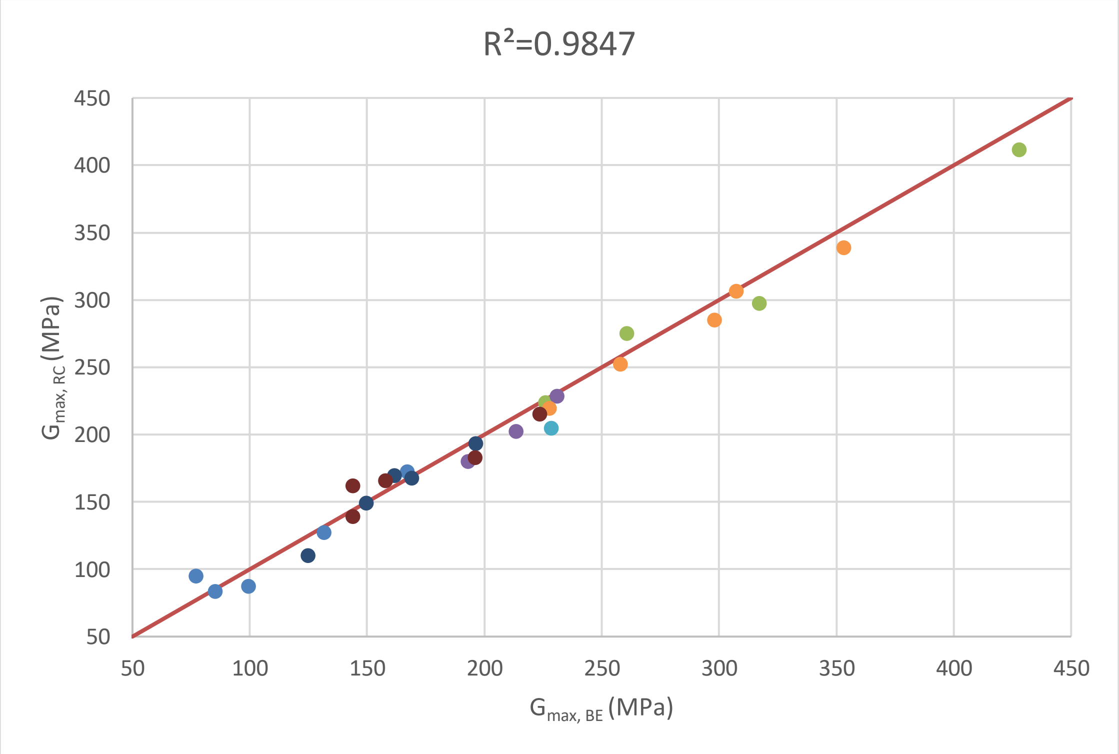

Figure 89. *Comparison of maximum shear modulus between bender elements and resonant column*

4.9 Proposing equations for determining very small strain shear stiffness of Viasvesi sand

A proposition will be done to define the very small strain shear stiffness for Viasvesi sand. Earlier it is mentioned test 6, 7 and 8 are not comparable with test 9, 10, 11, 12 and 13. Therefore, this line remains followed and two equations will be proposed. Test 6, 7 and 8 will be compared to resonant column data because data from bender elements is missing in test 7 and 8. Additionally, test 9, 10, 11, 12 and 13 will be compared to data collected via bender elements.

Figure 29 [15] in section 2.2.5 shows *OCR* does not have a negligible effect on Drammen clay. This line is also found by the tested Viasvesi sand, which is in contradiction with what [14] mentions. [14] mentions *OCR* has a neglectable effect on G_{max} by non-plastic soils. Because *OCR* is noticed to not have a negligible effect in this research, it is introduced in equation (54) and (55). A possible explanation that *OCR* has an effect on the stiffness is that deformations of the grain structure occur, which might cause the grains to have more or better localized contacts and restraints, which is also noticed by [15]. Therefore *OCR* might have an increasing effect on the stiffness of the tested soil.

The equation for test 6, 7 and 8 will have the form, as given in equation (54):

$$\boldsymbol{G_{max} = A * \frac{(x-e)^2}{1+e} * \frac{p'^n}{p'_a{}^n} * OCR^m} \tag{54}$$

For test 6, 7 and 8:

$$\boldsymbol{A = 323.2734}$$

$$\boldsymbol{x = 1.4335}$$

$$\boldsymbol{m = 0.1046}$$

$$\boldsymbol{n = 0.4921}$$

The equation for test 9, 10, 11, 12 and 13 will have the form, as given in equation (55):

$$\boldsymbol{G_{max} = A * \frac{(x-e)^2}{1+e} * p'^n * p'_a{}^{(1-n)} * OCR^m} \tag{55}$$

For test 9, 10, 11, 12 and 13:

$$\boldsymbol{A = 28.8202}$$

$$\boldsymbol{x = 1.0028}$$

$$\boldsymbol{m = 0.1286}$$

$$\boldsymbol{n = 0.3850}$$

With the overconsolidation as mentioned in [65]:

$$OCR = \frac{p'}{\sigma'_m}.$$

Where

p' is the maximum occured pressure in the sample

σ'_m is the pressure step of the calculation

Additionally, Table 29 gives an overview of the *OCR* used during the calculations.

Table 29. *OCR for different pressure steps*

Step	P' (kPa)	OCR (-)
First	50	2
Second	100	1
Third	300	0.33
Fourth	100	3
Fifth	50	6

It can be noticed equation (54) looks similar to a combination of equation (2) and (4). Next, equation (55) looks similar to equation (4). Therefore it might be concluded that (2) and (4) are good equations to base on to define new equations for different sands.

The result of equation (54) for test 6, 7 and 8 is plotted in Figure 90, compared to the values received via the resonant column. As can be seen in Figure 90, an R^2 value of 0.9218 is received with equation (54). Additionally, equation (55) is plotted in Figure 91 for test 9, 10, 11, 12 and 13 and it can be seen in Figure 91 the proposed equation matches with an R^2-value of 0.9361.

Additionally, Figure 92 and Figure 93 show the curves from equation (54) respectively equation (55) compared to different test data and different void ratios. As can be seen, the data in both Figure 92 and Figure 93 can be noticed a lower void ratio, means a higher stiffness is received. Besides, a higher effective confining pressure means a higher stiffness. This is noticed both by the conducted tests and the proposed equations.

It needs to be noted the test data with void ratio 0.60 (test 11) and 0.64 (test 9) in Figure 93 deviate from the rest of the data. A possible explanation might be that, due to the problem that the used caliper sometimes changes incorrect, one of the diameters is measured wrong. Therefore, the density and void ratio might have been determined incorrect.

Compared to the R²-values from equation (2), (4) and (5) as shown in Figure 88, the proposed equations (54) and (55) have a higher reliability for Viasvesi sand, as shown in Figure 90 and Figure 91.

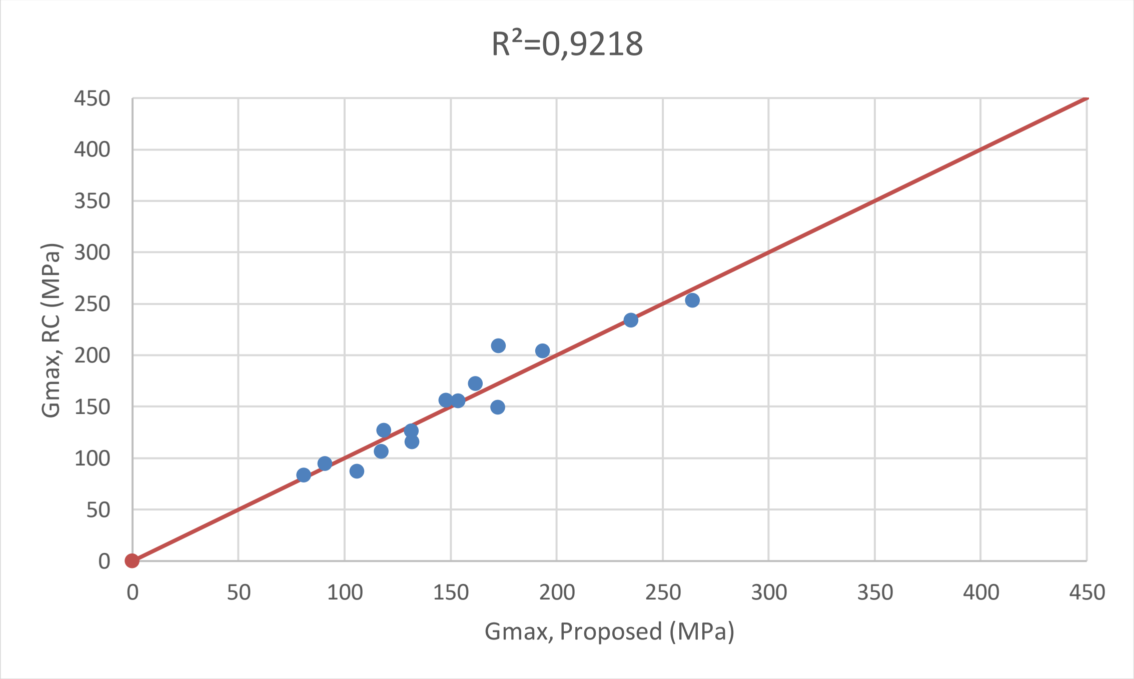

Figure 90. *Test 6, 7 and 8 compared to the proposed equation (54)*

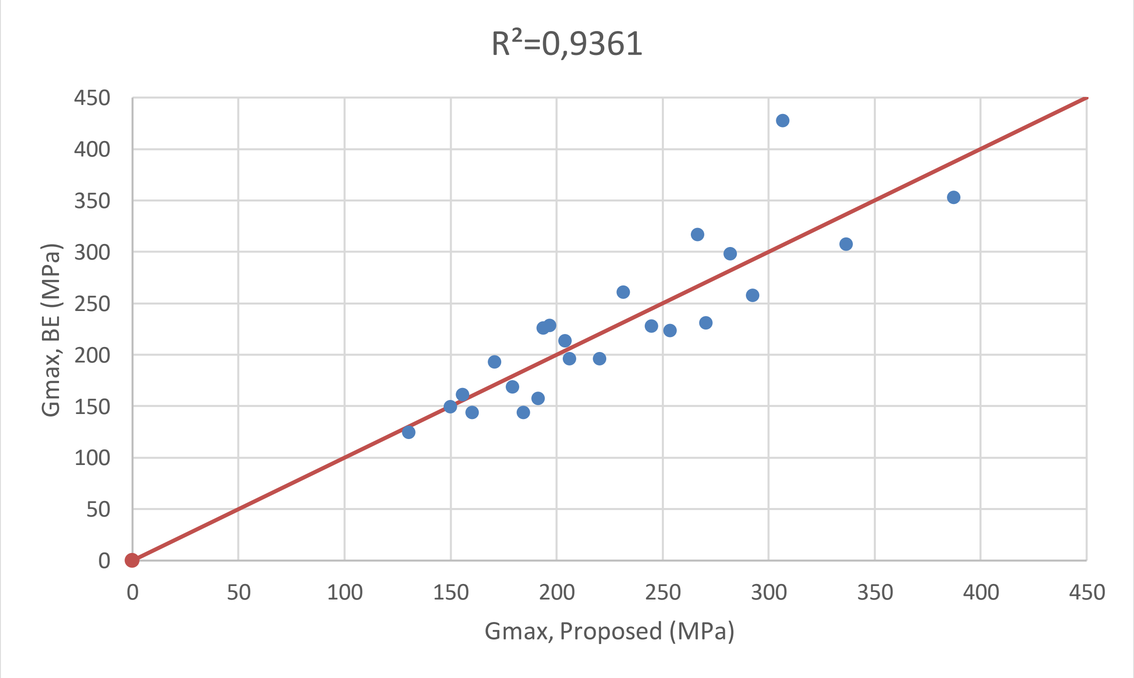

Figure 91. *Test 9, 10, 11, 12 and 13 compared to the proposed equation (54)*

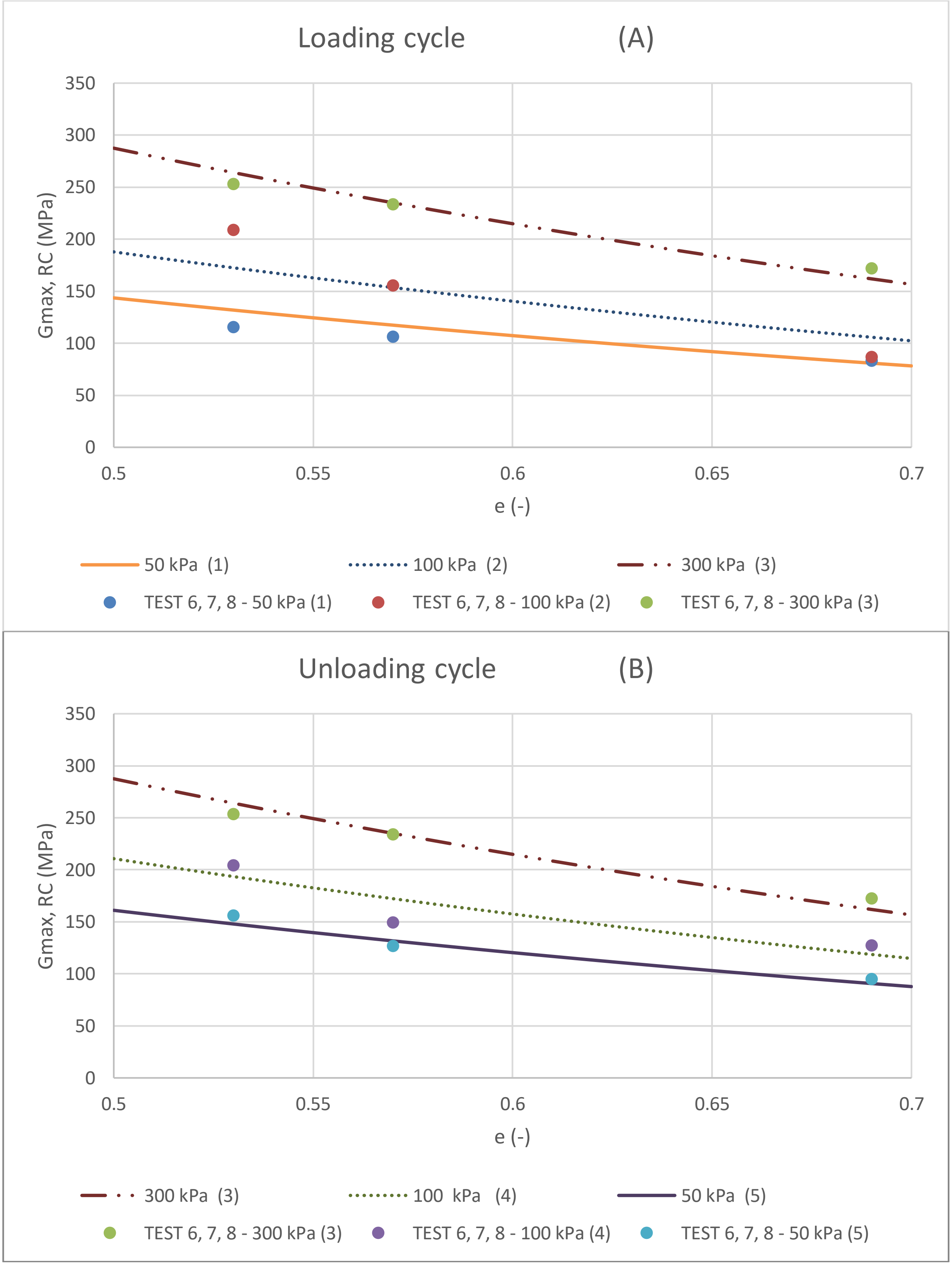

Figure 92. *Loading and unloading cycle compared with equation (54) for test 6, 7 and 8*

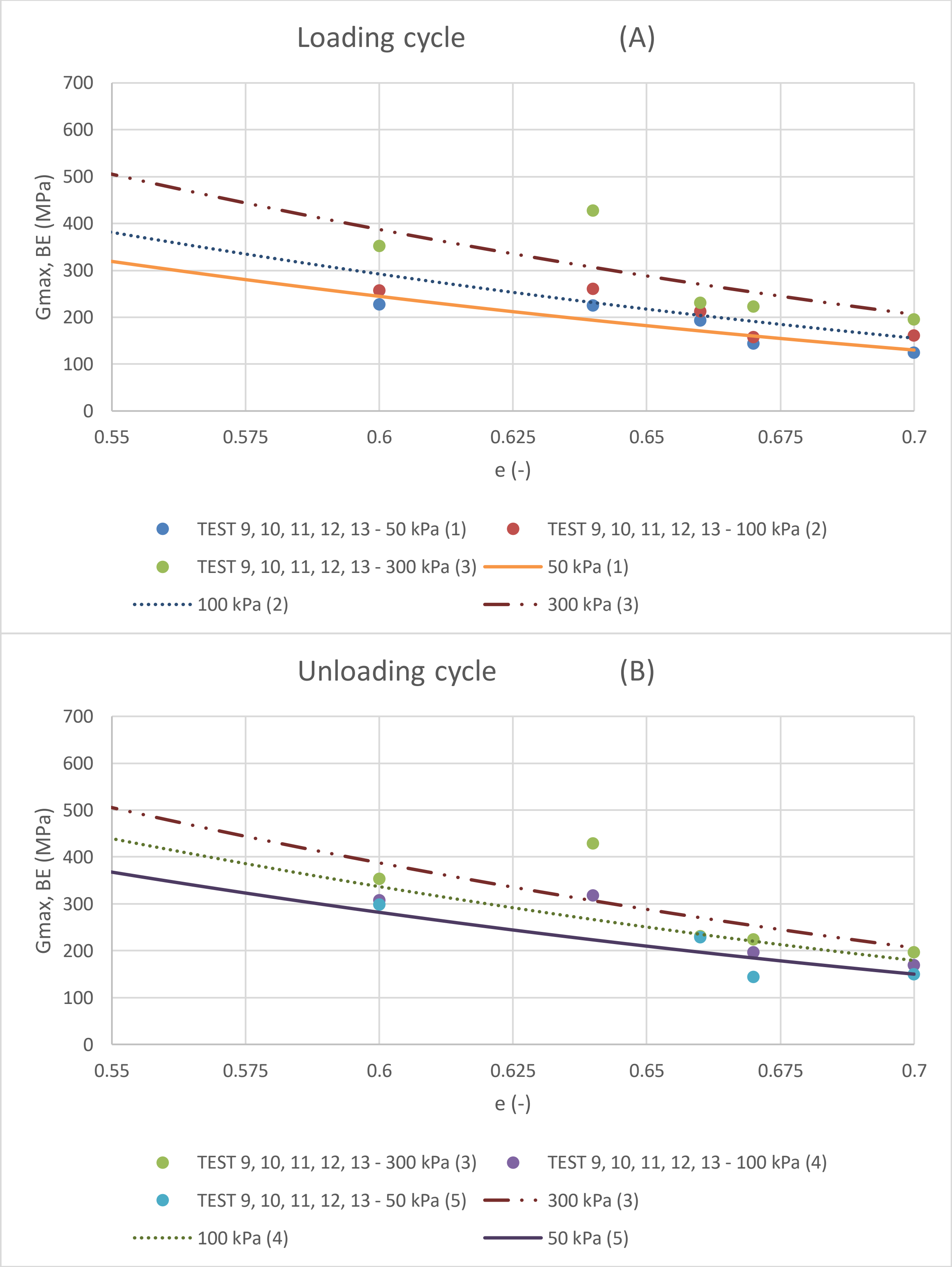

Figure 93. *Loading and unloading cycle compared with equation (55) for test 9, 10, 11, 12 and 13*

5. DISCUSSION

5.1 Occurred difficulties

During the testing series a lot of difficulties occurred. First of all, the difficulties regarding the bender elements will be discussed. Additionally, the difficulties regarding the resonant column will be briefly discussed. Next to this, a few global problems will be discussed.

Regarding the bender elements, it was noticed the piezoceramic elements are very vulnerable. First of all, the bender elements in the original set up had to be changed because they did not work anymore. Because of this, the elements came out of the top and pedestal for a longer distance, which made them more vulnerable. Due to this, an element was broken again. Additionally, after performing a resonant column measurement, a bender element got also broken once. The problem which occurred when a bender element got broken is that it took up to 30 hours to repair it, because a waiting time had to be respected to repair it.

Next to the vulnerability of the bender elements, the problem occurred that with the used function generator it is only possible to send one frequency. Due to this it was hard to define where the point had to be taken to define the first time of arrival and peak to peak method. The first time of arrival was still possible, but it seemed impossible to define the peak to peak and therefore this method is not used. Regarding the send amplitude no problems occurred.

Performing the resonant column test was an elaborate task. First of all, the device had to be calibrated. This is done according to ASTM D 4015-15 [49]. The problem with this standard is that it is very complicated. It took a long time before it was fully understood how to calibrate the device. Due to learning to work with this standard and because the stress in the springs in the resonant column had been changed because the device stopped working, the calibration of the resonant column had to be done over a few times, both with and without calibration rod.

Next, it was hard to make a working program to calculate the actual shear stiffness according to ASTM D 4015-15 [49]. The problem hereby was that a lot of equations had to be used, and a complex number had to be calculated iterative.

Once the actual resonant column tests started, it was hard to learn to know what to measure and which parameters had to be changed. Eventually this took a while before a first ‘good’ stiffness reduction curve was obtained from the measurements, because trial and error had to be done.

To keep the triaxial cell in balance a contra-weight is used. Nevertheless, this weight needed to be changed when the pressure cell was at its place, to bring the motor in balance with this contra-weight. A few samples got crushed because the correct weight to keep the motor in balance had to be searched, or because something went wrong during changing the contra-weight.

Sometimes during saturating the sample, it occurred because of a damaged membrane, the pore water pressure kept increasing in the Skempton-B measurements. In the beginning, it was not known the cause was a damaged membrane, which caused loss of time because after a while oil or air started to leak through the burette.

Another problem which occurred in every test, was an oil leakage through the connections between the different parts of the cell. When the pressure increased, more oil started to leak. This is caused by the rubber ring used to close the cell. Because it had too big dimensions, a band had to be cut off a roll. This caused the problem it did not fully conceal the bottom part from the top part of the cell. Due to this, at the locations where a leakage was noticed, a scale was placed to try to catch as much oil as possible to try to reuse it later.

Additionally, it was told to try to prepare samples with the wet pluviation method. The problem with this method is that even when an increased static load is used, the samples do not get densified enough. Therefore, after a while the preparing method is changed to moist tamping, which is faster, less elaborate and easier to get a wider range of densities.

5.2 Resonant column tests

5.2.1 Shear modulus reduction for Viasvesi sand

It can be concluded via Figure 68 soil has a memory, as well known in soil mechanics, when neglecting the 100 kPa cycles in test 7 and 10 (respectively Figure 68 (B) and (E)). The unloading step on a same pressure has a higher stiffness then the first step on this pressure. This is interesting, because by loading and unloading a soil you can make it react stiffer, and thus resist higher loads in a later stage, during service. Additionally, this might also be useful during excavations.

With caution taken into mind because the data in Figure 69 and Figure 70 is not significant enough, it can be concluded soil reacts stiffer until higher strain levels during unloading cycles, compared to the loading cycles. A possible explanation for this might be that relocation occurs during the consolidation in the grain structure. Therefore, the soil will deform less during unloading and thus reacts stiffer until higher strains.

As Figure 71 shows clearly, the stiffness is higher in every pressure step with lower void ratio. Additionally, Figure 72 shows the same as Figure 71, except a small deviation with a reversed effect occurs in Figure 72 (test 9) and (test 11). An explanation for this deviating data is that the caliper sometimes changes incorrect. Therefore, the diameter might have been measured wrong by one of these two tests, and thus the density and void ratio might have been determined incorrect. Though, the rest of the data - test 6, 7, 8, 10, 12 and 13 - follow the expectations. This effect can be explained by lower void ratios, more contact points are occurring in the sample, which lets the sample react stiffer. Additionally, the contact points might also be localized at better positions, which might also let the samples react stiffer.

5.2.2 Normalized shear modulus reduction with normalisation with resonant column for Viasvesi sand

From the data of Figure 74 and Figure 75 it is hard to draw a conclusion. It is both by 50 and 100 kPa that the unloading cycle starts to decrease at a higher strain level approximately the same amount of times as the loading cycles starts to decrease at a higher strain level. Next to this, test 10 (Figure 74 (E) and Figure 75 (E)) starts to decrease by both 50 kPa curves at the same strain level. An explanation might be that more parameters play a role in determining the shear modulus reduction curves. By example *OCR* plays a role, but also *p'*, *e* and C_u might play a role. Therefore, when all these parameters their effect are cumulated, they might affect each other differently. Possibly due to this reason, no correlation is found between the curves.

About the inclination of the curves it is actually possible to draw a conclusion. Most curves are parallel to each other, although they start to decrease at different strain levels. Therefore, it can be stated that the curves should have the same inclination during resonant column tests.

According to Figure 18 [15], G/G_{max} needs to start to decrease at higher strains, when tests are conducted with higher void ratios. Figure 76 shows the reversed effect, which might be caused because [15] only changes the void ratio, while other parameters (for example the strength and *OCR*) are kept constant. Therefore the effect of changing the void ratio is studied on a constant failure point. This constant failure point is not the case in laboratory tests, and therefore this curve is only comparable to see what the influence is from the void ratio. Actually more parameters change during an actual test, which might cause Figure 76 to be the real behaviour that needs to be expected.

Additionally, Figure 77 gives no more information about the correlation between the void ratio and the normalized shear modulus reduction. An explanation for this is that during the testing series some major problems occured, for example inaccurate reading the different graphs on the computer, which cause the data to have no correlation.

5.2.3 Normalized shear modulus reduction with normalisation with bender elements for Viasvesi sand

Figure 78 shows the difference between the normalized shear modulus reduction curves during different pressure steps for each test, normalized with G_{max} determined with bender elements. As shown in Figure 2 [16] and Figure 30 [15], a relation should be noticed between the curves in Figure 78. In Figure 2 [16], at low plasticity indexes, as for sand is the case, the normalized curves start to decrease at higher strain levels when higher confining pressures are initiated. This is something that should have been noticed during the testing series. Additionally, Figure 30 [15] mentions the normalized curves from low plastic clays should decrease at higher strain levels when overconsolidated clays are studied. This would mean during the unloading steps, the normalized shear modulus decreases at higher strain levels compared to the virgin loadings.

What can be noticed in this data is that in test 6, 9, 11 and 12, respectively Figure 78 (A), (B), (D) and (E), the 300 kPa cycle starts to decrease at the lowest strain level. This is against expectations, where the normalisation of 300 kPa should come after the loading 100 kPa, which should come after the loading 50 kPa, as earlier explained by Figure 2 [16]. An explanation might be that measurements in the 300 kPa pressure step start at lower strains, which causes to give a higher resonant column value during this strain level. Additionally, other curves are only measured in the stiffness-decreasing part of the curve, which causes the normalisation to be not complete. A possible cause that these curves are only shown in the stiffness decreasing part is, as Figure 89 shows, the bender elements give slightly higher maximum shear moduli compared to the resonant column and therefore the normalized part is different. Next to this, some curves have a horizontal part, but the decrease of the stiffness starts at a higher strain level, but in an order which is not expected, according to Figure 2 [16]. Therefore, no conclusion can be drawn out of Figure 78.

If looked to test 10, 11 and 13, respectively Figure 79 (C), (D) and (F), a possibility exists the unloading curve needs to decrease at a higher strain level than the loading curve. Caution should be taken with this conclusion, because test 11 and 13 both have a curve without horizontal part, and thus have no part with ‘constant’ stiffness. Nevertheless, this theory is confirmed by analysing theoretical data in Figure 30 [15], where higher overconsolidation ratios decrease at higher strain levels.

Confirming the conclusion of Figure 79 via Figure 80 is hard, because not much useable data is available. Therefore, to draw a conclusion is mainly looked at Figure 79.

5.3 Bender element tests

Figure 82, Figure 85 and Figure 86 show a stiffer reaction during unloading, which can be explained by consolidation. Due to deformation of the particle structure, more contact points are available. This causes more restraints or better localized, and thus a stiffer reaction.

Additionally, a lower value of stiffness measured via the bender elements at the end of a cycle is noticed. This higher stiffness can be explained as follows: the resonant column loads the sample at different frequencies and amplitudes. Due to this, when a measurement is done at the end of the cycle, a certain disturbance might have occurred, for example less good contact between the soil and bender elements. Therefore, when a second measurement is done, it takes a longer time to receive a good signal.

5.4 Comparison of G_{max} from bender elements, resonant column and predictions

As noticed in the section 4.8, a general line was found between the maximum stiffness obtained by the tests and the equation of ‘Wichtmann and Triantafyllidis (4)’, ‘Menq (2)’ and ‘Senetakis et al. (5)’. It can be concluded all three equations give acceptable accuracy, as Figure 88 shows clearly that most predicted values are lower compared to the testing series. Although, ‘Wichtmann and Triantafyllidis (4)’ – with the highest R^2-value of 0.3701 - is in most cases the most correct equation, as Figure 88 shows. All three equations give a less stiff result compared to the reality, or in a single case a comparable value.

Additionally, Figure 89 gives a view about the difference between G_{max} obtained with the resonant column and the bender elements. As can be seen, the results stroke with each other, which can indicate that the measurements are done correctly. Next, it is possible to see in Figure 89 the bender elements give slightly higher results compared to resonant column, which is also noticed in previous conducted research, such as [43]. This might be a possible reason why the normalization via G_{max} from the bender elements is slightly deviating from the normalization via G_{max} from the resonant column tests.

5.5 Proposition of equation to determine very small strain shear stiffness of Viasvesi sand

It can be concluded both equation (54) and (55) matches in both cases with the measurements. This can be stated because data shown in both Figure 90 and Figure 91 have a R^2 above 0.90. Therefore both equations match with the testing data.

Additionally, equation (54) and (55) are more reliable compared to equation (2), (4) and (5), which are not fully correct to use for Viasvesi sand. This can be explained because these equations are proposed for more general use. For example, equation (4) is proposed to be useable for uniformity coefficients of 1.5 to 15 and d_{50} of 0.1 to 6 mm. Due to these wide ranges of uniformity coefficients and d_{50}, it is very hard to propose an equation which is correct for every type of sand. In comparison, the used Viasvesi sand during these testing series has a coefficient of uniformity of 2 and d_{50} is 0.5 mm. Therefore it can expected that due to the limited range of these 2 parameters, equation (54) and (55) are more reliable. In addition, equation (54) and (55) take the OCR in account, which makes them more correct.

6. CONCLUSIONS

During the tests, loading and unloading resonant column and bender element measurements are done on Viasvesi sand, which is a uniform sand. The resonant column is mainly used to define the shear modulus reduction curve, while the bender elements are used to define the maximum shear stiffness G_{max}. The tests are conducted on a wide range of void ratios. $(Test\ 6, 7, 8\text{: } e = 0.53\ to\ 0.69;\ Test\ 9, 10, 11, 12, 13\text{: } e = 0.60\ to\ 0.70)$.

With the resonant column tests, in Figure 68 the 300 kPa has in all cases the highest stiffness. Additionally, the loading cycle of 50 kPa has the lowest stiffness in all cases. Besides, in most cases the unloading 50 kPa has the second lowest stiffness, followed by loading and unloading 100 kPa. The bender elements follows the same line as the resonant column, where is noticed the G_{max} by the unloading cycles is higher compared to the loading cycles. Due to this, it can be concluded from the shear modulus reduction curves and the maximum shear modulus, soil has a ’memory’. Besides, Figure 69 and Figure 70 makes clear with a bit of caution due to some insignificance in the data, the sand reacts stiffer until higher strain levels during unloading cycles. An explanation is due to consolidation the grain structure deforms. Therefore the soil will become less deformable due to more or better localized restraints, which causes the sand to react stiffer during unloading.

Additionally, in Figure 71 and Figure 72 the sand reacts stiffer at lower void ratios. An explanation might be that more contact points occur by lower void ratios. Therefore, a higher resistance occurs against deformation.

When data received via the resonant column gets normalized, the results become less certain. First of all, no clear relation can be found between the measurements on different pressures at a constant void ratio, which is in contradiction with Figure 2 [16].

Besides, in Figure 74 and Figure 75 the data of the loading and unloading cycle at the same effective confining pressure is plotted next to each other. It is noticed both loading and unloading start to decrease approximately the same amount of times at a higher strain level. An explanation is that more parameters influence each other, which might make the results fluctuating. Therefore, a cumulation of effects can occur, which have a differing influence in different situations.

Additionally, Figure 76 and Figure 77 show stiffness reduction curves at a constant *p’*, with different *e*. In Figure 77, for test 9 to 13, no correlation is found. Next to this, Figure 76 shows that with increasing void ratio, the strain level at which the decrease of the curve becomes pronounced, is lower. This is in contradiction with Figure 18 [15], where the reversed effect occurs. An explanation for this is that [15] only changes the void ratio, with as few as possible other parameters. In reality more parameters change when something is changed in the set up. Therefore it is possible the outcome in this research is correct. Besides, the effect in Figure 77 is possibly explainable by some errors conducted during conducting the measurements.

In some cases a second measurement is done with the bender elements at the end of a pressure cycle. It is noticed at 100 kPa effective confining pressure the second measurement always had a lower stiffness compared to the measurement immediately after consolidation. It can be concluded that due to disturbance because of the resonant column, an irregularity occurs, which makes the sample react less stiff. This is for example a loss of good contact between the sand sample and the bender elements. At the 50 kPa cycles, this effect is less pronounced, which is possibly explainable by lesser support from the confining fluid and higher *OCR*.

The data received via the bender elements and resonant column tests are compared to equations (2), (4) and (5). One general line was hereby found: all 3 equations underestimate the stiffness and are therefore acceptable to use, although equation (4) is the most correct equation with $R^2 = 0.3701$. Additionally, the values received with the resonant column and bender elements are comparable with each other. Hereby, $R^2 = 0.9847$ is received. Therefore, it is possible to conclude that G_{max} is determined correct, although the bender elements give slightly higher stiffness values compared to the resonant column tests.

Finally, 2 equations (54) and (55) are proposed for the certain Viasvesi sand. Equation (54) is proposed for test 6, 7 and 8 and gives $R^2 = 0.9218$ compared with the G_{max} obtained via the resonant column, while equation (55) is proposed for test 9 to 13 and gives $R^2 = 0.9361$ compared with G_{max} obtained via bender elements. Therefore both equations are acceptable to use, because stiffness parameters determined with resonant column tests and bender elements can have a deviation up to 20 %. Compared to equations (2), (4) and (5), equation (54) and (55) are much more reliable to use on Viasvesi sand, because of the limited range of the grain size distribution wherefor they are proposed.

7. FUTURE (RESEARCH) POSSIBILITIES

During the research, it was first planned to do research both on isotropic and anisotropic loadings. Due to some problems which occurred, measurements in anisotropic stress states are not conducted. Therefore this is something that can be done in future research.

Next, it can be useful to determine the minimum and maximum void ratio of the used Viasvesi sand. When these two parameters are determined, it is possible to define the relative density, which makes it possible to define how wide the range of void ratios can be during the testing series. Additionally, it might be useful to do triaxial tests to define the friction angle of the certain sand.

Next, as not all collected data during this research is consistent, it is useful to conduct more tests on Viasvesi sand. In this case it is possible to see if more consistent data can be found or that the irregularities are something that can be noticed by more measurements.

Besides, it was not always easy to declare if resonance was reached. Next, it was not always easy to read the graph with the phase shift, voltage input and acceleration accurately enough. Therefore, it might be useful, if possible, to automate the computer program to determine the data for the resonant column. In this case, the data will be less dependent on the user of the set-up. Additionally, it might be useful to make a program to define the traveling time of the shear wave by the bender elements (APTP, MPTP, MFTOA). With the oscilloscope, it is possible to define the travel time, but you have to keep your mind more at what you are doing, while with the device where I learned to work with the bender elements, it is much easier to define the point of FTOA and PTP, without deleting the data by pressing on a wrong button.

To make it easier to work with the contra-weight, it can be useful to edit the set-up from the cell. Now, mass needs to be taken away or added manually, while it can be possible to make a set-up to lift the mass so it does not influence the contra-weight while doing tests. Additionally, this can make it possible to initiate anisotropic stress states easier.

If the used set-up is used later, it might be useful to replace it to a place where it is possible to walk completely around the table. At the current location, it is hard to manipulate some places of the cell. This was for example a problem while connecting the top- and bottom part of the cell with bolts.

REFERENCES

[1] ‘Fig. 1 Normalized stiffness degradation curve’, *ResearchGate*. https://www.researchgate.net/figure/Normalized-stiffness-degradation-curve_fig1_333479368 (geraadpleegd 20 april 2022).

[2] ‘NBN EN ISO 14688-1’. Bureau voor Normalisatie, 23 maart 2018. Geraadpleegd: 12 november 2021. [Online]. Beschikbaar op: https://edu.mynbn.be/nbnframework/index.php/pdfMeta/RO/568930?l=E

[3] ‘ISO 14688-1’. 2017. Geraadpleegd: 19 januari 2022. [Online]. Beschikbaar op: https://www.sis.se/api/document/preview/80000191

[4] T. Wichtmann, M. A. Navarrete Hernández, en T. Triantafyllidis, ‘On the influence of a non-cohesive fines content on small strain stiffness, modulus degradation and damping of quartz sand’, *Soil Dynamics and Earthquake Engineering*, vol. 69, pp. 103–114, feb. 2015, doi: 10.1016/j.soildyn.2014.10.017.

[5] A. Souto, J. Hartikainen, en K. Özüdoˇgru, ‘Measurement of dynamic parameters of road pavement materials by the bender element and resonant column tests’, *Géotechnique*, vol. 44, nr. 3, pp. 519–526, sep. 1994, doi: 10.1680/geot.1994.44.3.519.

[6] J. Knappett en R. F. Craig, *Craig’s Soil Mechanics*, 9de dr. London: CRC Press, 2019. doi: 10.1201/9781351052740.

[7] ‘NBN EN ISO 14688-2’. Bureau voor Normalisatie, 23 maart 2018. Geraadpleegd: 12 november 2021. [Online]. Beschikbaar op: https://edu.mynbn.be/nbnframework/index.php/pdfMeta/RO/568933?l=E

[8] ‘Engineering soil classification according to EN ISO 14688-2’. [Online]. Beschikbaar op: http://w.casopis-gradjevinar.hr/assets/Uploads/JCE-70-2018-10-3-2437-EN.pdf

[9] K. Gabryś, E. Soból, W. Sas, R. Šadzevičius, en R. Skominas, ‘Warsaw Glacial Quartz Sand with Different Grain-Size Characteristics and Its Shear Wave Velocity from Various Interpretation Methods of BET’, *Materials*, vol. 14, nr. 3, Art. nr. 3, jan. 2021, doi: 10.3390/ma14030544.

[10] ‘astm_d-2487_classification_of_soils_for_engineering_purposes_unified_soil_classification_system.pdf’. Geraadpleegd: 23 november 2021. [Online]. Beschikbaar op: https://lauwtjunnji.weebly.com/uploads/1/0/1/7/10171621/astm_d-2487_classification_of_soils_for_engineering_purposes_unified_soil_classification_system.pdf

[11] ‘NBN EN 933-1’. Bureau voor Normalisatie, 2012. Geraadpleegd: 19 november 2021. [Online]. Beschikbaar op: https://edu.mynbn.be/nbnframework/index.php/pdfMeta/RO/436710?l=E

[12] ‘EN 933-1’. 1997. Geraadpleegd: 19 januari 2022. [Online]. Beschikbaar op: https://baixardoc.com/download/en-933-1-tests-for-geometrical-properties-of-aggregates-5ccdf6765c4ff?hash=dcd4f9a2deedd2f6ff9926b894379dc2

[13] ‘NBN EN 933-2’. Bureau voor Normalisatie, 2020. Geraadpleegd: 19 november 2021. [Online]. Beschikbaar op: https://edu.mynbn.be/nbnframework/index.php/pdfMeta/RO/582383?l=E

[14] T. Benz, ‘small-strains stiffness of soils and its numerical consequences’. 2006.

[15] T. Länsivaara, ‘A study of the mechanical behavior of soft clay’, 1999. doi: 10.13140/RG.2.1.2842.0641.

[16] ‘(ASCE)0733-9410(1992)1185(830.pdf’. Geraadpleegd: 26 november 2021. [Online]. Beschikbaar op: https://ascelibrary-org.kuleuven.e-bronnen.be/doi/pdf/10.1061/(ASCE)0733-9410(1992)118%3A5(830.2)

[17] T. Wichtmann en T. Triantafyllidis, ‘Influence of the Grain-Size Distribution Curve of Quartz Sand on the Small Strain Shear Modulus Gmax’, *Journal of Geotechnical and Geoenvironmental Engineering*, vol. 135, nr. 10, pp. 1404–1418, okt. 2009, doi: 10.1061/(ASCE)GT.1943-5606.0000096.

[18] K. H. Stokoe en D. G. Anderson, ‘Shear Modulus: A Time-Dependent Soil Property’. https://www.astm.org/stp35672s.html (geraadpleegd 27 januari 2022).

[19] D. C. F. LO PRESTI, ‘Rate and creep effect on the stiffness of soils’, *Measuring and Modeling Time Dependent Soil Behavior, Geotech. Special Publication*, vol. 61, pp. 166–180, 1996.

[20] G. Masing, *Eigenspannungen und Verfestigung beim messing*. Zurich, 1926.

[21] L. Matešić en M. Vucetic, ‘Strain-Rate Effect on Soil Secant Shear Modulus at Small Cyclic Strains’, *Journal of Geotechnical and Geoenvironmental Engineering*, vol. 129, nr. 6, pp. 536–549, jun. 2003, doi: 10.1061/(ASCE)1090-0241(2003)129:6(536).

[22] M. Payan, A. Khoshghalb, K. Senetakis, en N. Khalili, ‘Effect of particle shape and validity of Gmax models for sand: A critical review and a new expression’, *Computers and Geotechnics*, vol. 72, pp. 28–41, feb. 2016, doi: 10.1016/j.compgeo.2015.11.003.

[23] T. Wood, ‘On the Small Strain Stiffness of Some Scandinavian Clays and Impact on Deep Excavation - ProQuest’. https://www.proquest.com/openview/827d2320d5d37e71f98b56ca2bf07d72/1?cbl=18750&diss=y&pq-origsite=gscholar&accountid=17215 (geraadpleegd 26 november 2021).

[24] S. K. Saxena en K. R. Reddy, ‘Dynamic Moduli and Damping Ratios for Monterey No. 0 Sand by Resonant Column Tests’, *Soils and Foundations*, vol. 29, nr. 2, pp. 37–51, jun. 1989, doi: 10.3208/sandf1972.29.2_37.

[25] FY. Menq, ‘Dynamic properties of sandy and gravelly soils’. University of Texas at Austin, 2003.

[26] T. Wichtmann en T. Triantafyllidis, ‘Stiffness and Damping of Clean Quartz Sand with Various Grain-Size Distribution Curves’, *Journal of Geotechnical and Geoenvironmental Engineering*, vol. 140, nr. 3, p. 06013003, mrt. 2014, doi: 10.1061/(ASCE)GT.1943-5606.0000977.

[27] ‘The Small-Strain Shear Modulus and Damping Ratio of Quartz and Volcanic Sands’. https://www.astm.org/gtj20120073.html (geraadpleegd 27 januari 2022).

[28] H. B. Seed, R. T. Wong, I. M. Idriss, en K. Tokimatsu, ‘Moduli and Damping Factors for Dynamic Analyses of Cohesionless Soils’, *Journal of Geotechnical Engineering*, vol. 112, nr. 11, pp. 1016–1032, nov. 1986, doi: 10.1061/(ASCE)0733-9410(1986)112:11(1016).

[29] X. Chen en J. Zhang, ‘Influence of Relative Density on Dilatancy of Clayey Sand–Fouled Aggregates in Large-Scale Triaxial Tests’, *Journal of Geotechnical and Geoenvironmental Engineering*, vol. 142, nr. 10, p. 06016011, okt. 2016, doi: 10.1061/(ASCE)GT.1943-5606.0001542.

[30] M. Keramatikerman en A. Chegenizadeh, ‘Effect of Particle Shape on Monotonic Liquefaction: Natural and Crushed Sand’, *Exp Mech*, vol. 57, nr. 8, pp. 1341–1348, okt. 2017, doi: 10.1007/s11340-017-0313-z.

[31] B. Ruan, Y. Miao, K. Cheng, en E. Yao, ‘Study on the small strain shear modulus of saturated sand-fines mixtures by bender element test’, *European Journal of Environmental and Civil Engineering*, vol. 25, nr. 1, pp. 28–38, jan. 2021, doi: 10.1080/19648189.2018.1513870.

[32] M. Goudarzy, N. Rahemi, M. M. Rahman, en T. Schanz, ‘Predicting the Maximum Shear Modulus of Sands Containing Nonplastic Fines’, *Journal of Geotechnical and Geoenvironmental Engineering*, vol. 143, nr. 9, p. 06017013, sep. 2017, doi: 10.1061/(ASCE)GT.1943-5606.0001760.

[33] J. I. Sun, R. Golesorkhi, en H. B. Seed, ‘DYNAMIC MODULI AND DAMPING RATIOS FOR COHESIVE SOILS’, p. 56.

[34] D. V. Okur en A. Ansal, ‘Stiffness degradation of natural fine grained soils during cyclic loading’, *Soil Dynamics and Earthquake Engineering*, vol. 27, nr. 9, pp. 843–854, sep. 2007, doi: 10.1016/j.soildyn.2007.01.005.

[35] S. Seyedan en W. Sołowski, ‘A coupled constitutive model for modelling small strain behaviour of soils’, 2018. doi: 10.1201/9781351003629-79.

[36] R. L. Kondner, ‘Hyperbolic Stress-Strain Response: Cohesive Soils’, *Journal of the Soil Mechanics and Foundations Division*, vol. 89, nr. 1, pp. 115–143, feb. 1963, doi: 10.1061/JSFEAQ.0000479.

[37] ‘2001_01_0063.pdf’. Geraadpleegd: 8 mei 2022. [Online]. Beschikbaar op: https://www.issmge.org/uploads/publications/1/30/2001_01_0063.pdf

[38] R. L. Kondner, ‘Hyperbolic Stress-Strain Response: Cohesive Soils’, *Journal of the Soil Mechanics and Foundations Division*, vol. 89, nr. 1, pp. 115–143, feb. 1963, doi: 10.1061/JSFEAQ.0000479.

[39] R. Dyvik en T. S. Olsen, ‘Gmax measured in oedometer and DSS tests using bender elements’, 1989, pp. 39–42. Geraadpleegd: 8 mei 2022. [Online]. Beschikbaar op: http://pascal-francis.inist.fr/vibad/index.php?action=getRecordDetail&idt=6663766

[40] E. A. Suescun-Florez, ‘Development Of A Suction-controlled Resonant Column Apparatus With Self-contained Bender Elements’, jul. 2010, Geraadpleegd: 3 november 2021. [Online]. Beschikbaar op: https://rc.library.uta.edu/uta-ir/handle/10106/4955

[41] 'Introduction to Bender Element testing'. https://www.vjtech.co.uk/blog/introduction-to-bender-element-testing (geraadpleegd 20 oktober 2021).

[42] K. Özüdogru, 'Shear wave velocity measurements at the TTKK geotechnical laboratory'. Tampere University of Technology, 1991.

[43] Y. Cai, Q. Dong, J. Wang, C. Gu, en C. Xu, 'Measurement of small strain shear modulus of clean and natural sands in saturated condition using bender element test', *Soil Dynamics and Earthquake Engineering*, vol. 76, pp. 100–110, sep. 2015, doi: 10.1016/j.soildyn.2014.12.013.

[44] 'Dynamic laboratory testing facilities at the tampere university of technology geotechnical laboratory'. Tampere University of Technology. Geraadpleegd: 12 januari 2022. [Online]. Beschikbaar op: https://researchportal.tuni.fi/en/publications/dynamic-laboratory-testing-facilities-at-the-tampere-university-o

[45] 'NBN EN 13286-2'. https://edu.mynbn.be/nbnframework/index.php/pdfMeta/RO/360482?l=E (geraadpleegd 1 maart 2022).

[46] Mehedy Amin, *Wet Pluviation*, (26 januari 2021). Geraadpleegd: 31 januari 2022. [Online Video]. Beschikbaar op: https://www.youtube.com/watch?v=VHNFJIvXyuI

[47] VJTechLimited, *Triaxial Sample Preparation using Pluviation Method*, (21 augustus 2019). Geraadpleegd: 31 januari 2022. [Online Video]. Beschikbaar op: https://www.youtube.com/watch?v=4DS3OO-5LVU

[48] *Special procedures for testing soil and rock for engineering purposes*. ASTM International, 1970.

[49] 'ASTM-D4015-15'. ASTM International. Geraadpleegd: 17 januari 2022. [Online]. Beschikbaar op: https://www.astm.org/d4015-15.html

[50] J. H. Dane en C. G. Topp, *Methods of Soil Analysis, Part 4: Physical Methods*. John Wiley & Sons, 2020.

[51] 'NBN EN 1097-6'. Bureau voor Normalisatie, 2013. Geraadpleegd: 19 november 2021. [Online]. Beschikbaar op: https://edu.mynbn.be/nbnframework/index.php/pdfMeta/RO/491022?l=E

[52] 'SFS EN 1097-6'. https://online.sfs.fi/en/index/tuotteet/SFS/CEN/ID2/1/241372.html.stx (geraadpleegd 19 januari 2022).

[53] 'NBN EN 1097-3'. Bureau voor Normalisatie, 1998. Geraadpleegd: 19 november 2021. [Online]. Beschikbaar op: ://edu.mynbn.be/nbnframework/index.php/pdfMeta/RO/105442?l=E

[54] 'SFS EN 1097-3'. https://online.sfs.fi/en/index/tuotteet/SFS/CEN/ID2/1/177788.html.stx (geraadpleegd 19 januari 2022).

[55] J. Knappett en R. F. Craig, *Craig's Soil Mechanics*, 9de dr. London: CRC Press, 2019. doi: 10.1201/9781351052740.

[56] K. Thooft, *Grondmechanica*, 2020ste dr. ACCO.

[57] W. S. Kwan en C. E. Mohtar, 'A review on sand sample reconstitution methods and procedures for undrained simple shear test', *International Journal of Geotechnical Engineering*, vol. 14, nr. 8, pp. 851–859, nov. 2020, doi: 10.1080/19386362.2018.1461988.

[58] S. Zlatović en K. Ishihara, 'Normalized Behavior of very Loose Non-Plastic Soils: Effects of Fabric', *Soils and Foundations*, vol. 37, nr. 4, pp. 47–56, dec. 1997, doi: 10.3208/sandf.37.4_47.

[59] K. Thooft, 'Theoretisch-experimentele beschrijving van het spannings-vervormingsgedrag van onsamenhangende gronden onder uitwendige dynamische belastingen, in het bijzonder bij grote verglijdingen', dissertation, Ghent University, 1991. Geraadpleegd: 11 november 2021. [Online]. Beschikbaar op: http://hdl.handle.net/1854/LU-8561314

[60] W. Van Impe, 'Studie van het vervormingsgedrag van molzand onder cyclisch wisselende belastingen', dissertation, Ghent University, 1981. Geraadpleegd: 11 november 2021. [Online]. Beschikbaar op: http://hdl.handle.net/1854/LU-8536006

[61] 'Skempton's Pore Pressure Parameters', *Civil Engineering Notes*, 7 mei 2021. https://civilengineeringnotes.com/skemptons-pore-pressure-parameters/ (geraadpleegd 11 november 2021).

[62] M. Vernay, M. Morvan, en P. Breul, 'Evaluation of the degree of saturation using Skempton coefficient B', *Geomechanics and Geoengineering*, vol. 15, nr. 2, pp. 79–89, apr. 2020, doi: 10.1080/17486025.2019.1620349.

[63] S. Nordal, *BA8305 Geodynamics*. Norwegian university of Science and Technology, 2009.

[64] I. Sanchez-Salinero, J. M. Roesset, en I. I. Stokoe, 'Analytical Studies of Body Wave Propagation and Attenuation', TEXAS UNIV AT AUSTIN GEOTECHNICAL ENGINEERING

CENTER, sep. 1986. Geraadpleegd: 28 oktober 2021. [Online]. Beschikbaar op: https://apps.dtic.mil/sti/citations/ADA179487

[65] ‘Overconsolidation Ratio - an overview | ScienceDirect Topics’. https://www-sciencedirect-com.kuleuven.e-bronnen.be/topics/engineering/overconsolidation-ratio (geraadpleegd 26 april 2022).

APPENDIX A: SKEMPTON-B

	ΔU_c (kPa)	$\Delta \sigma_c$ (kPa)	B-value (-)
TEST 6	1.06	12.65	0.08
	1.24	13.05	0.10
	1.24	13.01	0.10
	1.10	13.02	0.08
	1.18	13.08	0.09
	1.30	13.08	0.10
	1.15	13.05	0.09
	1.25	13.05	0.10
	1.15	13.12	0.09
	1.16	13.01	0.09
	1.24	13.07	0.09
	1.19	13.03	0.09
	1.22	12.99	0.09
	1.24	13.14	0.09
	1.29	13.05	0.10
	1.27	13.19	0.10
TEST 7	1.13	10.24	0.11
	1.10	10.56	0.10
	1.12	10.65	0.11
	1.10	10.69	0.10
	1.18	10.63	0.11
	1.11	10.60	0.10
	1.20	10.62	0.11
	1.27	10.70	0.12
	1.15	10.66	0.11
	1.18	10.75	0.11
	1.19	10.65	0.11
	1.23	10.64	0.12
	1.09	10.62	0.10
	1.38	11.20	0.12
	1.62	11.69	0.14
	1.78	11.85	0.15
	1.68	11.82	0.14
	1.78	11.88	0.15
	1.79	11.96	0.15
	1.85	12.06	0.15
	1.72	11.98	0.14
	1.80	12.07	0.15
	1.83	11.77	0.16
	1.78	11.56	0.15
	1.76	11.94	0.15
	1.91	12.03	0.16
	1.84	11.96	0.15

	1.66	11.49	0.14
	1.77	12.02	0.15
	1.87	12.00	0.16
	1.87	12.02	0.16
	1.75	11.80	0.15
	1.62	11.57	0.14
	1.68	11.55	0.15
	1.72	11.63	0.15
	1.78	11.61	0.15
	1.70	11.73	0.14
	1.83	11.84	0.15
	1.78	11.77	0.15
	1.76	11.66	0.15
	1.70	11.45	0.15
	1.74	11.74	0.15
	1.87	11.96	0.16
	1.92	12.07	0.16
	1.87	11.96	0.16
	1.90	12.03	0.16
	1.85	12.09	0.15
	1.79	11.97	0.15
	1.86	11.93	0.16
	1.88	11.95	0.16
	1.72	11.88	0.14
	1.81	11.87	0.15
	1.75	11.76	0.15
	1.88	11.64	0.16
	1.64	11.65	0.14
	1.74	11.65	0.15
	1.84	11.91	0.15
	1.92	11.98	0.16
	1.92	11.93	0.16
	1.79	11.71	0.15
	1.71	11.71	0.15
	1.72	11.85	0.14
	1.93	11.96	0.16
	1.93	11.98	0.16
	1.92	11.98	0.16
	1.92	11.98	0.16
	1.85	11.74	0.16
	1.82	11.56	0.16
	1.74	11.72	0.15
TEST 8	1.54	9.25	0.17
	1.74	9.71	0.18
	1.82	9.75	0.19
	1.74	9.87	0.18
	1.81	9.84	0.18

	1.74	9.87	0.18
	1.65	9.85	0.17
	1.78	9.78	0.18
	1.82	9.79	0.19
	1.92	10.20	0.19
	2.01	10.34	0.19
	2.30	10.77	0.21
	2.38	11.09	0.21
	2.31	11.19	0.21
	2.30	11.02	0.21
	2.22	10.85	0.20
	2.25	10.72	0.21
	2.16	10.82	0.20
	2.13	10.82	0.20
	2.21	10.69	0.21
	2.19	10.70	0.20
	2.25	10.80	0.21
	2.20	10.69	0.21
	2.17	10.79	0.20
	2.32	11.12	0.21
	2.27	11.30	0.20
	2.32	11.06	0.21
	2.29	11.19	0.20
	2.33	11.18	0.21
	2.31	11.18	0.21
	2.38	11.10	0.21
	2.21	10.94	0.20
TEST 9	1.98	12.03	0.16
	2.13	11.95	0.18
	2.14	11.99	0.18
	2.27	12.02	0.19
	2.41	12.04	0.20
	2.36	12.03	0.20
	2.55	11.97	0.21
	2.73	11.96	0.23
	2.73	11.95	0.23
	2.86	11.95	0.24
	2.85	11.92	0.24
	2.96	11.92	0.25
	3.08	11.88	0.26
	3.39	12.15	0.28
	3.50	12.74	0.27
	3.75	12.87	0.29
	3.89	13.06	0.30
	4.12	13.26	0.31
	4.09	13.24	0.31
	4.31	13.37	0.32

	4.31	13.27	0.32
	4.27	13.17	0.32
	4.29	12.94	0.33
	4.46	13.04	0.34
	4.67	12.97	0.36
	4.72	13.11	0.36
	4.88	13.35	0.37
	4.91	13.23	0.37
	5.06	13.22	0.38
	5.10	13.24	0.38
	5.27	13.25	0.40
	5.35	13.24	0.40
	5.25	12.87	0.41
	5.36	13.05	0.41
	5.52	13.14	0.42
	5.62	13.12	0.43
	5.62	13.18	0.43
	5.71	12.99	0.44
	5.68	12.85	0.44
	5.95	13.23	0.45
	6.03	13.17	0.46
	6.15	13.14	0.47
	6.08	12.95	0.47
	6.08	12.81	0.47
	6.36	13.28	0.48
	6.43	13.23	0.49
	6.46	13.18	0.49
	6.51	12.84	0.51
	6.51	12.82	0.51
	6.58	12.91	0.51
	6.82	13.16	0.52
	6.79	13.24	0.51
	6.89	12.96	0.53
	6.92	12.75	0.54
	6.91	12.77	0.54
	6.91	12.82	0.54
	6.98	12.75	0.55
	7.24	12.86	0.56
	7.38	13.09	0.56
	7.52	13.15	0.57
TEST 10	1.14	12.82	0.09
	1.10	13.14	0.08
	1.39	13.35	0.10
	1.39	13.45	0.10
	1.28	13.50	0.10
	1.45	13.49	0.11
	1.36	13.54	0.10

	1.42	13.61	0.10
	1.39	13.48	0.10
	1.38	13.49	0.10
	1.41	13.58	0.10
	1.30	13.50	0.10
	1.42	13.55	0.10
	1.43	13.51	0.11
	1.55	13.81	0.11
	1.59	14.06	0.11
	1.74	14.35	0.12
	1.89	14.61	0.13
	1.94	14.68	0.13
	1.88	14.80	0.13
	2.02	14.86	0.14
	1.97	14.78	0.13
	1.99	14.77	0.13
	1.98	14.77	0.13
TEST 11	1.15	12.37	0.09
	1.16	12.31	0.09
	1.19	12.38	0.10
	1.33	12.93	0.10
	1.55	13.40	0.12
	1.71	13.64	0.13
	1.66	13.69	0.12
	1.68	13.67	0.12
	1.56	13.46	0.12
	1.46	13.28	0.11
	1.58	13.30	0.12
	1.46	13.33	0.11
	1.56	13.47	0.12
	1.68	13.60	0.12
	1.63	13.62	0.12
	1.67	13.73	0.12
	1.55	13.35	0.12
	1.51	13.27	0.11
	1.42	13.35	0.11
	1.59	13.25	0.12
	1.54	13.26	0.12
	1.72	13.44	0.13
	1.68	13.72	0.12
	1.70	13.72	0.12
	1.71	13.78	0.12
	1.61	13.55	0.12
	1.60	13.24	0.12
	1.47	13.27	0.11
	1.51	13.42	0.11
	1.55	13.44	0.12

1.59	13.39	0.12
1.62	13.46	0.12
1.69	13.66	0.12
1.70	13.70	0.12
1.67	13.53	0.12
1.66	13.59	0.12
1.65	13.64	0.12
1.67	13.73	0.12
1.78	13.73	0.13
1.75	13.70	0.13
1.59	13.61	0.12
1.56	13.24	0.12
1.64	13.49	0.12
1.60	13.70	0.12
1.69	13.69	0.12
1.68	13.58	0.12
1.70	13.45	0.13
1.62	13.27	0.12
1.78	13.69	0.13
1.71	13.77	0.12
1.66	13.65	0.12
1.80	13.65	0.13
1.77	13.66	0.13
1.74	13.61	0.13
1.70	13.56	0.13
1.62	13.30	0.12
1.63	13.46	0.12
1.75	13.74	0.13
1.68	13.72	0.12
1.55	13.28	0.12
1.66	13.54	0.12
1.72	13.72	0.13
1.73	13.67	0.13
1.70	13.51	0.13
1.53	13.36	0.11
1.47	13.36	0.11
1.62	13.23	0.12
1.57	13.24	0.12
1.64	13.24	0.12
1.64	13.26	0.12
1.69	13.40	0.13
1.73	13.67	0.13
1.73	13.56	0.13
1.69	13.67	0.12
1.65	13.61	0.12
1.58	13.26	0.12
1.50	13.39	0.11
1.79	13.61	0.13

	1.81	13.63	0.13
	1.68	13.53	0.12
	1.70	13.43	0.13
	1.45	13.22	0.11
	1.59	13.19	0.12
	1.58	13.36	0.12
	1.53	13.25	0.12
	1.57	13.45	0.12
	1.66	13.44	0.12
TEST 12	0.98	12.21	0.08
	0.64	12.24	0.05
	0.86	12.19	0.07
	0.97	12.67	0.08
	1.23	13.10	0.09
	1.33	13.61	0.10
	1.42	13.55	0.10
	1.37	13.62	0.10
	1.42	13.52	0.10
	1.27	13.59	0.09
	1.25	13.56	0.09
	1.34	13.61	0.10
	1.30	13.59	0.10
	1.35	13.57	0.10
	1.35	13.57	0.10
	1.43	13.46	0.11
	1.21	13.43	0.09
	1.21	13.39	0.09
	1.31	13.53	0.10
	1.38	13.48	0.10
	1.42	13.51	0.11
	1.37	13.53	0.10
	1.41	13.55	0.10
	1.34	13.37	0.10
	1.31	13.11	0.10
	1.22	13.13	0.09
TEST 13	0.96	11.56	0.08
	0.94	11.73	0.08
	1.00	11.88	0.08
	1.10	12.06	0.09
	1.06	12.06	0.09
	1.09	12.04	0.09
	0.99	12.02	0.08
	1.10	12.22	0.09
	1.11	12.02	0.09
	1.07	12.06	0.09
	1.22	12.07	0.10

1.19	12.11	0.10
1.13	11.94	0.09
1.09	12.09	0.09
1.23	12.14	0.10
1.35	12.54	0.11
1.59	13.09	0.12
1.59	13.33	0.12
1.58	12.93	0.12
1.51	12.91	0.12
1.58	13.01	0.12
1.64	13.36	0.12
1.75	13.43	0.13
1.66	13.38	0.12
1.65	13.14	0.13
1.58	12.89	0.12
1.57	13.00	0.12
1.79	13.30	0.13
1.74	13.30	0.13
1.71	13.33	0.13
1.61	13.20	0.12
1.56	13.09	0.12
1.56	13.03	0.12
1.74	13.31	0.13
1.86	13.39	0.14
1.76	13.37	0.13
1.64	13.04	0.13
1.76	13.11	0.13
1.83	13.44	0.14
1.75	13.44	0.13
1.81	13.37	0.14
1.82	13.52	0.13
1.83	13.47	0.14
1.72	13.45	0.13
1.85	13.36	0.14
1.81	13.41	0.14
1.72	13.30	0.13

APPENDIX B: OUTPUT CALCULATION RESONANT COLUMN

TEST 6

TEST 6	*p'* (kPa)	*G* (MPa)	Average strain (%)	$G/G_{max,\ RC}$ (-)	$G/G_{max,\ BE}$ (-)
first step	50	83	0.0008	1.00	0.98
		85	0.0009	1.00	1.00
		79	0.0009	0.95	0.93
		81	0.0040	0.97	0.94
		78	0.0076	0.94	0.92
		76	0.0164	0.91	0.89
		76	0.0274	0.91	0.89
second step	100	87	0.0006	1.00	0.87
		84	0.0016	0.97	0.84
		87	0.0021	1.00	0.87
		80	0.0084	0.91	0.80
		80	0.0129	0.92	0.80
		82	0.0156	0.95	0.83
		80	0.0308	0.92	0.81
		80	0.0392	0.92	0.80
third step	300	172	0.0009	1.00	1.00
		173	0.0011	1.00	1.00
		166	0.0015	0.96	0.99
		154	0.0027	0.89	0.92
		137	0.0119	0.80	0.82
		137	0.0144	0.80	0.82
		139	0.0159	0.81	0.83
		141	0.0160	0.82	0.84
		147	0.0168	0.85	0.88
fourth step	100	127	0.0011	1.00	0.96
		133	0.0017	1.00	1.00
		135	0.0019	1.00	1.00
		131	0.0026	1.00	0.99
		109	0.0131	0.86	0.83
		107	0.0242	0.84	0.81
fifth step	50	95	0.0015	1.00	1.00
		95	0.0020	1.00	1.00
		91	0.0034	0.96	1.00

		81	0.0088	0.85	1.00
		81	0.0122	0.86	1.00
		80	0.0212	0.84	1.00
		80	0.0257	0.84	1.00
		82	0.0261	0.87	1.00

TEST 7

TEST 7	***p'*** **(kPa)**	***G*** **(MPa)**	**Average strain (%)**	$G/G_{max, RC}$ **(-)**
first step	50	107	0.0037	1.00
		105	0.0044	0.98
		103	0.0052	0.97
		99	0.0071	0.93
		89	0.0158	0.84
		87	0.0250	0.81
		86	0.0332	0.80
		85	0.0405	0.80
		87	0.0381	0.82
second step	100	156	0.0025	1.00
		160	0.0027	1.00
		152	0.0040	0.98
		151	0.0053	0.97
		139	0.0127	0.89
		137	0.0199	0.88
		135	0.0293	0.87
		136	0.0328	0.87
third step	300	234	0.0011	1.00
		230	0.0014	0.98
		228	0.0017	0.98
		226	0.0023	0.97
		225	0.0027	0.96
		215	0.0049	0.92
		203	0.0142	0.87
		201	0.0204	0.86
		200	0.0298	0.85
fourth step	100	149	0.0027	1.00
		148	0.0035	0.99
		147	0.0043	0.98
		137	0.0076	0.92
		127	0.0155	0.85
		123	0.0258	0.83

		122	0.0362	0.82
fifth step	50	127	0.0032	1.00
		130	0.0036	1.00
		130	0.0042	1.00
		128	0.0055	1.00
		112	0.0163	0.88
		110	0.0239	0.87
		110	0.0290	0.87

TEST 8

TEST 8	***p'*** **(kPa)**	***G*** **(MPa)**	**Average strain (%)**	**$G/G_{max,\ RC}$ (-)**
first step	50	115	0.0020	1.00
		118	0.0022	1.00
		119	0.0027	1.00
		116	0.0038	1.00
		117	0.0047	1.00
		117	0.0057	1.00
		114	0.0079	0.99
		108	0.0137	0.94
		111	0.0141	0.96
		115	0.0164	0.99
second step	100	209	0.0017	1.00
		207	0.0026	0.99
		206	0.0032	0.98
		197	0.0042	0.94
		194	0.0050	0.93
		189	0.0081	0.90
		187	0.0094	0.89
		186	0.0106	0.89
third step	300	253	0.0012	1.00
		259	0.0014	1.00
		261	0.0016	1.00
		260	0.0020	1.00
		261	0.0024	1.00
		262	0.0029	1.00
		253	0.0037	1.00
		245	0.0055	0.97
		238	0.0080	0.94
		230	0.0110	0.91
		231	0.0120	0.91

fourth step	100	204	0.0016	1.00
		203	0.0020	0.99
		204	0.0025	1.00
		203	0.0031	1.00
		205	0.0036	1.00
		209	0.0037	1.00
		204	0.0046	1.00
		205	0.0057	1.00
		205	0.0072	1.00
		198	0.0109	0.97
fifth step	50	156	0.0016	1.00
		160	0.0018	1.00
		164	0.0020	1.00
		164	0.0025	1.00
		158	0.0033	1.00
		156	0.0037	1.00
		150	0.0054	0.96
		137	0.0109	0.88
		131	0.0187	0.84
		113	0.0211	0.72

TEST 9

TEST 9	***p'*** **(kPa)**	***G*** **(MPa)**	**Average strain (%)**	**$G/G_{max, RC}$ (-)**	**$G/G_{max, BE}$ (-)**
first step	50	224	0.0009	1.00	0.99
		218	0.0013	0.97	0.96
		217	0.0015	0.97	0.96
		197	0.0041	0.88	0.87
		203	0.0048	0.91	0.90
		188	0.0084	0.84	0.83
		182	0.0129	0.81	0.80
		178	0.0176	0.80	0.79
second step	100	275	0.0010	1.00	1.00
		269	0.0012	0.98	1.00
		260	0.0015	0.95	1.00
		250	0.0024	0.91	0.96
		251	0.0030	0.91	0.96
		245	0.0043	0.89	0.94
		240	0.0059	0.87	0.92
		230	0.0093	0.84	0.88
		213	0.0192	0.78	0.82

third step	300	411	0.0005	1.00	0.96
		412	0.0007	1.00	0.96
		406	0.0008	0.99	0.95
		395	0.0011	0.96	0.92
		379	0.0015	0.92	0.89
		341	0.0025	0.83	0.80
		299	0.0049	0.73	0.70
		281	0.0079	0.68	0.66
		274	0.0109	0.67	0.64
fourth step	100	297	0.0007	1.00	0.94
		310	0.0008	1.00	0.98
		307	0.0010	1.00	0.97
		305	0.0011	1.00	0.96
		312	0.0015	1.00	0.98
		309	0.0020	1.00	0.97
		306	0.0026	1.00	0.96
		303	0.0036	1.00	0.96
		277	0.0070	0.93	0.87
		272	0.0095	0.91	0.86
		259	0.0140	0.87	0.82
fifth step	50	237	0.0011	1.00	0.89
		244	0.0014	1.00	0.91
		236	0.0021	1.00	0.88
		237	0.0027	1.00	0.89
		234	0.0033	0.99	0.88
		234	0.0038	0.99	0.88
		235	0.0050	0.99	0.88
		235	0.0066	0.99	0.88
		224	0.0102	0.95	0.84
		212	0.0161	0.89	0.79

TEST 10

TEST 10	***p'* (kPa)**	***G* (MPa)**	**Average strain (%)**	**$G/G_{max, RC}$ (-)**	**$G/G_{max, BE}$ (-)**
first step	50	180	0.0018	1.00	0.93
		187	0.0020	1.00	0.97
		181	0.0028	1.00	0.94
		159	0.0053	0.88	0.82
		150	0.0083	0.83	0.78
		149	0.0111	0.83	0.77
		154	0.0109	0.85	0.80
		156	0.0123	0.87	0.81

second step	100	202	0.0011	1.00	0.95
		202	0.0014	1.00	0.95
		204	0.0016	1.00	0.96
		203	0.0018	1.00	0.95
		198	0.0022	0.98	0.93
		188	0.0035	0.93	0.88
		167	0.0080	0.83	0.78
		162	0.0132	0.80	0.76
		162	0.0164	0.80	0.76
		161	0.0221	0.80	0.76
third step	300	228	0.0014	1.00	0.99
		227	0.0016	0.99	0.98
		225	0.0019	0.99	0.97
		228	0.0022	1.00	0.99
		219	0.0027	0.96	0.95
		218	0.0032	0.95	0.94
		192	0.0092	0.84	0.83
		191	0.0118	0.84	0.83
		194	0.0129	0.85	0.84
fourth step	100	197	0.0011	1.00	0.77
		198	0.0013	1.00	0.77
		199	0.0016	1.00	0.78
		192	0.0019	0.98	0.75
		189	0.0021	0.96	0.74
		180	0.0029	0.92	0.70
		170	0.0049	0.86	0.67
		158	0.0100	0.81	0.62
		156	0.0149	0.79	0.61
fifth step	50	205	0.0013	1.00	0.90
		209	0.0018	1.00	0.92
		212	0.0022	1.00	0.93
		202	0.0029	0.99	0.88
		194	0.0038	0.95	0.85
		156	0.0162	0.76	0.68
		157	0.0164	0.77	0.69

TEST 11

TEST 11	***p'*** **(kPa)**	***G*** **(MPa)**	**Average strain (%)**	$G/G_{max, RC}$ **(-)**	$G/G_{max, BE}$ **(-)**
first step	50	219	0.0017	1.00	0.96
		217	0.0019	0.99	0.95

		214	0.0021	0.98	0.94
		213	0.0024	0.97	0.93
		212	0.0027	0.97	0.93
		210	0.0035	0.96	0.92
		206	0.0048	0.94	0.91
		200	0.0069	0.91	0.88
		184	0.0152	0.84	0.81
		187	0.0160	0.85	0.82
second step	100	252	0.0008	1.00	0.98
		255	0.0010	1.00	0.99
		253	0.0012	1.00	0.98
		242	0.0016	0.96	0.94
		241	0.0018	0.96	0.93
		233	0.0026	0.93	0.90
		202	0.0071	0.80	0.78
		203	0.0086	0.81	0.79
		200	0.0118	0.80	0.78
		205	0.0123	0.81	0.79
third step	300	338	0.0007	1.00	0.96
		334	0.0009	0.99	0.95
		321	0.0011	0.95	0.91
		317	0.0013	0.94	0.90
		286	0.0022	0.84	0.81
		270	0.0034	0.80	0.77
		248	0.0060	0.73	0.70
		234	0.0109	0.69	0.66
fourth step	100	306	0.0006	1.00	1.00
		308	0.0007	1.00	1.00
		304	0.0009	0.99	0.99
		293	0.0013	0.96	0.95
		298	0.0015	0.97	0.97
		281	0.0021	0.92	0.91
		283	0.0027	0.92	0.92
		241	0.0060	0.79	0.78
fifth step	50	285	0.0010	1.00	0.96
		285	0.0014	1.00	0.96
		278	0.0019	0.98	0.93
		258	0.0028	0.91	0.87
		233	0.0048	0.82	0.78
		214	0.0083	0.75	0.72
		203	0.0127	0.71	0.68

TEST 12

TEST 12	*p'* (kPa)	*G* (MPa)	Average strain (%)	$G/G_{max, RC}$ (-)	$G/G_{max, BE}$ (-)
first step	50	110	0.0017	1.00	0.88
		112	0.0021	1.00	0.90
		109	0.0029	1.00	0.88
		108	0.0038	0.99	0.87
		107	0.0050	0.97	0.85
		104	0.0071	0.95	0.84
		99	0.0119	0.90	0.80
		92	0.0261	0.84	0.74
second step	100	169	0.0009	1.00	1.00
		161	0.0013	0.95	1.00
		159	0.0017	0.94	0.99
		161	0.0020	0.95	1.00
		150	0.0038	0.89	0.93
		141	0.0074	0.83	0.87
		139	0.0104	0.82	0.86
		139	0.0136	0.82	0.86
		139	0.0170	0.82	0.86
third step	300	193	0.0013	1.00	0.98
		191	0.0017	0.99	0.97
		193	0.0020	1.00	0.98
		185	0.0026	0.96	0.94
		186	0.0027	0.96	0.95
		180	0.0041	0.93	0.92
		177	0.0057	0.91	0.90
		177	0.0071	0.92	0.90
		178	0.0091	0.92	0.90
fourth step	100	167	0.0009	1.00	0.99
		173	0.0011	1.00	1.00
		170	0.0014	1.00	1.00
		172	0.0017	1.00	1.00
		175	0.0021	1.00	1.00
		174	0.0027	1.00	1.00
		171	0.0038	1.00	1.00
		161	0.0062	0.96	0.95
		155	0.0095	0.92	0.91
		155	0.0131	0.92	0.92
fifth step	50	149	0.0011	1.00	1.00

		151	0.0012	1.00	1.00
		149	0.0021	1.00	1.00
		142	0.0031	0.95	0.95
		141	0.0041	0.95	0.95
		137	0.0061	0.92	0.91
		132	0.0091	0.89	0.88
		133	0.0112	0.90	0.89
		133	0.0149	0.89	0.89

TEST 13

TEST 13	***p'* (kPa)**	***G* (MPa)**	**Average strain (%)**	**$G/G_{max, RC}$ (-)**	**$G/G_{max, BE}$ (-)**
first step	50	139	0.0010	1.00	0.96
		131	0.0015	0.95	0.91
		131	0.0018	0.94	0.91
		125	0.0028	0.90	0.87
		126	0.0034	0.91	0.88
		119	0.0055	0.86	0.83
		113	0.0090	0.82	0.79
		107	0.0160	0.77	0.75
second step	100	166	0.0016	1.00	1.00
		165	0.0021	1.00	1.00
		162	0.0025	0.98	1.00
		161	0.0029	0.97	1.00
		157	0.0040	0.95	1.00
		152	0.0060	0.92	0.96
		148	0.0087	0.89	0.94
		151	0.0101	0.91	0.96
		152	0.0127	0.92	0.96
third step	300	215	0.0009	1.00	0.96
		215	0.0011	1.00	0.96
		209	0.0015	0.97	0.93
		204	0.0020	0.95	0.91
		200	0.0026	0.93	0.90
		190	0.0039	0.88	0.85
		188	0.0051	0.87	0.84
		181	0.0075	0.84	0.81
		178	0.0101	0.83	0.79
		177	0.0131	0.82	0.79
fourth step	100	182	0.0011	1.00	0.93
		186	0.0014	1.00	0.95

		177	0.0020	0.97	0.90
		176	0.0026	0.96	0.90
		156	0.0050	0.85	0.80
		155	0.0061	0.85	0.79
		155	0.0074	0.85	0.79
		159	0.0081	0.87	0.81
fifth step	50	162	0.0013	1.00	1.00
		159	0.0017	0.98	1.00
		163	0.0019	1.00	1.00
		157	0.0027	0.97	1.00
		154	0.0036	0.95	1.00
		150	0.0049	0.92	1.00
		149	0.0062	0.92	1.00
		146	0.0085	0.90	1.00
		141	0.0127	0.87	0.98
		141	0.0162	0.87	0.98

APPENDIX C: CHANGE IN VOLUME AND HEIGHT

	p' (kPa)	Measurement	Change in volume (ml)	Change in height (0.1 mm)
TEST 6	50	Start	0.6	14
		End	2.6	58
	100	Start	2.4	59
		End	4.4	62
	300	Start	3.2	27
		End	3.2	28
	100	Start	-0.8	-11
		End	-1	-15
	50	Start	-0.6	-8
		End	-0.6	-8
TEST 7	50	Start	0.8	2
		End	-	-
	100	Start	2.6	14
		End	-	-
	300	Start	1.4	1
		End	-	-
	100	Start	-1.6	1
		End	-	-
	50	Start	-0.6	-8
		End	-	-
TEST 8	50	Start	2	2
		End	-	-
	100	Start	1	3
		End	-	-
	300	Start	1.8	5
		End	-	-
	100	Start	-0.8	-8
		End	-	-
	50	Start	-0.6	-3
		End	-	-
TEST 9	50	Start	2.6	3
		End	4	3
	100	Start	2.2	3
		End	2.2	3
	300	Start	1.6	14
		End	1.8	14
	100	Start	-0.8	-15
		End	-0.8	-15
	50	Start	-0.6	-3
		End	-0.6	-3

TEST 10	50	Start	0.8	11
		End	1.2	11
	100	Start	1	1
		End	1.2	1
	300	Start	1.8	21
		End	2	24
	100	Start	-1	2
		End	-1	2
	50	Start	-0.4	0
		End	-0.4	0
TEST 11	50	Start	0.2	0
		End	0.2	-1
	100	Start	0.6	0
		End	0.6	0
	300	Start	1.2	8
		End	1.4	8
	100	Start	-0.6	-12
		End	-0.6	-12
	50	Start	-0.2	-2
		End	-0.2	-2
TEST 12	50	Start	0.6	37
		End	1.8	50
	100	Start	2	21
		End	2	21
	300	Start	1	23
		End	1	27
	100	Start	-0.4	-11
		End	-0.4	-6
	50	Start	0	2
		End	0	2
TEST 13	50	Start	0.8	6
		End	0.8	7
	100	Start	0.8	1
		End	0.8	0
	300	Start	1.6	5
		End	1.6	7
	100	Start	-0.8	-5
		End	-0.8	-6
	50	Start	-0.4	1
		End	-0.4	1

APPENDIX D: VALUES OF G_{MAX} GAINED WITH PREDICTING EQUATIONS

‘M’ is Menq (2)
‘SR’ is Saxena and Reddy (3)
‘WT’ is Wichtmann and Triantafyllidis (4)
‘S’ is Senetakis et al. (5)

	p' (kPa)	**$G_{max, RC}$ (MPa)**	**$G_{max, BE}$ (MPa)**	**M - G_{max} (MPa)**	**SR - G_{max} (MPa)**	**WT - G_{max} (MPa)**	**S - G_{max} (MPa)**
TEST 6	50	83	85	61	46	71	58
	100	87	100	87	68	97	81
	300	172	167	153	128	160	136
	100	127	132	87	68	97	81
	50	95	77	61	46	71	58
TEST 7	50	107	-	74	54	94	77
	100	156	-	106	81	128	107
	300	234	-	185	152	211	179
	100	149	-	106	81	128	107
	50	127	-	74	54	94	77
TEST 8	50	115	-	80	58	103	86
	100	209	-	114	86	141	119
	300	253	-	199	161	232	199
	100	204	-	114	86	141	119
	50	156	-	80	58	103	86
TEST 9	50	224	226	66	49	80	65
	100	275	261	94	73	110	91
	300	411	428	165	138	180	152
	100	297	317	94	73	110	91
	50	237	neglected	66	49	80	65
TEST 10	50	180	193	64	47	75	62
	100	202	214	91	71	103	85
	300	228	231	159	133	169	143
	100	neglected	neglected	91	71	103	85
	50	205	229	64	47	75	62
TEST 11	50	219	228	71	52	89	73
	100	252	258	101	78	121	100
	300	338	353	178	147	200	168
	100	306	307	101	78	121	100
	50	285	298	71	52	89	73
TEST 12	50	110	125	60	45	69	57

	100	169	162	86	67	94	79
	300	193	196	150	126	155	132
	100	167	169	86	67	94	79
	50	149	150	60	45	69	57
TEST 13	50	139	144	63	47	74	61
	100	166	158	90	70	102	85
	300	215	224	158	132	167	142
	100	182	196	90	70	102	85
	50	162	144	63	47	74	61